Preparation and cooling of magnesium ion crystals for sympathetic cooling of highly charged ions in a Penning trap

Präparation und Kühlung von Magnesium-Ionenkristallen zum sympathetischen Kühlen von hoch geladenen Ionen in einer Penningfalle
Vom Fachbereich Physik der Technischen Universität Darmstadt zur Erlangung des Grades eines Doktors der Naturwissenschaften (Dr. rer. nat.)
genehmigte Dissertation von Tobias Murböck Dipl. Phys. aus Recklinghausen
Tag der Einreichung: 23.11.2016, Tag der Prüfung: 12.12.2016
Darmstadt 2017 — D 17

1. Gutachten: Prof. Dr. Gerhard Birkl
2. Gutachten: Prof. Dr. Wilfried Nörtershäuser

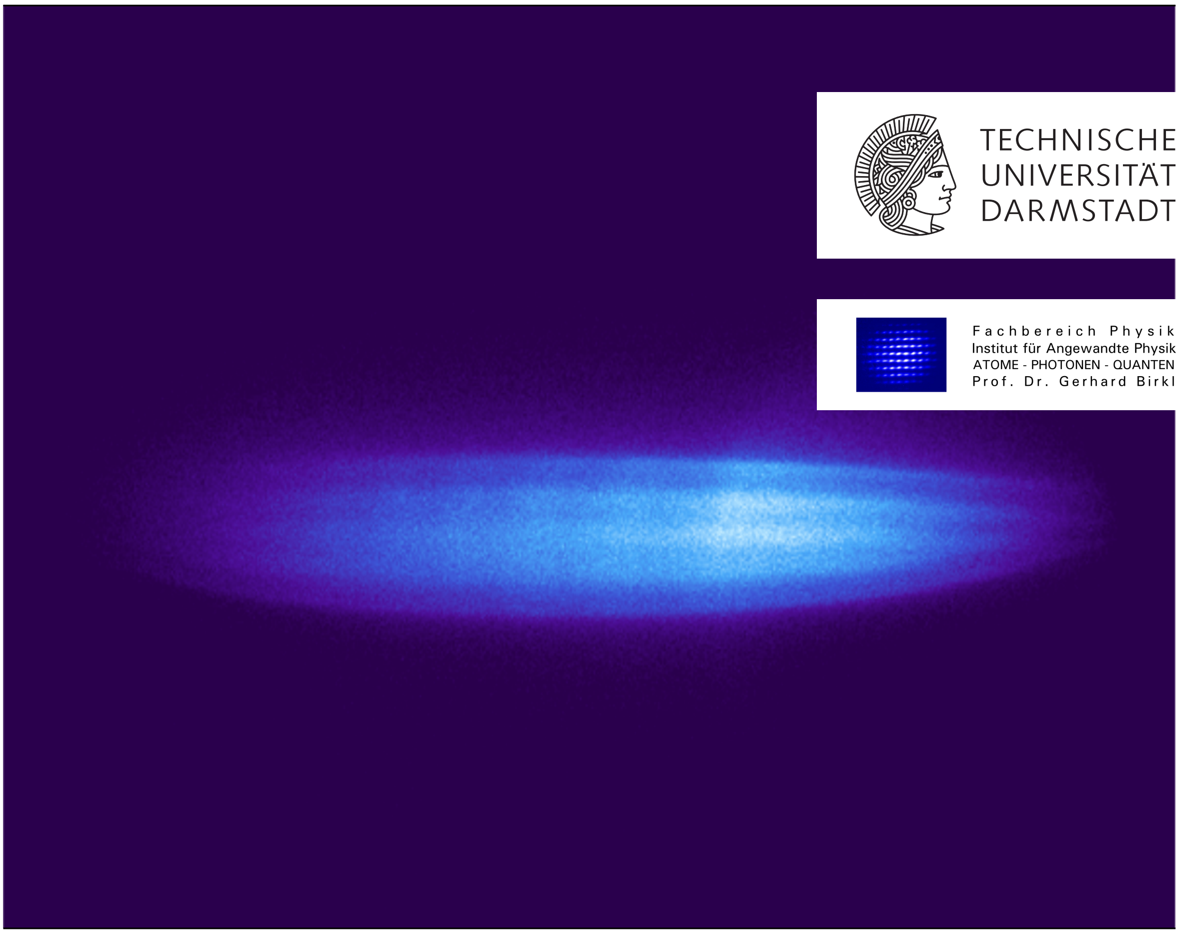
TECHNISCHE
UNIVERSITÄT
DARMSTADT
Fachbereich Physik
Institut für Angewandte Physik
ATOME - PHOTONEN - QUANTEN
Prof. Dr. Gerhard Birkl

Preparation and cooling of magnesium ion crystals for sympathetic cooling of highly charged ions in a Penning trap
Präparation und Kühlung von Magnesium-Ionenkristallen zum sympathetischen Kühlen von hoch geladenen Ionen in einer Penningfalle

Genehmigte Dissertation von Tobias Murböck Dipl. Phys. aus Recklinghausen

1. Gutachten: Prof. Dr. Gerhard Birkl
2. Gutachten: Prof. Dr. Wilfried Nörtershäuser

Tag der Einreichung: 23.11.2016
Tag der Prüfung: 12.12.2016

Darmstadt 2017 — D 17

Cover picture: Ion Coulomb crystal exhibiting several layers of singly charged magnesium ions.

Bitte zitieren Sie dieses Dokument als:
URN: urn:nbn:de:tuda-tuprints-60370
URL: http://tuprints.ulb.tu-darmstadt.de/6037

Dieses Dokument wird bereitgestellt von tuprints,
E-Publishing-Service der TU Darmstadt
http://tuprints.ulb.tu-darmstadt.de
tuprints@ulb.tu-darmstadt.de

Die Veröffentlichung steht unter folgender Creative Commons Lizenz:
Namensnennung – Keine kommerzielle Nutzung – Keine Bearbeitung
4.0 International
https://creativecommons.org/licenses/by-nc-nd/4.0

Contents

1 Motivation 3
- 1.1 Fine structure and hyperfine structure transitions 6
  - 1.1.1 Magnetic dipole transitions 6
  - 1.1.2 Fine structure transitions 8
  - 1.1.3 Hyperfine structure transitions 9

2 The SpecTrap experimental setup 13
- 2.1 Production and transport of highly charged ions (HCI) 15
  - 2.1.1 The EBIS for production of HCI 15
  - 2.1.2 The HITRAP low-energy beamline 17
  - 2.1.3 The SpecTrap beamline 20
- 2.2 The Mg^+ ion source 22
  - 2.2.1 Ion creation 22
  - 2.2.2 Ion extraction 23
  - 2.2.3 Ion numbers and bunch structure 25
- 2.3 The SpecTrap Penning trap system 28
  - 2.3.1 The magnet system 28
  - 2.3.2 Principles of charged particle trapping 30
  - 2.3.3 Single-ion motion in a Penning trap 31
  - 2.3.4 The Penning trap electrode design 33
  - 2.3.5 Expansion series for the potential of a cylindrical Penning trap 35
  - 2.3.6 Simulation of the coefficients C_n^i 37
  - 2.3.7 Measurements of the coefficients C_2^i 39
  - 2.3.8 Measurements of the coefficients C_1^i 41
- 2.4 Electronic components 42
  - 2.4.1 Non-destructive ion detector (NID) 42
  - 2.4.2 Axial resonators for resistive cooling 44
- 2.5 Experimental control and ion capture process 50
  - 2.5.1 The experiment control software 50
  - 2.5.2 The ion capture process 52
  - 2.5.3 Accumulation of ion bunches 53
  - 2.5.4 Ion capture with elevated potential or use of drift tube 2 54
- 2.6 Fluorescence detection 56
  - 2.6.1 The 280 nm laser system 57
  - 2.6.2 Fluorescence imaging and detectors 57
  - 2.6.3 Electronic transitions in $^{24}Mg^+$ 59

2.6.4 Single-ion fluorescence rate 61

3 Preparation of cold Mg$^+$ clouds 65
3.1 Buffer gas cooling 65
3.2 Laser Doppler cooling 68
3.2.1 Laser Doppler cooling of a free ion 69
3.2.2 Laser cooling of a trapped ion 70
3.3 Combined buffer gas and laser cooling of Mg$^+$ 74

4 Single- and multi-species Coulomb crystals 81
4.1 Properties of non-neutral plasma in thermodynamic equilibrium 83
4.2 The planar-shell model 90
4.3 Observation of single-species ion crystals 92
4.4 Multi-species ion crystals 95
4.5 Sympathetic cooling and storage time of multiply charged ions 101

5 Resonant-circuit measurements and a model for resistive cooling 105
5.1 Electronic ion detection with the resonant circuit 105
5.2 Temporal evolution of resonant circuit signals 108
5.3 A model for resistive cooling of large ion clouds 110
5.3.1 Resistive cooling of a single ion 111
5.3.2 Resistive cooling of an N-particle cloud 111
5.3.3 Resistive cooling beyond the center-of-charge motion 113
5.3.4 The rate equation for resistive cooling 116
5.3.5 Thermalization by ion-ion collisions (Spitzer self-collision rate) . 117
5.3.6 Shifts of the axial frequency in a non-linear potential 118
5.3.7 Comparison of the model with experimental signals 121

6 Conclusion and outlook 129

A Additional material 133
A.1 QED contributions to atomic quantities 133
A.2 Digital-trigger processing 134
A.3 Parameters of the HITRAP and SpecTrap beamline 135
A.4 Laser system, optical detection and atomic transitions 140
A.5 Emission characteristic of an oscillating dipole 142
A.6 The lineshape of atomic transitions 142
A.7 Matrix element for electric dipole transitions 144

B List of publications 145

Bibliography 147

Abstract

In this work, laser-cooled ion crystals containing 10^3 to 10^5 singly charged magnesium ions (Mg^+) were prepared in a Penning trap. The properties of the ion crystals and their structure displaying long-range ordering were analyzed by various non-destructive techniques. After creation of the Mg^+ ions in the form of ion bunches in an external source, the ions were injected into the Penning trap where their temperature was reduced by eight orders of magnitude within seconds using a combination of buffer gas cooling and Doppler laser cooling. The achieved temperatures in the millikelvin-regime were close to the theoretical Doppler-cooling limit and sufficiently low to induce the transition to a crystal phase exhibiting long-range ordering. The structure of these mesoscopic ion crystals is in agreement with a model describing the crystal as a set of planar shells. This allows for a derivation of properties such as the charge density or the temperature of the observed crystals. For the process of combined buffer-gas and Doppler laser cooling an analytical model has been developed, which explains the time development of the temperature and the fluorescence signal in agreement with the experimental results.

The external ion source for the production of singly charged magnesium ions was developed and characterized. A SIMION simulation of the ion creation and extraction process allows to describe the ion bunch structure and to increase the Mg^+ number by three orders of magnitude to 10^6 Mg^+ ions per bunch.

Other ion species with charge states between one (H_2^+, C^+, N_2^+, CO_2^+) and three (Ar^{3+}) were injected into the Mg^+ crystals. Ion crystals containing more than one ion species were observed with structures in agreement with the theory of centrifugal separation, which indicates sympathetic cooling of the non-fluorescing ion species. This preparation of mixed ion crystals is an important step towards the sympathetic cooling of highly charged ions (HCI) and paves the way to future investigations of HCI, which will enable a stringent test of bound-state quantum electrodynamics.

For supply of HCI to the SpecTrap experiment, the HITRAP low-energy beamline – including the pulsed drift tubes for ion deceleration and the electron beam ion source – were commissioned. Ion bunches containing several tens of thousands of argon ions (Ar^{13+}) were transported to the SpecTrap Penning trap. These ion numbers are sufficient for future spectroscopy of the fine structure splitting in boron-like Ar^{13+}.

In future experiments, the HCI shall be delivered by HITRAP and will possess large kinetic energies immediate after capture into the Penning trap, so that initial sympathetic cooling is not very efficient. Therefore, the SpecTrap Penning trap features axial resonators for pre-cooling of the HCI to the kelvin-regime by means of resistive cooling. An analytical model for resistive cooling of highly charged ions was developed in this work, which for the first time explained the measured resistive cooling signals of HCI given in literature. This model allows for a deeper understanding of the interaction between radial and axial degrees of freedom, it predicts the set of experimental parameters for optimum cooling, and it provides the time evolution of the HCI density and temperature during the cooling process.

Zusammenfassung

Im Rahmen dieser Arbeit wurden in einer Penningfalle lasergekühlte Ionenkristalle mit Teilchenzahlen zwischen 10^3 und 10^5 Magnesiumionen (Mg^+) erzeugt und die sich dabei ausbildenden Strukturen untersucht. Die Erzeugung der Ionenkristalle erfolgte dabei durch eine Kombination aus Puffergaskühlen und Laser-Dopplerkühlen, wodurch die Temperatur der Magnesiumionen innerhalb von wenigen Sekunden um acht Größenordnungen reduziert werden konnte. Die erreichte Temperatur der Mg^+-Ionen war mit einigen Millikelvin hinreichend gering zur Ausbildung einer Kristall-Phase. Die Struktur der Ionenkristalle aus mehreren, zueinander parallelen Kristallschalen konnte in Übereinstimmung mit einem theoretischen Modell beschrieben werden. Aus der Modellierung der Ionenkristalle ließen sich weitere Kristalleigenchaften wie die Temperatur oder Ladungsdichte ableiten. Der Prozess des kombinierten Kühlens wurde im Rahmen eines theoretischen Modells analytisch beschrieben und wesentliche Eigenschaften des Kühlverlaufs konnten in Übereinstimmung mit den experimentellen Befunden vorhergesagt werden.

Zur Erzeugung der einfach geladenen Magnesiumionen wurde eine zweistufige Quelle, bestehend aus Magnesiumofen und Ionisationseinheit, entwickelt. In Übereinstimmung mit einer Simulation der Ionenerzeugung und Ionenextraktion konnte die Ionenquelle experimentell und theoretisch beschrieben werden sowie die Mg^+-Produktion gegenüber einem vorherigen Design um mehr als drei Größenordnungen auf 10^6 Ionen pro Ionenpaket gesteigert werden.

In die Kristalle aus lasergekühltem Magnesium wurden weitere, sowohl einfach als auch mehrfach geladene Ionen injiziert und die Ausbildung von Ionenkristallen bestehend aus mehreren Ionenspezies beobachtet. Die Strukturen der heterogenen Ionenkristalle konnte im Einklang mit Theorien zur zentrifugalen Separation erklärt werden. Die Erzeugung von heterogenen Ionenkristallen bildet den Grundstein für das sympathetische Kühlen von hoch geladenen Ionen, welches an dreifach geladenem Argonionen beobachtet werden konnte. Dies ebnet den Weg zu weiterführenden Untersuchungen an gekühlten, hoch geladenen Ionen, welche einen präzisen Test von Vorhersagen der Quantenelektrodynamik ermöglichen werden.

Um hoch geladene Ionen für das SpecTrap-Experiment bereitzustellen, wurde die HITRAP-Beamline inklusive der beteiligten Komponenten wie der gepulsten Driftröhren in Betrieb genommen und Teilchenzahlen von mehreren zehntausend Argonionen (Ar^{13+}) an der SpecTrap-Falle nachgewiesen.

Im Ausblick auf das resistive Kühlen dieser hoch geladenen Ionen zur Vorbereitung auf laserspektroskopische Experimente in SpecTrap wurde ein theoretisches Modell zur Beschreibung des Kühlprozesses entwickelt, welches erstmals in der Lage ist, in der Literatur veröffentlichte Kühlspektren von hoch geladenen Ionen zu beschreiben. Durch eine Beschreibung der Wechselwirkung zwischen radialen und axialen Freiheitsgraden erlaubt dieses Modell ein tieferes Verständnis des Kühlprozesses und liefert darüber hinaus eine Vorhersage der Temperatur- und Dichteentwicklung der Ionenwolke im Verlauf des Kühlprozesses.

1 Motivation

Since the first stages of understanding the inner structure of atoms, simple atomic systems have been the testing ground for many fundamental theories in physics. Because of its simplicity, the hydrogen atom – consisting of a single proton and electron – allows a clear view to the fundamental properties of a quantum mechanical bound system. Consequently, the explanation of the hydrogen level structure with the non-relativistic Schrödinger equation in 1926 and only two years later with the relativistic Dirac equation were milestones in the development of quantum mechanics.

In 1947, an energy difference between the $^2S_{1/2}$ and $^2P_{1/2}$ hydrogen states was discovered, the so-called Lamb shift [1]. This was unpredicted by the Dirac theory, which states that two orbitals of both equal principal quantum number n and total angular momentum j should have the same energy. An explanation was provided in the framework of quantum electrodynamics (QED) [2], where the Lamb shift is a consequence of the self-energy of the electron and of vacuum fluctuations of the electromagnetic field.

Throughout the last decades, numerous experiments were performed addressing effects predicted by QED. Notably, the 1S–2S transition frequency in atomic hydrogen has been determined with a relative accuracy of 10^{-14}, which allows to determine one-loop contributions of QED to the Lamb shift with an accuracy of 10^{-5} [3]. Another example for a QED-sensitive quantity that has been determined with extraordinary precision is the anomalous magnetic moment of the electron. Over the recent decades it was the objective of ongoing investigation and has been measured with an accuracy of $2.8 \cdot 10^{-13}$ [4, 5, 6].

Among others, these experiments with low-mass systems have contributed to the reputation of QED as the best-tested theory in physics. Since QED in low-mass systems is by now well established, over the last 20-30 years increasing interest has been taken into QED sensitive measurements involving highly charged ions (HCIs). Like the hydrogen atom, highly charged ions with only a few or a single electron remaining are simple atomic systems from the viewpoint of spectroscopy and are thus accessible to high-precision experiments. However, they possess several characteristics that make them unique for high-precision tests of QED:

- While the contributions of free QED to particle quantities as the electron anomaly (Appendix, table A.1) has been tested with enormous precision, tests performed for bound-state QED (BS-QED) have been much less rigorous. High-Z ions offer a special opportunity to study BS-QED beyond the first-order contributions, since higher orders scale with $(\alpha Z)^n$ and thus increase rapidly with the atomic number Z: In H-like uranium, the second-order QED contribution to the Lamb shift accounts for $5 \cdot 10^{-3}$ of the total QED contributions, while it amounts

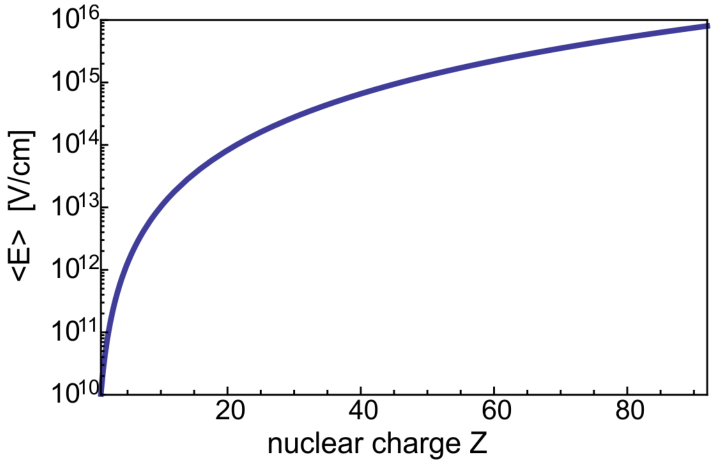

Figure 1.1: Expectation value of the electric field for an electron in the 1S ground state (non-relativistic approximation).

to $9 \cdot 10^{-5}$ in atomic hydrogen (Appendix, table A.2). For testing higher-order BS-QED, this makes HCI compatible to low-mass systems although the overall precision cannot yet compete.

- In HCI the nuclear charge Z approaches α^{-1} and the electron binding energy thus becomes comparable to mc^2. This strong coupling regime implies a completely relativistic consideration. Regarding the application of QED, strongly coupled systems are more complicated than weakly coupled ones. While higher-order contributions in low-Z systems can be treated perturbatively, other methods are needed to calculate QED effects in all orders when $(Z\alpha) \approx 1$. This makes the strong-coupling regime an interesting test ground for theoretical methods.

- The spatial extension of the 1S ground state in a H-like HCI scales inversely with Z and a single remaining electron is thus localized near the nucleus, where electric and magnetic fields are extraordinary strong. The scaling with Z^3 of the average electric field, that is experienced by an electron in the 1S orbital of a point-like nucleus, leads to average fields of $10^{16}\,\mathrm{V/cm}$ in U^{91+} (Fig. 1.1) and even $2.3 \cdot 10^{19}\,\mathrm{V/cm}$ at the surface of the nucleus [7]. These fields make HCI the natural choice for QED tests in strong fields.

- In highly charged ions, the large overlap of the electron wavefunction with the nucleus makes atomic transitions very sensitive to nuclear properties. Since the nuclear size or the nuclear magnetic moment and its distribution are often known with an insufficient accuracy, this is a challenge for theoretical QED predictions. In principle, there are two ways to deal with this situation: On one side, measurements with different electronic configurations of the same nucleus can be used to cancel most of the nuclear contributions. This scheme was e.g. proposed for the hyperfine structure transition of $^{209}\mathrm{Bi}^{80+}$ and $^{209}\mathrm{Bi}^{82+}$ by Shabaev and coworkers [8]. On the other side, the sensitivity of atomic transitions to the nucleus also offers an opportunity to determine nuclear properties, if QED calculations are trusted to give correct results [9].

During the last years, experiments with HCI sensitive to bound-state QED laid focus on measurements of the Lamb shift [10, 11, 12], the g-factor of a bound electron [13, 14], on fine structure (FS) and hyperfine structure (HFS) transitions [15]. Resonant laser spectroscopy of fine structure and hyperfine structure transitions has so far been performed in electron beam ion traps (EBITs) with low-Z [16, 17] and high-Z HCI [18, 9], and with high-Z HCI in storage rings [19, 20, 21, 22].

Although the achieved precision was high enough to allow stringent tests of QED, these experiments are still limited by severe restrictions due to the large Doppler broadening of the ions at high kinetic energies.

Therefore, the SpecTrap experiment aims at the precision laser spectroscopy of FS and HFS transitions of low-velocity highly charged ions stored in a Penning trap. For a reduction of the Doppler broadening, resistive and sympathetic cooling will be applied to reduce the ions' temperature to the sub-kelvin regime and thus allow laser spectroscopy of FS and HFS transitions with a precision of 10^{-8}.

To reach this goal, laser-cooled ion clouds of singly charged magnesium have been prepared in this thesis. The temperatures achieved are close to the theoretical Doppler-cooling limit and sufficiently low to allow the transition to a crystal phase. As a further step towards sympathetic cooling, other ion species with charge states between between one (H_2^+, C^+, N_2^+, CO_2^+) and three (Ar^{3+}) were injected into the Mg^+-Coulomb crystals. In the case of Ar^{3+}, an increase of the charge state lifetime provided clear evidence for sympathetic cooling. An electron beam ion trap (EBIT) has been connected to the Penning trap to deliver highly charged ions to the experiment, however, further investigation with HCI were hindered by poor vacuum conditions due to a helium leak in the superconducting magnet system. In the near future, the magnet system will be replaced by a new design (see Sec. 6), which will increase the storage times of HCI by several orders of magnitude. Once the new setup is operational, the SpecTrap experiment is ready to perform laser spectroscopy of highly charged ions. Boron-like Ar^{13+} will be the first candidate of choice, since the laser system for spectroscopy of the fine structure transition at 441 nm wavelength has already been set up [23].

This thesis is organized in six sections: This first chapter will give an overview of the basic properties of fine structure and hyperfine structure transitions, which are the main objective for precision laser spectroscopy of highly charged ions. The second chapter is dedicated to the experimental setup of the SpecTrap experiment. The third and fourth chapters present results of the preparation and structure analysis of Coulomb crystals. The fifth chapter presents a theoretical analysis of the resistive cooling process, which can be employed as an alternative cooling scheme for the highly charged ions in future experiments. Finally, the thesis concludes with an outlook to next steps and future prospects of the experiment.

1.1 Fine structure and hyperfine structure transitions

The fine structure (FS) and hyperfine structure (HFS) transitions, which are the objective of the SpecTrap experiment, are both transitions involving no change of the angular momentum ($\Delta L = 0$) and are thus not allowed according to the electric dipole selection rules. Consequently, these transitions are referred to as dipole forbidden transitions. However, the magnetic dipole moment of the radiation field still induces transitions between FS and HFS levels, but the transition rates are low compared to electronic dipole transitions.

Another complication arises from the wavelength of these dipole forbidden transitions: In common systems like atoms or singly charged ions, the energy difference involved with FS and HFS transitions is very small and the radiation for this transition lies in the microwave regime. Therefore, the detection of fluorescence photons from this transition would be very difficult (if not impossible).

However, the scaling of the transition energy of FS and HFS with the nuclear charge Z shifts these transitions for HCI into the optical regime. For the FS of few-electron ions, this is the case for ions with medium nuclear charge Z and for the HFS transition for high-Z ions.

1.1.1 Magnetic dipole transitions

The Hamiltonian describing the interaction of an electron with the time-dependent radiation field $\mathbf{A}$ can be expressed by ([24], p. 477 − 482)

$$\begin{aligned} H =& \frac{1}{2m_e}(\hat{\mathbf{p}} + e\mathbf{A})^2 + V(\mathbf{r}) \\ =& \frac{\hat{\mathbf{p}}^2}{2m_e} + V(\mathbf{r}) + \frac{e}{m_e}(\hat{\mathbf{p}} \cdot \mathbf{A} + \mathbf{A} \cdot \hat{\mathbf{p}}) + \frac{e^2}{2m_e}A^2 \\ =& \frac{\hat{\mathbf{p}}^2}{2m_e} + V(\mathbf{r}) + \frac{e\,\mathbf{A} \cdot \hat{\mathbf{p}}}{m_e} + \frac{e^2}{2m_e}A^2, \end{aligned} \tag{1.1}$$

where m_e denotes the electron mass, e the elementary charge, $\hat{\mathbf{p}} = -i\hbar\nabla$ the momentum operator, $\mathbf{A} = \mathbf{A}(\mathbf{r}, t)$ the vector potential of the field, and $V(\mathbf{r})$ the inner-atomic potential. In the last step of Eq.(1.1), it was used that in Lorenz gauge $\nabla \cdot \mathbf{A} = 0$ the operators $\hat{\mathbf{p}}$ and $\mathbf{A}$ commute. So far, all interactions involving the electron spin have been neglected.

The radiation field contributes two terms to the total Hamiltonian, one proportional to the vector potential $\mathbf{A}$ and one to A^2. The latter one describes two-photon transitions and is only relevant for very intense fields. It is thus neglected in the following discussion, and the interaction Hamiltonian H_I, which is responsible for electronic transitions between different atomic states, is defined by the remaining term proportional to $\mathbf{A} \cdot \hat{\mathbf{p}}$:

$$H_I = \frac{e\,\mathbf{A} \cdot \hat{\mathbf{p}}}{m_e}. \tag{1.2}$$

In the case of a monochromatic wave with frequency ω, the vector potential $\mathbf{A}$ can be written as

$$\mathbf{A}(\mathbf{r},t) = \frac{A_0}{2}\left(\mathbf{e}_{\text{pol}}\,e^{i(\mathbf{k}\cdot\mathbf{r}-\omega t)} + \mathbf{e}^{*}_{\text{pol}}\,e^{-i(\mathbf{k}\cdot\mathbf{r}-\omega t)}\right), \tag{1.3}$$

where $\mathbf{e}_{\text{pol}}$ is a unit vector describing the polarization and A_0 the amplitude of the field. With the abbreviations

$$\hat{T} = \frac{e^{i\mathbf{k}\cdot\mathbf{r}}}{\omega m_e}\mathbf{e}_{\text{pol}}\cdot\hat{\mathbf{p}} \approx \frac{1+i\mathbf{k}\cdot\mathbf{r}+\ldots}{\omega m_e}\,\mathbf{e}_{\text{pol}}\cdot\hat{\mathbf{p}}, \tag{1.4}$$

the interaction Hamiltonian H_I can be written as

$$H_I = \frac{e}{m_e}\mathbf{A}\cdot\hat{\mathbf{p}} = \frac{e\omega A_0}{2}\left(\hat{T}e^{-i\omega t} - \hat{T}^{*}e^{+i\omega t}\right). \tag{1.5}$$

For optical transitions, the wavelength is much larger than the involved atomic orbitals so that $\mathbf{k}\cdot\mathbf{r} \ll 1$. Therefore the expansions of the exponential function in equation (1.4) can be aborted after the first few terms. In the dipole approximation $e^{\pm i\mathbf{k}\cdot\mathbf{r}} \approx 1$ and the transition rate between the two states a and b is proportional to the matrix element

$$(\hat{T}_{ab})_{E1} = \langle b|\hat{T}|a\rangle = \frac{1}{\omega_{ab}m_e}\langle a|\mathbf{e}_{\text{pol}}\cdot\hat{\mathbf{p}}|b\rangle = i\langle b|\mathbf{e}_{\text{pol}}\cdot\mathbf{r}|a\rangle, \tag{1.6}$$

where the relation $\hat{\mathbf{p}} = -i(m_e/\hbar)\left[\mathbf{r},\hat{H}\right]$ has been used. Only transitions between states a and b with non-vanishing matrix element $\hat{T}_{ab}$ can be excited by electric dipole radiation, which is expressed by the well-known selection rules (table 1.1).

For electric-dipole-forbidden transitions, the transition probability is determined by the second-order term $i\,\mathbf{k}\cdot\mathbf{r}$, and the operator $\hat{T}$ becomes ([24], p. 172-177):

$$\hat{T} = \frac{i}{\omega\, m_e}(\mathbf{k}\cdot\mathbf{r})(\mathbf{e}_{\text{pol}}\cdot\hat{\mathbf{p}}). \tag{1.7}$$

Using the relations $\mathbf{r}\times\hat{\mathbf{p}} = \hat{\mathbf{L}}$ and $\mathbf{k}\times\mathbf{e}_{\text{pol}} \parallel \hat{\mathbf{B}}$, this term can be evaluated to

$$T_0\hat{T} = i\frac{e_0}{2m_e}\hat{\mathbf{L}}\cdot\hat{\mathbf{B}}_0 - \frac{e_0E_0}{2\hbar\omega}\left[\hat{H}\;(\mathbf{k}\cdot\mathbf{r})\;(\mathbf{e}_{\text{pol}}\cdot\mathbf{r}) - (\mathbf{k}\cdot\mathbf{r})\;(\mathbf{e}_{\text{pol}}\cdot\mathbf{r})\;\hat{H}\right], \tag{1.8}$$

where $T_0 \equiv eE_0 = ecB_0$ was introduced. The first part of equation (1.8) is responsible for magnetic dipole transitions ($M1$), the second one for electric quadrupole transitions ($E2$). As in the case of the electric dipole transitions, the strength of the transition and the selection rules are determined by the matrix elements $(\hat{T}_{ab})_{M1}$ and $(\hat{T}_{ab})_{E2}$ (table 1.1).

For $M1$ transitions, the interaction Hamiltonian can be interpreted as the interaction energy $\mathbf{M}\cdot\hat{\mathbf{B}}_0$ of the magnetic moment $\mathbf{M}$ with an external magnetic field $\hat{\mathbf{B}}_0$. With the Bohr magneton defined as $\mu_B = e\hbar/2m_e$ and the magnetic moment $\mathbf{M} = \mu_B\hat{\mathbf{L}}/\hbar$, the $M1$ term of the transition operator $T_0\hat{T}$ can be rewritten as:

$$\frac{1}{i}(T_0\hat{T})_{M1} = \mu_B\frac{\hat{\mathbf{L}}}{\hbar}\cdot\hat{\mathbf{B}}_0 = \mathbf{M}\cdot\hat{\mathbf{B}}_0. \tag{1.9}$$

If the spin of the electron is included, the magnetic moment in equation (1.9) has to be replaced with $\mathbf{M} = \mu_B(\hat{\mathbf{L}} + 2\hat{\mathbf{S}})/\hbar$.

E1	M1	E2
$\Delta J = 0, \pm 1$ ($J = 0 \not\to 0$)	$\Delta J = 0, \pm 1$ ($J = 0 \not\to 0$)	$\Delta J = 0, \pm 1, \pm 2$
$\Delta M_J = 0, \pm 1$	$\Delta M_J = 0, \pm 1$	$\Delta M_J = 0, \pm 1, \pm 2$
(M: $0 \not\to 0$ when $\Delta J = 0$)	(M: $0 \not\to 0$ when $\Delta J = 0$)	
parity change	no parity change	no parity change
$\Delta l = \pm 1$	$\Delta l = 0$	$\Delta l = 0, \pm 2$
$\Delta n =$ any	$\Delta n = 0$	$\Delta n =$ any
$\Delta L = 0, \pm 1$ ($0 \not\to 1$)	$\Delta L = 0$	$\Delta L = 0, \pm 1, \pm 2$ ($0 \not\to 0, 1$)
$\Delta S = 0$	$\Delta S = 0$	$\Delta S = 0$

Table 1.1: Selection rules for electric dipole (E1), magnetic dipole (M1) and electric quadrupole (E2) transitions. The rules in the upper half of the table are rigorous, while the rules in the lower half apply only in the case of LS-coupling, where L and S are good quantum numbers.

1.1.2 Fine structure transitions

The fine structure (FS) describes the splitting of spectral lines due to the combined effect of the electron spin and relativistic corrections to the non-relativistic Schrödinger equation.

The full Hamiltonian is given by ([24], p. 220-222)

$$H = H_0 - \frac{\hat{\mathbf{p}}^4}{8m_e^3c^2} + \frac{1}{2m_e^2c^2}\frac{1}{r}\frac{\mathrm{d}V}{\mathrm{d}r}\hat{\mathbf{L}}\cdot\hat{\mathbf{S}} + \frac{\hbar^2}{8m_e^2c^2}4\pi\left(\frac{Ze^2}{4\pi\epsilon_0}\right)\delta(\mathbf{r}). \tag{1.10}$$

H_0 represents the non-relativistic part of the Hamiltonian, the other terms are the relativistic correction to the kinetic energy, the spin-orbit coupling and the Darwin term, which is a correction to the potential energy. For an H-like ion the total energy does only depend on n and J and can be expressed in the form

$$E_{nj} = -E_R\frac{Z^2}{n^2}\left[\frac{Z^2\alpha^2}{n}\left(\frac{1}{J+1/2} - \frac{3}{4n}\right)\right], \tag{1.11}$$

where E_R denotes the Rydberg energy, Z the nuclear charge, α the fine structure constant, n the principal quantum number, and J the total angular momentum.

With regard to FS transitions in HCI, the importance of equation (1.11) lies in the fact that the energy difference for a FS transition with $\Delta n = 0$ and $\Delta J = 1$ scales with Z^4. This scaling behavior can be contributed to relativistic correction to the kinetic energy, which scales with p^4 according to equation (1.10) [25]. Since the orbital angular momentum $\mathbf{L} = \mathbf{r} \times \mathbf{p}$ is fixed for a given atomic orbital, and the orbital radius is proportional to $1/Z$, the momentum p increases with Z.

The resulting Z^4-dependence of the transition energy shifts FS transitions for medium-Z few-electron systems into the optical regime. A selection of laser-accessible fine structure transitions involving the ground-state of medium-Z HCI is given in the outlook in table 6.2.

1.1.3 Hyperfine structure transitions

The hyperfine structure (HFS) is caused by the interaction of the nuclear magnetic moment μ_I with the magnetic field B_J, which is created by the motion of the electron.

If the hyperfine structure is small compared to the fine structure, the nuclear spin I and the total electronic angular momentum J are good quantum numbers and the hyperfine Hamiltonian $\hat{H}_{\text{HFS}}$ can be written as

$$\hat{H}_{\text{HFS}} = -\mu_I \cdot \mathbf{B}_J = A\,\hat{\mathbf{I}} \cdot \hat{\mathbf{J}}, \tag{1.12}$$

where A is the hyperfine structure constant that has to be determined by experiment.

For hydrogen-like ions, the shift ΔE_{HFS} of the 1S-state relative to the unperturbed energy can be expressed in relativistic units ($\hbar = c = m_e = 1$) [8, 7]:

$$\begin{aligned} \Delta E^{1\text{s}}_{\text{HFS}} =& \frac{\alpha(\alpha Z)^3}{n^3} g_I \frac{m_e}{m_p} \frac{F(F+1) - I(I+1) - J(J+1)}{2J(J+1)(2L+1)} m_e c^2 \\ & \times M \left[A^{1\text{s}}(\alpha Z)(1-\delta^{1\text{s}})(1-\epsilon^{1\text{s}}) + (\frac{\alpha}{\pi}\Delta E_{\text{QED}}) \right], \end{aligned} \tag{1.13}$$

where m_e and m_p are the electron and the proton mass, g_I the nuclear g-factor defined by $g_I = \mu_I/\mu_N I$ with the nuclear magneton μ_N, I is the nuclear spin, J is the total electronic angular momentum, L is the orbital angular momentum, and $F = I + J$ is the total atomic angular momentum.

The first line of (1.13) contains the main contribution, whereas the second line contains several correction terms: The factor M is the correction for the finite nuclear mass, $A^{1\text{s}}(\alpha Z)$ the relativistic factor (i.e. corrections to the non-relativistic Fermi contact term), δ the correction due to the finite nuclear size, ϵ the distribution of the nuclear magnetization (Bohr-Weisskopf effect), and ΔE_{QED} indicates the quantum electrodynamical contributions.

According to (1.13), the hyperfine structure splitting scales with Z^3. This can be understood by considering the magnetic field generated by an electron in a circular orbit: The law of Biot-Savart states that $B(r) \sim I(r')|r - r'|^{-2}$. Since the current I is inversely proportional to the radius r', which in turn has an inverse dependence on the nuclear charge Z, the hyperfine structure separation is $\sim Z^3$ [25].

Whereas mid-Z ions possess FS transitions in the optical regime, laser-accessible HFS transitions are found in high-Z ions and are thus even more suited for a stringent test of bound-state QED in the regime of strong fields. Notable candidates for HFS spectroscopy are H-like $^{207}\text{Pb}^{81+}$ ($\lambda = 1020\,\text{nm}$), H-like $^{209}\text{Bi}^{82+}$ ($\lambda = 244\,\text{nm}$), H-like $^{235}\text{U}^{91+}$ ($\lambda = 1538\,\text{nm}$), and Li-like $^{209}\text{Bi}^{80+}$ ($\lambda = 1555\,\text{nm}$).

Measurements of HFS transition in HCI have so far been performed in electron beam ion traps [18, 9] and at the experimental storage ring (ESR) at GSI [19, 20, 21, 22], where a total accuracy of $6 \cdot 10^{-5}$ eV was achieved [22].

Although the accuracy of these experiments already exceeds the bound-state QED contributions to the measured transitions, a stringent test of QED is hindered by

	$^{209}\mathrm{Bi}^{82+}$	$^{209}\mathrm{Bi}^{80+}$	$\Delta' E = \Delta E^{2s} - \xi \Delta E^{1s}$
$\Delta E_{\mathrm{HFS,rel.}}$ [eV]	5.8393(3)	0.95849	
finite nuclear size effect [eV]	−0.6482(7)	−0.1138(2)	
Dirac value (including f.s.) [eV]			$-31.809 \cdot 10^{-3}$
Bohr-Weisskopf effect [eV]	−0.061(27)	−0.0134(2)	
one-electron QED [eV]	−0.0298	−0.0051(2)	$0.036 \cdot 10^{-3}$
interelectronic interaction [eV]			
order (1/Z)		−0.02948	$-29.995 \cdot 10^{-3}$
higher orders in (1/Z)		0.00024(12)	$0.255(3) \cdot 10^{-3}$
screened self-energy			$0.381 \cdot 10^{-3}$
screened vac. polarization			$-0.188(2) \cdot 10^{-3}$
screened total		0.00018(9)	
theory, total [eV]	5.100(27)	0.7971(2)	$-61.320(4) \cdot 10^{-3}$

Table 1.2: Contributions to the hyperfine structure in H-like $^{209}\mathrm{Bi}^{82+}$ and Li-like $^{209}\mathrm{Bi}^{80+}$ from [7], p. 196–199. The Bohr-Weisskopf effect for Li-like bismuth was not obtained with ab-initio methods, but was extracted from a combination of theoretical and experimental results for H-like bismuth [26]. $\Delta E_{\mathrm{HFS,rel.}}$ includes the non-relativistic contact-energy and relativistic corrections. The value of ξ in the specific difference Δ' is chosen to cancel the contribution of the Bohr-Weisskopf effect. Values for Δ' from [27]. Used abbrevations: finite-size (f.s.).

the large influence of nuclear properties, which are only known with an insufficient certainty. For HFS transitions in HCI the uncertainty of the Bohr-Weisskopf (BW) effect is typically the main contribution to the theoretical uncertainty, which is of the order of the total QED contributions (table 1.2). This means that QED contributions are effectively masked and a stringent QED test is not possible until nuclear models significantly advance in the description of the nuclear magnetic moment distribution.

A different approach for disentangling the nuclear and QED contributions is to compare the hyperfine structure transition of two different electronic configurations of the same nucleus. One prominent example is the nucleus of $^{209}\mathrm{Bi}$, which offers this opportunity with both HFS transitions in H-like $^{209}\mathrm{Bi}^{82+}$ and the Li-like $^{209}\mathrm{Bi}^{80+}$ in the optical regime. It was shown that the contributions of the Bohr-Weisskopf effect cancel in the calculation of the specific energy difference $\Delta' E = \Delta E^{2s} - \xi \Delta E^{1s}$ [28]. Measurements of the specific energy thus allow a stringent test of the QED and screened QED contributions to the hyperfine structure and were performed at the GSI in 2011 [21] and 2014 [29].

Once SpecTrap and HITRAP are fully operational, laser spectroscopy of sympathetically cooled H-like $^{209}\mathrm{Bi}^{82+}$ and the Li-like $^{209}\mathrm{Bi}^{80+}$ will be one of the main objectives. The QED contributions to the specific energy difference $\Delta' E$, which are mostly due to the screened self-energy and the screened vacuum polarization, amount to about $2 \cdot 10^{-4}$ eV. Assuming a HCI temperature of 4 K (conservative estimate), the Doppler broadening of the highly charged bismuth can be estimated to be of the order of 100 MHz (corresponding to an energy of $5 \cdot 10^{-7}$ eV). Accordingly, SpecTrap aims at a measurement of the HFS splitting in bismuth with a precision better than 10^{-8}, allowing a test of bound-state QED on the level of 10^{-3} (possibly limited by the uncertainty of theory).

2 The SpecTrap experimental setup

The SpecTrap experiment is located at the *GSI Helmholtzzentrum für Schwerionenforschung* (GSI) and the *Facility for Antiproton and Ion Research* (FAIR) at Darmstadt as a part of the HITRAP facility [30, 31]. HITRAP provides highly charged ions (HCI) to several experiments of the HITRAP collaboration, one being the SpecTrap experiment.

In general, techniques for the production of HCI include electron cyclotron resonance [32], optical ionization with high intensity lasers [33] and electron impact ionization. The latter is used in electron beam ion sources (EBISs), in which even the highest charge states up to bare uranium have been produced [34, 35]. However, the production rates are very low and are not sufficient for fluorescence spectroscopy, which is the goal of the SpecTrap experiment.

At GSI, highly charged ions of most elements in any charge state are routinely produced by shooting an ion beam of low charge state through a thin metal or carbon foil, the so-called stripper target. During this process, the ions in the primary beam donate electrons to the stripper target. The charge-state distribution after the stripping process depends on the velocity of the primary beam and can be adjusted to create large quantities of ions of even the highest charge states like Ur^{91+}, Bi^{82+}, Pb^{81+}.

Once created, the highly charged ions can be stored for experiments in the experimental storage ring (ESR), a synchrotron storage ring with 108 m circumference. Bunches of about 10^5 ions are extracted from the ESR and guided to the HITRAP facility, where a linear decelerator – consisting of a double drift buncher (DDB), an interdigital H-type (IH) structure and a radiofrequency quadrupole (RFQ) – decelerates the ions from energies of 4 MeV per nucleon to 6 keV per charge (Fig.2.1) [30]. Such energies are sufficiently low to allow dynamic capture in a cryogenic Penning trap, the *HITRAP cooling trap*, which is currently in commission and will be used to further reduce the ions' kinetic energy to $k_B \cdot 4\,\mathrm{K}$ by sympathetic cooling with electrons and by resistive cooling with a resonant circuit.

From the cooling trap, the cold HCI will be distributed via a low-energy beamline to the experiments. It features electrostatic elements, such as einzel lenses, kicker-benders and quadrupole doublets for guiding and re-focusing of the ion beam. Several diagnostic chambers are used for monitoring the beam quality and beam intensity. A detailed description of the beamline setup and performance is given in [36].

The low-energy beamline also features a dedicated EBIS as a source for highly charged ions. It allows experiments independent from the GSI accelerators and has been used in this work to produce Ar^{13+} bunches with ion numbers larger than

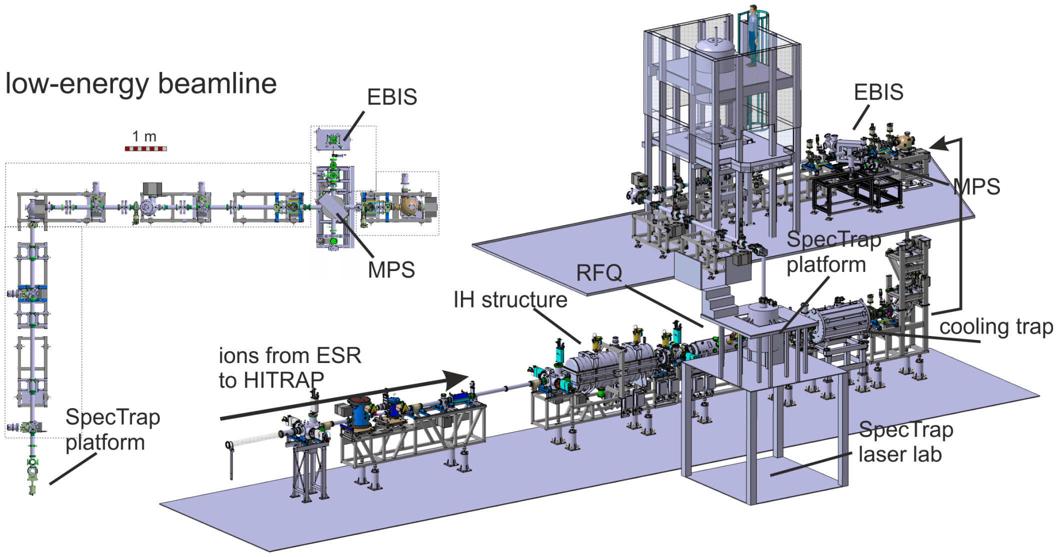

Figure 2.1: HITRAP platform (right) and top view of the horizontal low-energy beamline (left), which presents the part of the beamline located at the upper level. Drawings with courtesies from Zoran Andelkovic.

10^5. The ions have been transported at energies of 4 keV per charge from the EBIS through the beamline to the SpecTrap platform where they are decelerated by pulsed drift tubes (DT) to energies of a few hundreds of eV per charge. An electrostatic quadrupole bender directs the ions to the vertical part of the SpecTrap beamline, where they are transported to the SpecTrap Penning trap and dynamically captured by fast switching of the trap electrodes.

For sympathetic cooling, the HCI can be stored simultaneously with laser-cooled, singly-charged magnesium ions. To this end, a homebuilt electron-impact ion source is used, which is placed in the horizontal part of the SpecTrap beamline and produces μs-bunches of up to 10^6 Mg^+ ions at a repetition rate of 1 Hz. The setup and performance of the Mg^+ source are described in [37]. The laser system for Mg^+ laser cooling is placed in the SpecTrap laser lab below the SpecTrap platform. It consists of single-mode fiber laser providing light at 1118 nm and two cavities, each of them doubling the frequency to ultimately obtain 20 mW laser power at 280 nm for laser cooling.

The following chapter is designated to an overview of the experimental setup, including the beamlines, the ion sources, the Penning trap system and the experiment control software. The discussion of the individual components also includes the experimental characterization of the presented elements with an evaluation of the obtained results.

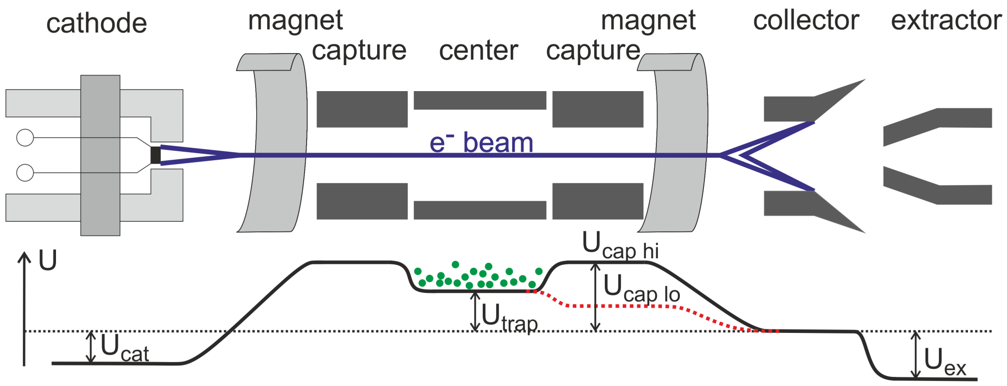

Figure 2.2: Schematic drawing of an EBIS (top) and the potential (below). The dashed line indicates the potential during the ion extraction process.

2.1 Production and transport of highly charged ions (HCI)

For supply of highly charged ions, the SpecTrap experiment is connected to the low-energy beamline, which is part of the HITRAP facility (Fig. 2.1). In this work, the creation of highly charged ions, their transport and capture into the SpecTrap Penning trap with consecutive confinement were realized. Setup and performance of the low-energy beamline are described in [36, 38]. A non-destructive ion detector (NID), which detects incoming ion bunches by the image charges induced in the upper capture electrode, is described in [39].

2.1.1 The EBIS for production of HCI

For the creation of highly charged ions, the low-energy beamline features a compact, commercially available electron beam ion source (EBIS) (model *Dresden EBIT* by DREEBIT). It is reliable, easy to use, and served as a source for HCI during this work, since there was no beam available from the GSI accelerators.

In an EBIS, an electron beam of several milliampere is created in the cathode by thermal emission (Fig. 2.2). The electrons are accelerated by the potential difference between the cathode and the trapping region where a magnetic field focuses the electron beam. After leaving the trapping volume, the electron beam is dumped at the collector electrodes.

Ions are created by electron impact ionization from neutral gas in the trap center. The electron impact energy, which is given by the acceleration voltage of the electron beam, defines the ionization efficiency as well as the highest achievable charge state. Radial confinement of the ions is provided by the magnetic field and the negative space-charge potential of the electron beam, which attracts the ions to the trap axis. Confinement along the trap axis is provided by two capture electrodes, which are set to a higher potential with regard to the trap center.

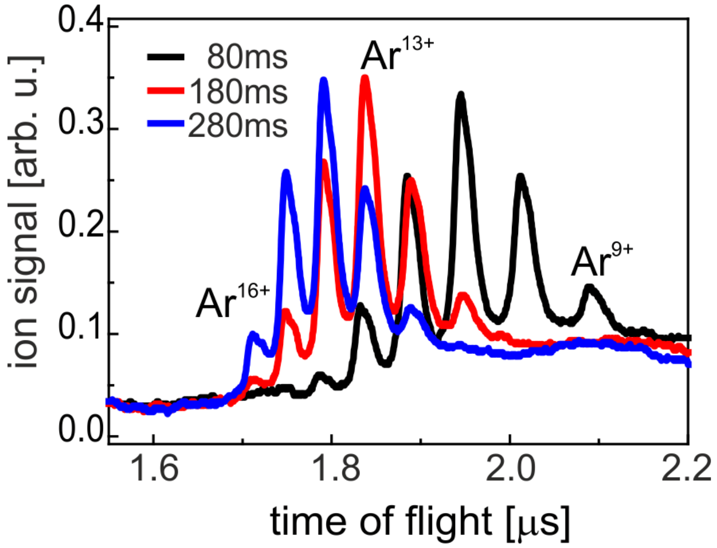

Figure 2.3: Time-of-flight signal of Ar^{n+} ions at the first Faraday cup after the EBIS. The ions were produced with breeding times τ_{breed} between 80 ms and 280 ms.

As long as the ions are confined in the EBIS their charge state increases due consecutive ionization processes until an equilibrium between electron-impact ionization and electron capture processes is reached. The trapping duration is hence referred to as the breeding time τ_{breed} and can be used to optimize the production of a specific charge state (Fig. 2.3).

For ion extraction from the EBIS, the voltage of exit capture electrode is reduced. To quicken the extraction process, a negative potential is applied to the extractor electrode, which increases the initial acceleration of the ions out of the trap volume. The transport energy of the ions through the beamline is determined by the trap potential, which is was usually set to 4 kV. A transport energy of 4 keV per charge has been found to be the optimum trade-off between transport losses due to space charge effects, which are more severe for lower energies, and the reduction in deceleration efficiency of the pulsed drift tube, which significantly decreases for higher transport energies. Typical EBIS parameters for the production of Ar^{13+} are summarized in table A.4.

With the present type of EBIS, highly charged ions can be produced from any neutral atom or singly charged ion species that is introduced into the trapping volume. Ions of gases or substances with significant vapor pressure are most easily produced, since the neutral atoms can enter the EBIS via a needle valve, which allows to adjust the residual gas pressure. However, HCI can be created from almost any element, if a separated ion source is used to first create bunches of singly charged ions, which are in a second step injected into the EBIS for consecutive charge breeding [40].

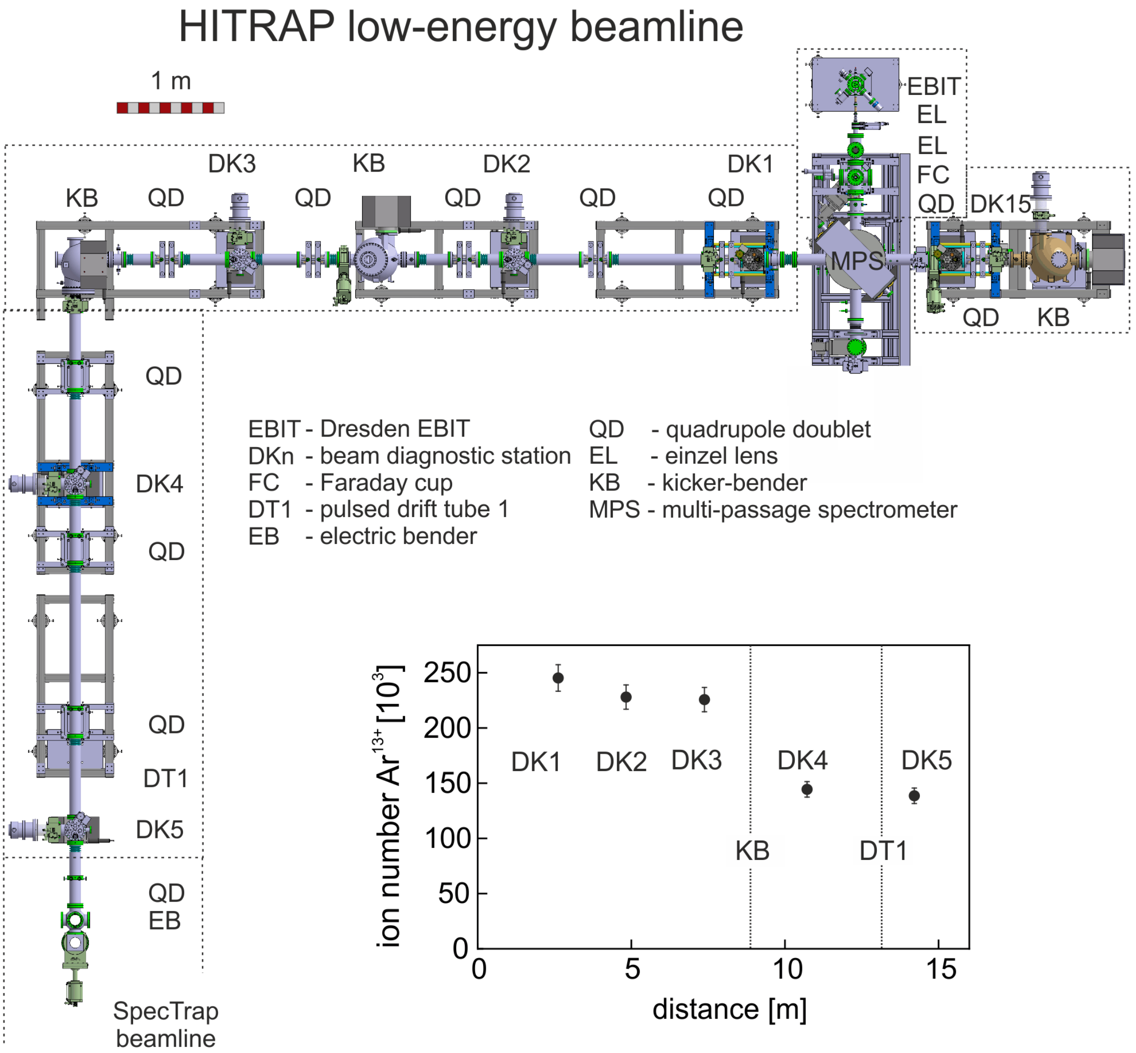
HITRAP low-energy beamline
1 m
EBIT
EL
EL
FC
QD
DK15
QD
KB
KB
QD
DK3
QD
KB
DK2
QD
QD
DK1
QD
MPS
QD
DK4
QD
QD
DT1
DK5
QD
EB
SpecTrap beamline
EBIT - Dresden EBIT
DKn - beam diagnostic station
FC - Faraday cup
DT1 - pulsed drift tube 1
EB - electric bender
QD - quadrupole doublet
EL - einzel lens
KB - kicker-bender
MPS - multi-passage spectrometer
ion number Ar13+ [10³]
250
200
150
100
50
0
DK1
DK2
DK3
DK4
DK5
KB
DT1
0
5
10
15
distance [m]

Figure 2.4: To-scale drawing of the low-energy beamline connecting the SpecTrap experiment with the HITRAP facility and the Dresden EBIT. The inset shows the number of Ar^{13+} ions with a transport energy of 4 keV per charge at the diagnostic stations DK1 to DK5. Drawing of the beamline with courtesies of Zoran Andelkovic.

2.1.2 The HITRAP low-energy beamline

A to-scale drawing of the horizontal part of the beamline is shown in figure 2.4. Exact positions of the beamline elements are given in table A.3. For refocusing of the ion beam, the beamline features einzel lenses (EL) and quadrupole doublets (QD) every few meters. Typical parameters for the transport of Ar^{13+} are given in tables A.5–A.7 and are also discussed in [38]. To first order, the parameters of the electrostatic components are independent of the charge-to-mass ratio of the transported ion species which allows fast switching between different charge states. To this end, a multi-passage spectrometer (MPS) functions as a charge-selective element. A current of several amperes creates a static magnetic field which bends the ion beam by 90° and at the same time acts as a velocity filter. The resolving power of the MPS was found sufficient to select a single charge state from the distribution created in the EBIS. Besides small hysteresis effects, the MPS currents to select a specific charge state are reproducible over weeks. Therefore, switching between different charge states is possible in less than a minute without significant adjustment of the beamline parameters.

Five diagnostic stations DK1 to DK5 are placed along the beamline to monitor beam parameters such as the spatial distribution and the beam intensity. For this purpose, the diagnostic stations are equipped with one micro-channel plate (MCP) and one Faraday cup (FC) each. Both devices are mounted on a retractable stage which allows to move them in and out of the ion beam. The Faraday cup, in combination with a highly sensitive amplifier (DHPCA-100), is used to record time-resolved spectra of the ion bunch. Examples of time-of-flight spectra recorded at the first Faraday cup after the EBIT are shown in figure 2.3. The MCP amplifies the incident charges onto a phosphorous screen, so that the spatial beam distribution can be observed with a CCD video camera (Fig. 2.5). Depending on the amplification voltage, the MCP is capable of detecting low-intensity ion beams which are not easily detected with the Faraday cup. On the other side, compared to the Faraday cup, the MCP lacks the direct proportionality between the incident charges and the detected signal.

After the third diagnostic station, a kicker-bender (KB) is used to deflect the ion beam by 90°. Between DK4 and DK5, a pulsed drift tube decelerates the ions to energies of several hundreds of eV per charge. An electrostatic bender (EB) deflects the decelerated ions from the horizontal to the vertical beamline that leads to the SpecTrap Penning trap.

The inset of figure 2.4 shows the number of Ar^{13+} ions detected along the beamline with the Faraday cups of the diagnostic stations DK1 to DK5. At DK1, the Ar^{13+} number amounts to $2.5 \cdot 10^5$ ions, which is, considering the EBIS space-charge limit of about 10^7 elementary charges, close to the expected maximal production. During transport, the ion number slowly decreases due to continuous losses induced by intra-beam scattering as well as a drop of the ion number at the electrostatic kicker-bender between diagnostic chambers DK3 and DK4. Here, the broadened ion beam suffers a cutoff at a narrow passage of 20 mm diameter. For small ion numbers below $5 \cdot 10^4$, the transport efficiency approaches unity, which excludes the contribution of residual gas collisions to ion loss [36, 38]. Higher ion numbers could possibly be achieved if a higher transport energy was used. Since this would require an adjustment of the deceleration process, and since Ar^{13+} numbers of 10^5 ions at DK5 are sufficient for the experimental purpose of the SpecTrap experiment, no additional effort was put into further optimization of the ion transport.

In contrast to the horizontal low-energy beamline, the transport energy of the vertical SpecTrap beamline is limited to kinetic energies of about 1 keV per charge. Therefore, before entering the vertical SpecTrap beamline, the HCI coming from the EBIS are decelerated with a pulsed drift tube (denoted DT1 in Fig. 2.4) to about 10% of

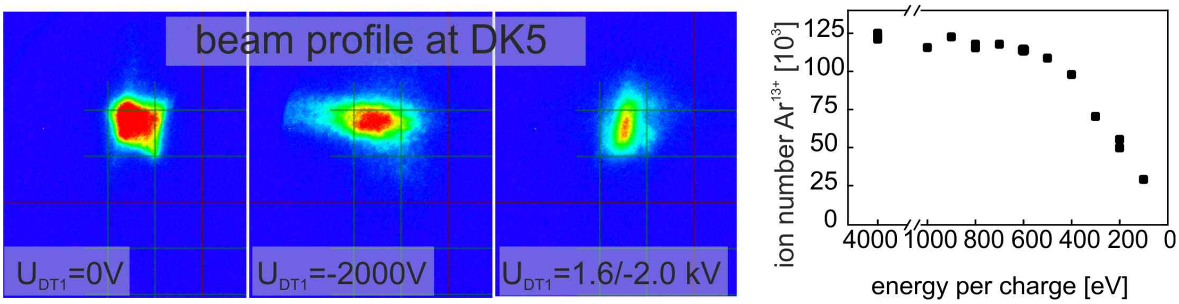

Figure 2.5: Left: Beam profiles at the MCP of DK5. The position of the beam on the MCP remains unaffected by application of constant or switched drift tube voltages, indicating the correct alignment of the ion beam with regard to the drift tube axis. Right: Number of Ar^{13+} detected with the FC of DK5 after deceleration with DT1 from an initial energy of 4 keV per charge. Statistical error bars lie within the symbols.

their initial energy. This deceleration is achieved by reducing the initial potential U_{hi} of the pulsed drift tube with a 5 kV HV-switch (HTS 51-06, Behlke) in less than 50 ns by $\Delta U \approx 3.5\,\mathrm{kV}$ to $U_{\mathrm{lo}} = U_{\mathrm{hi}} - \Delta U$. The switching time is adjusted such that the HCI are in the drift tube center when the potential is changed. Hence, the kinetic energy of the ions is reduced in two steps upon entering and leaving the drift tube by a total of $\Delta U \cdot q$. The switching times for different argon charge states can be found in table A.8 in the Appendix.

To achieve the maximum deceleration efficiency, the parameters of the quadrupole doublets before the drift tube are adjusted such that the ion beam enters the drift tube along its central axis. This condition can be checked by observing the influence of the drift tube on the ion beam position at the MCP of DK5 (Fig. 2.5): The left image depicts the ion beam for zero voltage applied to the drift tube. In the middle image, a constant voltage is applied to the drift tube so that it acts as an einzel lens. The beam position remains unchanged, indicating that the ion beam acts like the principal ray of an optical lens. The right image depicts the ion beam after deceleration by switching the drift tube from +1.6 kV to −2.0 kV. Again, the beam position remains unchanged, indicating that the ion beam travels parallel to the drift tube axis with nearly no vertical velocity component. One should note that due to a slight misalignment of the drift tube with regard to DK5, the optimum tuning does not result in a central position of the ion beam at the MCP of DK5.

The right part of figure 2.5 shows the deceleration efficiency of Ar^{13+} ions with an initial energy of 4 keV per charge. For residual energies between 500 eV and 1 keV per charge, the deceleration efficiency is close to unity. Deceleration to energies as low as 100 eV per charge is possible, but leads so significant ion loss so that typically deceleration to residual energies of about 500 eV per charge was performed. Hence, Ar^{13+} numbers of more than 10^5 were obtained at diagnostic station DK5.

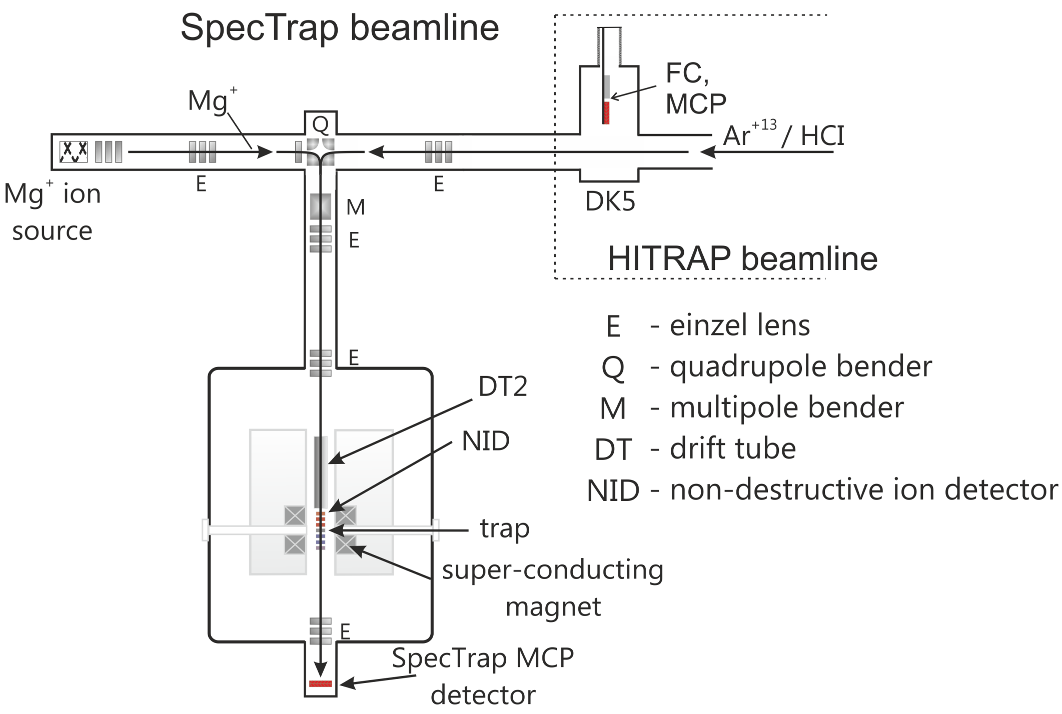
SpecTrap beamline
Mg+
Q
FC,
MCP
Ar+13 / HCI
Mg+ ion
source
E
E
M
E
DK5
HITRAP beamline
E
DT2
NID
trap
super-conducting
magnet
E
SpecTrap MCP
detector
E - einzel lens
Q - quadrupole bender
M - multipole bender
DT - drift tube
NID - non-destructive ion detector

Figure 2.6: Drawing of the SpecTrap magnet and beamline. Adaption of a drawing by Zoran Andelkovic [41].

2.1.3 The SpecTrap beamline

The SpecTrap beamline consists of a vertical beamline, which is connected to the SpecTrap magnet system, and a horizontal beamline, which includes the Mg^+ ion source and connects the SpecTrap beamline to the HITRAP low-energy beamline (Fig. 2.6).

An electrostatic quadrupole bender (Q) deflects the ions, either coming from the Mg^+ source or from the EBIS, by 90° downwards to the SpecTrap Penning trap. Depending on its polarity, the quadrupole bender only deflects ions coming from one side at a time. To change from which source ions are transported to the trap, the polarity of the quadrupole segments can be inverted with a homebuilt HV switch featuring HV relay switches. In principle, this switching process is as fast as a few ms. However, for an adequate transport efficiency, the power supplies for the einzel lenses along the vertical beamline have to be set to new values, which usually takes a few seconds.

Although the SpecTrap Penning trap can capture ions with kinetic energies of several hundreds of eV per charge, further deceleration is desirable, since any amount of remaining energy has to be removed before the ion cloud is in a state that allows controlled experiments. Therefore, a pulsed drift tube (DT2) close to the entrance of the trap is available for further deceleration. It consists of two segments, which were connected and used in combination for the experiments presented here. The drift tube is close to the trapping region, where the magnetic field of the Penning trap

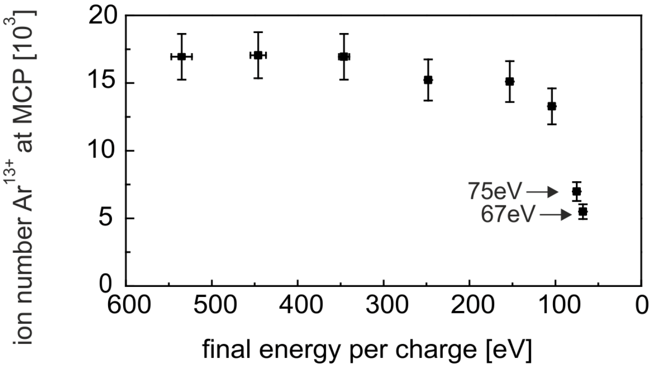

Figure 2.7: Ar^{13+} ion number after deceleration with DT2 detected at the SpecTrap MCP. For each data point the beamline settings were adjusted to guarantee optimal transport efficiency. The measurement was performed without magnetic field.

magnet is considerable strong. This is beneficial for the transport efficiency of the decelerated ion beam, since the magnetic field provides radial focusing and prevents the ion beam from diverging after deceleration, as has been shown in simulations performed with the simulation software SIMION.

The vertical part of the SpecTrap beamline features two different types of detectors: A non-destructive ion detector (NID) attached to the upper capture electrode and the SpecTrap MCP, which is a micro-channel plate (MCP) detector mounted on a retractable stage at the low end of the full beamline. The NID creates a signal by amplification of the non-resonant pick-up induced in the upper capture electrode by an incoming ion bunch. It will be described in section 2.4.1 in detail and further information can be found in [39].

Figure 2.7 shows the number of Ar^{13+} ions at the SpecTrap MCP detector at the low end of the full beamline after deceleration with DT2. The horizontal axis depicts the residual kinetic energy per charge, determined from a TOF measurement. For each data point, the beamline settings have been adjusted to optimal transport efficiency. This way, it has been possible to reduce the kinetic energy to about 100 eV per charge without significant ion loss. For even lower energies, the transport efficiency to the MCP drops drastically. However, since the SpecTrap MCP is located in a distance of 1.03 m from DT2 – compared to a distance of 0.2 m between DT2 and the trap center (Tab. A.3) – the transport efficiency to the MCP can be regarded as a lower limit and higher ion numbers can be expected for transport to the trap. In spite of the disadvantageous location, the MCP was used for this measurement instead of the NID, because the switching of DT2 induces electric noise in the NID which obscures the Ar^{13+} signal. It should also be noted, that this measurement was performed without a magnetic field, because a magnetic field is only beneficial for the ion transport to the trapping region but not to the MCP which is located outside the region with strong magnetic fields.

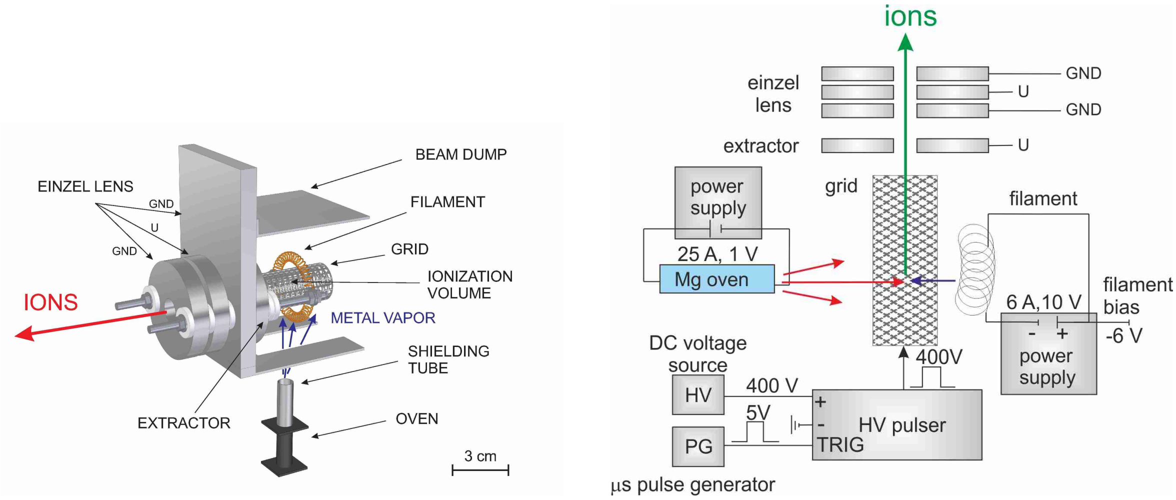
EINZEL LENS
GND
U
GND
IONS
EXTRACTOR
BEAM DUMP
FILAMENT
GRID
IONIZATION VOLUME
METAL VAPOR
SHIELDING TUBE
OVEN
3 cm
ions
einzel lens
extractor
GND
U
GND
U
power supply
25 A, 1 V
Mg oven
grid
filament
filament bias
6 A,10 V
- +
-6 V
power supply
DC voltage source
HV
400 V
5V
PG
µs pulse generator
400V
+
-
TRIG
HV pulser

(a) **(b)**

Figure 2.8: (a) Schematic of the ion source (true to scale). (b) Electric configuration of the ion source.

2.2 The Mg$^+$ ion source

A simple and reliable source for singly charged ions is used to provide Mg$^+$ ions for laser cooling in the SpecTrap experiment. The operation and characteristics of the source have already been presented in [37] and will be described here in more detail.

2.2.1 Ion creation

As in most sources for singly charged ions, ion production is achieved in two subsequent steps. First, a current-heated atomic-vapor source produces a beam of neutral atoms. In a second step, electron emission from a filament is used for impact ionization of the atomic vapor (Fig.2.8a).

The atomic vapor source ('oven') is a tube made of a tantalum foil placed between two shielding steel plates and filled with small grains of bulk material, presently magnesium containing all stable isotopes in natural abundances. The temperature necessary for efficient evaporation is produced by a direct current of several tens of amperes through the oven tube, in the present experiments usually 25 A at a voltage of about 1 V. The oven setup is capable of efficiently vaporizing alkali metals and alkaline earth metals, and may be operated well above 2000 K. From the measured pressure close to the oven of order 10^{-8} mbar and the vapor pressure curve [42] of Mg, an oven temperature of around 600 K can be estimated, which is still below the atmospheric melting point of Mg of about 900 K. Such a temperature is sufficient to produce enough vapor for the targeted ion numbers, while not unnecessarily deploying the evaporating material. The source has been operated for several hundreds of hours with one filling of Mg material. Another tube is mounted coaxially onto the tantalum tube to direct the vapor of neutral magnesium atoms to the ionization volume and prevent contamination of the vacuum system. The atomic beam is directed perpendicular to the axis of ion extraction and stopped by a beam dump beyond the ionization region. Hence it does not enter the beam line together with the ions.

The atom vapor is ionized by electron impact ionization in the interior of a cylindrical grid of 38 mm length and 16 mm diameter. The electron current of a few milliampere for ionization is provided by filaments made of thoriated tungsten (99% W and 0.9% ThO_2, temper annealed) with a diameter of 0.15 mm which are placed around the grid. The electric configuration of the ion source is schematically shown in figure 2.8b. For filament heating, a continuous current of typically 6 A is sent through the filament arrangement. A bias voltage applied to the filaments defines the kinetic energy of the electrons. For efficient ionization, the electron kinetic energy has to be about two to three times higher than the 7.65 eV ionization potential of magnesium [43, 44].

2.2.2 Ion extraction

Ion extraction from the creation region inside the grid is achieved by a high-voltage pulser which applies a pulse of several microseconds in duration to the grid. The rise and fall times of the pulser are below 100 ns and thus allow the creation of distinct ion bunches. The first ion optical element behind the grid is the extractor. When the grid potential is above the extractor potential, an electrostatic potential gradient is created which guides the ions from the interior of the grid towards the extractor. During the extraction pulse, the position-dependent potential energy of the ions' place of creation is partially or fully converted into kinetic energy. Only ions that are able to leave the grid volume during the short extraction pulse experience the full conversion of their potential energy. In many ion sources, the extractor electrode is set to a negative potential to enlarge the potential gradient and quicken the ion extraction. However, for this specific electrode configuration, the effect was found to be different from this general behavior. The potential distribution inside the grid was obtained by the particle trajectory simulator SIMION (Fig. 2.9). The black (red) line shows the potential distribution with the extractor electrode at 0 V (−900 V) and $U_{grid} = 400$ V. In the first case (black dots), only ions at a position $x \geq -16$ mm will be able to fully convert their potential into kinetic energy within the 3 μs pulse duration, while for a negative voltage of −900 V applied to the extractor, even ions that are farther inside the grid ($x \geq -21$ mm) are extracted (red dots). However, only ion bunches with a narrow energy distribution can be efficiently transported along the beam line and captured in a trap. Therefore, only ions created in a small area with a potential gradient just sufficient to leave the grid will contribute to the transportable ion bunch, i.e. $-15\,\mathrm{mm} \leq x \leq -10\,\mathrm{mm}$ and $-20\,\mathrm{mm} \leq x \leq -15\,\mathrm{mm}$, respectively. As a consequence, the main effect of the extractor voltage is to shift the zone of extraction along the axis of the grid. This means that an optimum combination of the position of the filaments and the voltage of the extractor has to be found in order to maximize the ionization efficiency in the desired volume of the grid. In our case, the best results have been obtained with the extractor set to zero voltage and the einzel lens operated at a voltage of −1000 V.

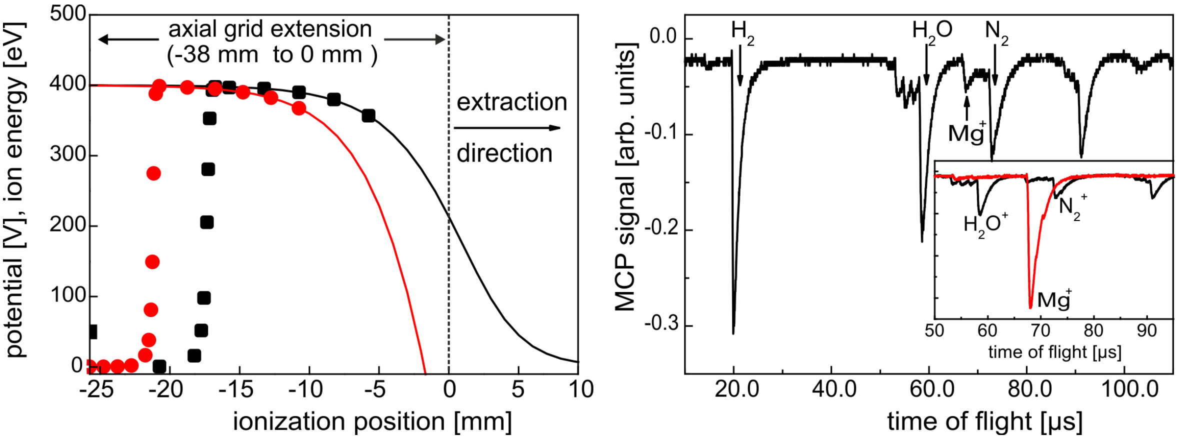

Figure 2.9: Left: Simulated electrostatic potentials (lines) and kinetic ion energies (data points) as a function of the position of ionization in the ionization volume for two different extractor voltages (black: 0 V, red: −900 V). The ions' kinetic energies (data points) are given after 3 µs of acceleration. Right: Time-of-flight spectrum at the SpecTrap MCP for the Mg^+ source operated with a filament bias of −20 V. The inset shows a detail of the spectrum (black), together with a spectrum where the optimum bias for Mg^+ production of −6 V was used (red).

A typical signal from the MCP in a time-of-flight measurement is shown in the right part of figure 2.9. With a filament bias of −20 V, beside Mg^+, also H_2^+, H_2O^+, and N_2^+ ions are produced from the residual gas. The inset shows a detail of this TOF-spectrum together with a signal with the bias voltage at the source grid optimized for production of Mg^+. With this reduced bias of −6 V, the kinetic energy of the electrons is just sufficient to ionize magnesium and none of the prominent contaminant ions are detected.

The kinetic energy of the electrons depends on the position at which they are emitted from the filament. The −6 V bias and the 10 V voltage drop across the filament (at presently 6 A filament heating current) result in electron emission with kinetic energies in the range of 6–16 eV. In the present configuration, this choice leads to efficient Mg^+ production while avoiding energetically close contaminants. From the ion bunch containing all stable Mg isotopes, only $^{24}Mg^+$ is loaded into the trap by dynamically switching the trap electrodes.

Experimentally, it has been found that the ion yield was highest when the einzel lens was set to a negative rather than positive potential. Since the focusing functionality of an einzel lens does not depend on the polarity, this unexpected behavior could been attributed to the creation of a guiding potential for the electrons emitted from the filaments. The paths of flight of electrons emitted from the filament were simulated with SIMION for two different electrode settings (Fig. 2.10). In both sim-

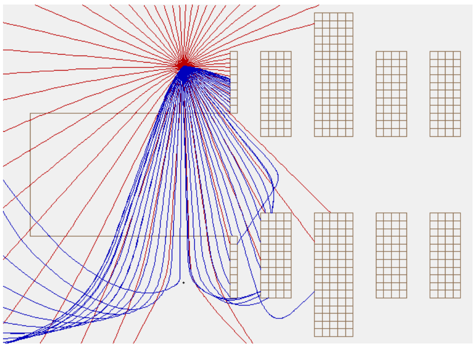

Figure 2.10: A SIMION simulation showing the paths of flight for electrons emitted from the filament for einzel lens potentials of $U_e = 0\,\mathrm{V}$ (brown) and $U_e = -900\,\mathrm{V}$ (blue). For $U_e = -900\,\mathrm{V}$ the electrons are directed towards the ionization volume and the ion yield increases. The used potentials are $U_{\text{bias}} = -6\,\mathrm{V}$, $U_{\text{grid}} = 0\,\mathrm{V}$, $U_{\text{extractor}} = 0\,\mathrm{V}$ and the initial kinetic energy of the electrons is $\mathrm{E}_{\text{kin}} = 30\,\mathrm{meV}$.

ulations the filament bias was set to −6 V and all other electrodes to zero potential. The einzel lens voltage was set to a potential of 0 V and −900 V for the brown and the blue paths, respectively. The initial kinetic energy of the electrons was set to 30 meV. The effect of the negative einzel lens potential is to direct the electrons towards the ionization volume. As a consequence, the overlap of the electron current with the neutral atom beam and thus the ion yield increases.

2.2.3 Ion numbers and bunch structure

The temporal width of the ion bunch detected with the SpecTrap MCP was found to be smaller than 1 µs and independent of the grid pulse duration (Fig. 2.11, left). For extraction pulse lengths shorter than 3 µs, the amount of Mg^+ produced increases with the pulse duration. For even longer pulses, the main peak saturates and the signal develops a tail at longer times of flight. This behavior can be understood by the characteristics of the extraction process. With increasing grid pulse duration, ions created further inside the grid are extracted and follow the main bunch in the time-of-flight spectrum. Because of the small potential gradient in the grid interior, the extractable volume increases only slowly with grid pulse duration and the signal declines at later times of flight.

A SIMION simulation of the extraction process and the bunch structure after ion extraction and transport to the MCP confirms this result (Fig. 2.11, right). For simplicity, ion creation was assumed to take place only on the grid's axis of symmetry. The earliest arriving ions at $t \approx 65\,\mu\mathrm{s}$ form the main bunch, followed by a tail of ions with longer times of flight. The simulated time of flight to the SpecTrap MCP detector (Fig. 2.11, right) is reduced by 2 µs compared to the actual measurement (Fig. 2.11, left). This small discrepancy can be explained by the decelerating effect of the ion optical elements, that has not been included in the simulation.

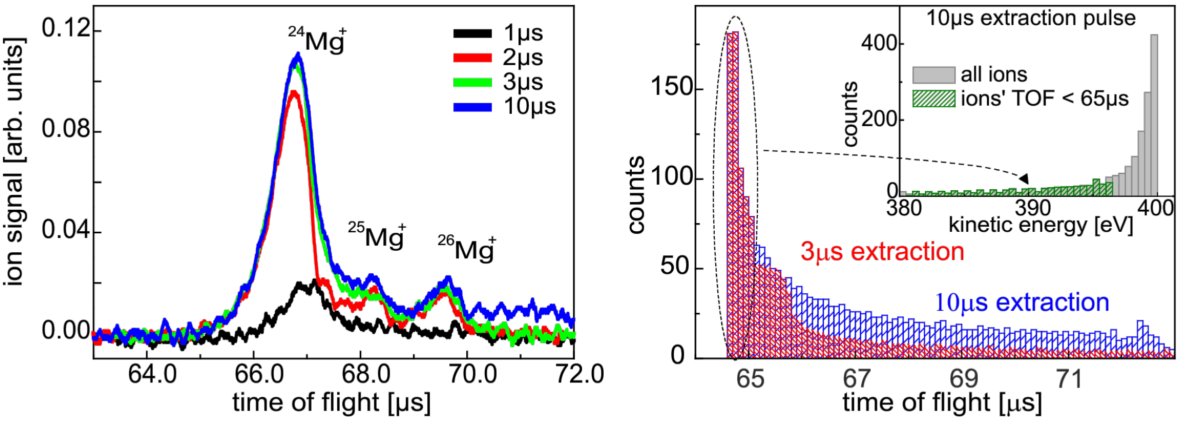

Figure 2.11: Left: Time-of-flight spectrum at the SpecTrap MCP for ions extracted with different grid-pulse lengths. Each ion bunch contains all stable magnesium isotopes in natural abundances. Right: SIMION simulation of the ions' time of flight to the MCP detector for grid-pulse durations of 3 µs and 10 µs. Inset: The corresponding distribution of ion kinetic energies for 10-µs grid-pulse duration (gray histogram). The kinetic energy of 400 eV with the highest probability is given by the potential applied to the grid electrode. The subset of ions arriving at times < 65 µs (green-hatched histogram) shows a kinetic energy distribution at lower energies.

Similar to the TOF measurements recorded with the MCP, the TOF histograms resulting from simulations with grid pulse durations of 3 µs and 10 µs, respectively, reveal the a main peak at early times of flight. Again, the tail of ions with longer times of flight is more pronounced for a longer grid-pulse length. This shows that the ions forming the main bunch stem from the volume close to the front end of the extraction region, where extraction with a short pulse duration is possible. This is also confirmed by two histograms showing the kinetic energy distribution for ions in different parts of the ion bunch (Fig. 2.11, inset). The gray-filled histogram shows the energy distribution of the whole ion ensemble inside the grid volume, where the energy with the highest occurrence is given by the grid voltage $U_{\text{grid}} = 400\,\text{V}$. The green-hatched histogram shows the energy distribution of the ions within the main peak, i.e. ions with times of flight less than 65 µs. The kinetic energy of these ions is slightly reduced with regard to the voltage applied to the grid, as can be expected in the region close to the front end of the extraction region. Of course, the bunch structure evolves with time and is shown here only for that specific time of flight.

The ion number per pulse detected with the NID has been recorded as a function of the grid pulse duration (Fig. 2.12, left). An exponential saturation behavior has been fitted to the data, indicating that for the present conditions, pulse durations above roughly 7.5 µs do not change the ion number any more. Thus, a grid pulse duration of 7.5 µs allows a reliable full extraction of ion bunches, but pulses as short as 3 µs extract 70% of the maximum ion number already. For the given configuration, the expected space charge limit is about 10^6 ions.

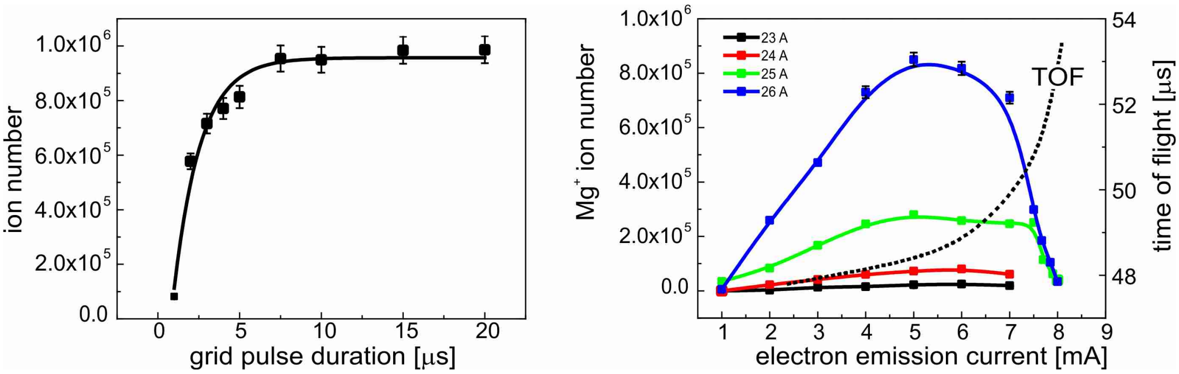

Figure 2.12: Left: Measured ion number per pulse detected with the NID as a function of the grid-pulse duration. Right: Number of extracted ions per pulse as a function of the electron emission-current I_{em} for different values of the oven current, measured with the NID. The grid-pulse duration was set to 3 µs and the extraction voltage to 0 V. Lines have been drawn to guide the eye. With increasing electron emission-current, the effective potential of the extraction pulse is reduced. As a consequence, for higher I_{em} the ions' time-of-flight (dotted curve) increases from 48 µs to 52 µs and the ion yield saturates or even decreases again.

The right part of figure 2.12 shows the number of extracted ions per pulse (left hand scale) as a function of the electron emission current I_{em} for different oven currents. The ion yield increases significantly with increasing oven current. Currents above 26 A were not applied in order not to deplete the source unnecessarily fast. The ion yield increases with increasing electron emission current from the filaments, up to a point where the electron current to the grid reduces the voltage applied by the extraction pulse. This is visible in the right part of figure 2.12, where the yield starts to saturate for I_{em} above 4.5 mA and even decreases again for higher I_{em}. To prove the influence on the pulse, the dotted curve (referring to the right hand scale) shows the corresponding time of flight of the ions which increases significantly in the regime of high electron emission currents.

The high efficiency of the magnesium source allowed to produce several hundreds of thousands of magnesium ions (Fig. 2.12). The production can be further increased, if a larger amount of magnesium is evaporated by applying higher currents to the magnesium oven. However, vacuum conditions will suffer from higher evaporation rates and leakage currents may occur when the insulating ceramics of the electron impact source are contaminated. In this case, the complete ionization source has to be disassembled to clean the ceramics. Since the number of produced ions per bunch is large enough for the requirements of the SpecTrap experiment (and nearly four orders of magnitude higher than the ones of a previous setup described in [41, 45]), no further effort to increase the Mg^+ production has been undertaken.

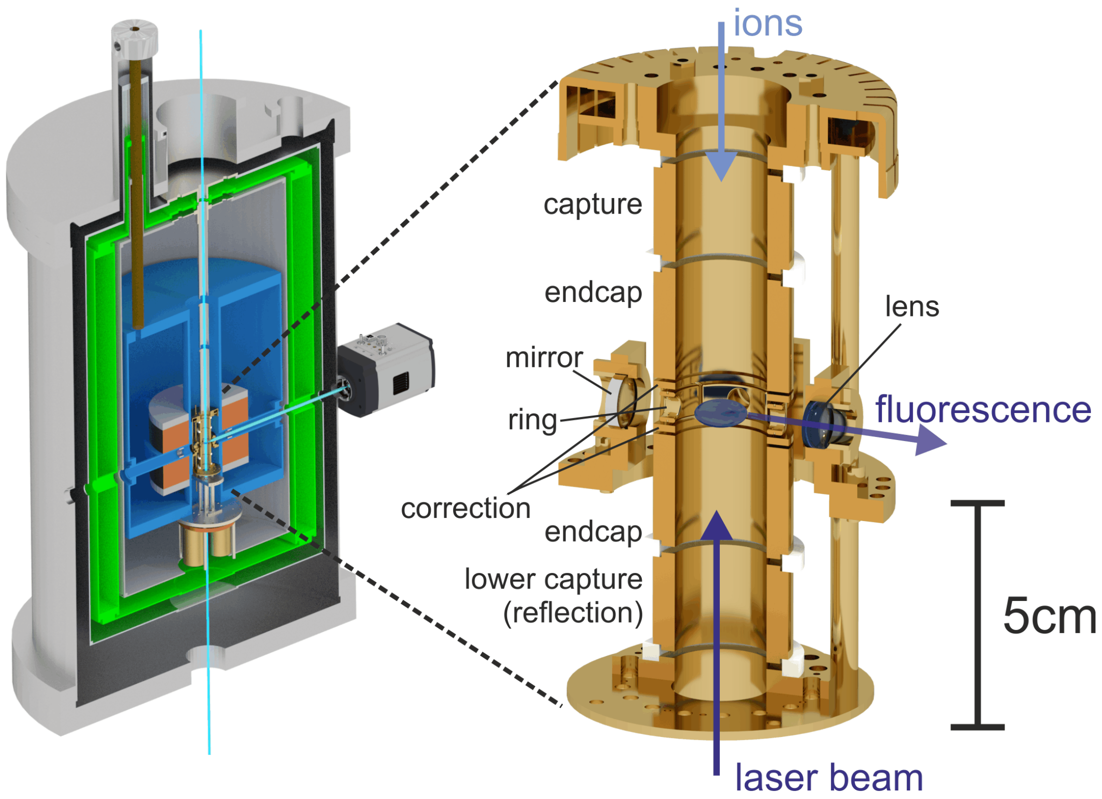

Figure 2.13: Left: Cross section of the SpecTrap magnet. Right: Drawing of the SpecTrap Penning trap. Drawings with courtesies of Wolfgang Geithner.

2.3 The SpecTrap Penning trap system

The heart of the SpecTrap experiment is the cryogenic magnet system and the cylindrical Penning trap as shown in figure 2.13. Precise knowledge of the magnetic and electric trapping field e.g. is required to determine the frequency of optical transitions and to identify charge states or kinetic energies of trapped particles. For this reason, the properties of the trapping fields have been studied in detail and results are presented in this section. Additional information about the trap design is given in [41, 45].

2.3.1 The magnet system

The magnetic field for operation of the SpecTrap Penning trap is provided by a cold-bore, split-coil superconducting magnet (Fig. 2.13, left). The magnet systems allows optical access to the central field region along the magnet axis and via six radial optical ports. The cylindrical Penning trap (Fig. 2.13, right) is placed in the central region of the magnetic field, where the thermal contact to the liquid-helium reservoir cools all mechanical and electronic parts to a temperature of 4 K. A benefit of such a cryogenic trap is that at 4 K the trap electrodes adsorb most atoms and molecules

parameter	value	magnetic field [T]
magnet current I	40.09 A	4.097(6)
$^{24}\mathrm{Mg}^{+}$ Zeeman shift	$2\pi \cdot 56.6(2)\,\mathrm{GHz}$	4.044(14)
$^{24}\mathrm{Mg}^{+}$ cyclotron frequency ω_c	$2\pi \cdot 2.586(1)\,\mathrm{MHz}$	4.039(2)

Table 2.1: Comparison of different methods to determine the magnetic field of the SpecTrap magnet.

present in the residual gas. For such a design, the vacuum conditions should be mainly determined by the steady flow of gas along the magnet axis. Unfortunately, the vacuum conditions are impaired by a leak in the liquid-helium container. With a helium detector, a leak rate of 3–30$\cdot 10^{-6}$ mbar l/s was determined. In consideration of the pumping speed of the turbo-molecular pump attached to the vacuum system this leak rate is equivalent to a partial helium pressure of 1–10$\cdot 10^{-8}$ mbar. Thus, the residual gas is nearly exclusively constituted of helium.

A simulation of the magnetic field, performed with the software SIMION, showed that in the central region the relative field variation is less than 10^{-4} over a distance of a few millimeters. A detailed discussion of the magnet setup and the magnetic field is given in [41].

For the experimental runs performed in the course of this thesis, the magnetic field was set to a field strength of $B \approx 4\,\mathrm{T}$. According to the data sheet provided by the manufacturer, a maximum magnetic field of 6 T can be created with a current of 58.7 A, giving a calibration factor of 0.1022 T/A. Since the power supply for energization of the superconducting coils allows the current adjustment only with a precision of 0.1 A, the magnetic field is only known to several millitesla and had to be determined for each experimental run separately.

Three different methods were employed to determine the magnetic field:

- the field follows directly from the magnet current and the calibration factor,
- it can be calculated from the Zeeman shift of the laser cooling transition (table A.11),
- and it can be calculated from the free cyclotron frequency of any ion species with known charge-to-mass ratio.

The results are exemplarily given for the experimental run performed in September 2015 (table 2.1).

To determine the Zeeman shift of the $^2\mathrm{S}_{1/2,m_j=-1/2} \rightarrow {}^2\mathrm{P}_{3/2,m_j=-3/2}$ transition in $^{24}\mathrm{Mg}^{+}$, the laser was scanned across the cooling transition. The absolute frequency of the transition was measured with an accuracy of $2\pi \cdot 200\,\mathrm{MHz}$ by a High-Finesse WS-7 wavemeter. The accuracy was limited by the wavelength uncertainty of the HeNe laser used for calibration. The magnetic field B was then determined by comparison of the measured frequency with the value given for $B = 0$ in literature.

The cyclotron frequency ω_c of the ^{24}Mg$^+$ ions was determined by scanning the frequency of an RF signal applied to one of the ring segments. The excitation of the center-of-mass mode with frequency ω_c is indicated by a sudden change of the Mg$^+$ fluorescence signal. The main contribution to the error is due to shifts of the excitation frequency with regard to the scanning direction of the RF signal. This effect may be due to the excitation of the cloud to larger cyclotron radii, where the ions experience a different magnetic field, or the finite extension of the ion cloud in combination with inhomogeneities of the magnetic field.

The value obtained from the magnet current is in slight disagreement with the values obtained by the other two alternative measurements, which are in good agreement with each other. For experiments, where the precise value of the magnetic field is important, systematic measurements of the cyclotron frequency ω_c seem to give the most promising results.

2.3.2 Principles of charged particle trapping

Confinement of a charged particle within a finite volume requires a 3-D potential with a local minimum where the particles are localized. Assuming an electrostatic potential V of the form

$$V(\vec{r}) = Ax^2 + By^2 + Cz^2, \tag{2.1}$$

the force $\vec{F}$ acting on the particle is given by

$$\vec{F} = -q\nabla V = -2q\vec{r}\begin{pmatrix} A \\ B \\ C \end{pmatrix}. \tag{2.2}$$

For the force F always to be directed towards the minimum of potential, all coefficients A, B, and C must be of positive sign. On the other hand, in free space the potential (2.1) has to satisfy Poisson's equation $\triangle V = -\rho(\vec{r})/(\epsilon_r \epsilon_0)$ or $\triangle V = 0$. This leads to the condition $A+B+C=0$ and the conclusion that an electrostatic potential cannot possess a minimum in all three dimensions, which is known as Earnshaw's theorem.

For confinement of charged particles in spite of this restriction, several types of ion traps have been developed in the last decades, among which the Paul and the Penning trap are the most common. In an ideal Paul trap, an oscillating electric potential is superimposed on the static component and can be written as [46]

$$V = \frac{U_0 + V_0 \cos \Omega t}{2d^2}(x^2 + y^2 - 2z^2), \tag{2.3}$$

where d is a normalizing factor depending on the size of the trap. For the potential in (2.3) it is $A = B = -C/2$, hence the resulting potential is rotational symmetric and exhibits a saddle point. For any given direction, the resulting force will alternately direct the particle towards and away from the center of trap. However, by appropriate choice of field amplitude and frequency, it is possible to have a time-averaged restoring force in all three dimension. The combination of amplitude and frequency forms zones of stability, which are both depending on the charge and the mass of the stored particle. This complicates the simultaneous storage of more than one ion species as required for sympathetic cooling. One additional inconvenience of the Paul trap is the oscillating electric field interfering with any type of low noise electronics and the time-dependent force resulting in a residual micromotion and particle heating.

For these reasons the SpecTrap experiment makes use of a Penning trap, where an electrostatic potential with $A = B = -C/2$ provides axial confinement. Instead of an oscillating electric field, in a Penning trap an additional static magnetic field prohibits particle loss in the radial direction. For trapping of externally produced ions the trap depth must exceed the kinetic energy of the injected ions. For a Penning trap this can be done straightforward by applying a large voltage at the endcaps, whereas for a Paul trap there are technical constraints to the amplitude of the oscillating field.

2.3.3 Single-ion motion in a Penning trap

To create an ideal quadrupole potential in a Penning trap, the surfaces of the trap electrodes must follow the surface of equal potential. This prerequisite is strictly fulfilled by a trap design featuring hyperbolic electrodes. Therefore, a hyperbolic Penning trap consists of three electrodes, one of them being the ring electrode and two forming the endcaps of the trap (Fig. 2.14, left).

The resulting quadrupole potential has a minimum at the trap center in axial direction and a maximum at the trap center in radial direction, which means that of the coefficients in equation (2.1) we have $A < 0, B < 0$ and $C > 0$. The quadrupole potential ϕ of the hyperbolic trap can be expressed as

$$\phi = \frac{\tilde{C}_2 U_0}{4d^2}(2z^2 - r^2), \tag{2.4}$$

where z and r denote the axial and radial coordinate, U_0 denotes the potential difference between the ring and the endcap and $\tilde{C}_2$ is a dimensionless scaling factor of the order of 0.5. Furthermore, d denotes the characteristic trap dimension which is defined as

$$d^2 = \frac{1}{2}(z_0^2 + r_0^2/2), \tag{2.5}$$

with z_0 as the distance from the center of the trap to the endcaps and r_0 the inner radius of the ring electrode.

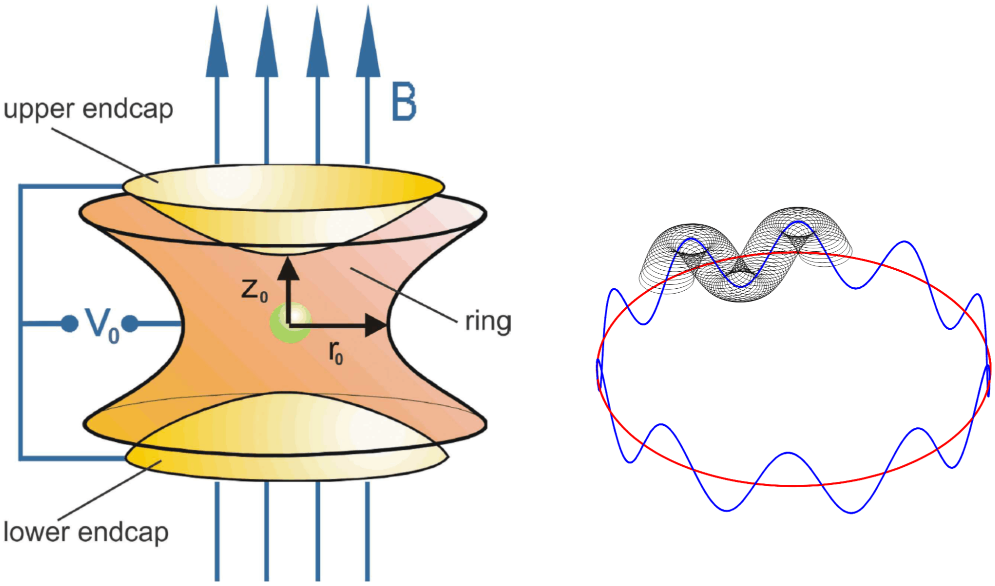

Figure 2.14: Left: Schematic representation of a hyperbolic Penning trap. Figure with courtesies from [41]. Right: Visualization of the motion of a single ion in a Penning trap (black). The contributions of the magnetron drift with frequency ω_- around the center of trap (red) and the axial oscillation with frequency ω_z (blue) are displayed separately.

The force $\vec{F}$ acting on a charged particle caused by the electric potential ϕ and the magnetic field $\vec{B} = B_0\vec{e}_z$ is given by $\vec{F} = -q\nabla V + \frac{q}{c}\vec{v} \times \vec{B}$ and leads to three equations of motion, which are written in Cartesian coordinates

$$\frac{\mathrm{d}^2 x}{\mathrm{d}t^2} - \omega_c^2 \frac{\mathrm{d}y}{\mathrm{d}t} - \frac{1}{2}\omega_z^2 x = 0, \tag{2.6}$$

$$\frac{\mathrm{d}^2 y}{\mathrm{d}t^2} + \omega_c^2 \frac{\mathrm{d}x}{\mathrm{d}t} - \frac{1}{2}\omega_z^2 x = 0, \tag{2.7}$$

$$\text{and} \quad \frac{\mathrm{d}^2 z}{\mathrm{d}t^2} + \omega_z^2 z = 0. \tag{2.8}$$

In equations (2.6–2.8), the free cyclotron frequency ω_c and the axial oscillation frequency ω_z are defined by

$$\omega_c = \frac{qB_0}{m} \tag{2.9}$$

$$\text{and} \quad \omega_z = \sqrt{\frac{q\tilde{C}_2 U_0}{md^2}}. \tag{2.10}$$

The axial symmetry of the potential decouples the axial from the radial motions, and equation (2.8) is solved by a harmonic oscillator with frequency ω_z. The two

	$\omega_c/(2\pi{\cdot}\mathrm{s}^{-1})$	$\omega_+/(2\pi{\cdot}\mathrm{s}^{-1})$	$\omega_z/(2\pi{\cdot}\mathrm{s}^{-1})$	$\omega_-/(2\pi{\cdot}\mathrm{s}^{-1})$
Mg^+	$2.560 \cdot 10^6$	$2.512 \cdot 10^6$	$485 \cdot 10^3$	$48 \cdot 10^3$
Ar^{13+}	$19.970 \cdot 10^6$	$19.922 \cdot 10^6$	$1.379 \cdot 10^6$	$48 \cdot 10^3$
Bi^{82+}	$24.108 \cdot 10^6$	$24.060 \cdot 10^6$	$1.515 \cdot 10^6$	$48 \cdot 10^3$

Table 2.2: Free cyclotron, reduced cyclotron, axial and magnetron frequency for selected ion species. Trapping parameters: $B = 4\,\mathrm{T}$, $U_0 = 200\,\mathrm{V}$, $\tilde{C}_2 = 0.563$, $d = 7.06\,\mathrm{mm}$.

radial equations are coupled and the solution is given by the superposition of two independent, circular eigenmotions with the frequencies [47]

$$\omega_+ = \frac{\omega_c}{2} + \sqrt{\left(\frac{\omega_c}{2}\right)^2 - \frac{\omega_z^2}{2}} \tag{2.11}$$

$$\text{and} \quad \omega_- = \frac{\omega_c}{2} - \sqrt{\left(\frac{\omega_c}{2}\right)^2 - \frac{\omega_z^2}{2}}. \tag{2.12}$$

Here, ω_+ denotes the reduced cyclotron frequency and ω_- the magnetron frequency. The typical hierarchy is $\omega_+ \gg \omega_z \gg \omega_-$, as can be seen in table 2.2 where some typical values the SpecTrap Penning trap are given.

The motion of a single ion is visualized in figure 2.14 (right), where the parameters were chosen such that the radius of the magnetron orbit with frequency ω_- (red) is much larger than the cyclotron orbit with frequency ω_+ (black). For the root in equations (2.11) and (2.12) to be real, the condition $\omega_z < \omega_c/2$ has to be fulfilled. However, for Mg^+ ions and a magnetic field of 4 T this limits the voltage to a maximum of $U_0 = 1500\,\mathrm{V}$. This is no restriction in practice.

Some useful relations between the motional frequencies exist, which can be readily derived from their definitions in Eq. (2.10)–(2.12):

$$\omega_+ + \omega_- = \omega_c, \tag{2.13}$$

$$2\omega_+ \omega_- = \omega_z^2, \tag{2.14}$$

$$\text{and} \quad \omega_+^2 + \omega_-^2 + \omega_z^2 = \omega_c^2. \tag{2.15}$$

To first order, equation (2.15) also holds in the presence of trap imperfections such as deviations of the trap electrodes from the ideal geometry or a misalignment of the trap with respect to the magnetic field direction. It is hence known as the Brown-Gabrielse invariance theorem [48].

2.3.4 The Penning trap electrode design

Instead of using hyperbolically shaped electrodes, the SpecTrap Penning trap employs cylindrical electrodes that allow much better access to the trap center for the injection

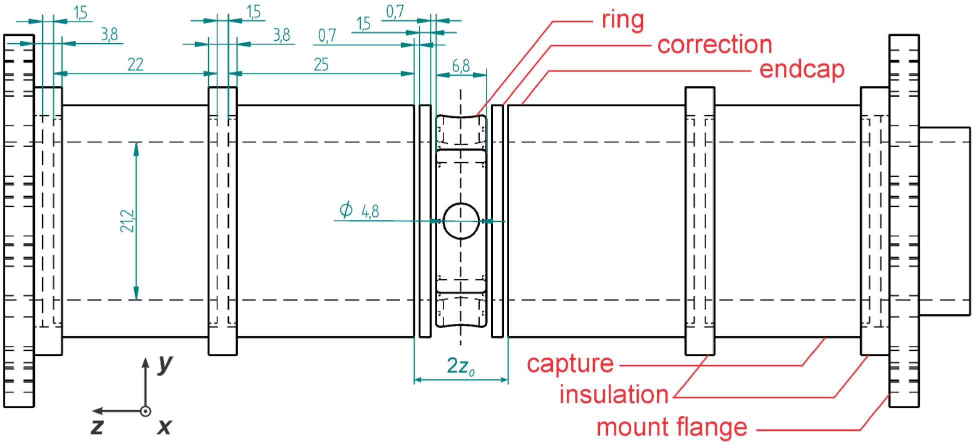

Figure 2.15: Drawing of the SpecTrap Penning trap. All dimensions are in mm. The inner radius of the electrodes is $r_0 = 10.6\,\mathrm{mm}$, the center-endcap distance is $z_0 = 6.3\,\mathrm{mm}$, and the gap width is $z_g = 0.7\,\mathrm{mm}$. Figure with courtesies from Z. Andelkovic [41]. Different values for z_g and z_0, determined from a measurement of the C_n coefficients of the trapping potential, are given in table 2.3.

of externally created ions or axial irradiation of a laser beam. On the other side, an open trap design requires more care to achieve good vacuum conditions and the trapping potential is slightly less harmonic.

A technical drawing of the SpecTrap Penning trap is depicted in Fig. 2.15. The trap consists of seven electrodes: The ring electrode defining the trap center, and three pairs of electrodes that are placed symmetrically to both sides of the ring electrode. The ring electrode is fourfold segmented to facilitate the irradiation of dipole and quadrupole fields. An imaging system, described in more detail in section 2.6, guides the fluorescence of ions confined in the trap center through holes in the ring segments to the radially placed detectors. The three pairs of electrodes are referred to as the (upper/lower) correction electrodes, the (upper/lower) endcap electrodes and the (upper/lower) capture electrode. To discriminate the two outermost electrodes by their function in the capture process, the lower capture electrode is also referred to as the reflection electrode. The electrostatic trap potential is for the most part defined by the voltage difference between the ring and the endcap electrodes, whereas the potential applied to the correction electrodes is used to compensate residual anharmonicities. Upper and lower capture electrode find use in the dynamical capture process.

The maximum voltage applicable to the electrodes is limited by the insulation between neighboring electrodes. For all but the capture electrodes, sapphire balls with 1 mm diameter are used to separate electrodes from each other, allowing a maximum potential difference of about 1 kV. The capture electrodes are insulated with MACOR rings with a diameter of 1.5 mm, hence permitting a higher break-down voltage of approximately 2 kV.

The value of gap width created by the sapphire balls is influenced by the compression of the copper electrodes and is given in Fig. 2.15 as $z_g = 0.7\,\mathrm{mm}$. However, as will be discussed in section 2.3.8, an analysis of the trap potential indicates that the gap width is slightly different for upper and lower correction electrode and about $z_g \approx 0.85\,\mathrm{mm}$. The difference between upper and lower electrodes is probably due to an unequal electrode compression by the mounting rods holding the trap electrodes.

2.3.5 Expansion series for the potential of a cylindrical Penning trap

In the following discussion, an expression for the potential of a rotation-invariant trap of total length z_t is derived. The potential is then evaluated numerically for the electrode configuration of the SpecTrap Penning trap. The potential is decomposed into contributions due to the individual trap electrodes, which allows for a calculation of the trap potential and thus properties like ion oscillation frequencies for arbitrary electrode voltages. The higher-order terms of the potential will be of specific interest for the discussion in chapter 5.

Following the discussion in [49] and [50], the electrostatic potential $\phi(r,z')$ in the trap volume with radial and axial coordinate r and z', respectively, can be expressed as a linear superposition of the potentials $U_i\phi_i$ which are created by the i'th electrode at a voltage U_i. The index i iterates all electrodes:

$$\phi(r,z') = \sum_i U_i \phi_i(r,z'). \tag{2.16}$$

The functions ϕ_i are solutions of the Laplace equation with the boundary conditions $\phi_i(r,z') = 1$ at the surface of the electrode i, $\phi_i = 0$ at the surface of all other electrodes, and a linear slope in the gaps between electrodes. Additionally, the condition $\phi_i(r,0) = \phi_i(r,z_t) = 0$ applies, which means that the outermost electrodes are closed. The total trap length is z_t and the center of the trap is at $z' = z_t/2$, accordingly. Solving the potential for a closed trap design allows an approach for the potential expansion as presented in [49]. The influence on the potential in the central region is negligible due to the axial elongation of the design of the SpecTrap Penning trap.

A solution to the Laplace equation of the rotation invariant and closed trap can be written as a linear combination of the basis functions b_n with coefficients a_n^i [49]:

$$\phi_i(r,z') = \sum_n a_n^i b_n(r,z'), \tag{2.17}$$

$$b_n(r,z') = \frac{J_0\left(\frac{n\pi r}{z_t}\right)}{J_0\left(\frac{n\pi r_0}{z_t}\right)} \sin\left(\frac{n\pi z'}{z_t}\right). \tag{2.18}$$

Here, J_0 denote the zero-order Bessel function. To determine the coefficients a_n^i the potential is first evaluated on the surface of the cylinder. With $r = r_0$, equation (2.18) simplifies to $b_n = \sin(n\pi z'/z_t)$ and by inserting into equation (2.17) one gets:

$$\phi_i(r_0, z') = \sum_n a_n^i \sin\left(\frac{n\pi z'}{z_t}\right). \tag{2.19}$$

The Fourier expansion of the potential (2.19) can be rewritten as an expression for the coefficients a_n^i:

$$a_n^i = \frac{2}{z_t}\int_0^{z_t} dz'\, \phi_i(r_0, z') \sin\left(\frac{n\pi z'}{z_t}\right).$$

At the cylinder surface, this integral can be evaluated with the boundary condition of the potential ϕ_i. With $z' = a^i$ and $z' = b^i$ as the upper and lower boundaries of the i'th electrode, one receives an explicit expression for the coefficients a_n^i:

$$a_n^i = \frac{2}{n\pi}\left(\cos\left(\frac{n\pi a^i}{z_t}\right) - \cos\left(\frac{n\pi b^i}{z_t}\right)\right) \cdot \sin\left(\frac{n\pi z_g}{2z_t}\right) \frac{2z_t}{n\pi z_g}. \tag{2.20}$$

The last two terms in (2.20) represent the linear potential slope between adjacent electrodes. For $z_g \to 0$ they approach unity. Inserting the coefficients a_n^i given by Eq. (2.20) into Eq. (2.17), one receives an expression for the potential $\phi_i(r, z)$ created by the i'th electrode. Finally, by summation over all electrodes, the total electrostatic potential $\phi(r, z')$ is obtained.

The potential of the SpecTrap Penning trap has been calculated numerically according to the approach presented here. To give a more handy expression than Eq. (2.17) with the expansion in basis functions b_n, the potential $\phi(r, z')$ has been rewritten in a power-series expansion around the trap center z_0. The axial coordinate is redefined with $z = z' - z_t/2$, such that the center of the trap is now at $z = 0$. In the most general form, the potential can be written as:

$$\phi(r, z) = \sum_{n=0}^{\infty} \frac{C_n}{d^n} \sum_{j=0}^{n/2} B_n^j \cdot z^{n-2j} r^{2j}. \tag{2.21}$$

Here, d denotes the characteristic distance as defined in Eq. (2.5). The coefficients B_n^j are readily determined by the requirement to fulfill the free-space Poisson equation $\triangle\phi = 0$. The general expression for the B_n^j can be found in [51], and the first terms of (2.21) explicitly evaluated read:

$$\begin{aligned}\phi(r, z) = {}& \frac{C_1}{d} z + \frac{C_2}{d^2}\left(z^2 - \frac{1}{2}r^2\right) + \frac{C_3}{d^3}(\dots) + \frac{C_4}{d^4}\left(z^4 - 3z^2r^2 + \frac{3}{8}r^4\right) \\ & + \frac{C_5}{d^5}(\dots) + \frac{C_6}{d^6}\left(z^6 - \frac{15}{2}z^4r^2 + \frac{45}{8}z^2r^4 - \frac{5}{16}r^6\right) + \dots . \end{aligned} \tag{2.22}$$

The equations (2.21) and (2.22) define the coefficients C_n, which have the dimension of a voltage. In equation (2.22), the terms of higher order in z contribute to the energy dependence of the axial oscillation frequency. The terms of the form $z^2 r^k$ alter the potential to an axially harmonic potential that depends on the radial position. Since these terms will be later discussed in detail (Sec. 5.3.6), they are listed here for the sake of completeness.

In many cases it is sufficient to consider the potential on the axis of symmetry $r = 0$, where Eq. (2.22) takes the much simpler form

$$\phi(0,z) = \sum_n C_n \left(\frac{z}{d}\right)^n . \tag{2.23}$$

Following the idea of equation (2.16), the total potential ϕ and the coefficients C_n are decomposed into contributions due to the i-th electrode set to the voltage U_i:

$$\begin{aligned} \phi(0,z) = \sum_i U_i \phi_i(0,z) &= \sum_i \left(U_i \sum_n C_n^i \left(\frac{z}{d}\right)^n \right), && (2.24) \\ C_n &= \sum_i U_i C_n^i. && (2.25) \end{aligned}$$

Because the trap electrodes are symmetrically arranged with respect to the plane $z = 0$, the absolute values of the coefficients C_n^i and C_n^k are the same for corresponding electrodes i,k. For even n, we have $C_n^i = C_n^k$ and for odd n we have $C_n^i = -C_n^k$, accordingly. Thus, only terms in (2.24) with even n contribute to the potential, if corresponding electrodes are set to the same potential.

To avoid confusion, it should be stressed that the potential in a Penning trap is often written in a different form $\phi(0,z) = U_0/2 \sum_n \tilde{C}_n (z/d)^n$. In this case, the potential is expressed with a single voltage U_0 that is symmetrically applied to both endcaps. The voltage applied to the correction electrodes U_c is defined by $U_c = \kappa \cdot U_0$ with the tuning ratio κ. The fixed ratio between different electrode potentials allows an expression with a combined coefficient $\tilde{C}_n$ that subsumes the effects of the individual electrodes. In this case, the coefficients $\tilde{C}_n$ are dimensionless and $\tilde{C}_2$ is usually of the order of 1/2. In contrast, the coefficients C_n used in the expansion of equation (2.23) have the dimension of a voltage $[C_n]$ =V. The relation between the different notations is given by

$$\frac{U_0 \tilde{C}_n}{2} = \sum_i U_i C_n^i. \tag{2.26}$$

2.3.6 Simulation of the coefficients C_n^i

A technical drawing of the SpecTrap Penning trap is shown in figure 2.15. According to the dimensions of trap electrodes as given in this drawing, the trap potential $\phi(r,z)$ has been evaluated numerically with equations (2.16), (2.17) and (2.20).

coefficient C_n^i	C_1^i	C_2^i	C_4^i	C_6^i	$C_1^i/C_1^{\mathrm{up.end}}$
electrode i					
upper endcap	0.2501	0.1441	-0.0256	-0.0031	1
upper correction	0.0988	-0.0019	-0.0296	0.0171	0.395
capture electrode	$8.3 \cdot 10^{-4}$	$6.6 \cdot 10^{-4}$	$1.4 \cdot 10^{-4}$	$1.2 \cdot 10^{-5}$	0.0033
ring electrode	0	-0.2837	0.1112	-0.0294	0

gap width z_g=0.85 mm
center-endcap distance z_0=6.6 mm
characteristic distance $d = 7.062$ mm
tuning ratio $r = -C_4^{\mathrm{up.end}}/C_4^{\mathrm{up.cor}} = -0.8596$

Table 2.3: The expansion coefficients C_n^i of the SpecTrap Penning trap potential as obtained by numerical evaluation of equation (2.16). A gap width $z_g = 0.85$ mm was chosen in the simulation to obtain best agreement with the measured coefficients C_n (see Sec. 2.3.7 and 2.3.8). The gap width z_g and the center-endcap distance z_0 are defined in figure 2.15. The characteristic distance d was defined by $d^2 = (z_0^2+r_0^2/2)/2$ in equation 2.5. The values given for z_0 and d have been re-evaluated with the new value for $z_g = 0.85$ mm and thus differ from the ones given in Fig. 2.15 and [41].

To separate the correction electrodes from the adjacent electrodes, the correction electrodes are equipped with small blind holes that hold sapphire balls with a diameter of 1.0 mm ([41], p. 35). The spacing between the electrodes depends on the compression of copper holding the sapphire balls and can only be estimated. In figure 2.15, the gap width is given as $z_g = 0.7$ mm, but a measurement presented in the following section determined the actual gap width to $z_g = 0.85$ mm and the values for the coefficients C_n^i are given in table 2.3 accordingly. The absolute value of z_g also influences the tuning ratio of the correction electrode, which is -1.1 and -0.86 for gap widths of $z_g = 0.7$ and $z_g = 0.85$, respectively. The dependence of the coefficients C_n^i from the gap width is illustrated in table A.9 in the Appendix, where values for the coefficients C_n^i are given for z_g in the range 0.7 mm to 0.9 mm.

The voltage applied to the correction electrode can be chosen that $U_{\mathrm{cor}} \cdot C_4^{\mathrm{cor}} = -U_{\mathrm{end}} \cdot C_4^{\mathrm{end}}$. Hence, the C_4 coefficient, which represents the main anharmonicity of the trap potential, is tuned to zero. The ratio $r = C_4^{\mathrm{end}}/C_4^{\mathrm{cor}}$ is called tuning ratio accordingly. For an orthogonal trap like the SpecTrap Penning trap, it is $|\mathrm{C}_2^{\mathrm{cor}}| \ll |\mathrm{C}_2^{\mathrm{end}}|$ and thus the total C_2 that determines the axial oscillation frequency is nearly independent of the correction electrode voltage.

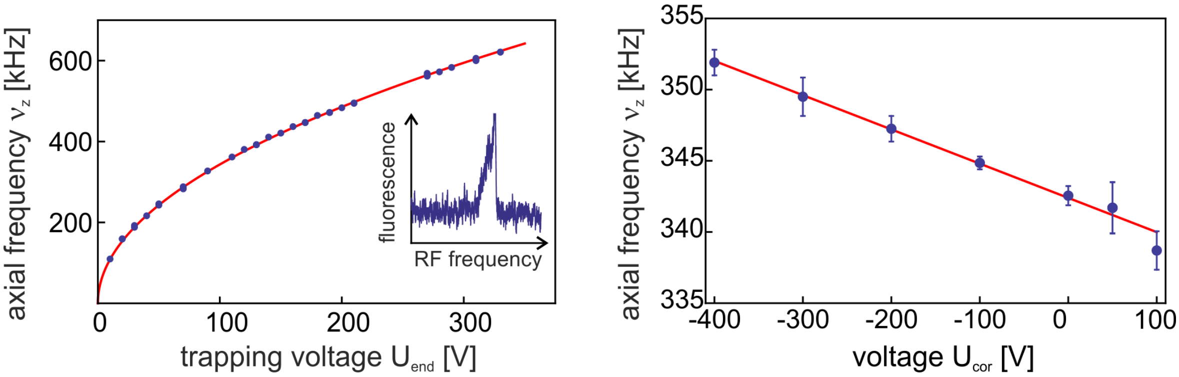

Figure 2.16: Left: Axial oscillation frequency ν_z as a function of the endcap voltage U_{end} to determine the combined coefficients $C_2^{\text{u.e.}} + C_2^{\text{l.e.}}$ of upper and lower endcap. Right: Axial oscillation frequency ν_z as a function of the correction voltage U_{cor} to determine the combined C_2 of upper and lower correction electrode ($U_{\text{end}} = 100\,\text{V}$).

2.3.7 Measurements of the coefficients C_2^i

The axial oscillation frequency of an ion with charge q and mass m in a harmonic potential of the form $\phi = Az^2$ is given by $\omega_z = \sqrt{2A} \cdot \sqrt{q/m}$ (Eq. (2.4) and (2.10)). Following equation (2.23), the potential on the axis of symmetry is given in lowest order by

$$\phi \approx \frac{C_2}{d^2} z^2 \tag{2.27}$$

and the axial frequency thus becomes

$$\omega_z \approx \sqrt{\frac{2C_2}{d^2}} \sqrt{\frac{q}{m}}. \tag{2.28}$$

Together with Eq. (2.25), this relation has been used to experimentally determine the coefficients C_2^i for each electrode pair i by measuring the axial oscillation frequency as a function of the voltage U_i applied to the respective electrode pair i.

To this end, the fluorescence signal of laser-cooled magnesium was observed while a sinusoidal excitation of a few hundreds of millivolt was applied to one of the trap electrodes. When the axial center-of-mass motion of the ion cloud was resonantly excited, the fluorescence signal changed due to rapid heating of the ions. Depending on the excitation amplitude and the laser detuning, an increase or a decrease of fluorescence was observed. The inset of figure 2.16 shows an example of the fluorescence signal while scanning the frequency of the RF excitation over the axial oscillation frequency. In this specific case, the ion fluorescence increased upon excitation. Because all electrodes but the capture and the ring electrode are protected by low-pass filters that block the RF signal, the excitation was in most cases applied to the capture electrode.

electrode i	$C_1^i/C_1^{\mathrm{lo.end}}$	C_2^i
upper endcap	-0.977	0.1445(25)
lower endcap	1	0.1445(25)
upper correction	-0.456	-0.0020(1)
lower correction	0.395	-0.0020(1)
(upper) capture	-0.0038	$5.4(4) \cdot 10^{-4}$
(lower) reflection	0.0038	$5.4(4) \cdot 10^{-4}$

Table 2.4: The coefficients C_n^i for the SpecTrap Penning trap obtained by measurements of the axial oscillation frequency. For the coefficients C_1^i, only ratios could be determined. The given values are normalized to the coefficient $C_1^{\mathrm{lo.end}}$ of the lower endcap electrode.

The combined coefficients $C_2^{\mathrm{up.end}} + C_2^{\mathrm{lo.end}}$ of upper and lower endcap were determined by a measurement of the axial oscillation frequency as a function of the voltage applied to both upper and lower endcap (Fig. 2.16). All other electrodes had been set to zero potential. The coefficients for the upper and lower endcap are listed in table 2.4 and were determined to $C_2^{\mathrm{up.end}} = C_2^{\mathrm{lo.end}} = 0.1445(25)$.

The coefficients C_2^{cap} and C_2^{cor} of the capture and the correction electrodes were determined from the shift of the axial oscillation frequency when an additional potential was applied to the capture and correction electrodes, respectively. When the endcap electrodes are kept at the voltage U_{end}, the change of the axial oscillation frequency per voltage applied to the capture and correction electrodes can be calculated according to equation (2.25) and (2.28):

$$\frac{\mathrm{d}\omega_z}{\mathrm{d}U_{\mathrm{cap/cor}}} = \sqrt{\frac{2q}{md^2}}\frac{C_2^{\mathrm{cap/cor}}}{2\sqrt{C_2}}. \tag{2.29}$$

The right part of figure 2.16 shows the measurement of the coefficient C_2^{cor}. The coefficient C_2^{cap} for the capture electrodes was determined in an analogous measurement (Tab. 2.4).

The actual value $C_2^{\mathrm{cor}} = -0.0020(1)$ for the correction electrodes could be used to determine the gap width z_g between the correction electrode and its adjacent electrodes, which is not known to high accuracy due to the unknown electrode spacing created by the separating sapphire balls. As one can see in table A.9 in the Appendix, which lists the C_2^i coefficients for z_g in the range of 0.7 mm to 0.9 mm, C_2^{cor} is strongly dependent on z_g and the actual value of C_2^{cor} was thus used to determine $z_g \approx 0.85$ mm. As a major application, the precise value of z_g increases the accuracy of the coefficients C_4^i for both endcap and correction electrodes. These coefficients determine the tuning ratio $r \approx -0.86$, for which the trap potential is compensated to a nearly harmonic potential with $C_4 = 0$.

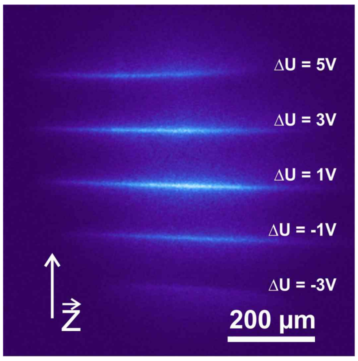

Figure 2.17: Combination of several images of an ion cloud with different potential differences ΔU between upper and lower endcap. The cloud position changes according to equation (2.34).

2.3.8 Measurements of the coefficients C_1^i

When the same voltage is applied to corresponding electrodes, the axial potential minimum coincides with the geometric trap center ($r = 0$, $z = 0$). When an additional voltage ΔU^i is applied to the electrode i, an additional potential ϕ^{a} is created which shifts the potential minimum and thus breaks the symmetry of the potential ϕ with regard to the $z = 0$ plane. To lowest order, the modified potential is given by

$$\begin{aligned} \phi(0,z) &= \phi^{\mathrm{sym}}(0,z) + \phi^{\mathrm{a}}(0,z), && (2.30)\\ \text{with} \quad \phi^{\mathrm{sym}}(0,z) &= C_2\left(\frac{z}{d}\right)^2 + \dots && (2.31)\\ \text{and} \quad \phi^{\mathrm{a}}(0,z) &= \Delta U_i\left(C_1^i\left(\frac{z}{d}\right) + C_2^i\left(\frac{z}{d}\right)^2\right) + \dots. && (2.32)\\ \rightarrow \frac{\partial\phi}{\partial z} &= \frac{2z(C_2 + \Delta U_i C_2^i)}{d^2} + \frac{\Delta U_i \cdot C_1^i}{d} + \dots. && (2.33) \end{aligned}$$

The electric center of the total potential is given by the zero point of Eq. (2.33)

$$z_{\mathrm{center}} = -\Delta U_i \cdot \frac{d}{2} \cdot \frac{C_1^i}{(C_2 + \Delta U_i C_2^i)}. \tag{2.34}$$

Equation (2.34) allows to determine the C_1^i coefficients of the individual electrodes from a measurement of the cloud position with an imaging system (Fig. 2.17). Because the scale of the imaging system is not known with high precision, only the ratios of the coefficients C_1^i/C_1^j for electrodes i,j have been determined experimentally (table 2.4). The ratios are in good agreement with the modeled potential, however, it stands out that the absolute values of corresponding coefficients are not equal as one would expect from the trap symmetry. A possible explanation for the deviation of the upper endcap's (correction) value is that the gap width z_g is smaller in the upper half of the trap (compare also to table A.9).

2.4 Electronic components

In this section, the electronic components which process signals going to and coming from the trap electrodes are discussed.

To reduce the influence of thermal noise on the trapping potential, all signal lines going towards the individual electrodes are equipped with low-pass filters that are kept at 4 K in the cryogenic environment directly under the trap. The low-pass filters are by-passed by diodes, which allows irradiation of high-frequency signals, if the signal amplitudes are above a threshold of 400 mV (table 2.5). A detailed description of the filter design is given in [41]. Since the frequencies for excitation of the axial and the reduced cyclotron motion are typically $> 100\,\text{kHz}$, RF signals were only applied via the capture electrode or the ring segments.

For processing of signals coming from the trap electrodes, specialized cryogenic amplifiers are installed in thermal contact with the liquid helium reservoir:

- a non-destructive ion detector (NID) is attached to the upper capture electrode for pick-up and amplification of the signals induced by incoming ion bunches,
- a resonant circuit is attached in combination with a MESFET-based amplifier to each of the endcap electrodes for non-destructive detection of the signal induced by the axial ion oscillation,
- a MESFET-based amplifier is attached to one ring segment for detection of the signal induced by the radial ion motion [41].

The circuit layouts of all three amplifiers have already been described in [41]. The NID and both resonant circuits, which have been characterized and used for measurements presented in this work, will be discussed in the following. The analysis of the NID has also been presented in a publication [39].

2.4.1 Non-destructive ion detector (NID)

The non-destructive ion detector (NID) serves both as a charge counter and for providing timing information for the capture process. The signal detection is based on

low-pass cut-off frequency	endcap/correction	ring	reflection	capture
filter [2π·kHz]	7.5	11	0.7	0
diodes [2π·MHz]	$\ll 0.01$	56	0.02	2

Table 2.5: Cut-off frequencies of the low-pass filters for signals going towards the trap electrodes. Signals with an amplitude larger than 400 mV by-pass the filters via a pair of diodes. In this case, the upper frequency limit is defined by the larger diode cut-off frequency. All values according to [41].

the non-resonant pick-up and subsequent low-noise amplification of image charges induced in the upper capture electrode by an incoming ion bunch. This primary signal is amplified by the cryogenic NID and a second, room-temperature amplifier (CBC-1, Stahl Electronics). A low-noise gallium-arsenide field-effect transistor builds the first stage of the NID, which provides a total amplification by a factor between 3.2 (room temperature) and 4.0 (for $T < 77\,\mathrm{K}$). The room-temperature amplifier (CBC-1) has an additional amplification factor of 78 so that the total voltage amplification amounts to $\alpha = 250(30)$. The complete setup is also described and characterized in [39].

The induced signal $U_{\mathrm{in}} = Q_{\mathrm{in}}/C_{\mathrm{in}}$ at the capture electrode is defined by the induced image charge Q_{in} and the input capacitance $C_{\mathrm{in}} = 49.2(8)\,\mathrm{pF}$, which is mainly defined by the capacitance of the capture electrode. The induced charge can be calculated with the ion charge distribution ρ and the geometry function $\Xi(r,z)$ of the capture electrode, which can be determined (with the length of the capture electrode of $L = z_r - z_l = 22\,\mathrm{mm}$) with the same formalism as presented for the endcap electrode in equation (2.50). For the induced charge Q_{in}, one obtains in analogy to equation (2.50) [51]:

$$U_{\mathrm{in}}(t) \cdot C_{\mathrm{in}} = Q_{\mathrm{in}}(t) = \int \mathrm{d}z\; \rho(vt - z)\,\Xi(z,0). \tag{2.35}$$

In general, the induced charge Q_{in} as given by Eq. (2.35) also depends on the radial distribution of the ions. However, if we are only interested in the integrated signal $\int \mathrm{d}t\; Q(t)$ we can assume without restriction that all ions move along the axis $r = 0$ and ρ is thus a 1-D distribution, because the integrated signal is independent of the radial distribution.

The ion number N can be expressed through the charge distribution $\rho(t)$, respectively $\rho(z)$, with

$$N = \frac{1}{q}\int \mathrm{d}z\; \rho(vt - z) = \frac{v}{q}\int \mathrm{d}t\; \rho(vt - z). \tag{2.36}$$

Here, q denotes the charge per ion and v the velocity of the ion bunch. The detected signal $U(t)$ is determined from the induced signal $U_{\mathrm{in}}(t)$ with the amplification factor $\alpha = 250(30)$ and a correction factor $\kappa = 1.13$ which accounts for the limited frequency acceptance range of the amplifiers [39]. Thus the detected signal is expressed with $U(t) = (\alpha/\kappa) \cdot (Q_{\mathrm{in}}(t)/C_{\mathrm{in}})$.

Combining equation (2.35) and equation (2.36), we obtain the relation

$$\begin{aligned}\int \mathrm{d}t\; U(t) &= \frac{(\alpha/\kappa)}{C_{\mathrm{in}}} \cdot \int \mathrm{d}t \int \mathrm{d}z\; \rho(vt - z) \cdot \Xi(z,0)\\ &= \frac{(\alpha/\kappa)}{C_{\mathrm{in}}} \cdot \frac{Nq}{v} \int \mathrm{d}z\; \Xi(z,r)\\ &= \frac{(\alpha/\kappa)}{C_{\mathrm{in}}} \cdot \frac{Nq}{v} L. \end{aligned} \tag{2.37}$$

In the last step, use was made of the fact that the integral $\int dz\ \Xi(z,r)$ evaluates, independently of the radial coordinate r, to the electrode length L. Equation (2.37) provides an expression for the ion number as a function of the integrated NID signal and was used for the evaluation of NID spectra presented in this work.

2.4.2 Axial resonators for resistive cooling

The upper and lower endcap electrode of the SpecTrap Penning trap are each equipped with an axial resonator. These resonant circuits have two main applications: The induced signal of ions oscillating in the trapping volume can be used for non-destructive ion detection and at the same time, the ions are cooled because the induced signals are damped due to energy dissipation in the circuit.

This cooling technique is referred to as resistive cooling and can be used to cool a single ion or an ion ensemble until it is in thermal equilibrium with the resonant circuit, which is usually held at cryogenic temperatures of about 4 K. Two characteristics make resistive cooling especially suited for cooling of externally created, highly charged ions: first, resistive cooling is possible for any ion species in any charge state. This is in contrast to other cooling techniques like Doppler laser cooling, which requires a suitable (i.e. fast), laser-accessible transition and is therefore difficult to employ with highly charged ions. Secondly, in a harmonic potential the time constant for resistive cooling is independent on the ions' kinetic energies, which allows efficient cooling of ions with large kinetic energies after injection into the trap. Resistive cooling of HCI has been demonstrated e.g. with small ion ensembles of C^{5+} [52, 53] as well as with Xe^{44+} [54].

For non-destructive ion detection, the charge-to-mass ratio of trapped ions can be calculated by the trapping voltage that brings their axial oscillation frequency in resonance with the resonant circuits. The two resonance frequencies are $\nu_r = 536.5\,\mathrm{kHz}$ and $\nu_r = 1138.9\,\mathrm{kHz}$ for the circuit attached to the lower and to the upper endcap, respectively.

The circuit coils were constructed out of a PTFE-insulated constantan cable. Compared to other experiments [55, 56], where superconducting coils are used, this results in a rather low quality factor Q of 200–300 for both circuits. A low Q value was chosen for the benefit of a larger bandwidth $b = \nu_r/Q$ and the possibility of ion cooling in a broader frequency range. This is especially important for ion cooling at high kinetic energies in a non-ideal harmonic potential.

Figure 2.18 shows the equivalent circuit diagram of the resonant circuits attached and the electronic components for signal processing. Two amplifier stages are used: one low-noise amplifier directly attached to the trap at cryogenic conditions, and one ambient-condition, rack-mounted amplifier. The amplifications denoted in the figure are valid for an infinite input impedance, under consideration of the impedance matching the resulting voltage amplification amounts to $\alpha = 156.25$.

The characteristics of the resonant circuits were directly determined from the amplified thermal-noise signal. The noise spectrum of the RLC circuit can be modeled

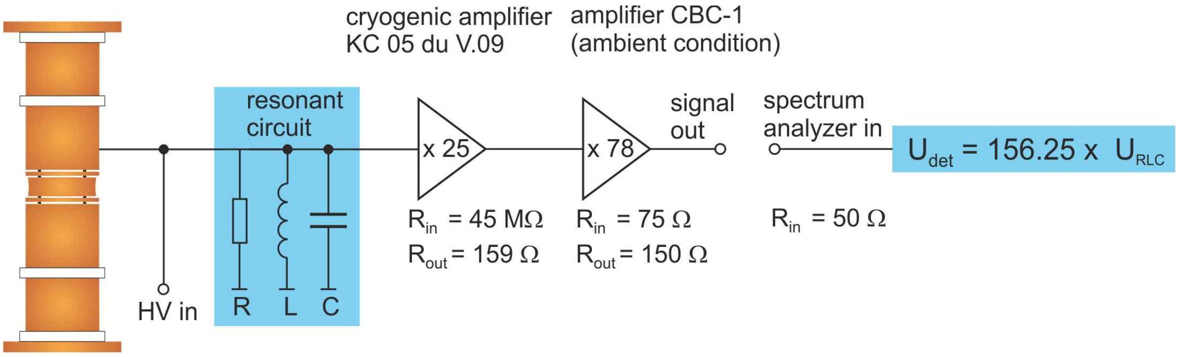
cryogenic amplifier
KC 05 du V.09
amplifier CBC-1
(ambient condition)
resonant circuit
x 25
x 78
signal out
spectrum analyzer in
U_{det} = 156.25 x U_{RLC}
R_{in} = 45 MΩ
R_{out} = 159 Ω
R_{in} = 75 Ω
R_{out} = 150 Ω
R_{in} = 50 Ω
HV in
R
L
C

Figure 2.18: Equivalent circuit diagram of the resonant circuits. The resonant circuit signal is amplified by a first amplifier placed in the cryogenic environment and a second one placed in ambient conditions. Under consideration of the specific input impedances the total voltage amplification amounts to $\alpha = 156.25$.

by the noise of a voltage source giving a voltage drop across the noise-free resistance of the circuit [57]. In this model, the noise characteristics of the voltage source is dominated by $1/f$-noise at lower frequencies and thermal Johnson noise at higher frequencies. For an Ohmic resistance R at temperature T, the root-mean-square of the thermal noise amplitude is given by [58]

$$U_{\mathrm{thermal}} = \sqrt{4k_B T R \delta}, \tag{2.38}$$

where the measurement bandwidth is denoted δ and k_B is the Boltzmann constant. The noise amplitude of an RLC-circuit with capacitance C_0 and inductance L_0 follows from Eq. (2.38), when the resistance R is replaced by the real part of the complex resistance $Z(\omega)$:

$$Z_{\mathrm{RLC}} = \left(\frac{1}{R} + i\omega C_0 + \frac{1}{i\omega L_0} \right)^{-1}. \tag{2.39}$$

With the amplification factor α of the two amplifiers, the noise amplitude detected with the spectrum analyzer becomes

$$U_{\mathrm{noise}} = \alpha \sqrt{4k_B T \delta \mathrm{Re}[Z_{\mathrm{RLC}}]}. \tag{2.40}$$

The noise spectra of the upper and lower resonant circuit have been recorded at a temperature of 4 K (Fig. 2.19). A function according to Eq. (2.40) was fitted to the data, where R, the quality factor Q, and ω_r were used as free parameters. The general agreement with the data is good, minor discrepancies may be due to the neglect of additional noise sources or an oversimplification of the circuit diagram.

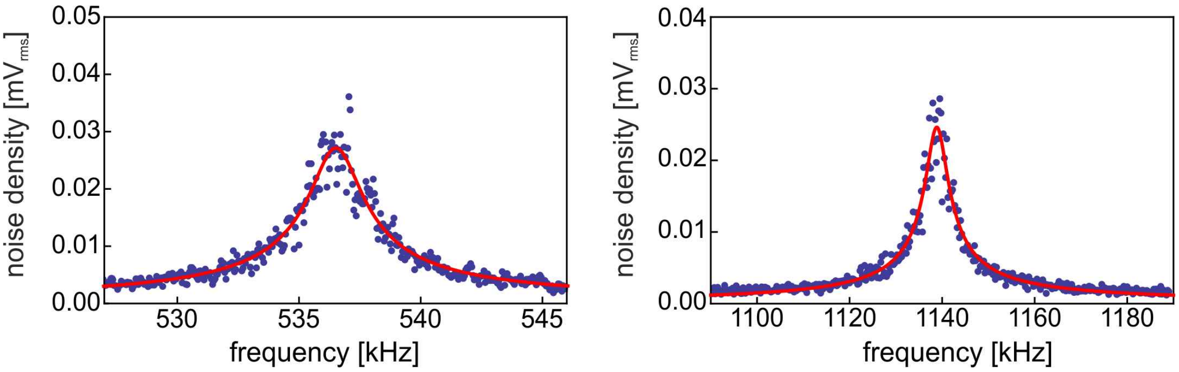

Figure 2.19: The thermal Johnson-noise spectra of the lower and upper resonant circuit at a temperature of 4 K. The main properties of the resonant circuit are listed in table 2.6.

	lower resonant circuit	**upper resonant circuit**
resonance frequency ν_r	536.3 kHz	1138.9 kHz
quality factor Q	254.5	237
resonance resistance R	1.72 MΩ	1.61 MΩ
capacitance C	44 pF	21 pF
inductance L	2.01 mH	0.95 mH
design value for L	1.73 mH	0.77 mH
$\tau_1(\mathrm{Mg}^+)$	812 s	870 s
$\tau_1(\mathrm{Ar}^+)$	487 s	522 s
$\tau_1(\mathrm{Ar}^{13+})$	8.0 s	8.6 s
$\tau_1(\mathrm{Bi}^{82+})$	1.05 s	1.1 s

Table 2.6: Characteristics of the upper and lower resonant circuit and resistive-cooling time constants τ_1 for selected ion species.

From the fit to the data, the capacitance C_0 and inductance L_0 were calculated with the relations

$$C_0 = \frac{Q}{R\omega_r}, \tag{2.41}$$

$$L_0 = \frac{R}{Q\omega_r}. \tag{2.42}$$

The resulting values are summarized in table 2.6. Also listed is the modeled value of the coil inductance, which has been calculated for both circuits from the coil design. The experimental and the modeled values for L are in good agreement, which corroborates the assumed values for C and R.

Effective electrode distance D and single-ion resistive cooling time τ_1

With the specific value of the Ohmic resonance resistance R of the resonant circuits (table 2.6), the rate for resistive cooling of a single ion can be calculated. Assuming an ideal harmonic potential and thus regarding an ion performing a sinusoidal oscillation with frequency ω_z, the axial position of an ion with (axial) energy E reads

$$z(t) = \frac{1}{\omega_z}\sqrt{\frac{2E}{m}}\sin(\omega_z t + \phi). \tag{2.43}$$

For small oscillation amplitudes, the induced charge on the endcap is linear in the axial coordinate z, hence the induced current is proportional to the ion velocity:

$$i(t) = \frac{q}{D}\frac{\mathrm{d}z(t)}{\mathrm{d}t} = \frac{q}{D}\sqrt{\frac{2E}{m}}\cos(\omega_z t + \phi). \tag{2.44}$$

Equation (2.44) defines the effective electrode distance D (not to be mistaken for the characteristic trap dimension d) as the constant of proportionality between the ion velocity and the current induced in the endcap. As will be shown below, the effective electrode distance D can be calculated from the electrode geometry of the trap.

The expectation value of the squared single-ion current I is given by

$$I^2(t) := \langle i(t)^2 \rangle = \frac{1}{T}\int_0^T \mathrm{d}t\ i(t)^2, \tag{2.45}$$

where the integral is performed over one axial oscillation period T. The ion oscillation is damped on time scales much larger than one oscillation period, so that we can assume the energy E to be constant over one axial oscillation period. Inserting (2.44) into (2.45) leads to

$$I^2(t) = \frac{q^2 2E}{D^2 m}\frac{1}{T}\int_0^T \mathrm{d}t\ \cos^2(\omega_z t + \phi) = \frac{q^2 E}{D^2 m}. \tag{2.46}$$

Due to the current I induced in the Ohmic resonance resistance R, the ion dissipates energy via the resonant circuit with power P. From equation (2.46) one also obtains the cooling rate γ_1 and its inverse, the single-ion cooling time $\tau_1 = \gamma_1^{-1}$:

$$\begin{aligned} -P &= \frac{\mathrm{d}E}{\mathrm{d}t} = -I^2 R = -\frac{q^2 R}{D^2 m}E, && (2.47)\\ \Rightarrow E(t) &= E_0 \exp(-\gamma_1 t), && (2.48)\\ \gamma_1 &= \frac{q^2 R}{D^2 m} = \tau_1^{-1}. && (2.49) \end{aligned}$$

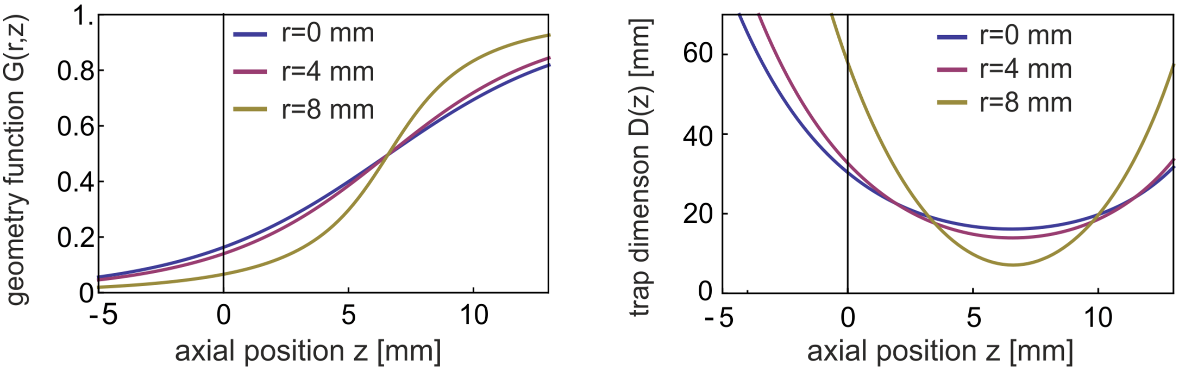

Figure 2.20: The geometry function G (left) and the effective electrode distance D (right) for the upper endcap electrode. The geometry function and the effective electrode distance are given as a function of the axial ion position z for three different radial ion positions r.

To give an absolute value for the single-ion cooling rate, it remains to determine the effective electrode distance D for the SpecTrap electrode geometry. The charge Q induced in the endcap by an ion of charge q at the axial and radial positions z and r, respectively, is expressed via the geometry function $G(r,z)$ and can be calculated for a cylindrical electrode with radius R [51]:

$$Q(r,z) \equiv -q \cdot G(r,z) \tag{2.50}$$

$$= \frac{q}{R\pi}\int_0^\infty dx\, \frac{I_0(xr/R)}{I_0(x)}\left[\mathrm{sinc}\left(x\frac{z-z'}{\pi R}\right)(z-z')\right]_{z'=zL}^{z'=zR}. \tag{2.51}$$

Here, I_0 is the modified Bessel function of the first kind and the function *sinc* denotes the normalized, cardinal sine function defined by $\mathrm{sinc}(x) = \sin(\pi x)/\pi x$. By comparison of equation (2.44) and equation (2.50), one finds that $\partial_z G(r,z) = D^{-1}$.

In case of the upper endcap electrode, one finds that for sufficiently small amplitudes $z_0 < 1\,\mathrm{mm}$ and radii $r_0 < 4\,\mathrm{mm}$, the trap dimension D can be regarded as constant and amounts to $D \approx 30\,\mathrm{mm}$ (Fig. 2.20). The energy related with an axial amplitude of 1 mm depends on the ion species. For singly charged magnesium ($\nu_z = 536\,\mathrm{kHz}$) it is $E = 1.5\,\mathrm{eV}$ and for $^{209}\mathrm{Bi}^{82+}$ ($\nu_z = 1139\,\mathrm{kHz}$) it is 55 eV. This demonstrates that the simplification of $D = 30\,\mathrm{mm}$ is strictly valid only for thermal ions and does not apply to the conditions directly after ion injection into the trap.

Resonant amplification of induced RF signals

When an RF signal with amplitude U and frequency ω is applied to the electrode j, an oscillating potential ϕ is created whose gradient excites the axial motion of a single ion or an ion cloud:

$$\phi(z,t) = U\sin(\omega \cdot t)\frac{z}{d}C_1^j + \dots \tag{2.52}$$

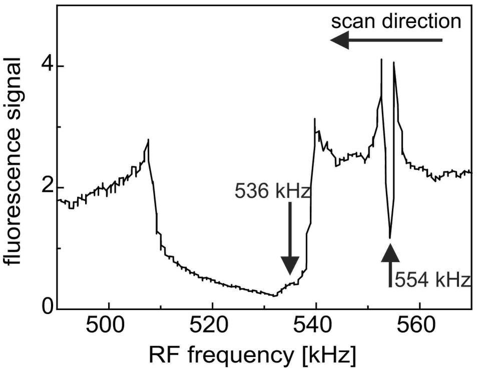

Figure 2.21: Mg^+ fluorescence while scanning the excitation frequency ν_{ex} of a signal applied to the ring electrode. For a frequency of $\nu_{ex} = 554\,\mathrm{kHz}$, the fluorescence dip indicates the excitation of the ions' axial motion (trapping voltage $U_0 = 260\,\mathrm{V}$). For frequencies around $\nu_{ex} = 536\,\mathrm{kHz}$, the fluorescence is heavily influenced by the signal induced to the lower resonant circuit.

The strength of the potential gradient, as defined in equation (2.52), depends on the value of the electrode's coefficient C_1^j, which can be found in table 2.3. Because all electrodes besides the ring and capture electrode are protected by low-pass filters, RF signals can only be applied to the ring and the capture electrode, which have the smallest coefficients C_1^j of all electrodes.

However, to resonantly affect the Mg^+ fluorescence and thus allow detection of the axial oscillation frequency, even small excitations with signal amplitudes of 100 mV at the capture or ring electrode were sufficient. On the other hand, axial oscillations with amplitudes that are large enough to induce a detectable signal in the resonant circuits require a stronger excitation. In this case, even signal amplitudes of several volts turned out to be insufficient.

This observation is supported by a simple estimation: for a driven oscillator, the excitation amplitude depends both on the strength of the driving force and the frequency matching between excitation and oscillator. Assuming a frequency matching of the order of the axial frequency distribution $\Delta\nu_z \approx 1\,\mathrm{kHz}$ and an excitation amplitude of 1 V at the capture electrode, by numerically solving the equation of motion of the driven oscillator it was found that a Mg^+ ion will be excited to energies of the order of 1 meV or $k_B \cdot 10\,\mathrm{K}$, which would be not easily detected with the resonant circuit.

It is, however, possible to induce a signal in the endcap electrode via excitation of the neighboring electrode. The potential gradient created by this induced signal for ion excitation can exceed the one of the primary excitation by orders of magnitudes, as follows from the discussion below.

The electric-circuit simulation software *LT Spice* was used to determine the signal which is induced in the upper endcap electrode when an external RF excitation is applied to the capture or ring electrode. The capacitance that couples the electrodes was estimated with $C = \epsilon_0 A/s$, where s is the electrode distance and A the area of the electrode surfaces. With the resulting capacities $C_{\text{ring-end}} = 0.5\,\text{pF}$ and $C_{\text{cap-end}} = 1\,\text{pF}$, the simulation of the electric circuits shows an on-resonance amplification of 9 dB and 13 dB, respectively. Besides the signal amplitude, the effect of an RF signal also depends on the C_1^i coefficient of the electrode. Since the coefficient C_1^{end} is two orders of magnitude larger than C_1^{cap} and $C_1^{\text{ring}} = 0$, the influence of the signal induced in the endcap is by more than three orders of magnitudes larger than the primary excitation via the ring or capture electrode.

An example of the resonantly enhanced excitation is shown in figure 2.21. The frequency of a signal applied to the ring electrode was scanned from 570 kHz to 490 kHz. When the signal frequency matches the axial oscillation frequency of the ions of $\nu_z = 554\,\text{kHz}$, axial excitation results in a sudden change of the fluorescence rate. When the frequency of the excitation signal approaches the resonant circuit frequency of 535 kHz, the resonantly enhanced signal in the endcap leads to non-resonant axial excitation of the Mg^+ ions and thus influences the fluorescence signal over a wide range of frequencies.

When $^{24}\text{Mg}^+$ was axially excited for resonant circuit detection, the trap voltage was set to about $U = 240\,\text{V}$ during the excitation so that the resonant circuit frequency, the axial oscillation frequency and the signal frequency were all identical to 536 kHz. Directly after excitation, the endcap electrode voltage was switched to 200 V and subsequently scanned to 300 V. In this way, the resonant circuit signal of figure 5.1 (right) was recorded.

2.5 Experimental control and ion capture process

Central part of the experimental control is the main control software, which has been developed in this thesis within a LabVIEW environment. The complete system, including the experimental components and the control software, the *SpecTrap control and operation center at HITRAP* (SCOTCH), is depicted in a schematic diagram in figure 2.22 which shows the interconnections between the components and the software.

The control software coordinates the devices involved in an experiment and takes care of event timing and synchronization in dynamical experiments, e.g. the timing involved in the capture process or ramping of electrode voltages.

2.5.1 The experiment control software

Most communication between the computer and the experiment is mediated via a NI-PXI system (NI PXI 1036, National Instruments), which is equipped with two PCI cards: the PXI-6224 card provides 32 analog-in channels (AI) and 48 digital-in/out channels (DI/O), the PXI-6723 card provides 32 analog-out channels (AO). An additional PCI-DAC 6702 card, which is not implemented in the PXI 1036 system but is directly connected to the computer, provides another 16 analog-out channels. The

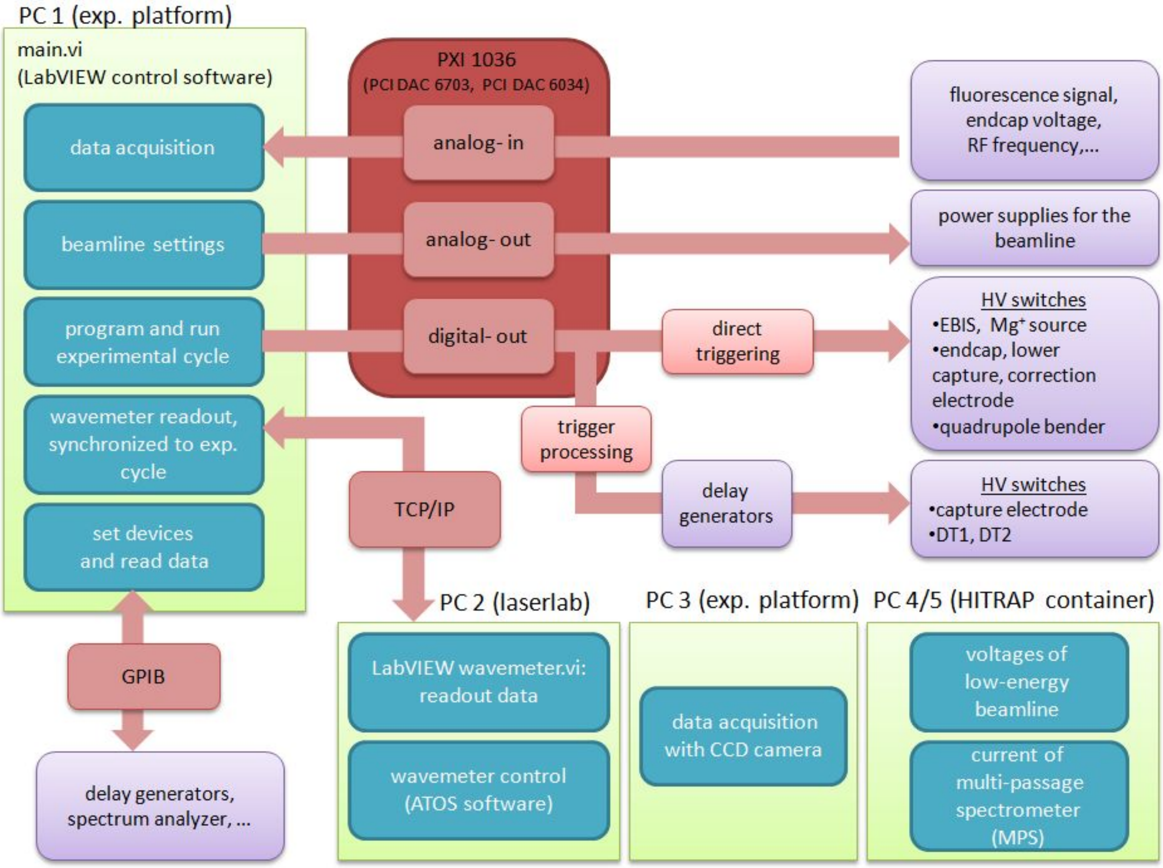
PC 1 (exp. platform)
main.vi
(LabVIEW control software)
data acquisition
beamline settings
program and run experimental cycle
wavemeter readout, synchronized to exp. cycle
set devices and read data
PXI 1036
(PCI DAC 6703, PCI DAC 6034)
analog- in
analog- out
digital- out
fluorescence signal, endcap voltage, RF frequency,...
power supplies for the beamline
direct triggering
HV switches
•EBIS, Mg⁺ source
•endcap, lower capture, correction electrode
•quadrupole bender
trigger processing
delay generators
HV switches
•capture electrode
•DT1, DT2
TCP/IP
GPIB
delay generators, spectrum analyzer, ...
PC 2 (laserlab)
LabVIEW wavemeter.vi: readout data
wavemeter control (ATOS software)
PC 3 (exp. platform)
data acquisition with CCD camera
PC 4/5 (HITRAP container)
voltages of low-energy beamline
current of multi-passage spectrometer (MPS)

Figure 2.22: The SpecTrap control and operation center at HITRAP (SCOTCH).

analog-out channels directly control the power supplies of the SpecTrap beamline elements, whereas the analog-in channels are used for data acquisition. The digital channels are used to trigger events such as the creation of ion bunches in the EBIS or Mg^+ source, or for continuous definition of the status (*on/off*) of elements as the laser shutter or the trap electrodes.

The digital channels are used by running experimental cycles, which in this context means the creation and execution of a finite-length waveform for several digital-out channels in parallel. The waveform is defined by the user and exhibits a train of pulses for each digital channel with arbitrary pulse number, pulse duration and pulse separation. This way, the experimental cycles allow the temporal definition of events with precise synchronization. At the end of an experimental cycle, all digital channels remain in their last defined status (*high/low*) which allows to continue experiments beyond the end of the cycle. The execution of the digital waveform is controlled by the internal clock of the NI-PXI system, which guaranties an absolute timing of <100 ns for the output of the digital channels. In principle, the rate of the internal clock also sets the lower limit for the temporal step-size of the digital waveform, but due to its long duration of typically 10 to 30 seconds, the waveform is generated with a time-step resolution of typically 1 ms.

Data acquisition with the analog-in channels is implemented with a continuous and a finite measuring scheme. A continuous measurement has no predefined duration but records the signals at the analog-in channels until it is aborted. The continues acquisition mode is independent of the experimental cycle and during a measurement the status of the DI/O channels remains usually (but not necessarily) unchanged. A measurement in the finite-duration mode records data synchronously to an experimental cycle and thus ends with the execution of the digital-channel waveform. The advantage of this finite mode is a higher degree of automation for the price of reduced flexibility.

The analog-out channels of the PXI-6723 card are used for remote control of the power supplies for the electrostatic elements of the SpecTrap beamline. Two independent sets of parameters are defined with the control software, which can switch them to change the beamline from the transport of Mg^+ to highly charged ions and vice versa. When an experimental cycle is performed, which controls via the digital channels e.g. the ion injection process and the status (Mg^+/HCI) of the quadrupole bender, one can define the time at which the set of beamline parameters is switched. This way the consecutive or alternating trapping of Mg^+ and highly charged ions is automated.

Some devices, notably the delay generators (DG535, Stanford Research Systems) and a spectrum analyzer (HP 3589A, Hewlett Packard), are connected to the computer via a GPIB interface and are also programmable with the control software. The CCD camera for fluorescence imaging and the wavemeter for laser stabilization run independently on additional computers. The LabVIEW software controlling the wavemeter features a synchronization with the main control via a TCP/IP connection. This way parallel readout to an experimental cycle with a timing $<10\,\mathrm{ms}$ is possible.

The process of ion loading is initialized with a digital pulse which is sent either to the Mg^+ source or the EBIS. The drift tubes DT1 and DT2 as well as the capture electrode are not triggered independently, but with a trigger that is derived from the one going to the ion sources. For this purpose, the ion source trigger is processed and delayed by two delay generators (DG535, Stanford Research Systems). The delay generators each possess two channels for producing gates with arbitrary delay and duration. Two gates are adjusted to the times of flight of the highly charged ions to drift tube 1 and drift tube 2, respectively. The remaining two gates are reserved for the capture gate delay of Mg^+ and the HCI. A signal processing scheme using logic devices (Fig. A.1 in the Appendix) guaranties that each source trigger results in application of the correct capture gate.

2.5.2 The ion capture process

Incoming ions are captured dynamically in the trapping volume by fast switching of the upper capture electrode. When the ions arrive at the capture electrode, its potential is reduced with a fast low-noise high-voltage switch (HS-1000, Stahl Electronics)

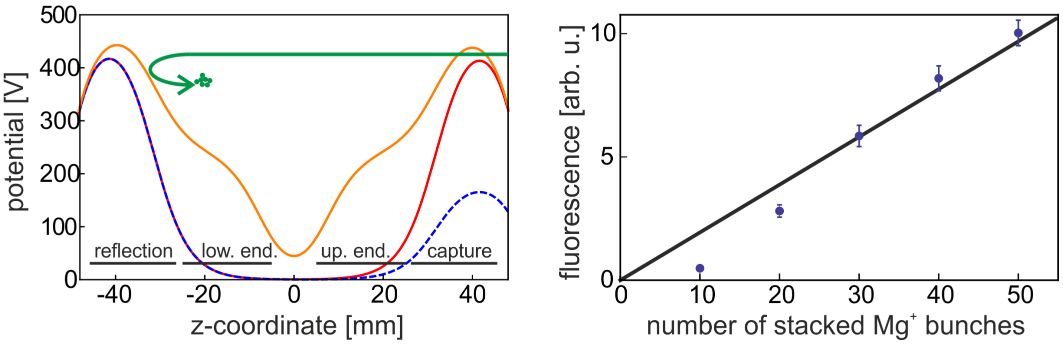

Figure 2.23: Left: Calculated potential on the trap axis for three different stages of the ion capture process. First, the ions are allowed to enter the trap (blue), then the capture electrode potential is raised (red), and in a last step a harmonic potential is created by use of the endcap and correction electrodes (orange). The set of voltages $(U_{\text{cap}}, U_{\text{ref}}, U_{\text{end}}, U_{\text{cor}})$ for the capture, reflection, endcap and correction electrodes are $(500, 200, 0, 0)\,\text{V}$, $(500, 500, 0, 0)\,\text{V}$ and $(500, 500, 240, -206)\,\text{V}$ for the blue, the red and the orange graph, respectively. Right: Fluorescence after accumulation of up to 50 bunches of Mg^+ ions.

for a short duration (the so-called capture gate) such that incoming ions are allowed to enter the trap. The lower capture electrode is set to a high potential so that the ions are reflected, and before the ions leave the trapping region the capture electrode potential is raised to a potential that confines the ion bunch. The trapping cycle is completed by slowly compressing the ion cloud towards the trap center by raising the endcap potential (Fig. 2.23, left).

The capture gate is adjusted using the TOF signal of the MCP at the bottom of the beamline. A usual procedure is as follows: Starting with zero potential at all trap electrodes and an undisturbed TOF signal at the MCP, the potential of the capture electrode is raised until the ion bunch is blocked and the TOF signal vanishes. Once the correct capture gate is applied, the ion bunch is no longer blocked by the capture electrode and the TOF signal is again detected at the MCP. A first guess for the ion bunch TOF to the trap center and the timing of the capture gate can be obtained from a measurement with the NID detector (Fig. 2.24, inset): The signature of an ion bunch, which passes the capture electrode before and after reflection at the reflection electrode, directly reveals the arrival time at the capture electrode of $t = 46\,\mu\text{s}$. Typical parameters for the capture process of Mg^+ with a kinetic energy of 400 eV are a gate duration of 1–3 μs and the capture electrode set to a higher and lower potential of 500 V and 200 V, respectively.

2.5.3 Accumulation of ion bunches

A typical capture gate duration of a few μs was found to be short enough to prevent significant loss of the already confined ions in the trap. This is an important requirement for the creation of multi-species ion clouds and it also allows the accumulation

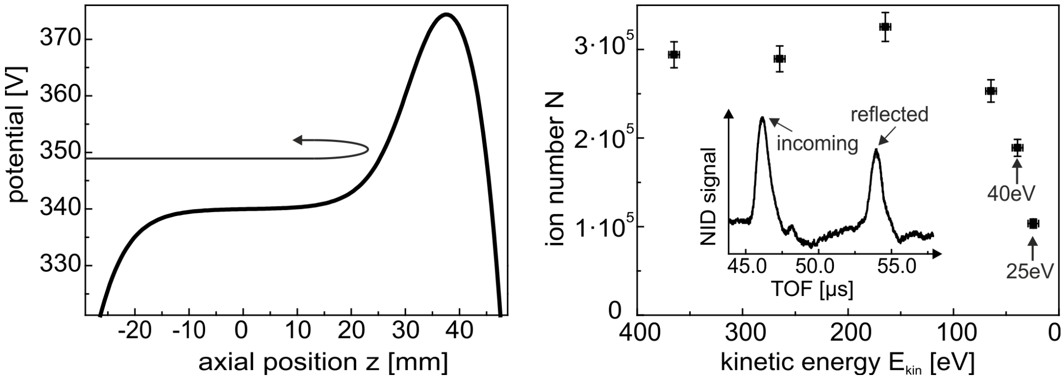

Figure 2.24: Left: Trap potential with a bias of 340 V applied to each trap electrode. The Mg^+ ions with an initial kinetic energy of 365(3) eV are reflected at the reflection electrode. Right: Number of reflected ions detected with the NID as a funtion of the kinetic energy at the trap center, which was calculated by $E_{kin} = 365\,\text{eV} - eU_{\text{bias}}$. The inset shows a signal detected at the NID.

of ion bunches (2.23, right): The number of stored particles and thus the fluorescence increases linearly with the number of ion bunches loaded into the trap. For the first data point, 10 Mg^+ bunches were loaded with a temporal bunch separation of 250 ms. The denoted fluorescence is the signal which was detected once the fluorescence rate had stabilized after the initial laser cooling. The data points for higher ion bunch numbers were obtained in the same way after consecutively loading additional 10 bunches to the ions already confined in the trap. A linear regression was fitted to the data. The fluorescence rate of the first data points significantly deviate from the linear trend. This could indicate that the capture efficiency is low at first and increases for the subsequent bunches, possibly induced by more rapid laser cooling when pre-cooled ions are already confined in the trap. However, one should note that the error bars in the present case merely indicate the statistical uncertainty of the florescence measurement and may underestimate the actual error, to which the reproducibility of the accumulation process also contributes.

2.5.4 Ion capture with elevated potential or use of drift tube 2

An important aspect of the ion capture process is the minimal kinetic energy for which injection with sufficient ion numbers is possible, because any kinetic energy that remains after the trapping process has to be removed by ion cooling. One method to decelerate the ions is the use of the drift tube 2, which has already been discussed in section 2.1.3 (Fig. 2.7). Another deceleration scheme is the elevation of the trap potential by applying a bias voltage to each of the electrodes [59]. The advantage of this method, compared to a deceleration with the drift tube, is that the deceleration takes place at the trap center where the magnetic field is strongest. According to (p. 58 in [41]), the magnetic field at SpecTrap is in the trap center by a factor of 50 larger than the field at the location of drift tube 2.

Two measurements with elevated trap potential and Mg^+ ions were performed, the first one without and the second one with magnetic field applied. The first experiment determined the ion number after passing the trap and being reflected at a potential wall created by the reflection electrode (Fig. 2.24). For each data point, the same bias voltage was applied to the ring electrode, both endcaps and both correction electrodes, while the potential of the capture and the reflection electrode were optimized with regard to the reflection efficiency. As an example for the such created potential, the left part of figure 2.24 depicts the trap potential for $U_{\mathrm{bias}} = 340\,\mathrm{V}$ together with an illustration of the ions' path of flight. Since the potential exhibits a flat plateau in the trap center, the kinetic energy of the ions is easily calculated with the initial kinetic energy 365(3) eV and the voltage applied to the electrodes. The ion numbers after reflection as a function of the remaining kinetic energy were determined from the NID signal (Fig. 2.24, right). The inset exemplary shows one of the NID signals, from which the ion numbers of the reflected ion bunches were determined. Deceleration to energies as low as 40 eV was possible with still half of the maximum efficiency, which is a significant improvement compared to the DT2-deceleration of Ar^{13+} (Fig. 2.7).

In a second experiment, which in contrast to the previous one included the application of a magnetic field of 4 T, the deceleration with subsequent trapping of Mg^+ was demonstrated (Fig. 2.25). As in the experiment before, a bias was applied to the ring electrode, the endcap and correction electrodes to create a plateau-shaped potential in the trap center. For each value of U_{bias}, the capture- and reflection-electrode voltages were set to values that were found to be appropriate for the capture process. The kinetic energy of 368(8) eV of the incoming ion bunch was determined from a TOF measurement and the remaining kinetic energy after deceleration was calculated for each data point by $\mathrm{E}_{\mathrm{kin}} = 368(8)\,\mathrm{eV} - eU_{\mathrm{bias}}$. The fluorescence rate of the trapped ions, normalized to the fluorescence rate obtained for $U_{\mathrm{bias}} = 0\,\mathrm{V}$, was used as a measure of the ion number. To this end, after injection, the ions were first laser cooled until a stable fluorescence signal was obtained. In a second step, the potential of the endcaps was raised to $U = U_{\mathrm{bias}} + 50\,\mathrm{V}$ to 'compress' the ions in the trap center. This way, the fluorescence signal increased and – more importantly – the ions were confined in a region were the influence of the varying capture and reflection potential could be neglected. The fluorescence rates depicted in figure 2.25 are the ones that were obtained with raised endcap potential. With decreasing kinetic energy, the fluorescence increases at first and reaches a maximum for kinetic energies of about 70 eV. For stronger deceleration, the fluorescence drops significantly with $\mathrm{E}_{\mathrm{kin}} = 8(8)\,\mathrm{eV}$ as the lowest energy for which a fluorescence signal was obtained. From this observation one can conclude that the kinetic energy of an injected ion bunch can be nearly completely removed. Furthermore, this result sets a limit to the energy conversion from the axial to the radial degrees of freedom while the ions approach the center of the magnetic field. Since no significant magnetic-mirror effect was observed upon deceleration by 95% to 18 eV, the conversion from axial to radial kinetic energy is apparently less than 5%. There is, however, evidence based on the fluorescence data

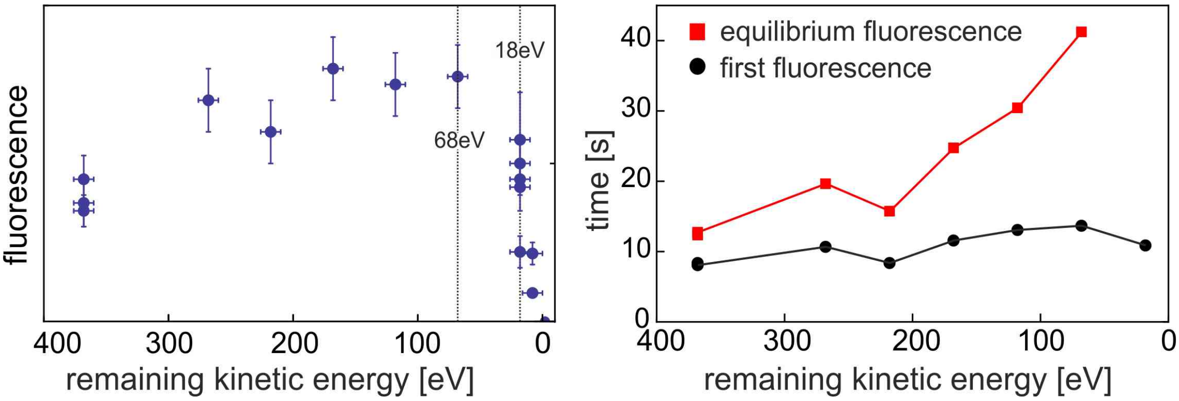

Figure 2.25: During the injection of Mg^+ into the trap with an initial kinetic energy of 368(8) eV, a bias voltage U_{bias} was applied to each trap electrode for ion deceleration. The remaining kinetic energy E_{kin} of the Mg^+ ions was calculated with $E_{\mathrm{kin}} = 368\,\mathrm{eV}{-}eU_{\mathrm{bias}}$. Left: Normalized Mg^+ fluorescence as a function of the remaining kinetic energy after injection. Right: The duration after injection until a first fluorescence signal was detected (black) and the duration until the fluorescence rate was stable (red). See the text for a discussion of the results.

for energy conversion to the radial degrees of freedom in the process of deceleration. The time for which the first fluorescence signal was detected (black) and the time after which a stable fluorescence signal was obtained (red) were measured as a function of the remaining kinetic energy (Fig. 2.25, right). The first time corresponds to the point at which the axial temperature is sufficiently reduced to allow significant fluorescence, the latter one corresponds to the axial temperature being reduced to the (detuning-dependent) Doppler temperature. According to the data, the duration to establish an equilibrium increases with the deceleration of the injected ion bunch, while the initial reduction of the axial temperature remains more or less constant. Apparently, for stronger deceleration there is a larger amount of kinetic energy transferred to the radial degrees of freedom, which has then to be removed via an axial-radial coupling before an equilibrium near the Doppler temperature is reached. Since the cloud densities, the collision times, and thus also the energy transfer rates in this specific experiment are unknown, it is, however, not possible to determine the absolute energy that is transferred to the radial degrees of freedom.

2.6 Fluorescence detection

Fluorescence photons emitted by the ions stored in the Penning is the main source of information obtained from the trapped particles in the SpecTrap Penning trap. The fluorescence signal has been detected in form of a signal rate with a photo-multiplier tube (PMT) or with a CCD camera to image the shape and structure of the stored ion cloud. The following section is dedicated to a description of the experimental equipment, which is related to fluorescence excitation and detection, as well as a discussion of typical fluorescence signals and the expected signal rates.

2.6.1 The 280 nm laser system

The laser system for Mg^+ laser cooling and fluorescence detection consists of a fiber laser producing light at 1118.5 nm and two enhancement cavities, each of them doubling the frequency to obtain up to 20 mW laser power at 279.6 nm. The setup was already described in [45, 60] and the modifications to the original system are documented in-depth in [61]. Here, a brief overview is given.

The fundamental at 1118.5 nm is created by an ytterbium-doped fiber amplifier (Koheras Boostik), which delivers an output power of up to 2 W. It is seeded by an external fiber laser (Menlo Systems) with 16 mW output power and a linewidth of less than 100 kHz. For first stage second-harmonic generation (SHG), a lithium triborate crystal (LBO), placed in a bow-tie resonator, is used. For non-critical phase matching the LBO crystal is heated to 96° Celsius and an output power of a few hundreds of mW is received at a wavelength of 559.3 nm. The second stage of frequency doubling is achieved with a β-barium borate crystal (BBO) placed in a second bow-tie resonator. Here, critical phase matching is employed and maximum output power of 20 mW at 279.6 nm is reached. After passage through a $\lambda/2$-plate and a polarizing beam splitting cube (PBS), a $\lambda/4$-plate is used to adjust the beam polarization for excitation of the ${}^2\mathrm{S}_{1/2,m_j=-1/2} \rightarrow {}^2\mathrm{P}_{3/2,m_j=-3/2}$ transition, which is used for laser cooling.

From the laser lab below the experimental platform, the laser beam is transported vertically through a hole in the ceiling to the experimental setup. For a coarse alignment of the laser beam with the trap center, the laser beam is adjusted to cross the centers of both viewports terminating the beamline at the top and bottom. Fine adjustment is provided by a system of two movable mirrors, which are attached to a set of remote-controllable stepping motors. This way, parallel beam transport with a precision of 0.1 mm is possible. The laser beam is imaged with a two-lens telescope and has a Gaussian beam profile with a waist of $w_0 = 1\,\mathrm{mm}$ at the trap center (table A.12).

2.6.2 Fluorescence imaging and detectors

Whereas the laser beam for ion spectroscopy is irradiated axially, the emitted fluorescence is guided by an imaging system to radially placed detectors. To this end, each of the four ring segments has a central hole of 4.8 mm diameter which allows radial optical access to the center of the trap (Fig. 2.26). Two of the four holes are equipped with a fused silica lens (Edmund Optics #48-024, $d = 12\,\mathrm{mm}$, $f_{\mathrm{eff}} = 25\,\mathrm{mm}$, Fig. A.3), adjusted such that its focal point coincides with the center of the trap. This way, the fluorescence of confined ions is collimated and directed to the detectors

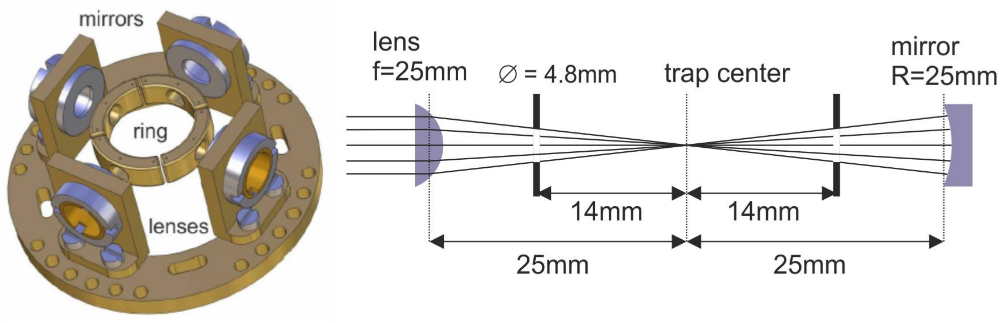

Figure 2.26: The SpecTrap imaging system. Drawing (left) with permission of Zoran Andelkovic. The figure (right) was reproduced from [41]. The focal length of the lens is depicted in dependence of the wavelength in the Appendix (Fig. A.3).

placed outside of the magnetic field. Two spherical aluminum mirrors, with their center of curvature aligned to the center of the trap, are placed opposite to the lenses and thus double the solid angle from which the fluorescence signal is collected. This design with double access to the trap center offers the possibility for simultaneous fluorescence detection of laser-cooled Mg^+ ions and a highly charged ion species at the same time. The geometric solid angle Ω, in which emitted photons are collected by the detection system, is defined by the radius of the ring electrode and the radius of a segment hole.

For the two aluminum mirrors, a coating with high reflectivity for wavelengths between 450–650 nm and for wavelengths larger than 1000 nm has been chosen, since the detection of infrared transitions is much more challenging compared to UV transitions. For UV transitions, such as the laser cooling transition of Mg^+, the aluminum mirror does not contribute significantly to the detection efficiency. Without including the reflecting mirror, the solid angle for detection of Mg^+ fluorescence amounts to 0.09 sr, which is a fraction of

$$\Omega = 7.34 \cdot 10^{-3} \tag{2.53}$$

out of 4π.

Two different detectors have been used for fluorescence detection: A CCD camera (EM-CCD C9100-24B, Hamamatsu) was used for imaging of the Mg^+ ion clouds, while a channel photomultiplier (CPM) (C1993P, Perkin Elmer) continuously measured the Mg^+ fluorescence rate. For imaging the fluorescence onto the chip of the CCD camera, a second lens was used (Edmund Optics Lens PCX UV FS 30 X 150 UV-AR TS, $f = 150\,\mathrm{mm}$). The resulting magnification factor of 4.69(8) was determined by applying an asymmetric potential ΔU to the trap electrodes and measuring the resulting ion cloud shift in the image plane. The actual shift in the trap was calculated with the asymmetric potential ΔU and the electrode coefficients C_n^i according to equation (2.34).

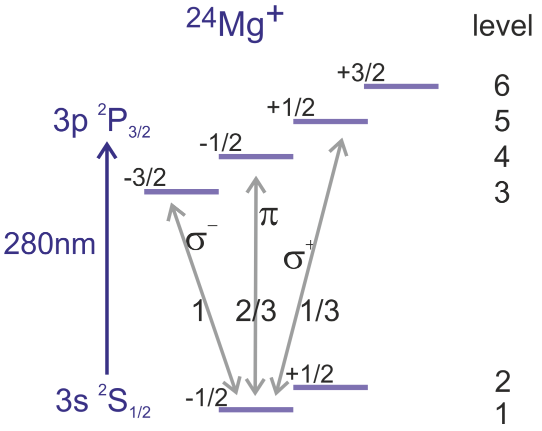

level	m$_j$	g$_j$	ΔE$/(h \cdot B)$ [GHz/T]
$^2S_{1/2}$	-1/2	2.0023	-14.0123
$^2S_{1/2}$	+1/2	2.0023	14.0123
$^2P_{3/2}$	-3/2	1+1.0023/3	-28.0085
$^2P_{3/2}$	-1/2	1+1.0023/3	-9.3362
$^2P_{3/2}$	+1/2	1+1.0023/3	9.3362
$^2P_{3/2}$	+3/2	1+1.0023/3	28.0085

$\nu_0 = 1\,072\,082\,934.33(16)\,\text{MHz}$
$\Gamma = 2\pi \cdot 41.5\,\text{MHz}$
$\lambda_{\text{vac}} = 279.635\,509\,90(4)\,\text{nm}$

Figure 2.27: Left: Level scheme of the ^{2}S$_{1/2} \rightarrow {}^2$P$_{3/2}$ transition in ^{24}Mg$^+$. The squared Clebsch-Gordon coefficients for the three depicted transitions are indicated. Right: Zeeman shifts according to $\Delta E = g_j m_j \mu_B B$, where g_j is the Landé factor, $\mu_B/h = -13.9962\,$GHz/T the Bohr magneton divided by the Planck constant, and B the magnetic field ([64], p. 239). The transition wavelength in vacuum λ_{vac}, the frequency ν_0, and the natural linewidth Γ are given for the ^{2}S$_{1/2} \rightarrow {}^2$P$_{3/2}$ transition and zero magnetic field [62].

The CPM detector has a quantum efficiency of 0.18 at 280 nm, whereas the quantum efficiency of the CCD camera is, according to the manufacturer, in the range of 0.05 to 0.35. Due to this large uncertainty, only data obtained with the CPM detector were evaluated for a quantitative analysis based on fluorescence rates.

To determine the single-ion fluorescence rate at the CPM detector, an estimate of the total detection efficiency ξ for the Mg$^+$ fluorescence at 279.6 nm will be given in the following discussion. In this context, the total detection efficiency ξ is defined as the product of the transmission from the trap center to the detector and the detector's quantum efficiency. Taking into account the losses due to absorption and reflection at optical elements, the total transmission to the CPM detector is estimated to be 0.56. Table A.13 in the Appendix lists the elements, whose contributions to the transmission have been considered. With the CPM quantum efficiency of about 0.18 the resulting total detection efficiency at 280 nm is

$$\xi_{\text{CPM}} = 0.56 \cdot 0.18 = 0.10. \tag{2.54}$$

No uncertainty is given for the total detection efficiency, since the reliability of the quantum efficiency is unknown.

2.6.3 Electronic transitions in ^{24}Mg$^+$

Laser cooling of ^{24}Mg$^+$ addresses the transition between the levels ^{2}S$_{1/2}$ and ^{2}P$_{3/2}$ with a wavelength of 279.6 nm and a natural linewidth of $\Gamma = 2\pi \cdot 41.5\,$MHz

(Fig. 2.27) [62]. The level scheme of the upper and lower state consists of in total six Zeeman-shifted levels . The Mg^+ levels are numbered from 1 to 6 and referred to by this number in the following. The Zeeman shifts have been calculated in the frame of the low-field approximation, which applies since the fine structure splitting between the levels $3p^2P_{3/2}$ and $3p^2P_{1/2}$ of 11.35 meV=$h \cdot 2.74$ THz is much larger than the typical Zeeman shift of $2\pi \cdot 100$ GHz in a magnetic field $B = 4$ T at SpecTrap ([63], [64] p. 221).

For laser cooling, the $S_{1/2,m_J=-1/2} \rightarrow P_{3/2,m_J=-3/2}$ transition is driven with a σ^--polarized laser beam, which is irradiated parallel to the magnetic field. If an ion is excited to the $P_{3/2,m_J=-3/2}$ level, the $\Delta m_J = \{-1, 0, 1\}$ selection rules requires that the ion decays to the $S_{1/2,m_J=-1/2}$ ground state. As a consequence, the ion will cycle nearly continuously between these two levels producing a steady rate of fluorescence.

Non-resonant excitation of the $1 \rightarrow 5$ transition leads to population of the $S_{1/2,m_J=+1/2}$ dark state and a sudden cease of fluorescence. Transitions between the levels 1 and 5 are driven by the σ^+-component of the laser beam, which has an intensity of the order of $I_+ = 10^{-2} \cdot I_-$. The intensity of the σ^+-component is determined by the inevitable imperfections of the optical components. From level 5, decay to both sublevels 1 and 2 with $m_J = \pm 1/2$ is possible. If the ion decays to level 2 with $m_J = +1/2$, it is no longer continuously excited by the σ^--component until it returns to the level 1 $S_{1/2,m_J=-1/2}$ ground state via an excitation to level 4 $P_{3/2,m_J=-1/2}$. Besides a σ^+-component, pumping into a dark state can be caused by a π-component of the laser beam. However, a π-component with electric field parallel to the magnetic field only occurs if the laser is irradiated with a finite angle to the magnetic field. It can be neglected in this discussion, since the alignment of the laser beam sets an upper limit of $I_\pi < 10^{-4} \cdot I_-$ to its intensity.

The ratio between the populations of the levels 1 and 2 is given by the ratio of the transition rates $1 \rightarrow 5$ and $2 \rightarrow 4$, which is in turn determined by the intensities I_+, I_- and the laser detuning relative to respective transitions. The transition $2 \rightarrow 6$ has no influence on the level 1 to level 2 population ratio, because it is a closed transition that decays within nanoseconds back to the original state.

The resulting dark-state population amounts to $(1/16) \cdot (I_+/I_-) \approx 10^{-3}$ and does hence not significantly reduce the total fluorescence of a large ion cloud[1]. However, for a single ion, transitions to a dark state can be observed in the fluorescence signal and have been reported in literature [65, 66, 67].

To give some absolute values: If both $\sigma\pm$-components have an intensity equal to the saturation intensity I_0 (i.e. $I_+ = I_- = I_0$), the $2 \rightarrow 4$ transition occurs with a rate of $13\,\mathrm{s}^{-1}$ while the rate for the $1 \rightarrow 5$ transition is $0.8\,\mathrm{s}^{-1}$. These low transition rates

---

[1] The factor of (1/16) is due to the ratio of 1/4 between the detunings of transitions between the levels 2–4 and 1–5: The σ^--transition between levels 1 and 3 shifts by $1\mu_B$ per tesla to lower frequencies. The σ^--transition between levels 2 and 4 shifts by $(5/3)\mu_B$ per tesla to lower frequencies and is thus detuned by $(2/3)\mu_B$ per tesla with respect to the 1–3 transition. The σ^+-transition between levels 1 and 5 shifts by $(5/3)\mu_B$ per tesla to higher frequencies and is thus by $(8/3)\mu_B$ detuned with respect to the 1–3 transition.

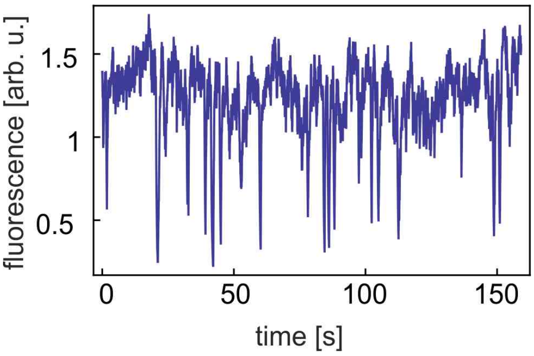

Figure 2.28: Fluorescence of a single Mg$^+$ ion. The occurring dips in the fluorescence signal can be explained by transitions to a dark state.

are due the large detuning of 153 GHz and 38 GHz (relative to the laser frequency tuned to the 1 → 3 transition) at a magnetic field of $B = 4$ T. These detunings are larger than 10^3 times the natural linewidth $\Gamma = 2\pi \cdot 41.5$ MHz and reduce the transition rates accordingly by more than a factor of 10^6. Consideration of the transitions' Clebsch-Gordon coefficient of 1/3 further reduces the transition rate compared to the 1 → 3 transition. Typical conditions at SpecTrap are $I_- = I_0$ and $I_+ = 10^{-2} \cdot I_0$, so that the expected rates for the 2 → 4 and 1 → 5 transitions are 13 s^{-1} and $0.8 \cdot 10^{-2}$ s^{-1}, respectively.

The fluorescence signal of a single Mg$^+$ ion has been recorded with the CPM detector (Fig. 2.28). The most apparent feature are the sudden dips in the fluorescence signal that occur with a rate of 0.1 s^{-1} and have an average duration of the order of 100 ms. If one interprets these dips as off-resonant transitions to a dark state, the corresponding rates for the 1 → 5 and the 2 → 4 transition are 0.1 s^{-1} and 10 s^{-1}, respectively. These rates are reasonably close to the expected transition rates, however, the interpretation as off-resonant transitions could not be confirmed, since alternative explanations (e.g. residual gas collisions of the Mg$^+$ ion or fluctuations of the laser intensity) could not be excluded.

2.6.4 Single-ion fluorescence rate

According to the discussion in the Appendix (Appendix Eq. (A.9), Eq. (2.26) in [68]), the fluorescence rate Γ_{sc} of an atomic transition is the product of the natural linewidth Γ and the upper state population ρ_e. It can be expressed in terms of the laser intensity I, the saturation intensity I_0, and the laser detuning Δ:

$$\Gamma_{sc}(\Delta) = \Gamma \cdot \rho_e = \frac{\Gamma}{2} \cdot \frac{I/I_0}{1 + I/I_0 + (2\Delta/\Gamma)^2} \tag{2.55}$$

$$= \left(\frac{I/I_0}{1 + I/I_0}\right)\left(\frac{\Gamma/2}{1 + (2\Delta/\Gamma')^2}\right), \tag{2.56}$$

$$\text{where } \Gamma' = \Gamma\sqrt{1 + I/I_0}. \tag{2.57}$$

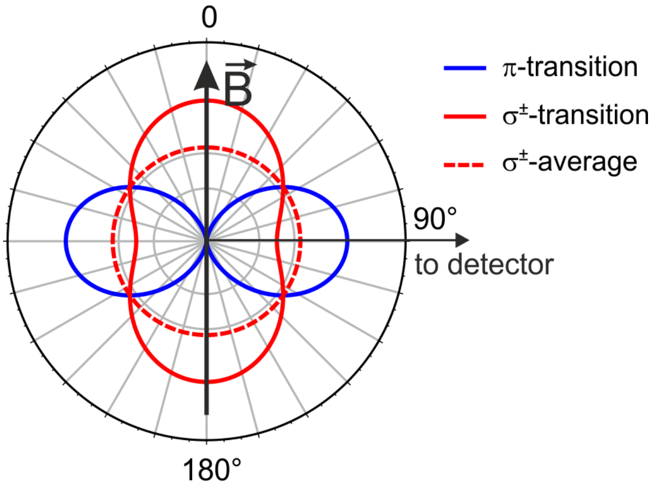

Figure 2.29: Emission profiles of π- (blue) and $\sigma^{\pm}$-transitions (red) in a magnetic field B. At SpecTrap, excitation and fluorescence detection take place under an angle to the magnetic field of 0° and 90°, respectively. The spatial average of the $\sigma^{\pm}$-emission is indicated with a red-dashed line.

For the ${}^{2}\mathrm{S}_{1/2,m_j=-1/2} \rightarrow {}^{2}\mathrm{P}_{3/2,m_j=-3/2}$ transition in Mg^{+}, we have $\Gamma = 2\pi \cdot 41.5\,\mathrm{MHz}$ and accordingly $I_0 = 2.46\,\mathrm{mW\,mm^{-2}}$ (Eq. (A.12) and Tab. 2.7) [62].

Because the fluorescence of the σ-transition used for ion cooling is non-isotropic, the angle under which the detector is placed has to be taken into account for the calculation of the signal rate r. A σ-transition has an emission profile proportional to $(1 + \cos^2\theta)$, where θ is the angle between the magnetic field $B = B_0 e_z$ and the direction towards the detector. Since the averaged emission is proportional to $\langle 1 + \cos^2\theta \rangle = 4/3$, the intensity $I_{\perp}$ perpendicular to B is a fraction of $3/4$ of the 4π-average [69] (Fig. 2.29) [2].

The theoretical Mg^{+} single-ion fluorescence count rate r detected with the CPM detector is therefore:

$$
\begin{aligned}
r_{\mathrm{th}} =& (0.75 \cdot \Gamma_{sc}) \cdot \Omega \cdot \xi_{\mathrm{CPM}} && (2.58)\\
\approx& 5 \cdot 10^{-4} \cdot \Gamma_{sc}. && (2.59)
\end{aligned}
$$

Here, Γ_{sc} denotes the total fluorescence rate and Ω the fraction of the solid angle out of 4π and ξ_{CPM} the CPM detection efficiency as discussed in section 2.6.2. For

---

[2] The same result is achieved with simple considerations in the framework of classic electrodynamics. For an atomic ion a magnetic field $B = B_0 e_z$, the observed Zeeman component of the σ-transition can be regarded as the superposed emission of two radiating dipoles, which oscillate perpendicular to each other in the x-y-plane. The emission intensity of a dipole observed under an angle α to the dipole's axis is proportional to $\sin^2\alpha$ [70]. The combined emission in arbitrary direction in the x-y-plane is proportional to $\sin(\alpha)^2 + \sin(\alpha + \pi/4)^2 = 1$. Hence, without loss of generality, we can chose $\alpha = 0$ such that only the emission of one of the dipoles contributes to the detected intensity. Since a dipole's emission perpendicular to its axis is 1.5 times the 4π-average intensity, we can conclude for the combined emission of the two dipoles that the emission intensity in the x-y-plane is fraction of 0.75 of the total 4π-average intensity. See also equation (A.1) and discussion in the Appendix.

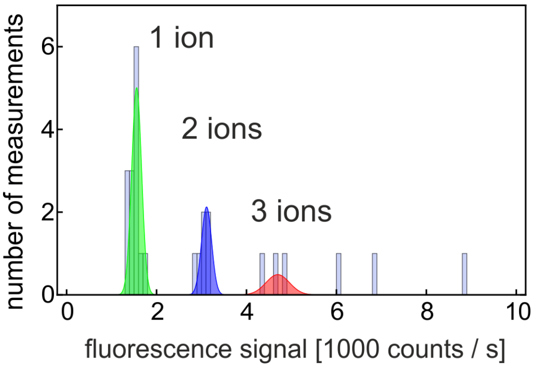

Figure 2.30: Histogram of Mg^+ single-ion fluorescence count rates. Laser beam parameters for fluorescence excitation: waist $w_0 = 1\,\mathrm{mm}$, laser power $P = 4\,\mathrm{mW}$, peak intensity $I = 2.55\,\mathrm{mW\,mm^{-2}}$, and detuning $\Delta = -2\pi \cdot 32\,\mathrm{MHz}$. The lowest occurring rate of $1560\,\mathrm{s}^{-1}$ can be identified as the Mg^+ single-ion fluorescence count rate.

a typical laser intensity $I \approx I_0$, the scattering rate on resonance $\Delta = 0$ becomes $\Gamma_{sc} = \Gamma/4$ and the CPM count rate for a single Mg^+ ion is thus $r_{\mathrm{th}} \approx 3.4 \cdot 10^4\,\mathrm{s}^{-1}$.

This theoretical value can be compared to the experimentally determined Mg^+ single-ion count rate. To this end, the production in the Mg^+ was reduced to the point where only a few or a single ion were injected into the trap. A laser beam with power $P = 4\,\mathrm{mW}$, peak intensity $I = 2.55\,\mathrm{mW\,mm^{-2}}$, beam waist $w_0 = 1\,\mathrm{mm}$ and a detuning of $\Delta = 2\pi \cdot 32\,\mathrm{MHz}$ was used for Mg^+ excitation. The fluorescence of a single ion or a few-ion ensemble was observed for several seconds before the ions were ejected from the trap and the procedure was repeated. The lowest count rate observed was the one of a single ion with 1560 counts per second, with multiples of this value as second and third lowest rate for a two- and three-ion ensemble, respectively (Fig. 2.30).

The measured count rate are in agreement with the theoretical expectations if the (not precisely known) laser intensity was $I = 0.10 \cdot I_0$. However, regarding the laser power of 4 mW and the assumed beam radius of 1 mm (table A.12), the laser intensity was most likely of the order of $I = 0.5 \cdot I_0$. The discrepancy of about a factor of five is most probably due to a misalignment of the optical system and the detector, which results in an overestimation of the actual fluorescence transmission of the imaging system. The misalignment of the magnet system was caused when the system was damaged on the transport to its current location and could unfortunately not be completely repaired. Therefore, the theoretical value should rather be regarded as a benchmark for the performance capability of the trap design and not as a prediction for actual experiments.

The detection efficiency and the resulting single ion count rate is relevant for the spectroscopy of dipole-forbidden transitions in HCI, where low signal count rates are expected. For the transitions in some selected HCI, the signal rates have been calculated using the natural linewidths Γ given in table 2.7 and are listed in table 2.8. The very low dark-count rates of the detectors for wavelengths below 1050 nm

ion species	transition	wavelength λ [nm]	natural linewidth Γ	reference
$^{24}\mathrm{Mg}^{+}$	$^2S_{1/2} \rightarrow {}^2P_{3/2}$	279.63550990(4)	$2\pi \cdot 41.5\,\mathrm{MHz}$	[62]
$^{40}\mathrm{Ar}^{13+}$	$^2P_{3/2} \rightarrow {}^2P_{1/2}$	441.25568(26)	$2\pi \cdot 16.6\,\mathrm{Hz}$	[17, 71]
$^{209}\mathrm{Bi}^{80+}$	F=4 → F=5	1554.66(33)(10)	$2\pi \cdot 1.5\,\mathrm{Hz}$	[21, 72, 73]
$^{209}\mathrm{Bi}^{82+}$	F=4 → F=5	243.87(4)	$2\pi \cdot 180\mathrm{Hz}$	[19, 73]

Table 2.7: Optical-regime transitions in selected ions.

wavelength range	200–400 nm	400–1050 nm	950–1600 nm
type	channel PMT	APD	NIR-PMT
model	C1993P	RMD S0223	H12397-75
quantum efficiency	18%	20–45% [74]	1–2%
dark-count rate	$20\,\mathrm{s}^{-1}$	$1\,\mathrm{s}^{-1}$	$5000\,\mathrm{s}^{-1}$
count rate (N=1000)	1040 $\left(^{209}\mathrm{Bi}^{82+}\right)$	90 $\left(^{40}\mathrm{Ar}^{13+}\right)$	0.4 $\left(^{209}\mathrm{Bi}^{80+}\right)$

Table 2.8: Signal rates for selected HCI with number of $N = 1000$ ions in the excited state. The wavelength range 200–400 nm is covered by the same photo-multiplier tube (PMT) as used for the detection of Mg^{+} fluorescence (PerkinElmer C1993P), the range 400–1050 nm is covered by an avalanche photo-diode (APD) (Radiation Monitoring Devices RMD S0223 [74]). For the range 950–1600 nm, the specifications of a commercially available near-infrared (NIR) PMT are given (Hamamatsu H12397-75). The signal rates have been calculated with the values for the natural linewidths Γ given in table 2.7 without consideration of the contribution of the aluminum mirror.

allow high signal-to-ratios with comparatively short integration times. On the other hand, for photons in the near infrared only detectors with high dark-count rates are available. As a consequence, the integrated measurement time to achieve a signal-to-noise ratio of 3σ is for the hyperfine structure transition in Li-like bismuth $^{209}\mathrm{Bi}^{80+}$ of the order of 100 hours. If the number of stored ions can be significantly increased to the yet realistic number of 10^5, the required measurement time to achieve a 3σ signal-to-noise ratio is less than an hour per wavelength step.

3 Preparation of cold Mg^+ clouds

Trapping of a Mg^+ ion cloud with particle numbers between one and several 10^5 ions – including the consecutive processes of ion production, transport to the trap, and ion-bunch capture – is a routine procedure that can be performed with repetition rates of up to 10 Hz at the SpecTrap experiment. After the capture process, the ions' energy is close to the transport energy of typically 400 eV. Consequently, this energy must be removed to cool the ion ensemble to the mK-regime and to produce dense and cold ion clouds.

In this chapter, the preparation of a laser-cooled cloud of singly charged magnesium as a first step on the way to sympathetically cooled HCI will be presented. A combination of buffer gas and laser cooling has been applied to reduce the ions' kinetic energy by eight orders of magnitude from initial energies of several hundreds of eV to the µeV-regime within seconds. At such temperatures in the mK range the ions enter the regime of strongly coupled plasmas and form ion Coulomb crystals, revealing structures that will be discussed in chapter 4.

The total cooling rate can be written as the sum of its contributions due to the damping with neutral buffer gas and the interaction with the cooling laser, which leads to laser Doppler cooling and recoil heating:

$$\frac{\mathrm{d}E}{\mathrm{d}t} = \left(\frac{\mathrm{d}E}{\mathrm{d}t}\right)_{\text{laser}} + \left(\frac{\mathrm{d}E}{\mathrm{d}t}\right)_{\text{recoil}} + \left(\frac{\mathrm{d}E}{\mathrm{d}t}\right)_{\text{buf}}. \tag{3.1}$$

To determine the cooling rate according to equation (3.1) the principles of buffer gas cooling and Doppler laser cooling will be summarized first, before the dynamics of the cooling process will be described with an extension of a cooling model presented in [75]. The modified cooling model will be applied to experimental data and provides complementary information about cloud properties like the cloud density and temperature, which are in this experimental setup not accessible to direct observation.

3.1 Buffer gas cooling

One of the simplest cooling techniques for trapped ions is cooling with a cold buffer gas, which may consist of either neutral or charged particles [76]. The hot ions transfer their kinetic energy to the buffer gas by multiple, weak collisions until they are in thermal equilibrium with both the buffer gas and the surrounding environment. As a neutral buffer gas, usually helium is used with typical gas pressures in the range of 10^{-2} – 10^{-8} mbar. Although this cooling technique is comparatively simple, it is yet

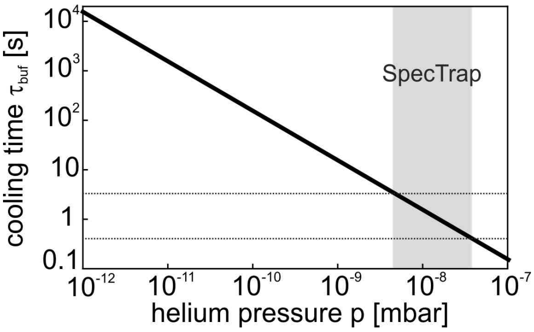

Figure 3.1: The buffer gas cooling time τ_{buf} for Mg$^+$ ions as a function of the helium gas pressure p. The helium temperature is $T = 4\,\text{K}$. The helium pressure range in the SpecTrap Penning trap is indicated by the gray area.

powerful and reduces the ion temperature within a few seconds from several tens of thousands of kelvin to room temperature and below. For highly charged ions, buffer gas cooling is not applicable, because the ion-atom collisions lead to electron capture from the neutral atoms, and other methods like resistive cooling or sympathetic cooling must be employed.

During an ion-atom collision, the ion interacts with the dipole moment induced in the buffer gas atom, which is of long range and involves a very small change in ion-energy per collision [77]. Thus, the effect of buffer gas cooling on the ion motion can be described as a viscous drag, which is expressed by a frictional force in the equation of motion. This classical treatment of the ion motion and the ion-atom interaction is justified for all but extremely low energies. The frictional force for an ion with mass m and velocity v is given by $F = m\dot{v} = -2\gamma_{\text{buf}} m v$ [78, 79], where the damping coefficient γ_{buf} has been introduced. The frictional force modifies the axial oscillation to that of a damped harmonic oscillator with exponentially decreasing amplitude $A = A_0 \exp(-\gamma_{\text{buf}} t)$. Hence, the energy is dissipated with the rate $2 \cdot \gamma_{\text{buf}}$ and the buffer gas cooling rate can be written as

$$\left(\frac{\mathrm{d}E}{\mathrm{d}t}\right)_{\text{buf}} = -2\gamma_{\text{buf}} E. \tag{3.2}$$

The buffer gas damping coefficient γ_{buf} of an ion with charge q in a buffer gas at temperature T and pressure p is related to the ion mobility M by

$$\gamma_{\text{buf}} = \tau_{\text{buf}}^{-1} = \frac{q}{2m} \cdot \frac{1}{M} = \frac{q}{2m} \frac{1}{M_0} \frac{p/p_0}{T/T_0}. \tag{3.3}$$

Here, the buffer gas cooling-time τ_{buf} has been defined as the inverse of the damping coefficient γ_{buf}.

The mobility M is defined as the ratio of the ion velocity and the strength of the accelerating electric field. The value of the mobility M_0 denotes the mobility at ambient conditions, i.e. for a pressure $p_0 = 1\,\text{bar}$ and a temperature $T_0 = 300\,\text{K}$. It only depends on the ion species and the type of buffer gas [80]. The damping coefficient γ_{buf} is therefore proportional to the buffer gas pressure and inversely proportional to both the temperature T of the gas and the ion mobility M_0. Typical values for the ion mobility M_0 in helium gas are 20–25 $\mathrm{cm^2V^{-1}s^{-1}}$, the higher values being for light ions and the lower values for heavy ions. For singly charged magnesium in helium, a mobility of $M_0 = 23.5\,\mathrm{cm^2V^{-1}s^{-1}}$ can be found in literature [81, 82]. For a given ion species and buffer gas temperature, τ_{buf} is a function of the buffer gas pressure p only (Fig. 3.1).

In a Penning trap, the collisions with residual gas atoms lead not only to damping of the axial oscillation, but also of the cyclotron and magnetron motion. A solution of the equation of motion for the radial oscillations, including the damping by buffer gas, can by found in [78]. The damping coefficients γ_+ and γ_- of the cyclotron and magnetron motion are related to one of the axial oscillation, γ_{buf}, by

$$\gamma_\pm = \pm 2\gamma_{\mathrm{buf}}\frac{\omega_\pm}{\omega_1}, \tag{3.4}$$

where ω_1 defined as

$$\omega_1 := 2\omega_+ - \omega_c \approx \omega_+ \tag{3.5}$$

has been used. Since the damping coefficients $\gamma_\pm$ have different signs with $\gamma_+ > 0$ and $\gamma_- < 0$, the radius of the cyclotron motion is shrinking under the influence of buffer gas cooling whereas the radius of the magnetron motion is increasing. For typical trapping potential, we have $\omega_+ \approx \omega_c$ and thus $\gamma_+ \approx 2\gamma_{\mathrm{buf}}$. The damping coefficient γ_+ for the reduced cyclotron motion is twice the one of the axial oscillation, reflecting the fact that the energy stored in the cyclotron motion is, in contrast to the axial oscillation, almost exclusively kinetic. Likewise, the damping constant γ_- of the magnetron motion, whose total energy is nearly completely potential, is reduced by a factor of ω_+/ω_- in comparison with γ_+.

In case of the SpecTrap Penning trap, the storage time of an ion cloud is mainly limited by collisions with buffer gas and the consequential widening of the magnetron radius. For the axial oscillation, typical buffer gas cooling rates of the order of 1 second have been determined. According to equation (3.4) one obtains a magnetron time constant of the order of 100 seconds, which is in agreement with the observed storage times, for example in the case of the ion cloud presented in figure 4.10. Although equation (3.4) was deduced for the single ion case, it should also apply for an ion cloud rotating with a frequency ω_r close to the magnetron frequency ω_-. For the ion cloud presented in figure 4.10 and for other ones studied in this work this was usually the case.

If the ions cannot be treated independently but as a collective plasma (which is adequate for a cold ion cloud), the damping effect of the collisions with residual gas must be described as an external torque to the cloud, which is rotating as a rigid body [83]. The (canonical) angular momentum L of a non-neutral plasma is [84]

$$L = m(\omega_c/2 - \omega_r) \int d^3\mathbf{r}\, n(r,z) r^2. \tag{3.6}$$

For a spheroidal plasma, equation (3.6) turns into [83]

$$L = \frac{3}{20} \frac{Nm}{\pi n_0 z_0} (\omega_c - 2\omega_r), \tag{3.7}$$

where N and m are the number and the mass of the ions, whereas z_0, n_0 and ω_r denote the axial radius, the density and the rotation frequency of the ion cloud. The total angular momentum L is positive if $\omega_r < \omega_c/2$, negative if $\omega_r > \omega_c/2$ and vanishes at the Brillouin limit for $\omega_r = \omega_c/2$. The external torque of the buffer gas decreases the rotation frequency ω_r, as has been reported in [83], while the aspect ratio changes accordingly. For an ion cloud rotating at the lower limit of the rotation frequency $\omega_r \approx \omega_-$, which was typically the case for the clouds presented in this thesis, the effect of the external torque is to decrease the axial extent z_0 and thus the aspect ratio. Examples for this behavior can be found in chapter 4, where several series of ion cloud images show the decreasing axial extent z_0 over a period of several minutes (e.g. Fig. 4.9 and 4.10).

An external torque can also cause heating of the ion cloud: When the total canonical angular momentum increases, the ion cloud radius grows and thus the electrostatic potential energy of the ions is converted into thermal energy. Besides collisions with buffer gas, an external torque can be applied by static field errors or by insufficient axial symmetry. These effects have been investigated experimentally [86, 87, 88, 89, 90] and theoretically [91, 92, 93]. The observed heating could be reduced by an improvement of the trap axial symmetry, as has been demonstrated by [87]. Besides an increase of the cloud radius, the external torque can also excite plasma instabilities and consequently lead to ion loss [88, 89].

3.2 Laser Doppler cooling

Laser cooling makes use of the momentum transfer that occurs when an atom or ion absorbs and re-emits a photon and was first proposed by Hänsch and Schawlow for a gas of neutral atoms [94] and by Wineland and Dehmelt for ions confined in an electromagnetic trap [95]. Assuming an isotropic distribution of spontaneously emitted photons, the average momentum transfer can be written as

$$\langle \Delta \mathbf{p} \rangle = \left\langle \sum_n \hbar \mathbf{k}_\mathrm{l} \right\rangle + \underbrace{\left\langle \sum_n \hbar \mathbf{k}_\mathrm{e} \right\rangle}_{0} = n\hbar \mathbf{k}_\mathrm{l}, \tag{3.8}$$

where n denotes the number of absorbed photons and $\hbar k_l$ and $\hbar k_e$ the momentum transfer on absorption and emission, respectively.

If the laser light is red-detuned with regard to the resonance frequency, a photon will be absorbed preferentially by those ions which are moving with a velocity v_z such that the laser detuning is compensated by the corresponding Doppler shift. This selective addressing of ions moving towards the laser is the mechanism that turns the light pressure into a cooling force. Although the average momentum transfer of many spontaneous emissions is zero, the root-mean-square of the momentum transfer is finite. This stochastic force due to continuous photon recoil causes heating at a rate [96, 97, 98, 75]

$$\left(\frac{\mathrm{d}E}{\mathrm{d}t}\right)_{\mathrm{recoil}} = \frac{(\hbar k)^2}{2m}\frac{dN}{dt}(1+\xi), \tag{3.9}$$

where $(\hbar k)^2/2m$ is the recoil energy associated with the photon scattering, $\mathrm{d}N/\mathrm{d}t$ is the scattering rate. The term $(1+\xi)$ reflects the two contributions to recoil heating: The photon recoil on absorption and the recoil effect on emission. In case of an isotropic emission we have $\xi = 1/3$, whereas for a dipole-radiation pattern with a $\cos(\theta)$ angular dependence $\xi = 2/5$ ([99], p. 39). Once a steady state is reached, recoil heating will balance the Doppler cooling rate. Thus, recoil heating is relevant only for temperatures close to the cooling limit.

3.2.1 Laser Doppler cooling of a free ion

If free atoms or atomic ions are being slowed by radiation pressure, as is performed in an optical molasses [100, 101], each laser beam only addresses a single degree of freedom. Consequently, a total of six laser beams is required for an optical molasses that provides viscous confinement in three dimensions.

In contrast to free atoms, a single laser beam is sufficient for 3-D laser cooling of trapped atoms, because confinement of the particle ensemble (in combination with the inevitable presence of symmetry-reducing field errors) leads to a coupling between different degrees of freedom. Furthermore, a fixed-frequency laser is sufficient to create a stopping force for atoms in a wide range of kinetic energies, since the velocity of the atoms changes periodically during one oscillation period and will eventually match the detuning of the laser beam, that is as long as the laser detuning is less than the maximum Doppler shift $v_{\mathrm{max}}/c \cdot \omega_0$.

The steady-state kinetic energy for laser cooling of a single degree of freedom is found to be [96, 98]

$$E_{\mathrm{Doppler}} = \frac{\hbar\Gamma}{8}(1+\xi)\left(\frac{2|\Delta|}{\Gamma} + (1+s_0)\frac{\Gamma}{2|\Delta|}\right). \tag{3.10}$$

The minimum temperature is reached for a laser detuning $\Delta = \Gamma\sqrt{1+s_0}/2$:

$$T_{\mathrm{min}} = \frac{\hbar\Gamma\sqrt{1+s_0}}{4k_B}(1+\xi). \tag{3.11}$$

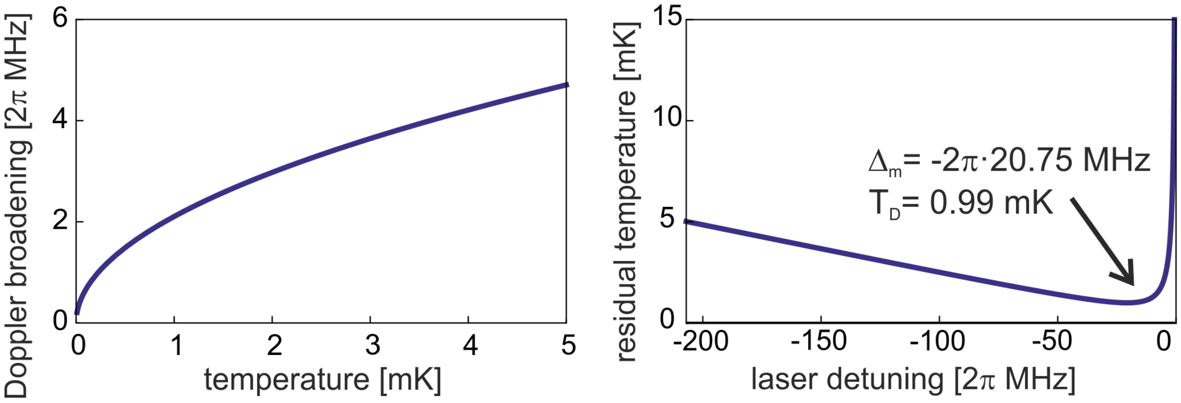

Figure 3.2: Left: The Doppler broadening of the $^2S_{1/2} \rightarrow {}^2P_{3/2}$ transition in Mg^+. Right: The residual temperature of a Doppler cooled Mg^+ ion.

For laser cooling in three dimensions, the minimum temperature in the limit of low intensities is the so-called Doppler temperature T_D and only depends on the natural linewidth Γ of the transition [68]:

$$T_D = \frac{\hbar\Gamma}{2k_B}. \tag{3.12}$$

The $^2S_{1/2} \rightarrow {}^2P_{3/2}$ transition in Mg^+ ions, which is used for laser cooling at SpecTrap, has a natural linewidth of $\Gamma = 2\pi \cdot 41.5\,\text{MHz}$ and the corresponding minimum and Doppler temperature are thus $T_{\text{min}} = 0.70\,\text{mK}$ and $T_D = 0.99\,\text{mK}$, respectively. The residual temperature of a laser cooled atom is weakly dependent on the detuning Δ and for typical detunings of a few hundreds of MHz the thermal Doppler broadening is much less than the natural linewidth (Fig. 3.2).

The potential power of laser Doppler cooling suffers from the intrinsic limitation that the level structure of the atomic system must offer a suitable cooling transition. For highly charged ions, this is generally not the case, because the transition rates of the dipole-forbidden transitions are rather low. This difficulty, however, can be circumvented by the use of sympathetic cooling, where one ion species is cooled by collisions with another laser-cooled species [99]. This indirect cooling method is applicable without requiring a specific kind of level structure. Furthermore, sympathetic cooling circumvents the necessity to turn off the cooling laser during the actual spectroscopic experiment, which would lead to heating and an increased linewidth. In contrast to this, sympathetic cooling allows continuous cooling and thus permits longer interrogation times with higher resolution [47].

3.2.2 Laser cooling of a trapped ion

For a typical transition used for laser-cooling, the decay rate Γ is much higher than the axial oscillation frequency ω_z. This so-called weak-binding regime also applies for Mg^+ ions confined in the SpecTrap Penning trap, for which the natural linewidth of

41.5 MHz is much larger than the axial oscillation frequency of typically 1 MHz. Since the upper-state relaxation is much faster than the change of the ion's instantaneous Doppler shift, the upper-state population is in a steady state and is determined by the periodically changing, instantaneous effective detuning $\Delta_{\text{eff}} = \Delta + \Delta_D(v_z)$ ([68], Eq. (2.24-2.26)):

$$\begin{aligned} \rho_e(v_z) &= \frac{s}{2(1+s)} = \frac{s_0/2}{1+s_0+(2\Delta_{\text{eff}}/\Gamma)^2}, &(3.13)\\ s_0 &= I/I_0 = I \cdot \frac{3\lambda_0^3}{\pi h c \Gamma}. &(3.14) \end{aligned}$$

In equation (3.13) the excited state population $\rho_e(v_z)$ has been written as a function of the ion's velocity v_z, since the ion's instantaneous Doppler shift Δ_D is given by $|\Delta_D| = v_z \cdot \omega_0/c = v_z \cdot k_z$. The saturation parameter s and the on-resonance saturation parameter s_0 have been introduced in equation (3.14) as a function of the laser intensity I and the saturation intensity I_0.

For a laser beam traveling in z-direction, the momentum change per photon scattering event is $\hbar k_z$. The energy change (per scattering event) depends on the ion's velocity v_z and can be expressed in terms of the instantaneous Doppler shift Δ_D:

$$\frac{\mathrm{d}E}{\mathrm{d}N} = \hbar k_z v_z = -\hbar\Delta_D. \tag{3.15}$$

On the other hand, the force experienced by the ion is the product of the momentum change $\hbar k_z$ (per absorbed photon) and the scattering rate $\Gamma_{\text{sc}} = \Gamma \cdot \rho_e(v_z)$:

$$F_z(v_z) = m\frac{\mathrm{d}v_z}{\mathrm{d}t} = \hbar k_z \Gamma \rho_e(v_z). \tag{3.16}$$

As the relative change of energy is small, the effect of laser cooling can be averaged over one motional cycle and the resulting cooling rate is

$$\left(\frac{\mathrm{d}E}{\mathrm{d}t}\right)_{\text{laser}} = \langle v_z F_z(v_z)\rangle = \langle -\hbar\Delta_D \Gamma \rho_e(v_z)\rangle\,. \tag{3.17}$$

Following the formalism in [75], energies and detunings are expressed in scaled units:

$$\{\epsilon, \delta, r\} = \{E, \hbar\Delta, \frac{(\hbar k_z)^2}{2m}\}/E_0, \tag{3.18}$$

$$E_0 = \frac{\hbar\Gamma}{2}\sqrt{1+s_0},\ \ t_0 = \frac{1+s_0}{\Gamma s_0/2},\ \ \tau = \frac{t}{t_0}, \tag{3.19}$$

$$\frac{\mathrm{d}N_{\text{ph}}}{\mathrm{d}\tau} = \frac{\mathrm{d}N_{\text{ph}}}{\mathrm{d}t} \cdot t_0 = \Gamma \cdot \rho_e \cdot t_0 = \frac{(1+s_0)}{(1+s_0)+(2\Delta_{\text{eff}}/\Gamma)^2} = \frac{1}{(1+\delta_{\text{eff}}^2)}. \tag{3.20}$$

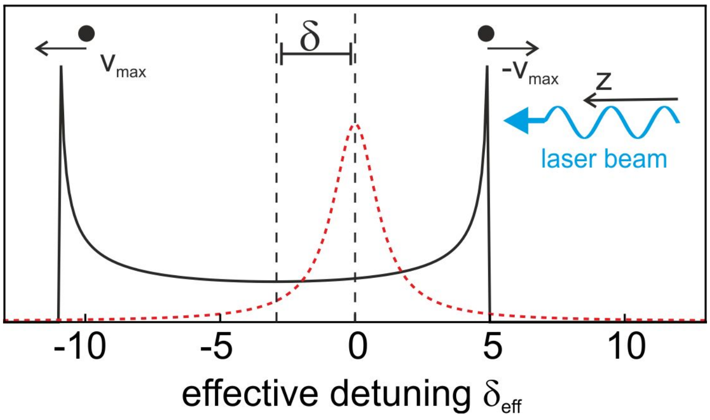

Figure 3.3: The instantaneous Doppler shift distribution $P_D(\delta_M, \delta_D)$ (black, solid) and the absorption probability (red, dashed) for $\delta_M = 8$ and $\delta = -3$. Vertical axis in arbitrary units.

In the last step of Eq. (3.20), $\delta_{\text{eff}} \equiv \hbar\Delta_{\text{eff}}/E_0 = 2\Delta_{\text{eff}}/\ \Gamma\sqrt{1+s_0}$ has been used. The energy ϵ and the frequency detuning δ are given in units of half the saturation-broadened linewidth and the time τ is expressed in units of t_0, which is the inverse of the on-resonance scattering rate. At SpecTrap, typical numbers for the on-resonance saturation and the detuning are $s_0 = 1$ and $\Delta = -2\pi \cdot 20\,\text{MHz}$, respectively. Therefore, in the case of $^{24}\text{Mg}^+$ ions the scaled units amount to $E_0 \approx 0.12\,\mu\text{eV}=\text{k}_B \cdot 1.4\text{mK}$, $t_0 \approx 1.6 \cdot 10^{-8}\,\text{s}$ and $r \approx 3.7 \cdot 10^{-3}$.

The average over one motional cycle in equation (3.17) can be obtained with the probability density P_D of the instantaneous Doppler shift δ_D of a harmonic oscillator

$$P_D(\delta_M, \delta_D) = \begin{cases} 1/\pi\sqrt{\delta_M^2 - \delta_D^2} & \text{if } |\delta_D| < \delta_M, \\ 0 & \text{otherwise,} \end{cases} \tag{3.21}$$

where δ_M denotes the maximum Doppler shift for a given energy.

Figure 3.3 shows a visualization of the distribution $P_D(\delta_M, \delta_D)$ (black solid) and the absorption probability (red dashed) as a function of the effective detuning δ_{eff}. The absorption probability is centered around an effective detuning of zero, whereas the center of the distribution P_D – the effective detuning experienced by an ion at rest – is shifted by laser the detuning δ. Laser cooling (heating) occurs for absorption processes in the right (left) part of the distribution P_D, where the ion is moving towards (away from) the laser beam. Obviously, for a detuning δ much larger than the natural linewidth, only the right wing of P_D has significant overlap with the absorption probability and the net effect of the ion-laser interaction is cooling.

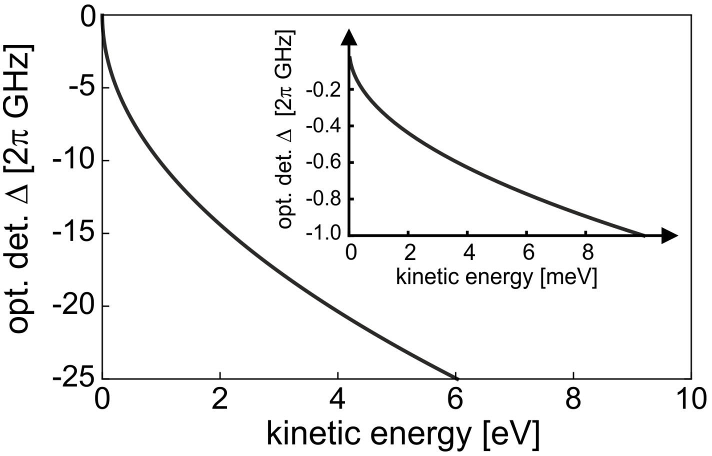

Figure 3.4: For a given kinetic energy, the laser detuning Δ that results in the optimum cooling rate is calculated according to the equation (3.26). Inset: Optimum detuning for a lower energy range.

With the probability distribution of the P_D the average of both the scattering rate $\mathrm{d}N_{\mathrm{ph}}/\mathrm{d}\tau$ and the laser cooling rate $\mathrm{d}\epsilon/\mathrm{d}\tau(\epsilon)$ are obtained in scaled units:

$$\begin{aligned}
\frac{\mathrm{d}N_{\mathrm{ph}}}{\mathrm{d}\tau} &= \int \mathrm{d}\delta_D \;\; P_D(\delta_M;\delta_D)\frac{1}{1+(\delta+\delta_D)^2} \\
&= \frac{1}{2\sqrt{\epsilon r}}\mathrm{Im}(\mathrm{Z}), && (3.22) \\
\left(\frac{\mathrm{d}\epsilon}{\mathrm{d}\tau}\right)_{\mathrm{laser}} &= \int \mathrm{d}\delta_D \;\; (-\delta_D)\,P_D(\delta_M;\delta_D)\frac{1}{1+(\delta+\delta_D)^2} \\
&= \frac{1}{2\sqrt{\epsilon r}}\left(\mathrm{Re}(\mathrm{Z})+\delta\ \mathrm{Im}(\mathrm{Z})\right), && (3.23) \\
\text{where } Z &= \frac{i}{\sqrt{1-(\delta+i)^2/(4\epsilon r)}}.
\end{aligned}$$

For large energies $\epsilon \gg (1+\delta^2)/r$ the distribution $P_D(\delta_M,\delta_D)$ can be replaced by $P_D(\delta_M,0)$ [1]. This can be understood when looking at figure 3.3: An ion with high energy has a large velocity distribution, so the variation of P_D and the overlap of the edges with the line profile is small. For example, with the parameters $s_0 = 1$ and a detuning $\Delta = -2\pi \cdot 20\,\mathrm{MHz}$, this limit is for $^{24}\mathrm{Mg}^+$ given by $\epsilon \gg 800$, i.e. $\mathrm{E} \gg \mathrm{k}_B \cdot 1.2\,\mathrm{K}$. In this high-energy limit, equations (3.22) and (3.23) simplify to

$$\frac{\mathrm{d}N}{\mathrm{d}\tau} \approx \frac{1}{2\sqrt{\epsilon r}}, \qquad (3.24)$$

$$\frac{\mathrm{d}\epsilon}{\mathrm{d}\tau} \approx \frac{\delta}{2\sqrt{\epsilon r}}. \qquad (3.25)$$

---

[1] For not too small detunings, the criterion $\epsilon \gg (1+\delta^2)/r$ can be replaced by $\epsilon \gg \delta^2/r$, which is equivalent to $\delta_M \gg \delta$.

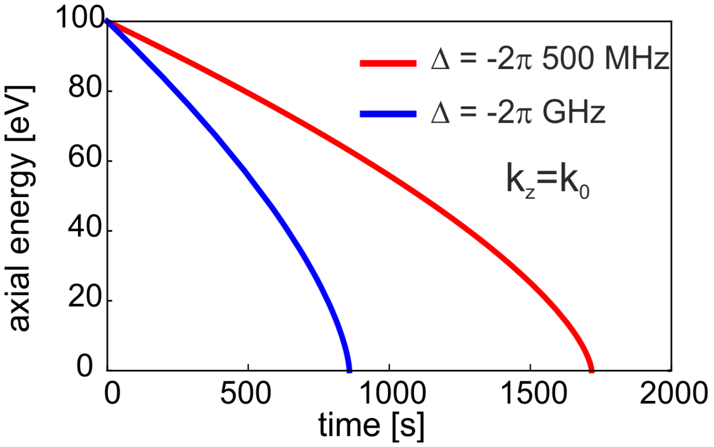

Figure 3.5: Laser cooling with an axially irradiated laser beam ($k_z = k_0$), and constant detuning of $\Delta = -2\pi \cdot 500\,\text{MHz}$ (red) and $-2\pi \cdot 1000\,\text{MHz}$ (blue).

From the exact solution of $\mathrm{d}\epsilon/\mathrm{d}\tau$, the critical energy ϵ_c, for which the cooling rate attains its maximum, is found to be

$$\epsilon_c = \frac{1+\delta^2}{2r} \cos\left(\frac{1}{3} \arccos\left(\frac{1-\delta^2}{1+\delta^2}\right)\right) \tag{3.26}$$

$$\approx \frac{\delta^2}{4r}, \quad \text{if} \quad \delta^2 \gg 1. \tag{3.27}$$

From equation (3.26) it follows that the possible maximum cooling rate is achieved for a laser detuning of $\delta \approx -\delta_M = -2\sqrt{\epsilon r}$. In this case, not only the overlap of the probability distribution P_D and the absorption probability is maximal, but also the energy change per scattering event $\Delta E \approx \hbar\Delta$. For Mg^+ ions, the optimum detuning exceeds several GHz for kinetic energies larger than 10 meV and several tens of GHz for energies larger than 1 eV (Fig. 3.4). Thus, the optimum detuning for ions with an initial energy of several hundreds of electron-volts is not easily reached in an actual experiment, because a fast sweep over such a frequency range is not possible with the presently used laser system.

Laser cooling with a detuning $|\Delta| < 2\pi\cdot$GHz is far outside the realm of efficient laser cooling and the total cooling time amounts to several hundreds of seconds (Fig. 3.5). This demonstrates the need to enlarge the scanable range of the laser system or to use other, more suitable cooling techniques as resistive cooling or buffer gas cooling instead.

3.3 Combined buffer gas and laser cooling of Mg^+

In the last two sections, the buffer gas cooling and laser cooling have been presented independently. In this section, the cooling of Mg^+ ions after injection is described by a model that is developed as an extension of the model presented in [75] and that combines these two cooling mechanisms.

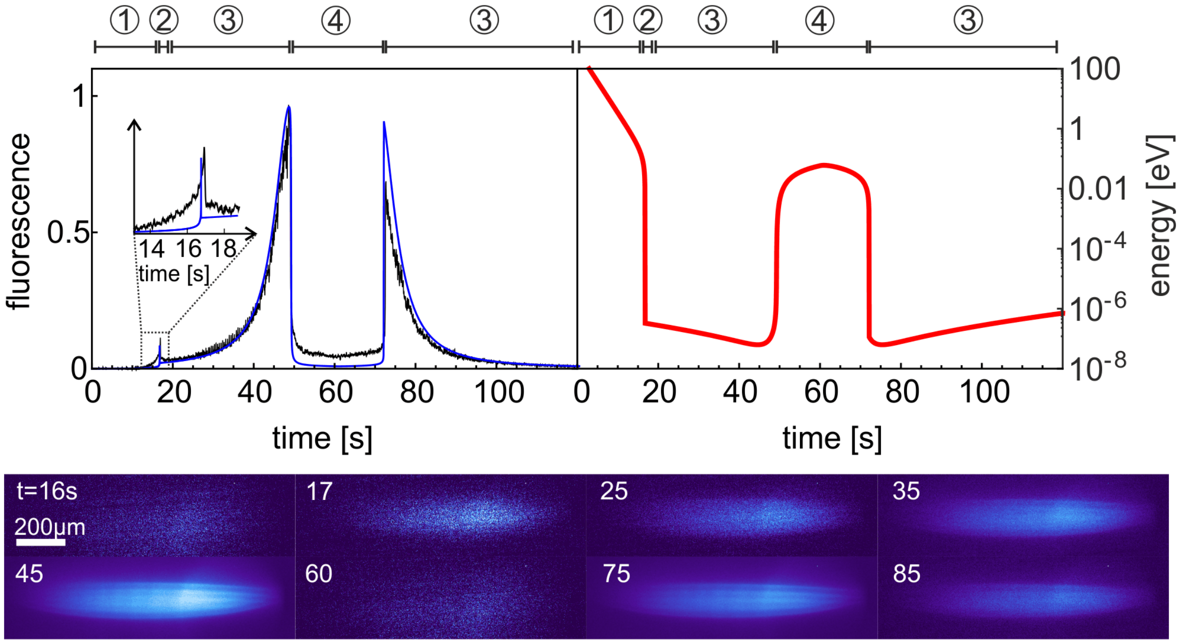

Figure 3.6: Left: Fluorescence signal of Mg^+ ions while cooling with a scanning laser. The black line represents the measured fluorescence, the blue line the fluorescence according to the model. The phases 1–4 (see text for explanation) are indicated. The laser performed a saw-tooth scan with calculated rate $2\pi \cdot 4.67\,\mathrm{MHz/s}$. The initial detuning was $\Delta_i = -2\pi \cdot 230\,\mathrm{MHz}$ for $t = 0$ and the maximum detuning was $\Delta_{\mathrm{max}} = +2\pi \cdot 50\,\mathrm{MHz}$ for $t = 60\,\mathrm{s}$. Initial ion energy $E_i = 400\,\mathrm{eV}$, $\gamma_{\mathrm{buf}} = 0.24\mathrm{s}^{-1}$, $s_0 = 0.15$. Right: Energy per ion according to the modeled cooling process. Bottom: Images of the ion cloud.

The overall single-particle cooling rate $\mathrm{d}\epsilon/\mathrm{d}\tau$ can be expressed as

$$\frac{\mathrm{d}\epsilon}{\mathrm{d}\tau} = \left(\frac{\mathrm{d}\epsilon}{\mathrm{d}\tau}\right)_{\mathrm{laser}} + \left(\frac{\mathrm{d}\epsilon}{\mathrm{d}\tau}\right)_{\mathrm{recoil}} + \left(\frac{\mathrm{d}\epsilon}{\mathrm{d}\tau}\right)_{\mathrm{buf}}. \tag{3.28}$$

The expressions for the laser cooling rate, the recoil heating and the buffer gas cooling have been derived in equations (3.23), (3.9), and (3.2). Accordingly, the total cooling rate reads

$$\frac{\mathrm{d}\epsilon}{\mathrm{d}\tau} = \frac{1}{2\sqrt{\epsilon r}}\big(\mathrm{Re(Z)} + \tilde{\delta}\ \mathrm{Im(Z)}\big) + \frac{1}{2\sqrt{\epsilon r}}\frac{7}{5}r\,(\mathrm{Im(Z)}) - 2\gamma_{\mathrm{buf}} \cdot (\epsilon - 4k_B T). \tag{3.29}$$

By numerical integration of equation (3.29) the energy and fluorescence rate are obtained as a function of time. Figure 3.6 shows the energy and fluorescence signals calculated by the model, together with an actual fluorescence measurement that was recorded while Mg^+ ions are being laser-cooled after injection with a transport energy of 400 eV. During the cooling process, the laser is scanned with a rate of $2\pi \cdot 4.67\,\mathrm{MHz/s}$ from an initial detuning of $\Delta_i = -2\pi \cdot 230\,\mathrm{MHz}$ to

$\Delta_{\mathrm{max}} = +2\pi \cdot 50\,\mathrm{MHz}$ and back again. The fluorescence maximum is normalized to unity and the only remaining, free parameters of the model – the buffer gas cooling rate $\gamma_{\mathrm{buff}} = 0.24\,\mathrm{s}^{-1}$ and the on-resonance saturation parameter $s_0 = 0.15$ – were chosen such that best agreement between the measured data and the model is obtained.

The temporal fluorescence behavior after ion injection can be divided into four phases:

- The initial cooling phase ($0\,\mathrm{s} \leq t \leq 14\,\mathrm{s}$), with ion energies in the range of $E \approx 400 \ldots 1\,\mathrm{eV}$, is dominated by buffer gas cooling since the ion Doppler shift is large and laser cooling is very inefficient at such energies.
- The second phase ($14\,\mathrm{s} \leq t \leq 17\,\mathrm{s}$) starts once the kinetic energy – and thus the Doppler broadening – are sufficiently reduced such that laser Doppler-cooling is the predominant cooling mechanism and the energy is decreased within fractions of a second to the μeV regime. This phase of fast laser cooling is revealed by a sudden increase of the fluorescence signal which is visible as the so-called cooling peak.
- During the third phase ($17\,\mathrm{s} \leq t \leq 50\,\mathrm{s}$) the ion temperature is defined by an equilibrium between laser cooling and recoil heating. The ions' temperature changes slowly as the laser detuning decreases. For a detuning of $\Delta = -\Gamma/2$ the temperature attains its minimum close to the Doppler limit of 0.99 mK.
- The fourth phase ($50\,\mathrm{s} \leq t \leq 60\,\mathrm{s}$) is characterized by a positive laser detuning Δ and the consequential laser heating. The temperature increases to about 100 K, where it stabilizes due to buffer gas cooling. After reaching its maximum detuning, the laser detuning and the fluorescence signal show an inverse temporal behavior without cooling peak.

The characteristic fluorescence peak during the second cooling phase is similar to features that have been observed in both Penning [102] and Paul traps [103, 104], and have in both cases been associated with a sudden decrease of the ion temperature. Depending on the experimental circumstances, the rapid cooling was accompanied by a phase transition to a state of high ion-ion correlation, i.e. to a liquid-like state or a Coulomb crystal. However, it should be noted that rapid cooling of the cloud is merely the prerequisite for the transition to a strongly correlated state, and not necessarily a certain indicator.

The temporal fluorescence behavior after injection has been also investigated for different sets of cooling parameters (Fig. 3.7). Starting from an initial detuning of $\Delta = -2\pi \cdot 130\,\mathrm{MHz}$ (left) and $\Delta = -2\pi \cdot 90\,\mathrm{MHz}$ (right) the laser is scanned in both cases with a rate of $2\pi \cdot 8\,\mathrm{MHz/s}$. A fluorescence peak appears in none of the two spectra, since the influence of laser cooling becomes visible not until the laser detuning is close to the resonance. For such detunings the height of the fluorescence peak – i.e. the factor by which the maximum scattering rate exceeds the steady state

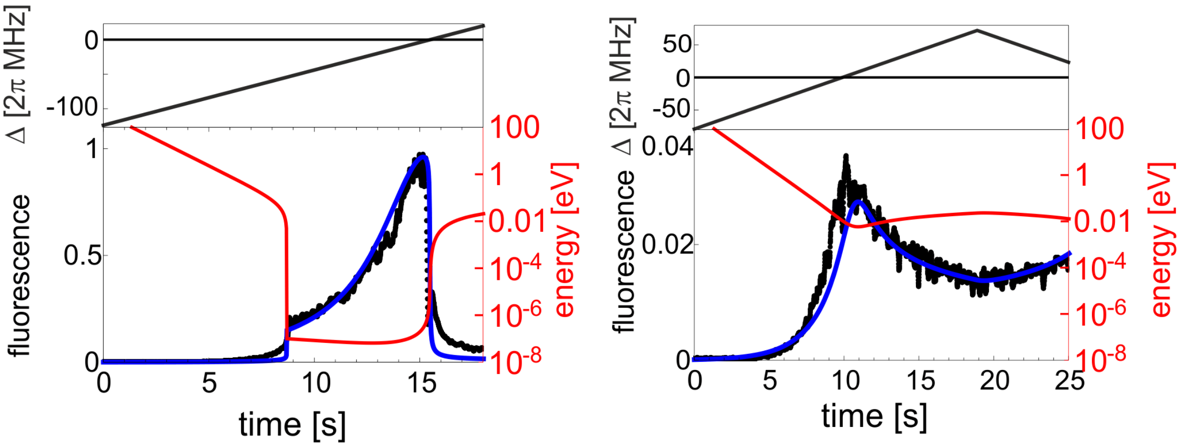

Figure 3.7: Left and right: Fluorescence signals during laser cooling (black line: measured, blue line: model). The modeled temperature is indicated (red line). The top graphs show the laser detuning. Parameters left: $E_i = 400\,\text{eV}$, $s_0 = 0.2, \gamma_{\text{buf}} = 0.52$. Parameters right: $E_i = 400\,\text{eV}$, $s_0 = 0.2, \gamma_{\text{buf}} = 0.51$.

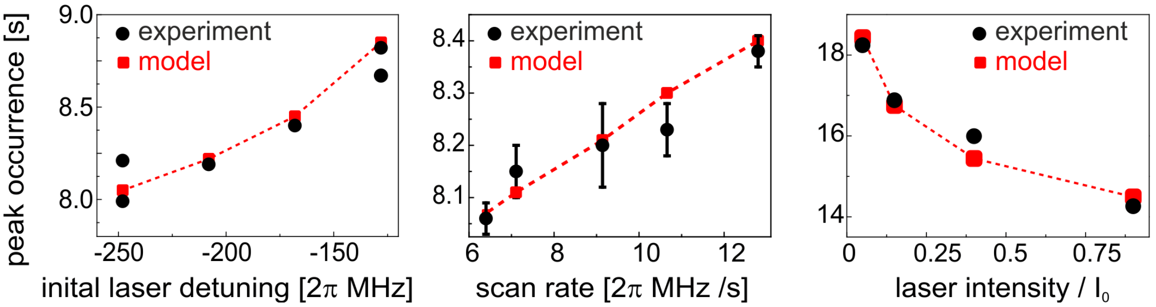

Figure 3.8: The time between the ion-bunch injection and the occurrence of the Doppler-cooling peak, measured as a function of the initial laser-detuning (left), the laser scan rate (middle), and the laser intensity (right). Error bars (if present) indicate the scattering of repeated measurements; the line is to guide the eye. Left: $\tau_{\text{buf}} = 0.48\,\text{s}$, $I/I_0 = s_0 = 0.2$, $\dot{\Delta} = 2\pi \cdot 8\,\text{MHz/s}$. Middle: $\tau_{\text{buf}} = 0.48\,\text{s}$, $s_0 = 0.2$, $\Delta_i = -2\pi \cdot 210\,\text{MHz}$. Right: $\tau_{\text{buf}} = 1.05\,\text{s}$, $\Delta_i = -2\pi \cdot 230\,\text{MHz}$, $\dot{\Delta} = 2\pi \cdot 4.66\,\text{MHz}$.

scattering rate directly after the cooling peak – decreases as the laser detuning δ approaches a critical detuning of $\delta_c = -1/\sqrt{3}$, and no peak occurs for $\delta > \delta_c$ [75].

Systematic measurements of the time between the ion-bunch injection and the occurrence of the Doppler-cooling peak have been performed. The occurrence time has been investigated as a function of the initial laser detuning, the scan rate and the laser intensity (Fig. 3.8). Since the ion energy is decreased by $\hbar\Delta$ per scattering event, the occurrence time of the fluorescence peak decreases for lower initial detuning and lower scan rate. The occurrence time also decreases with increasing laser intensity.

A direct measurement of the cloud temperature – for example with a probe beam in addition to the primary cooling beam – could not be performed. However, by fitting a Voigt profile to a resonance scan the temperature-dependent Doppler broadening of the resonance can be determined. Assuming a constant temperature T during the scan, this Doppler broadening allows to estimate an upper limit for the temperature of the order of $T \leq 100\,\mathrm{mK}$. Only an upper temperature limit is given, because the effect of saturation broadening masks the contribution of the Doppler broadening and adds an additional unwanted free parameter to the fitting routine.

A different approach is to estimate the temperature on the basis of structures visible in images of the ion cloud. Directly after passing the fluorescence peak, the cloud shape exhibits a well-defined boundary (Fig. 3.6), which indicates that the cloud temperature is – as a very conservative estimate – below 1 K. Shell structures are not visible until the fluorescence signal allows a sufficient signal-to-noise ratio at $t \approx 30\,\mathrm{s}$. Their formation implies that the coupling parameter is $\Gamma \gg 1$ and the temperature below 100 mK. However, it should be stressed again that this is just an upper limit and there are no indications that the temperature may be actually higher than the theoretical limit of a few millikelvins.

In literature, laser cooling of large ion clouds to temperatures close to the Doppler cooling limit has been reported [106, 107], which for a detuning of a few hundreds of MHz is in the millikelvins regime (Fig. 3.2). However, it has also been found that the presence of strong heating can limit cooling to temperatures two orders of magnitude larger than the Doppler cooling limit [83, 85, 106, 108, 109]. For perpendicular laser cooling the work done by the laser in applying a torque to the ion cloud has been identified as a strong source of heating [110]. It limits laser cooling to temperatures of a few hundreds of millikelvins, depending on experimental parameters such as the laser intensity and the spatial offset from the trap center.

On the basis of the results reported in the literature, one can conclude that the observed cloud temperature in the range 1 to 100 mK represents a typical value. Possible heating sources that increase the temperature above the Doppler cooling limit of 0.99 mK are for example the torque due to static field errors, insufficient axial symmetry or collisions with buffer gas (for a discussion of the torque applied by buffer gas see section 3.1).

Discussion of deviations between the model and experiment

Although the presented model of the cooling process reproduces the experimental data quite well, some characteristic features of the spectra are not fully reproduced:

1) The measured and the modeled fluorescence differ significantly during the 1–2 seconds immediately before the fluorescence peak (see e.g. inset of figure 3.6). Since the model was derived for a single particle and therefore neglects the distribution of ion energies, this pre-peak fluorescence can be contributed to the uncorrelated addition of individual fluorescence signals. After the fluorescence peak – during the third phase characterized by thermal equilibrium between the ions and the laser field – the ion energy distribution converges to the equilibrium energy and the single-particle model is again an appropriate simplification.

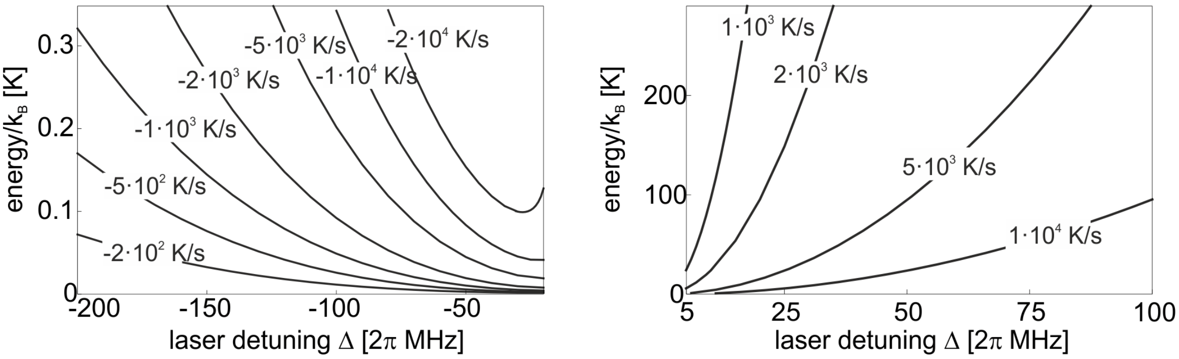

Figure 3.9: For a Mg^+ ion trapped in a harmonic potential, the lines of constant cooling rates (left) and constant heating rates (right) have been calculated in the $E-\Delta$-plane of the ion's kinetic energy E and the laser detuning Δ. The two contributions to the cooling and heating rates – $(\mathrm{d}\epsilon/\mathrm{d}\tau)_{\text{laser}}$ and $(\mathrm{d}\epsilon/\mathrm{d}\tau)_{\text{recoil}}$ – have been calculated for a laser intensity of $I = I_0$ according to equations (3.23) and (3.9).

2) During the phase of laser heating, the measured fluorescence is significantly higher than the one predicted by the theoretical model. This effect of an unexpected high fluorescence signal for a blue-detuned laser has already been reported in [41] and [45]. The large fluorescence rate indicates that the ion temperature is actually as low as 20 K, whereas the model predicts an equilibrium between laser heating and buffer gas cooling for an ion energy of 0.05 eV$\approx k_B \cdot 500\,\mathrm{K}$ (Fig. 3.6). This discrepancy between model and observation may be due to an overestimation of the effective laser heating. At these temperatures $T \gg 1\,\mathrm{K}$, the plasma is in a gaseous state and the ions can move freely within the plasma boundaries. Since only a fraction of the total cloud volume is irradiated by the laser beam, the ions are not permanently heated by the laser beam and the effect of laser heating is reduced [83]. As a consequence, the equilibrium between laser heating and buffer gas cooling is reached for a lower temperature than predicted by the cooling model.

A different explanation is given in [41], where it is noted that although the laser is blue detuned for the ${}^2\mathrm{S}_{1/2,m_j=-1/2} \rightarrow {}^2\mathrm{P}_{3/2,m_j=-3/2}$ transition, it is still red-detuned for all other σ^--transitions and this additional cooling effect might explain the observed fluorescence. Furthermore, laser cooling of ${}^{25}\mathrm{Mg}^+$ and ${}^{26}\mathrm{Mg}^+$ ions, which are trapped simultaneously with the ${}^{24}\mathrm{Mg}^+$, should also contribute to the total cooling rate. However, if there was a cooling mechanism that reduced the ion temperature to $T \approx 20\,\mathrm{K}$, it would have to compensate a laser heating rate of several thousands of K/s (Fig. 3.9, right). In the case of the measurement presented here, the expected rates due to laser cooling of ${}^{25}\mathrm{Mg}^+$ and ${}^{26}\mathrm{Mg}^+$ or other transitions in ${}^{24}\mathrm{Mg}^+$ are by orders of magnitudes too low to account for the observed effect. Coupling between the axial and radial degrees of freedom can also be excluded as a possible cooling mechanism, since it is does not provide continuous cooling but rather increases the heat capacity of the ion cloud. To conclude, a reduction of the laser heating rate due to ions moving in-and-out of the laser beam is better suited to explain the unexpected large fluorescence rate at positive laser detunings than the assumption of an additional, unidentified cooling mechanism.

4 Single- and multi-species Coulomb crystals

The cooling of large ion ensembles – as presented in the previous chapter – allows the preparation of an ion cloud in a cold and dense state of thermal equilibrium. The structure and dynamics of such cold and dense plasmas have been investigated in this work. The findings have partly been presented in [111] and will be more completely described in this chapter.

The consequence of the reduced kinetic energy and the simultaneously decreasing ion-ion distance in a cold plasma is a strong correlation between the ions, which is described by the plasma parameter Γ_p[1]. It is defined by the ratio of the Coulomb energy between neighboring charges to the thermal energy per degree of freedom $k_B T$ and reads [112]

$$\Gamma_p = \frac{q^2}{4\pi\epsilon_0 a_{\mathrm{WS}} k_B T}, \quad \text{or in cgs units:} \quad \Gamma_p = \frac{q^2}{a_{\mathrm{WS}} k_B T}, \tag{4.1}$$

with the Wigner-Seitz radius a_{WS}, which is the average inter-particle spacing and is defined by [113]

$$a_{\mathrm{WS}} = \left(\frac{3}{4\pi n}\right)^{1/3}. \tag{4.2}$$

Here, q denotes the charge of the particle, T the temperature, n the number density, ϵ_0 the electric constant, and k_B the Boltzmann constant. In this thesis, expressions will be given in SI units if not stated otherwise, and the expression for Γ_p in cgs units is just given for convenience.

With regard to the parameter Γ_p, a non-neutral plasma can be classified as weakly or strongly correlated with $\Gamma_p \ll 1$ and $\Gamma_p \gg 1$, respectively. With increasing correlation, a plasma exhibits fluid-like properties like local ordering, and for even larger Γ_p it undergoes a phase transition to an ion crystal, i.e. a state of global ordering.

Interest in ion crystals arose from possible applications in quantum information processing. They can also serve as a model for dense astrophysical matter, e.g. white dwarfs or the crust of neutron stars [114, 115, 116, 117, 118].

The first phase transition to a crystalline state has been observed for Coulomb clusters with ion numbers in the range $N = 2 - 50$ [112]. In this study, and as well in later ones with up to 3000 ions [104], the transition was accompanied by

---

[1] In the literature, the term *Coulomb coupling parameter* is also used for the plasma parameter Γ_p.

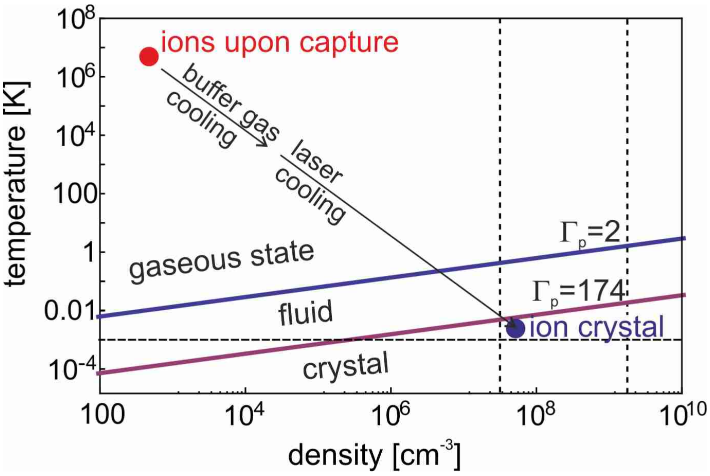

Figure 4.1: Phase diagram of the plasma parameter Γ_p for a trapping voltage of $U = 50\,\mathrm{V}$ and a magnetic field of $B = 4\,\mathrm{T}$. Dashed lines: Doppler limit of Mg^+ ions of 1mK, the minimum and the maximum density for a plasma in thermal equilibrium of $3.1 \cdot 10^7\mathrm{cm}^{-3}$ and $1.8 \cdot 10^9\mathrm{cm}^{-3}$, respectively.

a fluorescence dip, that is caused by a decreasing Doppler width due to the sudden reduction of RF heating in the ordered state[2].

While in Paul traps the creation of huge ion crystals is hindered by the influence of RF heating [104], in Penning traps ion crystals with particle numbers up to $N = 10^6$ have been observed [119, 120]. For such large plasmas, surface effects can be neglected in the plasma interior and they can thus be regarded as an infinitely large plasma. Plasmas that are sufficiently small such that correlations in the plasma interior are influenced or dominated by surface properties are referred to as mesoscopic plasmas ([84], p. 112). Depending on the plasma shape and the strength of the ion-ion correlation, the ion number of mesoscopic plasmas lies in the range of $100 \lesssim N \lesssim 10^5$. Ensembles with even smaller ion numbers $N < 100$ form Coulomb clusters that have been observed to form simple geometric configurations [112, 121, 122].

The value of Γ_p, for which the transition between the different phases occurs, has been evaluated both theoretically and experimentally. In this work the actual value of Γ_p for the phase transitions is of special interest, because it allows to estimate the cloud temperature from features visible in images of the ion cloud. For an infinitely large plasma, the radial distribution function, which is monotonic for $\Gamma < 2$, shows density oscillations at the boundary when $\Gamma_p \gtrsim 2$ [124]. These density oscillations signify the onset of local ordering and thus mark the transition to a fluid-like state. However, no discontinuous vapor-liquid transition, which requires an attractive potential between particles [84, 123], is observed. Instead, the system behaves like a fluid beyond the critical point [84].

---

[2] For larger plasmas, the transition was not necessarily to a crystalline state, but more often to a liquid-like state. Contrary to this, small Coulomb clusters were always found in the crystalline state after the occurrence of the fluorescence dip. Since for small systems – as Coulomb clusters – the distinction between local ordering (liquid state) and global ordering (ion crystal) is somehow arbitrary, the different behavior of the two systems means no contradiction.

The transition to a solid state with body-centered cubic (bcc) lattice structure was predicted for values of Γ_p in the range of 125 to 168 [124, 125, 126]. More recent results agree on a transition in the range of $172 < \Gamma_p < 178$ [127, 128, 129, 130] and are in agreement with an experimentally determined value of $\Gamma_p \approx 170$ [131]. The regimes of the different phases can be visualized for typical trapping parameters in a phase-diagram in the density-temperature plane (Fig. 4.1). Different to the vapor-liquid transition, the fluid-solid phase transition is of first order and liberates energy when the fluid freezes [84].

While for an infinitely large plasma the solid state is characterized by a bcc lattice structure, for mesoscopic plasmas this is no longer expected. Instead, the plasma crystal consists of concentric shells which can be thought of as lattice planes that have been deformed by the external confining potential [84]. For such crystals, face-centered cubic (fcc) and hexagonal close-packed (hcp) structures have been observed [132]. The critical ion number for a spherical plasma to form a bcc structure was predicted by theory to be $N > 1.5 \cdot 10^4$ [133], whereas experimentally $N > 2 \cdot 10^5$ was found [119]. In [84] (p. 112) a maximum of 60 crystal shells is given as a criterion for mesoscopic crystals. Accordingly, the ion crystals investigated in this work with axial dimension of less than 15 shells and with ion numbers ranging from 10^4 to 10^5 can be regarded as mesoscopic and a model developed to describe the shell structure of planar, mesoscopic crystals [84] was found appropriate to describe the imaged crystalline structures.

4.1 Properties of non-neutral plasma in thermodynamic equilibrium

In section 2.3.3 the equation of motion for a single particle and its solution have been given, introducing the two radial eigenmotions with oscillation frequencies $\omega_\pm$ and the axial oscillation with frequency ω_z. Instead of solving the equation of motion, this section will discuss under which conditions a stable, circular orbit is possible for a single ion. This approach is chosen, because it motivates the introduction of an effective potential, which in a second step allows the treatment of a cold plasma in thermal equilibrium in analogy to the single-ion case.

Effective potential for a single ion

An ion stored in a Penning trap and rotating with the frequency ω_r in a circular orbit, experiences the Lorentz force due to the magnetic field, the centrifugal force, and the force of the electrostatic potential:

$$F_{\text{ion}} = F_{\text{Lorentz}} + F_{\text{centrifugal}} + F_{\text{trap}} \tag{4.3}$$

$$= -qr\omega_r B + m\omega_r^2 r + q\left(\frac{U_0 C_2}{4d^2} 2r\right). \tag{4.4}$$

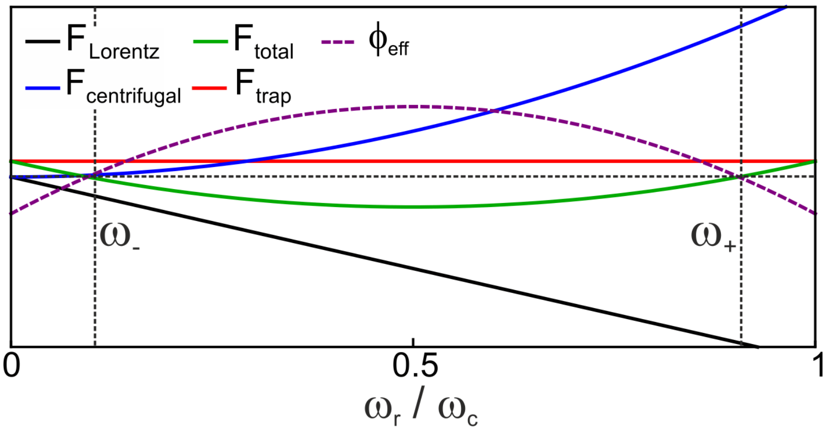

Figure 4.2: Illustration of the forces acting on a single ion in a Penning trap. The horizontal, dashed line indicates the equilibrium of $\phi^{\mathrm{eff}}_{\mathrm{ion}} = F_{\mathrm{total}} = 0$.

Using the relation $\omega_c = qB/m$ the effective potential describing these forces reads [134]:

$$\begin{aligned}\phi^{\mathrm{eff}}_{\mathrm{ion}}(r,z) &= \phi_{\mathrm{Lorentz}} + \phi_{\mathrm{centrifugal}} + \phi_{\mathrm{trap}} \\ &= \frac{mr^2}{2q}\omega_r(\omega_c - \omega_r) + \frac{C_2U_0}{4d^2}(2z^2 - r^2).\end{aligned} \tag{4.5}$$

The effective potential $\phi^{\mathrm{eff}}_{\mathrm{ion}}$ and the forces acting on an ion in the plane for $z = 0$ can be illustrated as a function of the ion orbital frequency ω_r for a fixed radial position r (Fig. 4.2). For an ion in a stable and circular orbit, the sum of the forces given by (4.4) and the potential $\phi^{\mathrm{eff}}_{\mathrm{ion}}(r,z)$ must equal zero. The two solutions of this quadratic equation are $\omega_r = \omega_-$ and $\omega_r = \omega_+$, i.e. a single ion only performs a circular rotation about the axis of symmetry, if its motion is a pure magnetron or cyclotron rotation. Since all three force contributions are proportional to the radius of the orbit, $\omega_\pm$ does not depend on the orbital radius r.

The free cyclotron frequency ω_c is given by the equilibrium between Lorentz force and centrifugal force. For typical trap voltages, the reduced cyclotron frequency ω_+ is of the order of ω_c, only slightly reduced by the electrostatic potential. To first order, the magnetron motion with ω_- is determined by the equilibrium between Lorentz force and electrostatic potential, with a small shift by the centrifugal force. Only the small centrifugal shift depends on the mass of the particle, thus the magnetron frequency is similar for particles with different masses.

Effective potential for a plasma

In a plasma, charges are free to move according to the electric and magnetic fields that are created by external sources as well as by the charges themselves. As a consequence, the charges in a plasma arrange such that external fields are shielded from the interior of the plasma. The scale of this shielding when viewed in the plasma's rest frame is called Debye length. As a strict criterion, an ion ensemble can be considered a plasma when the Debye length is less than the cloud dimension [135]. For a cloud of charged particles with density n and temperature T the Debye length λ_D is given by

$$\lambda_D = \left[\frac{\epsilon_0 k_B T}{n q^2}\right]^{1/2}, \quad \text{or in cgs units:} \quad \lambda_D = \left[\frac{k_B T}{4\pi n q^2}\right]^{1/2}. \tag{4.6}$$

By comparison of equations (4.1) and (4.6) one finds that the relation between the Debye length and the plasma parameter is given by $\Gamma_p = a_{\mathrm{WS}}^2/3\lambda_D^2$.

For a plasma in the sense of the definition given above, the space-charge potential is not negligible in the thermal-equilibrium density-distribution (p. 98 in [84]). Accordingly, the total electrostatic potential ϕ for a non-neutral plasma stored in a Penning trap is the sum of the trapping potential ϕ_{trap}, the ions' space-charge potential ϕ_{sc} and the image charge potential ϕ_{im}

$$\phi = \phi_{\mathrm{trap}} + \phi_{\mathrm{sc}} + \phi_{\mathrm{im}}. \tag{4.7}$$

For Penning traps with typical characteristic trap dimension d, the contribution of the image charge potential ϕ_{im} is negligible, because it scales with d^{-3} and is only relevant for much smaller traps [136]. For a large number of ions stored in a Penning trap at low temperatures, the Coulomb interaction drives the ensemble to a thermal equilibrium in which the ion cloud rotates as a rigid body with the global rotation frequency ω_r [137]. This rotation frequency ω_r depends on the initial conditions of the cloud, e.g. the total angular momentum and is free within the limits $\omega_- \leq \omega_r \leq \omega_+$. The total effective potential in the interior of the plasma is the same as the one given by equation (4.5), with an additional term due to the plasma space-charge potential ϕ_{sc}:

$$\begin{aligned} \phi_{\mathrm{plasma}}^{\mathrm{eff}}(r,z) &= \frac{m}{2q}\omega_r\omega_c r^2 - \frac{m}{2q}\omega_r^2 r^2 + \phi_{\mathrm{trap}}(r,z) + \phi_{sc}(r,z) && (4.8)\\ &= \frac{mr^2}{2q}\omega_r(\omega_c - \omega_r) + \phi_{\mathrm{trap}}(r,z) + \phi_{sc}(r,z). && (4.9) \end{aligned}$$

For a plasma at thermal equilibrium the density is given by [106]

$$n(r,z) = n_0 \exp\left(-q\phi_{\mathrm{pl.}}^{\mathrm{eff}}/kT\right), \tag{4.10}$$

hence the density in the trap center is $n(0,0) = n_0$. In the limit $T \to 0$, the effective potential must become $\phi_{\mathrm{pl.}}^{\mathrm{eff}}(r,z) = 0$ for the density $n(r,z)$ to remain finite. Thus, at zero temperature the plasma density is constant $n(r,z) = n_0$ in the interior of the plasma and drops to zero at the plasma edge. Consequently, the space-charge potential of a plasma in thermal equilibrium at zero temperature $T = 0$ completely

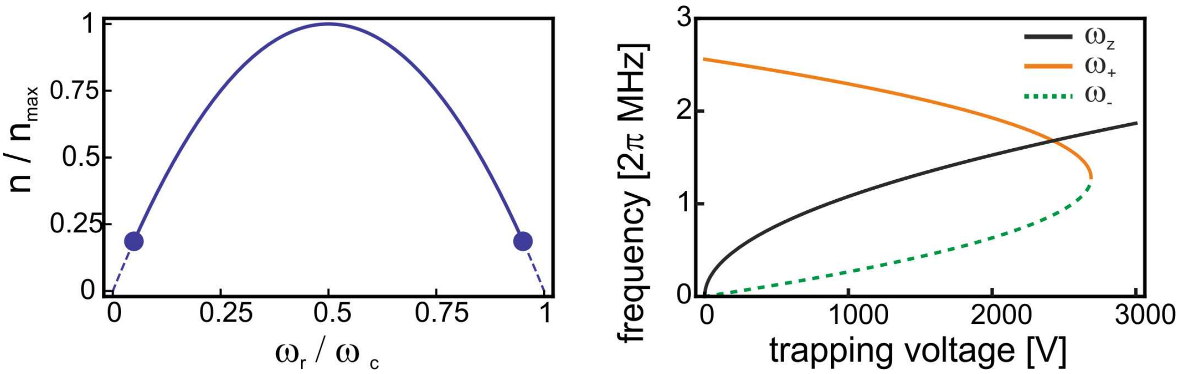

Figure 4.3: Left: The cloud density as a function of the rotation frequency ω_r. Limits of ω_r are given by $\omega_- \leq \omega_r \leq \omega_+$. Dots mark the frequencies $\omega_\pm$ and the corresponding densities for $^{24}\mathrm{Mg}^+$ at $B = 4\,\mathrm{T}$ and $U = 500\,\mathrm{V}$. Right: The axial frequency ω_z (black), the magnetron frequency ω_- (green), and the cyclotron frequency ω_+ (orange) of Mg^+ ions in a magnetic field $B = 4\,\mathrm{T}$.

compensates the external forces such that a particle within the cloud is in free flow. This can be used to deduce the precise form of the potential ϕ_{sc}:

$$\phi^{\mathrm{eff}}_{\mathrm{plasma}} = \phi_{\mathrm{trap}} + \phi_{sc} + \frac{mr^2}{2q}\omega_r(\omega_c - \omega_r) \overset{!}{=} 0. \tag{4.11}$$

Applying the Laplace operator $\triangle$ to both sides of equation (4.11) and using $\triangle\phi_{\mathrm{trap}} = 0$ as well as $\triangle\phi_{sc} = -\rho(r,z)/\epsilon_0 = -qn(r,z)/\epsilon_0$, one finds an expression for the density $n(r,z)$:

$$n(r,z) = n_0 = \frac{2m\epsilon_0}{q^2}\omega_r(\omega_c - \omega_r). \tag{4.12}$$

This important result shows that the plasma density in the zero-temperature limit is a function solely of the plasma rotation frequency ω_r. Its value is fixed by the potentials created by the plasma rotation and by the requirement that in thermal equilibrium these potentials are compensated by the space-charge potential ϕ_{sc}. As a consequence, control of the plasma rotation frequency, for example with the rotating wall technique [119, 138, 139], allows to determine the plasma density within the limits $n_{\mathrm{min}} \leq n \leq n_{\mathrm{max}}$. The dependence of the rotation frequency on the density according to equation (4.12) is depicted in figure 4.3 together with the radial frequencies $\omega_\pm$, which are a function of the trapping voltage and define the limits of the rotation frequency ω_r.

According to equation (4.12), the maximum density only depends on the particle mass m and the magnetic field B. The maximum density is reached for a rotation frequency of $\omega_r = \omega_c/2 = qB/2m$ at the so-called Brillouin limit [140]

$$n_{\mathrm{max}} = \frac{\epsilon_0 B^2}{2m}, \tag{4.13}$$

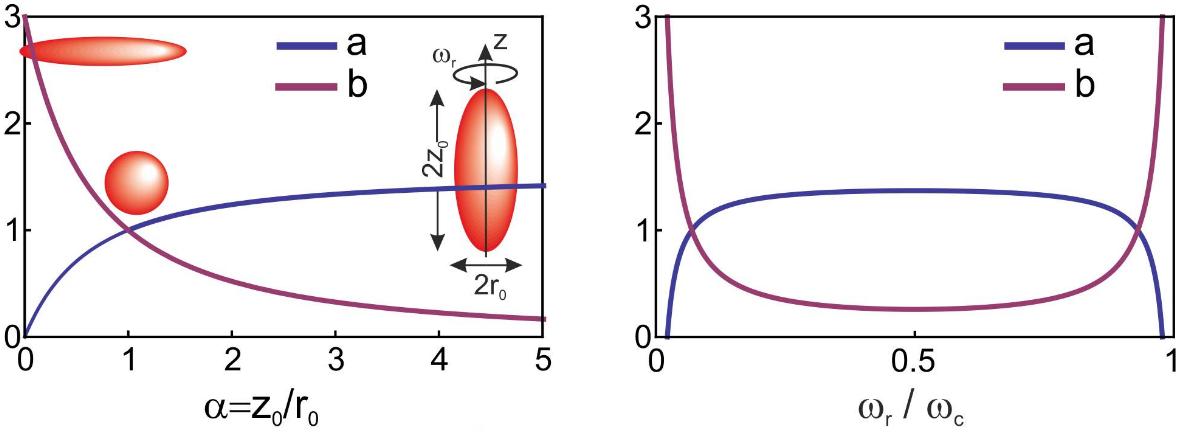

Figure 4.4: Left: The parameters a and b, as defined in equation (4.15), given as a function of the aspect ratio α. Three ellipsoids of rotation illustrate ion clouds with aspect ratios $\alpha < 1$, $\alpha = 1$, and $\alpha > 1$. Right: The parameters a and b as a function of the rotation frequency ω_r for typical trapping conditions ($U = 240\,\mathrm{V}$, $B = 4\,\mathrm{T}$, $m = 24\,\mathrm{u}$).

where ϵ_0 denotes the electric constant. Returning to equation (4.11) and inserting ϕ_{trap}, the explicit form of the space-charge potential reads:

$$\phi_{sc}(r,z) = -\left(\frac{mr^2}{2q}\omega_r(\omega_c - \omega_r) + \frac{U_0 C_2}{4d^2}(2z^2 - r^2)\right) \tag{4.14}$$

$$\equiv -\frac{qn_0}{6\epsilon_0}\left(a(\alpha)r^2 + b(\alpha)z^2\right). \tag{4.15}$$

By rewriting equation (4.14) in the form of equation (4.15) the parameters $a(\alpha)$ and $b(\alpha)$ have been defined. Equation (4.15) reflects the axial symmetry of both the external fields and the ion cloud shape, which is in axial-symmetric potentials an ellipsoid of rotation. In equation (4.15) the ion-cloud aspect ratio $\alpha = \mathrm{z}_0/\mathrm{r}_0$, defined as the ratio of the axial to the radial cloud extension, has also been introduced. The precise values of a and b are given as a (complicated) function of the aspect ratio [135]. The essential dependence is depicted in figure 4.4: For a spherical cloud $\alpha = 1$ and $a = b = 1$, for $a > 1 > b$ the cloud shape is a prolate ellipsoid with $z_0 > r_0$, and for $a < 1 < b$ the cloud is an oblate ellipsoid with $r_0 > z_0$. At the Brillouin limit $\omega_r = \omega_c/2$ the aspect ratio attains its maximum value that depends on the magnetic field B and the trapping potential U (Fig. 4.5).

Poisson's law, $\triangle\phi = -\rho/\epsilon_0$, requires [135]:

$$2a + b = 3. \tag{4.16}$$

Comparing (4.14) and (4.15), one finds two further expressions for the density n_0:

$$n_0 = \frac{6\epsilon_0}{qb(\alpha)}\frac{U_0 C_2}{2d^2}, \tag{4.17}$$

$$n_0 = \frac{6\epsilon_0}{qa(\alpha)}\left(\frac{m}{2q}\omega_r(\omega_c - \omega_r) - \frac{U_0 C_2}{4d^2}\right). \tag{4.18}$$

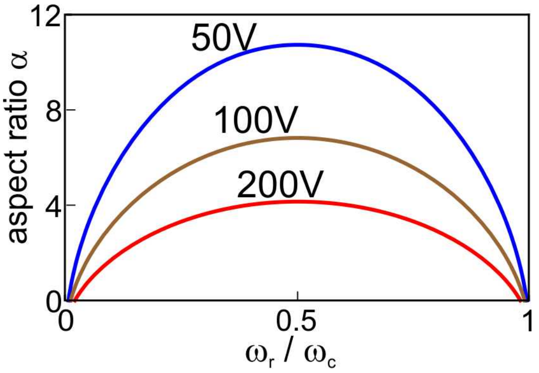

Figure 4.5: The aspect ratio α as a function of the rotation frequency ω_r for Mg^+ in a magnetic field $B = 4\,\mathrm{T}$ for different trapping voltages U. At the Brillouin limit $\omega_r = \omega_c/2$, the aspect ratio attains its maximum value.

On the axis of symmetry with $r = 0$ the space-charge potential is exclusively defined by the trap potential (Eq. (4.17)) and the expression for the density n_0 becomes independent of the rotation frequency ω_r. As the parameter b is a function of the aspect ratio α, the density n_0 can be determined by imaging the plasma and determining its aspect ratio.

In literature, the density is often expressed in terms of the plasma frequency ω_p [135],

$$\omega_p^2 = \frac{q^2 n_0}{\epsilon_0 m} = 2\omega_r(\omega_c - \omega_r), \tag{4.19}$$

$$b = \frac{3\omega_z^2}{2\omega_r(\omega_c - \omega_r)} = \frac{3\omega_z^2}{\omega_p^2}, \tag{4.20}$$

for which equations (2.10), (4.10), and (4.17) have been used.

The existence of a minimum plasma density $n_{\min}$ can be concluded from equation (4.17) with $b \leq 3$, as well as from equation (4.12) with $\omega_- \leq \omega_r \leq \omega_+$. Of course, both expressions for $n_{\min}$ give the same result, as $b \to 3$ for $\omega_r \to \omega_\pm$:

$$n_{\min} = \frac{2\epsilon_0}{q}\frac{U_0 C_2}{2d^2}, \tag{4.21}$$

$$n_{\min} = \frac{2m\epsilon_0}{q^2}\omega_\pm(\omega_c - \omega_\pm). \tag{4.22}$$

In the limit $\alpha \to 0$ and $n \to n_{\min}$ the description of the ion cloud as a cold plasma fails, as the ion cloud becomes an infinitely thin disk with $z_0 \leq \lambda_{\mathrm{Debye}}$ and the space-charge is not sufficient to balance the electrostatic trap potential. In this case the interior of the ion cloud is no longer shielded from the external fields and the cloud must be described regarding the individual particles.

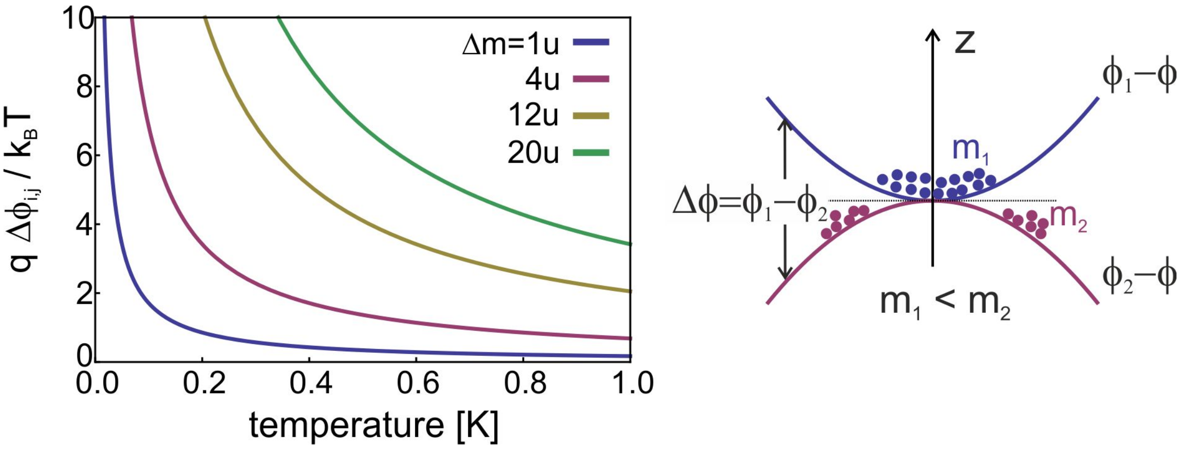

Figure 4.6: Left: The ratio $\Delta\phi/k_BT$ of the centrifugal potential and the thermal energy for an ion cloud with radius $a = 0.5\,\text{mm}$. Centrifugal separation becomes more pronounced for $\Delta\phi/k_BT \gg 1$. Right: Visualization of the different centrifugal potentials for ions with the masses m_1 and m_2. For the illustration, the fictional potential ϕ of an intermediate mass $m=(m_1+m_2)/2$ was subtracted from each potential $\phi_{1,2}$.

Centrifugal potential and centrifugal separation

For a multi-species plasma, the rotation tends to produce centrifugal separation of the plasma into its components. As long as the plasma is not yet in thermal equilibrium, the different species with masses m_i, m_j and charges q_i, q_j will rotate with different frequencies $\omega_{i,j}$. Because of the different rotation frequencies, collisions between the two species will cause a transfer of momentum. As a consequence, an inward radial flux of one species and an outward radial flux of the other species is created [141].

The plasma evolves, until it comes to a state of thermal equilibrium, which is characterized by rigid-body rotation [137]. The degree of separation depends on the plasma temperature and the difference of the species' mass-to-charge ratios. If the separation is complete, the species are arranged in separate concentric rings with the lighter ion, i.e. the ion with smaller ratio m_i/q_i, in the center of the trap. Complete separation has been observed for a multi-species cloud consisting of beryllium and mercury ions, for which the Hg^+ temperatures ranged from 0.4 to 1.8 K and Be^+ temperatures from less than 0.05 to 0.2 K [142].

In the case of rigid-body rotation, both species rotate with the same frequency ω_r but experience a different centrifugal potential due to their different masses. The difference in the effective potential, as given by equation (4.8), is:

$$\Delta\phi_{i,j} = \left(\frac{m_i}{q_i} - \frac{m_j}{q_j}\right)\left(\frac{\omega_r^2 r^2}{2}\right). \tag{4.23}$$

Centrifugal separation is a weak effect, if the energy difference $q_{i,j} \cdot \Delta\phi_{i,j}$ due to the centrifugal potential is much less than the thermal energy k_BT [141]. In the case of a plasma with radius R, and two ion species of the same charge $q = q_i = q_j$, this ratio becomes:

$$\frac{q \cdot \Delta\phi_{i,j}}{k_B T} = \frac{\left(m_i - m_j\right) \omega_r^2 R^2}{k_B T}. \tag{4.24}$$

For a cloud of radius $R = 0.5\,\mathrm{mm}$ this ratio is shown for various mass differences in figure 4.6.

4.2 The planar-shell model

In this work, ion crystals with particle numbers ranging from $N \approx 10^3$ to $N \approx 10^5$ have been prepared by combined buffer-gas- and laser cooling. The imaging system attached to one of the radial viewports was used to image the crystal structure and the temporal evolution of the ion cloud. To describe the structure of the imaged crystals, the planar-shell model will be presented according to the discussion in references [84, 113, 143], followed by a discussion of the experimental results. The planar-shell model applies for the case of a spheroidal plasma with a radius sufficiently large such that the shell curvature can be neglected, which is the case for the ion clouds presented here with aspect ratios typically less than $\alpha < 1/10$.

Within the frame of the planar-shell model, the plasma is described as a series of S planes at axial positions z_i with area number density σ_i. Minimizing the energy per ion implies that the area charge density $q\sigma_i$ of each lattice plane is identical and that the lattice planes are spaced at a uniform separation D (p. 138 in [84]). The total area number density is

$$\sigma = \sum_{i=1}^{S} \sigma_i \tag{4.25}$$

and the spacing D is linked to σ and S via the mean volume density n:

$$D = \frac{\sigma}{nS}. \tag{4.26}$$

The total energy per particle is given by the sum of the self-energy of the set of S planes, the energy due to the external potential, and the correlation energy within each 2-D lattice plane. No correlations between different shells, regarding the 2-D lattice of each shell, are taken into account. The energy per particle then reads

$$\frac{E}{N} = \pi e^2 \left[L\sigma - \frac{1}{6}\frac{\sigma^2}{n} \right] + \frac{U_{\mathrm{corr}}}{N}, \tag{4.27}$$

where $2L$ is the axial extension of the crystal and N the particle number. The term U_{corr} denotes the extra correlation energy of the shell model compared to the energy

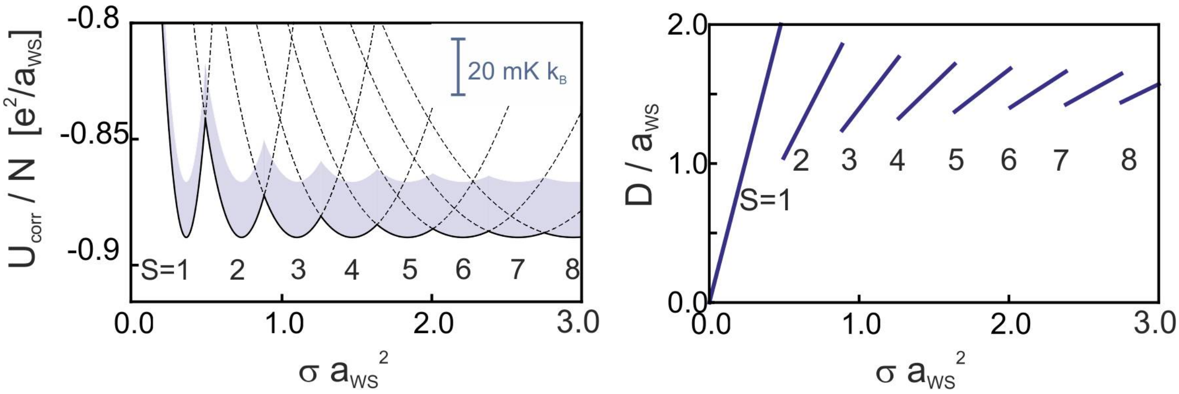

Figure 4.7: Left: Correlation energy per particle U_{corr}/N (see Eq. (4.28)) as a function of the parameter $\bar{\sigma} = \sigma a_{\text{WS}}$. The energy is given for shell numbers $S = 1$ to $S = 8$, the gray area depicts for a typical value of $a_{\text{WS}} = 20\,\mu$m the energy range of $E = 20\,$mK k_B. Right: The shell spacing D, for which U_{corr} has a minimum as a function of $\bar{\sigma}$.

per particle of a uniform slab of density σ. This correlation energy U_{corr} is given by [84]:

$$\frac{U_{\text{corr}}}{N} = \frac{e^2}{a_{\text{WS}}} \left[\frac{2\pi^2}{9} \left(\frac{\bar{\sigma}^2}{S} \right) - \frac{\eta}{2} \left(\frac{\bar{\sigma}}{S} \right)^{1/2} \right]. \tag{4.28}$$

The parameter η reflects the Madelung energy of the 2-D lattice. In the following, the value of $\eta = 3.921$ of a hexagonal lattice is used, which has the lowest Madelung energy of all 2-D lattices [84]. The parameter $\bar{\sigma}$ is the total particle number per unit area, $\bar{\sigma} = \sigma a_{\text{WS}}^2$.

The first term in (4.28) is positive, indicating that a system of S parallel planes has a higher energy than a uniform distribution. The second term, arising from correlations between particles within each plane, is negative and creates a tendency to form a finite set of ordered planes. The competition between these two terms determines the number of planes. The correlation energy U_{corr} as a function of the parameter $\bar{\sigma}$ is shown for different numbers of shells $S = 1$ to $S = 8$ in the left part of figure 4.7.

The energy per particle U_{corr}/N attains its minimum – with regard to the parameter S – for

$$S_{\min} = \left[16\pi^2/(9\eta) \right]^{2/3} \bar{\sigma}. \tag{4.29}$$

In this case, the distance D between two lattice planes becomes

$$\frac{D}{a_{\text{WS}}} = \left(\frac{3\eta^2}{4\pi} \right)^{1/3} = 1.54. \tag{4.30}$$

Of course, S must be an integer, so $S = S_{\min}$ can only be fulfilled for certain values of $\bar{\sigma}$ and the actual value of S will be an integer close to $S_{\min}$. Accordingly, the actual

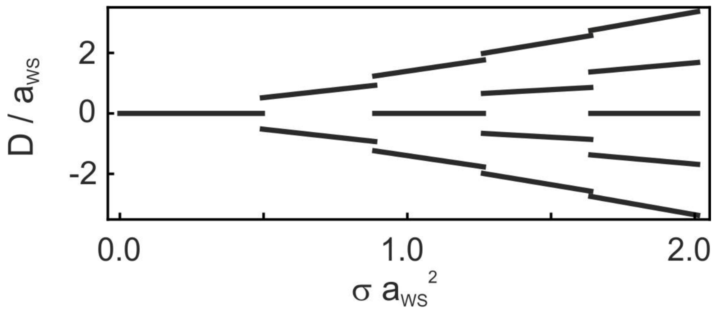

Figure 4.8: Visualization of the vertical cross section through a crystal described by the planer-shell model. The number of shells S and the inter-shell spacing D have been calculated as a function of the parameter $\bar{\sigma}$.

correlation energy per particle U_{corr}/N (thick line in left part of Fig. 4.7) does not always reach its global minimum. However, for larger charge densities $\bar{\sigma}$ the variation of the minimum correlation energy gets smaller, hence the actual correlation energy for large shell numbers S stays close to the minimal value. Depending on the value of the parameter $\bar{\sigma}$, the shell number S that gives the minimal correlation energy was chosen for calculating the normalized inter-shell distance D with equation (4.26) (Fig. 4.7, right). As in the case of the correlation energy, the variation of the shell spacing D declines for large shell number and approaches $D \approx 1.54\, a_{\mathrm{WS}}$. The actual number of shells and their positions z_i can be visualized as a function of the parameter $\bar{\sigma}$, resulting in a schematic axial cross section of an ion crystal with the given total particle number per unit area (Fig. 4.8).

4.3 Observation of single-species ion crystals

Ion clouds with crystalline structure have been observed after laser cooling of a few thousands of Mg^+ ions. Four false-color images of such a crystal and the corresponding cross sections are shown in figure 4.9. The ions were stored in a magnetic field of $B \approx 4.062(2)\,\mathrm{T}$ with a trapping voltage of $U = 50\,\mathrm{V}$. The cloud structure with parallel planar shells, seen sidewise, is clearly visible in both images and cross sections. The four images have been taken with a temporal separation of 100 seconds. The most apparent feature is that the number of ions and thus the number of lattice planes decreases with time. For each image, the contrast has been adjusted individually such that the shell structure is clearly visible. The actual intensity relations can be seen in the cross sections through the cloud center, which have been obtained by the projection of the averaged fluorescence signal in the central region (white, dashed lines in figure 4.9). Here, each shell appears as a small deviation from the averaged cloud profile.

The temporal evolution of the shell structure is shown in figure 4.10. The left part displays a false-color representation of the measured cross sections as indicated in figure 4.9. To increase the contrast in this representation, each cross section was

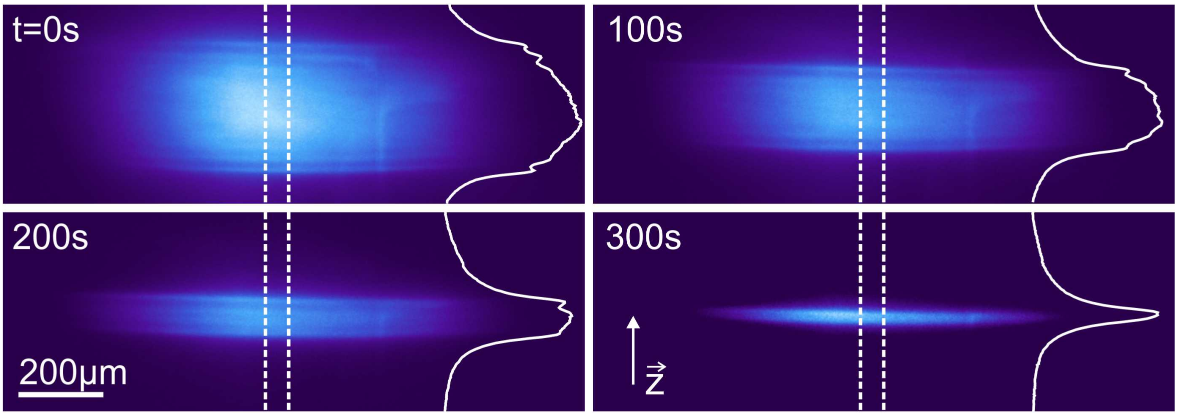

Figure 4.9: Four images of a Mg^+ ion crystal at different times. The trap's axis of symmetry is in vertical direction and the shell structure is visible in the images as well as in the cross sections through the central region (area within the dashed lines). With time, the number of ions and thus the number of shells decreases due to ion loss. At t=0, the images shows $3 \cdot 10^4$ ions that are irradiated by the laser beam. From the total (invisible) cloud volume, one can estimate the total ion number to be $N \approx 3 \cdot 10^5$.

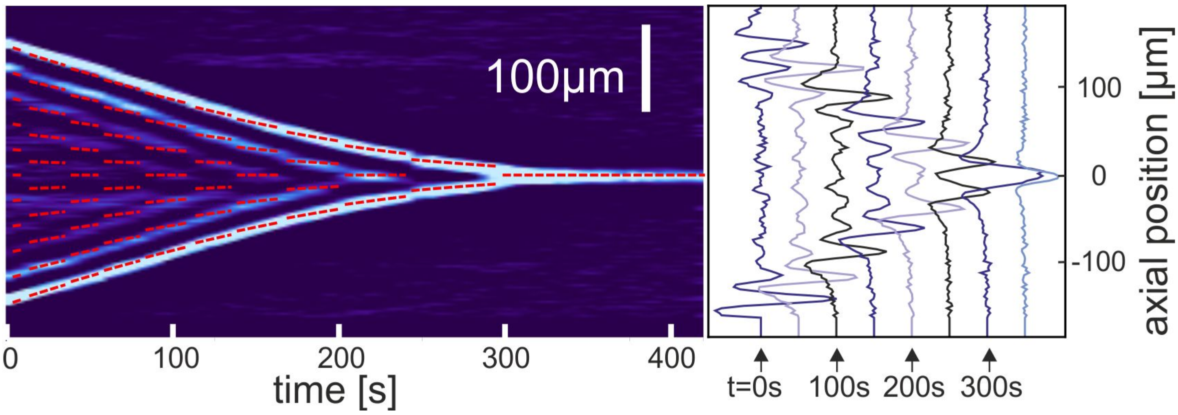

Figure 4.10: Left: Temporal evolution the ion crystal depicted in figure 4.9. The image shows a false-color representation of the residual cross sections as indicated in image 4.9. Right: The corresponding, residual cross sections. Up to eleven crystal shells can be seen.

divided by the averaged cloud profile. Some representatives of these residual cross sections are shown in the right part of figure 4.10. With increasing shell number, the contrast in the cloud center is reduced and for the largest cloud (leftmost cross section), the individual shells are hardly recognized. The total number of shells can, however, be determined by comparison with smaller clouds because the shell positions and shell distances are preserved.

The density of the cloud – and thus quantities like the ion number N, the rotation frequency ω_r and the aspect ratio α – is linked to the imaged shell distance by the projected area density σ and equation (4.26). Already a single image of the cloud and a measurement of the shell spacing D is sufficient to determine the density of the cloud with the estimate $D \approx (1.54 \pm 0.2)\, a_{\mathrm{WS}}$. As one can see in figure 4.7, the variation of the shell spacing D is smaller for larger shell numbers S.

An even more accurate value for the density can be obtained from a time-dependent measurement (Fig. 4.10). For each video frame, the normalized area density $\bar{\sigma}$ was calculated from the integrated fluorescence of a vertical cross section with a factor χ. This linear scaling factor χ was chosen constant for the complete video session. With this method, the area density was determined for each frame, and the vertical shell positions z_i therewith calculated according to equation (4.26). The choice of the scaling factor determines for each video frame the total shell number S and the shell spacing D. It was chosen such that best agreement between the model and the measurements was achieved. The calculated positions z_i of the crystal shells are shown by the red lines in figure 4.10. Besides the shell numbers S and the shell positions, also the times – respectively densities – where transitions from S to $(S+1)$ occur are predicted correctly.

The assumed proportionality between the fluorescence and the normalized area density $\bar{\sigma}$ may not be a priori evident, but was found to be valid for most of the measurements. Because the fluorescence per Mg^+ ion is constant, this can be expected if the number of observed Mg^+ ions is given by $N = \bar{\sigma} \cdot A$, where A is the base area – assumed to be constant – of the observed volume. Because $\bar{\sigma}$ expresses a charge density, to which also non-fluorescing ions may contribute, we have further to request that the contribution of Mg^+ to the total charge does not vary. The condition of a constant base area A will be met under most circumstances: Since the evaluated fluorescence is the integrated signal of a vertical cross section, it stems from a volume defined by $V = A \cdot \Delta z = \Delta x \cdot \Delta y \cdot \Delta z$. Here, Δx is the width of the cross section, whereas Δy and Δz are given by extent of the visible volume in the line of sight and the axial cloud extension, respectively. Δx does obviously not change, and the value of Δy along the line of sight is defined by the waist w_0 of the laser beam, as long as the waist w_0 is smaller than the ion cloud radius. This was usually the case, since most observed crystals had a small aspect ratio $\alpha \ll 1$.

For the Mg^+ cloud as shown in figures 4.9 and 4.10, the Wigner-Seitz radius was determined to $a_{\mathrm{WS}} = 19.1\,\mu\mathrm{m}$, what is equivalent to a density of $n = 3.4 \cdot 10^7\,\mathrm{cm}^{-3}$ (Eq. (4.2)) close to the minimum density of $n_{\mathrm{min}}(50\,V) = 3.2 \cdot 10^7 \mathrm{cm}^{-3}$. The corresponding rotation frequency and aspect ratio can be calculated to $\omega_r = 2\pi \cdot 12.2\,\mathrm{kHz}$ and $\alpha = 1/24.2$.

One can compare these results with the aspect ratio directly determined from the image at t=300 s, where a larger portion of the cloud is visible. From the curvature of the cloud a value of $\alpha \approx 1/20$ is estimated, which is in fair agreement with the value obtained from the measured Wigner-Seitz radius.

The total number of particles stored in the trap follows with $N = V \cdot n = 4/3 \pi z_0 r_0^2 \cdot n$, where z_0 and $r_0 = z_0/\alpha$ denote the axial and the radial cloud radius, respectively. For the time t=0 s one finds $z_0 = 150 \mu\mathrm{m}$ and thus $r_0 = 3.6\,\mathrm{mm}$, which gives a total particle number of $N \approx 3 \cdot 10^5$. Assuming that the visible volume is determined by the laser-beam with a waist of $w_0 = 1\,\mathrm{mm}$, only a fraction of $N_{\mathrm{vis}} \approx 3 \cdot 10^4$ Mg^+ ions is visible in the image.

The unscaled cross sections show that the fluorescence between the shells does not drop to zero intensity (Fig. 4.9). There are several mechanisms that reduce the contrast of the image and are possible explanations for this effect. For one thing, as the laser beam diameter is finite, the total charge per area is not necessarily constant along the line of sight, with the consequence of a varying shell spacing D in the imaged volume. This would especially reduce the contrast of the inner shells, where the dependence of the shell positions from the total charge per area is largest (Fig. 4.8). This is in agreement with the observed cross sections, where the outermost shells are always the best defined ones. Additional effects may be due to a small angle between the line of sight and the plane defined by the crystal shells or the finite resolution of the imaging system. The theoretical resolution is under the present conditions 3 μm, with a detector pixel size of 13 μm and a measured magnification factor of 4.69(8). The actual resolution is increased to about 10 μm by optical imperfections.

On the other side, it is also possible that the imaged fluorescence distribution reflects the actual density distribution of the ion cloud: For a plasma parameter $\Gamma_p > 10$ the radial density distribution of a fluid-like plasma is known to show oscillations, which are more pronounced at the plasma edge [113, 124]. A heuristic argument for this effect can also be found by looking at the correlation energy per particle (Fig. 4.7, left). For a given area density, there is an optimum configuration with S shells that results in the lowest energy per particle. The gray area marks the cloud configurations for which the energy per particle is increased by less than $k_B{\cdot}20\,\mathrm{mK}$ with regard to the optimum configurations. For large shell numbers, the energy difference between the configuration with S and $S+1$ shells is only of the order of a few $\mathrm{k}_B{\cdot}\mathrm{mK}$. By comparison of the charge distribution between the S and $(S+1)$ shell configuration (Fig. 4.8) one finds that the charge distribution differs predominantly for the innermost shells. Thus, for temperatures of the order of a few mK, the cloud interior is more diffuse while the plasma boundary formed by the outer shells remains more defined.

4.4 Multi-species ion crystals

Multi-species ion crystals were prepared by sympathetic cooling of singly charged ions after injection into a cloud of laser cooled magnesium ions. These ions were created from residual gas in the Mg^+ ion source. The selection of a specific ion species from the variety of created ions was achieved by adjustment of the capture gate for the trapping process. The amount of ions created in the source was controlled by the filament bias that determines the electron impact energy. Multi-species ion crystals composed of Mg^+ (m=24 u, 25 u, 26 u) and ion species with the masses m=2 u (H_2^+), 12 u (C^+), 28 u (N_2^+), and 44 u (CO_2^+) were investigated, so that a large range of charge-to-mass ratios was covered.

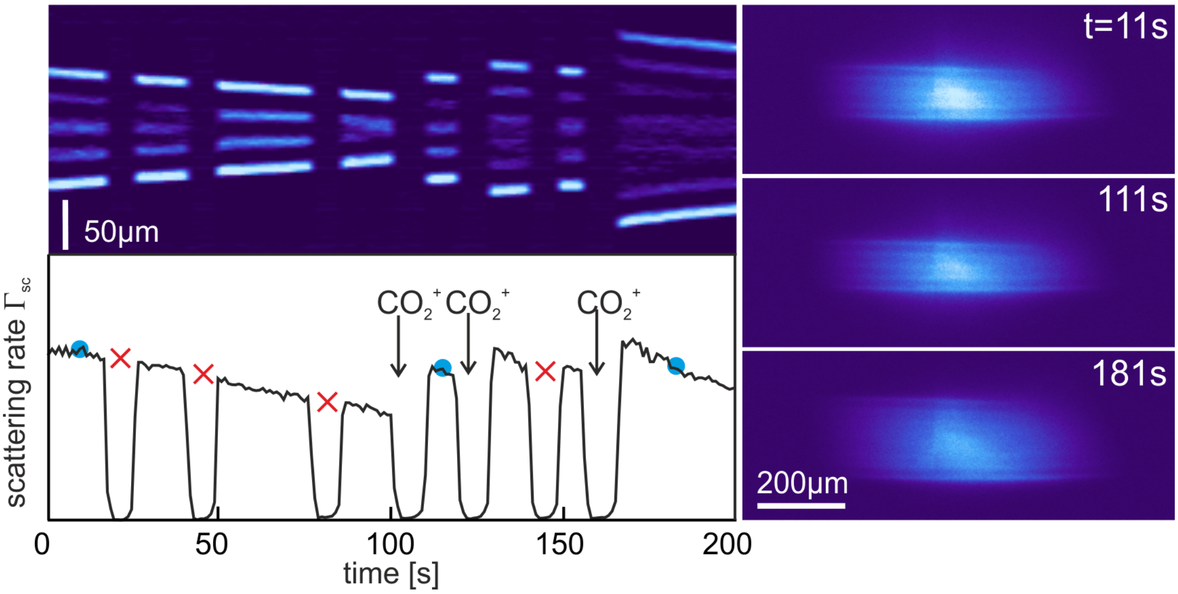

Figure 4.11: Fluorescence signal (bottom left) of a Mg^+ cloud during the consecutive injection of three bunches of CO_2^+ ions (m=44 u). Three cloud images (right) show exemplary the crystal structure at different times (blue dots in trace of the fluorescence signal). The temporal evolution of the cross sections for each video frame (top left) reveals the evolution of the crystal structure. Laser power $I = 2.7$ mW, laser detuning $\Delta = -2\pi \cdot 8$ MHz.

The characteristics of the mixed-ion crystals can be classified with regard to the mass-to-charge ratio of the sympathetically cooled species. After injection of CO_2^+ (m/q=44), the species with the largest mass-to-charge ratio under investigation, the axial extent of the ion cloud increased and – since the density remained unchanged – additional crystal shells were formed. Cloud images were taken before and after loading of CO_2^+ and the evolution of the fluorescence has been observed as well as the evolution of the crystal structures (Fig. 4.11). Dips in the fluorescence spectrum are produced by the switching of the capture electrode in the cause of the injection process. Red crosses mark those injection processes, for which the loading parameters (e.g. capture gate, capture electrode voltage, ion source grid voltage) were intentionally chosen such that no CO_2^+ was captured into the trap. The injection of CO_2^+ becomes apparent by an increase of both the fluorescence signal and the number of crystal shells.

Since the CO_2^+ ions are not fluorescing, it was not possible to determine their distribution with certainty. However, good reasons exist to assume that the CO_2^+ ions and the Mg^+ are radially separated. For one thing, upon loading CO_2^+ the fluorescence increases such that the detected fluorescence per shell remains approximately constant. This indicates that the number of Mg^+ in the observed volume increased, because the CO_2^+ ions accumulate at larger, unobservable radii and push the Mg^+ ions to the trap center and into the laser beam. For another thing, the clearly observable

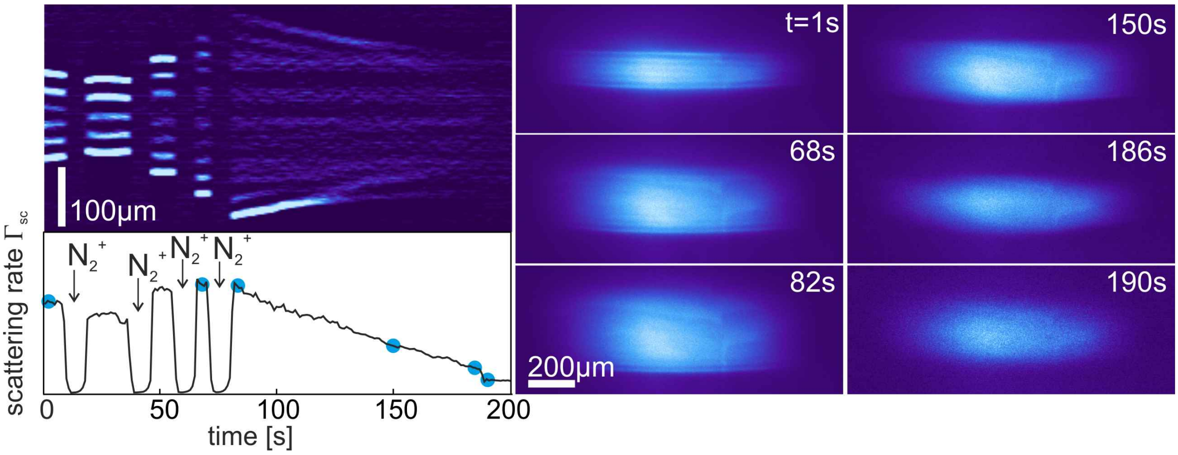

Figure 4.12: Fluorescence signal and cloud images before and after the injection of N_2^+ ions into a Mg^+ cloud. For a more detailed description, see the text and figure 4.11. Laser power $I = 2.7\,\text{mW}$, laser detuning $\Delta = -2\pi \cdot 8\,\text{MHz}$.

crystal structure suggests a plasma parameter $\Gamma_p > 20$ and accordingly a temperature considerably below 100 mK. At these temperatures Mg^+ and CO_2^+ ions should radially separate due to the different mass-to-charge ratio, as follows from the discussion in section 4.1.

After the injection of N_2^+ ions (m/q=28), similar effects like in the case of CO_2^+ were observed (Fig. 4.12). The slow decrease of the axial cloud extent, which can be seen for $t \leq 10\,\text{s}$, stops after the first injection of N_2^+. Thereafter, the cloud size increased upon further loading of N_2^+ (at $t = 45\,\text{s}$, $t = 65\,\text{s}$, and $t = 75\,\text{s}$) and the density, as determined from the shell distance, was constant before and after each injection of N_2^+. The fluorescence signal per shell was found to be approximately constant and the total fluorescence increased as additional shells were formed. The crystal structure of the two-species ion cloud was clearly observable. As in the case of CO_2^+, the increase of fluorescence directly after injection can be attributed to centrifugal separation of the two ion species. This is in accordance with theoretical expectations, since for temperatures sufficiently low for the observed crystallization the difference of the centrifugal potential for Mg^+ and N_2^+ is large enough for complete separation.

Figure 4.13 shows a typical injection process of C^+ (m/q=12) into a cloud of laser-cooled Mg^+ ions. The crystal structure was conserved after injection of C^+ and the axial cloud extension increased due to the formation of additional crystal shells. However, in contrast to the cases with N_2^+ and CO_2^+ described before, the injection of C^+ caused no increase of the total fluorescence (lower left of Fig. 4.13). Since the cloud extension increased nonetheless, this means that the fluorescence per shell was reduced, what can again be attributed to radial separation of the ion species. The lighter ions accumulate in the trap center whereas the Mg^+ ions are pushed to larger radii. Accordingly, the observed fluorescence stems from the Mg^+ ions surrounding the C^+ that are pushed out the central region and are irradiated by the less intense wings of the laser field distribution. Significant heating as an

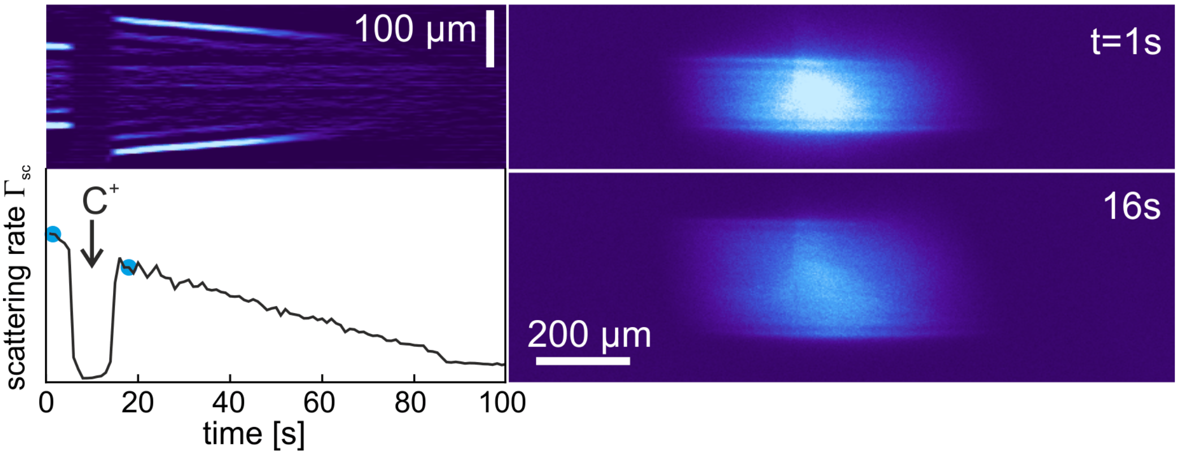

Figure 4.13: Fluorescence signal and cloud images before and after the injection of C^+ ions into a Mg^+ cloud. For a more detailed description, see the text and figure 4.11. Laser power $I = 3\,\mathrm{mW}$, laser detuning $\Delta = -2\pi \cdot 12\,\mathrm{MHz}$.

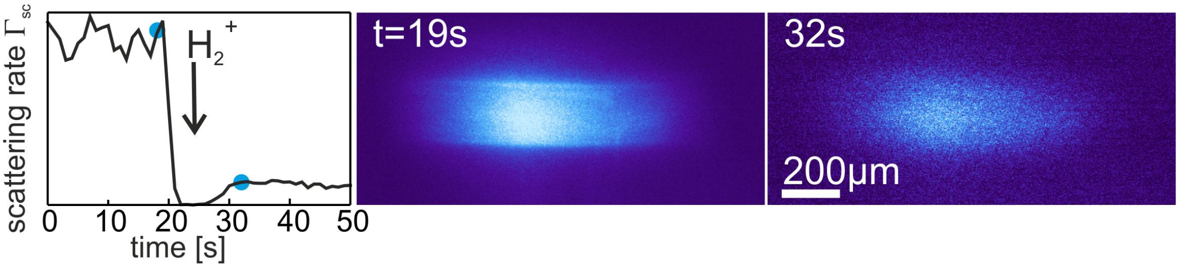

Figure 4.14: Fluorescence signal and cloud images before and after the injection of H_2^+ ions into a Mg^+ cloud. Laser power $I = 2.7\,\mathrm{mW}$, laser detuning $\Delta = -2\pi \cdot 8\,\mathrm{MHz}$.

explanation for the fluorescence reduction can be excluded, since the crystal shell structure is clearly preserved for the two-species ion cloud and consequently sets an upper limit to the ion cloud temperature.

After injection of H_2^+ (m/q=2) – the lightest ion species under investigation – a drastic loss of fluorescence per volume was observed (Fig. 4.14). Here, the fluorescence signal decreased to a small fraction of the initial value after the capture of a H_2^+, whereas the axial cloud extension remained constant. This indicates that no particles were lost in the capture process. In analogy to the discussion of the other ion species, this indicates a radial separation of H_2^+ and Mg^+ with the lighter hydrogen ions in the center of the trap. However, no crystalline shell structure was observed for the heterogeneous H_2^+-Mg^+ ion cloud. While it is in principle possible that the ion cloud was in a crystalline state and only the signal-to-noise ratio was insufficient to reveal the structure, this still means that in this case a fluorescence decrease due to heating of the ion cloud cannot be excluded. However, since the mass difference between Mg^+ and H_2^+ is the largest of all ion species under investigation, centrifugal separation in this case can be expected even for comparatively large temperatures of $T \approx 500\,\mathrm{mK}$.

Although there is evidence for centrifugal separation for each of the investigated ion species, some details of the formation process of the two-species crystals could not be resolved.

1) When an ion species lighter than Mg^+ accumulates in the trap center one would expect a central depression in the radial fluorescence distribution due to the displacement of the Mg^+ ions. In experiments where the complete cloud was imaged, such structures were reported [54]. For the results presented here, neither for H_2^+ nor for C^+ such an effect was observed. However, since the imaged area was not aligned to the trap center, these expectations may be misleading. The positions of the laser beam and the CCD camera were optimized with regard to the observable crystal structure. Therefore the observed volume is defined by the – possibly misaligned – lenses attached to the ring elements. Since the focal points of this lenses were not adjusted for the UV but with a He:Ne laser [41], the alignment of the focal point with the trap center along the line of sight is unsure. Furthermore, the magnet system was damaged during the transport to its current location at the GSI. As a consequence, the inner components of the magnet system, including the heat shields with the optical windows, are not fully aligned to each other and with respect to the trap center.

2) After injection of a second ion species, in some cases a rapid loss of fluorescence was observed. This becomes e.g. apparent after the injection of C^+ and N_2^+, when the fluorescence decreases with a higher rate than particles are lost from the trap (Fig. 4.12 and 4.13). After several tens of seconds, there is also an additional, abrupt loss of fluorescence (in Fig. 4.12 at $t \approx 188\,\mathrm{s}$ and in Fig. 4.13 at $t \approx 85\,\mathrm{s}$). Since the axial cloud extension before and after the loss of fluorescence is similar, this effect is not contributed to ion loss but rather to an unidentified heating mechanism. This heating occurred in this form only for two-species ion clouds. It is possibly caused by a torque applied to the Mg^+ ions by the C^+ and N_2^+ ions. Such an effect was reported by Larson et al. [142], who found that the introduction of sympathetically cooled Hg^+ to a cloud of laser cooled Be^+ introduced massive torque to the Be^+ ions, revealed by the decrease of the cloud aspect ratio.

The observed heating effects challenge the conclusion of centrifugal separation, because this conclusion partly relies on the assumption that the cloud temperatures are in a regime for which centrifugal separation is predicted by theory. However, the assumption of centrifugal separation and the observation of heating are not contradictory since the heating occurs on a longer time scale and does not affect the temperature directly after injection, as will be shown by the following analysis.

In order to give absolute numbers, the temperature at which the centrifugal potential $\Delta\phi$ is of the order of $5 \cdot k_B T$ is regarded as the maximum possible temperature for centrifugal separation to occur. For a cloud with radius 0.5 mm this temperature is $T_{\mathrm{crit}} = 140\,\mathrm{mK}$ for N_2^+, $T_{\mathrm{crit}} = 400\,\mathrm{mK}$ for C^+, and $T_{\mathrm{crit}} = 700\,\mathrm{mK}$ for CO_2^+, respectively. A cloud radius of 0.5 mm is assumed, because it is approximately the radial diameter of the imaged trap volume.

As long as the shell structure is preserved for the outermost shells, the plasma is under a very conservative estimate at least in a fluid-like state, which requires a plasma parameter of $\Gamma_p > 2$ and thus a temperature of $T < 400\,\mathrm{mK}$. Therefore, even slight signs of crystallization can be regarded as an indication for significant centrifugal separation in the case of C^+ and CO_2^+. The formation of crystal structures in the interior of the cloud requires an even lower temperature. From considerations of the energetic difference between different charge configurations of the cloud (see discussion p. 95) that temperature is estimated to be of the order of 10 mK. Thus, crystal shells apparent across the complete axial extent of the ion cloud are a strong indication for centrifugal separation for all ion species under investigation.

With these critical temperatures for centrifugal separation in mind, the characteristics of the ion clouds are reconsidered with regard to possible conclusions concerning the cloud temperature.

After the injection of CO_2^+ into a Mg^+ crystal, no heating was observed and the discussion of the fluorescence development in this case is unaffected (Fig. 4.11).

For N_2^+, the fluorescence and the axial cloud extent did not increase immediately after injection of N_2^+ (Fig. 4.12). However, the decreasing axial cloud extent during the first seconds $0 \leq t \leq 10\,\mathrm{s}$ is stabilized by the first injection of N_2^+ and after a second N_2^+ injection at $t \approx 50\,\mathrm{s}$, a significant increase of fluorescence occurred. After this second N_2^+ injection, the crystal structure still extends into the interior of the cloud, so that a cloud temperature of the order of $T \approx 10\,\mathrm{mK}$ can be expected. This temperature is well below the critical temperature for centrifugal separation $T_{\mathrm{crit}} = 140\,\mathrm{mK}$ and one can accordingly expect that the increase of fluorescence is caused by centrifugal separation. Furthermore, to receive a high fluorescence rate the images shown in this chapter were recorded with a laser detuning of $\Delta \approx -2\pi \cdot 10\,\mathrm{MHz}$. For such a small detuning the fluorescence rate is a monotonically decreasing function of temperature. Therefore, even if one assumes that the cloud temperature had slightly increased after the injection of N_2^+ at $t \approx 50\,\mathrm{s}$, this hypothetical heating could not account for the increase of fluorescence. This further supports the assumption of centrifugal separation. These conclusions remain valid until the last injection of N_2 at $t \approx 75\,\mathrm{s}$. For $t \geq 75\,\mathrm{s}$, the fluorescence decreases due to heating effects and the shell structure dissolves in the inner regions of the cloud.

The heating appears to be stronger after injection of C^+ ions (Fig. 4.13), where directly after the injection only the two outermost shells are clearly distinguishable. The fluorescence signal per shell drops within 50 seconds to half of the initial value, which corresponds to a temperature of 700 mK for the actual laser detuning of $\Delta = -2\pi \cdot 12\,\mathrm{MHz}$. Thus, in spite of the observed heating, one can conclude that the temperature is for several tens of seconds after injection below the critical temperature $T_{\mathrm{crit}} = 400\,\mathrm{mK}$ for centrifugal separation.

For further studies, a dedicated temperature measurement with a second probe beam in addition to the laser cooling beam would yield the information to fully resolve the remaining uncertainties. Molecular dynamics (MD) simulations of the ion cloud appearance at finite temperature, as have been performed for small ion

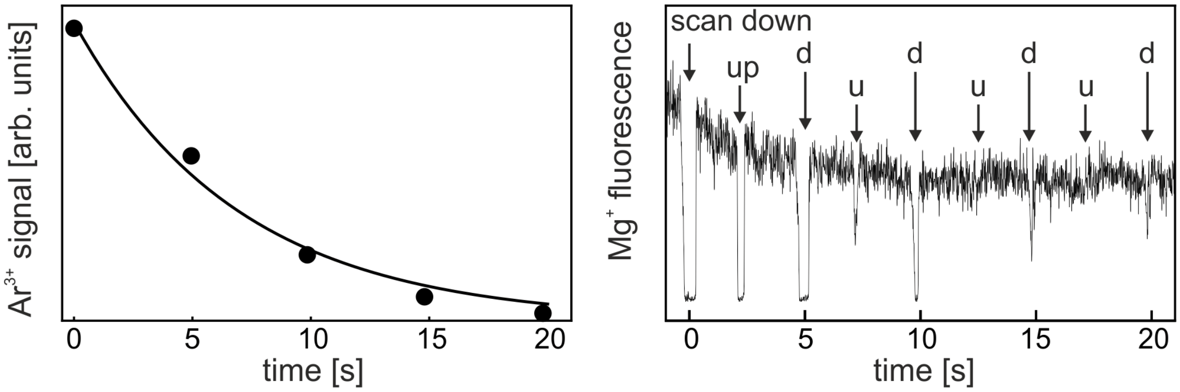

Figure 4.15: Left: Storage time of sympathetically cooled Ar^{3+}. An exponential decay fitted to the data yields a decay constant of 7 seconds. Right: Mg^{+} fluorescence signal recorded while scanning the frequency of an applied RF signal for excitation of the Ar^{3+} ions.

clouds in a linear Paul trap [144], would represent a useful means to estimate the temperature of the ion cloud from a single image.

4.5 Sympathetic cooling and storage time of multiply charged ions

Multiply-charged argon ions were injected into a laser-cooled cloud of Mg^{+} ions, where the argon ions were cooled with a combined approach of buffer gas cooling by neutral He and sympathetic cooling by Mg^{+}. In the course of the cooling, the storage time of the multiply charged ions increased by several orders of magnitude as the kinetic energy was reduced from several hundreds of eV to the μeV (i.e. millikelvin) regime (Fig. 4.16 and corresponding discussion). Therefore, detection of sympathetically cooled Ar^{3+} was possible for up to 20 seconds with a storage time of several seconds. For the detection of Ar^{3+}, a radio-frequency (RF) signal was applied to one trap electrode to excite the cyclotron motion of the ions. Every time the radio frequency was able to excite the Ar^{3+}, dips were produced in the Mg^{+} fluorescence signal (Fig. 4.15). The integrals of the fluorescence signal reduction following each RF excitation were used as a measure for the Ar^{3+} number. Since the Ar^{3+} signal strength alternates with the direction of the RF scan, every second signal was neglected and only the stronger signals caused by downward RF scans were used in the evaluation. An exponential decay fitted to the data yields a decay constant of 7 seconds. This rather long lifetime is evidence for sympathetic cooling of the Ar^{3+} ions, since the lifetime of highly and multiply charged ions strongly depends on the temperature of the ions, as will be explained in the following discussion.

The storage time of ions in a Penning trap is limited by the ion loss rate from the trap. For highly charged ions, the predominant loss mechanism is charge transfer in residual gas collisions, which changes the ion charge state. For a singly charged ion the most significant loss mechanism is magnetron heating, where collisions with

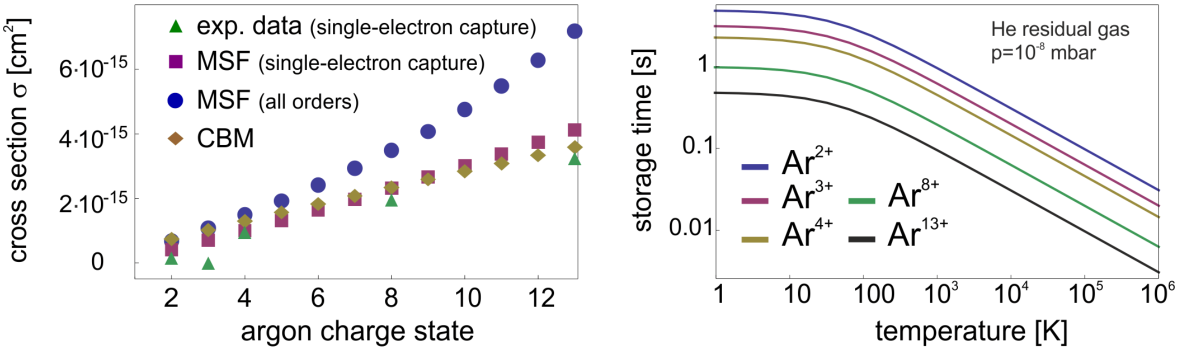

Figure 4.16: Left: Charge-transfer cross sections for argon ions according to the Müller-Salzborn formula (MSF) and the classical over-the-barrier model (CBM) [145]. Right: Storage times for argon ions with cross sections calculated according to the Müller-Salzborn formula (4.34).

residual gas increase the ion's magnetron radius until the ion hits the ring electrode and the ions are lost from the trap.

A collision between an ion of charge state q and a neutral residual gas atom or molecule can result in charge transfer between the neutral particle and the ion via the decay process

$$X^{q+} + ke^- \rightarrow X^{(q-k)+}. \tag{4.31}$$

In principal, k can assume any integer value, but usually the single-electron transfer with $k = 1$ is dominant, because the cross section for single-electron transfer is the highest and multi-electron transfer is statistically suppressed.

	σ_{exp} [cm^2]	$\sigma_{\text{MSF(single)}}$ [cm^2]	$\sigma_{\text{MSF(all orders)}}$ [cm^2]	σ_{CBM} [cm^2]
Ar^{2+}	$2 \cdot 10^{-16}$	$4.7 \cdot 10^{-16}$	$7.2 \cdot 10^{-16}$	$7.9 \cdot 10^{-16}$
Ar^{3+}	$5 \cdot 10^{-17}$	$7.5 \cdot 10^{-16}$	$1.1 \cdot 10^{-15}$	$1.1 \cdot 10^{-15}$
Ar^{4+}	$1 \cdot 10^{-15}$	$1.1 \cdot 10^{-15}$	$1.5 \cdot 10^{-15}$	$1.3 \cdot 10^{-15}$
Ar^{8+}	$2 \cdot 10^{-15}$	$2.4 \cdot 10^{-15}$	$3.5 \cdot 10^{-15}$	$2.4 \cdot 10^{-15}$
Ar^{13+}	$3.28 \cdot 10^{-15}$	$4.2 \cdot 10^{-15}$	$7.2 \cdot 10^{-15}$	$3.6 \cdot 10^{-15}$

Table 4.1: Experimentally and theoretically determined cross sections for electron transfers from residual helium gas to argon ions. Experimental values were determined for low kinetic energies ($E/q = 100-500$ eV) [146, 147], theoretical values are given by the Müller-Salzborn formula (MSF) and the classical over-the-barrier model (CBM) [145]. The cross sections according to the MSF are given separately for single-electron transfers and for electron transfers to all orders.

The decay time can be calculated from the total cross section and the collision rate, given by the product of neutral-gas density and the relative velocity v_{rel} of the two colliding particles

$$t = \frac{1}{\sigma n v_{\mathrm{rel}}} = \frac{k_B T_r}{\sigma p} \left(\frac{3 k_B T_i}{m_i} + \frac{3 k_B T_r}{m_r} \right)^{-1/2}, \tag{4.32}$$

where σ is the cross section for any charge-transfer process, m_i, m_r, T_i, T_r are the masses and temperatures of the ion and the residual-gas atoms, and p is the partial pressure of the residual gas. Several models exist to calculate the cross sections for single electron capture. In the frame of the classical over-the-barrier model (CBM), the cross section is expressed as

$$\sigma = \frac{1}{2} \pi R_C^2, \text{ where } R_C = \frac{27.2 a_0 (2\sqrt{q}+1)}{I}. \tag{4.33}$$

Here, a_0 denotes the Bohr radius, I the neutral gas ionization potential in electron-volt, and q is the charge state of the ion.

For highly charged ions with kinetic energies in the keV-regime, Müller and Salzborn have fitted a semi-empirical function to the data. According to [145], the cross section for electron capture can be calculated to

$$\begin{aligned} \sigma[\mathrm{cm}^2] = {} & 1.43 \cdot 10^{-12} \cdot q^{1.17} I^{-2.76} + 1.08 \cdot 10^{-12} \cdot q^{0.71} I^{-2.80} \\ & + 5.50 \cdot 10^{-14} \cdot q^{2.10} I^{-2.89} + 3.57 \cdot 10^{-16} \cdot q^{4.20} I^{-3.03} + \ldots \end{aligned} \tag{4.34}$$

where q is the ion charge state and I is the ionization potential of the residual gas given in eV. The first term in equation (4.34) describes the cross section for single-electron transfer, the second term for double-electron transfer, and so on.

Cross sections for argon and other rare gases have been measured by Justiniano [146] and Mann [147] and are listed for selected charge states in table 4.1. These experimental values are in good agreement with both the cross sections calculated according to the Müller-Salzborn formula and the classical over-the-barrier model (Fig. 4.16). For the present vacuum conditions in the SpecTrap Penning trap with a partial helium-gas pressure of 10^{-8} mbar, the Müller-Salzborn formula has been used to calculate the lifetimes of argon ions in dependence of the temperature (Fig. 4.16, right). The measured lifetime of 7 seconds for Ar^{3+} is in fair agreement with the values obtained with the Müller-Salzborn formula ($t_{\mathrm{MSF}} \approx 3$ s for T=1 K and $p_{\mathrm{He}} = 10^{-8}$ mbar), if the temperature of the Ar^{3+} is in the kelvin-regime or below. This confirms that the Ar^{3+} ions were sympathetically cooled by the Mg^{+} ions, since the lifetime without cooling would amount to a few milliseconds at temperatures of 10^6 K (corresponding to kinetic energies at ion injection of 100 eV).

An anomaly appears in [146] for the measured cross sections of argon, where the charge state Ar^{3+} has a cross section that is a factor of 20 lower than the one of Ar^{4+} and is even considerably lower than the cross section of Ar^{2+}. In [146], no explanation is given for this anomaly that does not appear in this form for other rare gases, but it offers an explanation as to why the attempts to measure the storage time of Ar^{4+} were not successful: Despite a significantly higher production rate in the EBIS of the low-energy beamline, it was not possible to detect any Ar^{4+} after a few seconds of buffer gas cooling. Scaling the measured lifetime of 7 s for Ar^{3+} gives an Ar^{4+} lifetime of 0.35 s which is too short for observing Ar^{4+} in SpecTrap. The anomaly for the Ar^{3+} cross section is not explained by the theoretical models, because they yield electron-transfer cross sections that show a much weaker dependence on the charge state.

5 Resonant-circuit measurements and a model for resistive cooling

In the first part of this chapter, the electronic detection of various ion species with the resonant circuit will be discussed with regard to the capability of the resonant circuits for ion detection and resistive cooling.

In the second part, a simple model for resistive cooling will be presented that accounts for the specific properties of ion clouds. The model allows both qualitative and quantitative predictions that are in agreement with the numerical simulation of the cooling process presented in [51]. In comparison with the numerical simulations, the presented model allows for a simple yet powerful description and facilitates the understanding of resistive cooling and its underlying dynamics.

5.1 Electronic ion detection with the resonant circuit

Signals of the resonant circuits have been recorded with either a fixed trapping voltage or a voltage sweep applied to the endcap electrodes.

In the voltage scanning mode, a spectrum of the ion species present in the trap is recorded, because each species induces a signal at an endcap voltage that is characteristic for the respective charge-to-mass ratio. The characteristic voltages for some selected ion species are given for the lower and upper resonant circuit in the Appendix (table A.10). The resolution of these spectra is limited by the quality factor Q of the resonant circuit. The corresponding resonance width is 4 kHz and 2 kHz for the circuits attached to the upper and lower endcap electrode with resonant frequencies of 1139 kHz and 536 kHz, respectively (Tab. 2.6). For this reason, the spectrum analyzer recording the signal was set to a bandwidth similar to the one of the resonant circuits. In this way, an optimum trade-off between signal strength and resolution was achieved.

To sweep the endcap voltages, the power supply for the electrode voltages was used with an external reference voltage instead of an internal one. The external reference voltage was directly controlled by the central experiment control software. This way, it was possible to run measurements with arbitrarily programmed voltage sweeps. The electronic stabilization of the power supply was fast enough to follow the external reference for a voltage scan rate of up to 100 V/s. The actual output voltage – attenuated by a factor of 100 – was recorded simultaneously to the resonant circuit signal by the analog input channels of the experimental control. The bandwidth of the voltage divider used for attenuation was large enough to introduce no measurable delay to the measured voltage sweep.

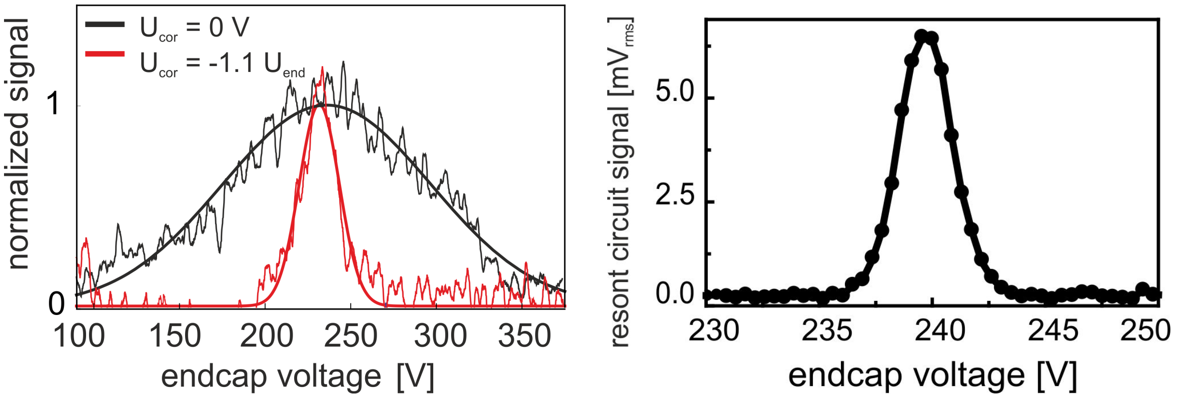

Figure 5.1: Left: The resonant-circuit signal of Mg^+ with and without use of the correction electrode. When the correction electrode is set to $U_{\mathrm{cor}} = -1.1\, U_{\mathrm{end}}$, the coefficient C_4 is almost tuned to zero and the width of the resonance is significantly reduced. Right: The resonant circuit signal of Mg^+ recorded with swept endcap voltage after the excitation of the axial center-of-mass mode with a 535 kHz RF signal. The correction electrode was set to $U_{\mathrm{cor}} = -1.63 \cdot U_{\mathrm{end}}$. The spectrum shows a narrow resonance at U=239.7(10) V. The line is to guide the eye.

Mass spectra have been recorded with the lower resonant circuit directly after the injection of a Mg^+ bunch (Fig. 5.1, left). For different correction electrode voltages U_{cor}, the Mg^+ signal occurs for voltages of 232 V and 236 V, which is in fair agreement with the calculated value of $U \approx 239.5\,\mathrm{V}$ (table A.10).

The small shift of the resonance voltage to a lower value can be explained by the energy and radial dependence of the axial oscillation frequency (Fig. 5.2). For $U_{\mathrm{cor}} = -1.1 \cdot U_{\mathrm{end}}$ (red) the coefficient C_4 is almost zero for small amplitudes and ω_z gets independent of the energy to first order[1]. This is, however, only true for a radius $r \approx 0$. For finite radii r is $C_4 \neq 0$ and the frequency ω_z increases for kinetic energies in the range $0 - 50\, q{\cdot}\mathrm{V}$. This implies that for ions with large oscillation amplitudes a lower voltage than given in table A.10 is needed to match the oscillation frequency to the resonant circuit. The same is true in the case of $U_{\mathrm{cor}} = 0$ (black), where for low energies $E < 50\,\mathrm{qV}$ the increase of the oscillation frequency ω_z is mainly due to the dependence on the radius r. A detailed discussion of the energy and radial dependence of the axial frequency ω_z is given in section 5.3.6, where the frequency shifts are expressed in terms of the coefficients C_4 and C_6.

These examples for resonant-circuit spectra directly recorded after the ion injection show very broad resonances and the identification of specific ion species was only possible, if the number of potential candidates of choice was very limited. On the other hand, high-resolution spectra could be recorded after the deliberate excitation of the axial motion of a cold ion cloud with a 535 kHz RF signal (Fig. 5.1,

---

[1] The correct tuning ratio for $C_4 \approx 0$ was determined to be $U_{\mathrm{cor}} = -0.86 \cdot U_{\mathrm{end}}$. Since this was not known at the time of this measurement a tuning ratio of -1.1 was used, which still reduces C_4 by a factor of three. See also discussion in section 2.3.6.

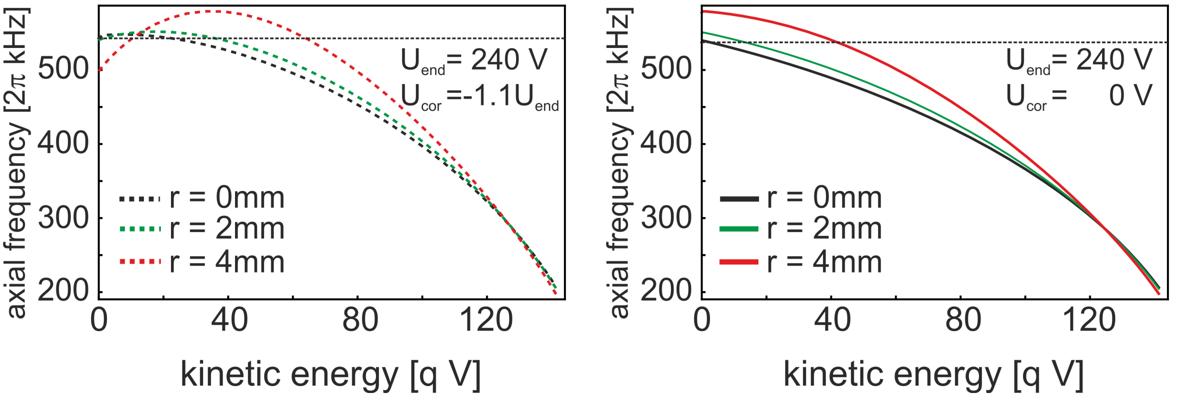

Figure 5.2: Axial oscillation frequency ω_z of a $^{24}Mg^+$ ion as a function of the kinetic energy for an endcap voltage of 240 V. The frequencies were calculated by integration of the equation of motion of Mg^+ in the full potential, because the expansion of the potential in coefficients C_n fails for high oscillation amplitudes. The dashed horizontal line depicts the resonance frequency of the lower axial resonator. Left: Correction-electrode voltage $U_{cor} = -1.1 \cdot U_{end}$ to tune the coefficient to $C_4 \approx 0$. Right: $U_{cor} = 0$ V.

right). The excitation frequency of 535 kHz was chosen to match the resonance of the lower resonant circuit. This way a higher excitation amplitude was achieved by the resonant coupling between the ring and the lower endcap electrode (see discussion in section 2.4.2). For $^{24}Mg^+$, the resonance appeared for an endcap voltage of (239.7 ± 1) V. From the modeled trap potential, a resonant voltage of 239 V is calculated, which is in good agreement with the experimental findings. The width of the resonance is comparable to the quality factor Q of the resonant circuit and demonstrates that under favorable conditions, the theoretical limit can actually be reached in a real measurement.

For the detection of Ar^{n+} produced in the EBIS and injected into the trap, swept voltage spectra were recorded with the upper resonant circuit in the first second after the injection of Ar^{13+} (Fig. 5.3, left). Due to the high kinetic energy of a few hundreds of V·q directly after the injection, the storage time of Ar^{13+} is limited to less than a millisecond by the helium present in the vacuum system. As a consequence, it was neither possible to detect any signal of Ar^{13+} nor of any other argon species Ar^{n+}. All identified ion species can be attributed to ionized residual gas atoms and molecules. Compared to the signals of Mg^+ (Fig. 5.1, left), the signals induced by He^+ and the species with m/q=2 (He^{2+} or H_2^+) are very narrow. This can be explained by the fact that the ions are produced from the 4 K residual gas, which is nearly at rest. On the other hand, the signal of H^+ – which is also produced from residual gas – is much broader. A possible explanation for this effect is the heating caused by the release of Coulomb energy as a result of the decomposition of the H_2 molecules.

Since the transport of argon ions from the EBIS takes place with a fixed transport energy, the absolute kinetic energy of the Ar^{n+} ions – and thus the storage time

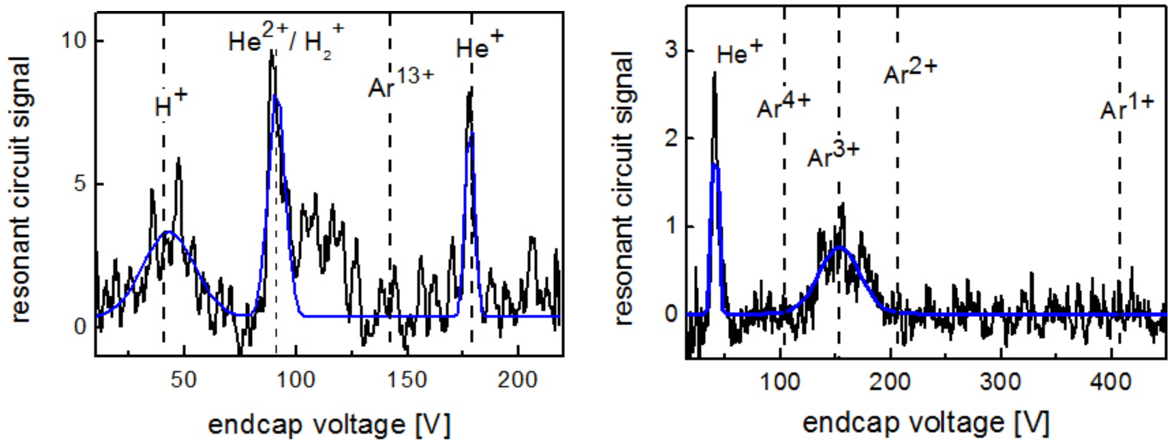

Figure 5.3: Left: Signal of the upper resonant circuit directly after the injection of Ar^{13+}. Identified species are He^{2+}, He$^+$ and H$^+$. Right: Signal of the lower resonant circuit directly after the injection of Ar^{4+}. Identified species are He$^+$ and Ar^{3+}. In both figures also the expected positions of some unobserved species (Ar^{13+}, Ar^{2+} and Ar^{1+}) are indicated.

after the capture – depends on the charge state. Accordingly, Ar^{n+} ions should be more easily observed, if a lower charge state than Ar^{13+} is injected into the trap. This was actually the case after the injection of Ar^{4+} (Fig. 5.3, right). In a spectrum recorded with the lower resonant circuit, Ar^{3+} and He$^+$ were detected, however, no signals of Ar^{2+} and Ar^{4+} were observed. The reason for the predominant signal of Ar^{3+} becomes clear by inspection of the cross sections for single-electron capture (table 4.1): Due to an anomaly in the cross sections for argon ions, the Ar^{3+} cross section is more than one order of magnitude lower than the one of Ar^{4+} and a factor of four lower than the one of Ar^{2+}. With the helium gas present in the trapping volume, the storage times of highly-energetic Ar^{4+} and Ar^{3+} are a few milliseconds and 100 milliseconds, respectively. Therefore, the amount of Ar^{3+} increases during the initial stage of the trapping process before it decays on a longer time scale. This interpretation is confirmed by the observation of He$^+$ ions that are a product of the electron transfer from the residual gas to Ar^{4+} and Ar^{3+}.

5.2 Temporal evolution of resonant circuit signals

The process of resistive cooling was investigated with singly charged Mg$^+$ and Ar$^+$. Other argon charge states – as discussed in the section before – were not present long enough for systematic experiments. For the production of the argon ions, an ion sputter gun was placed within the horizontal section of the SpecTrap beamline. A needle valve was used to adjust the flow of argon gas into the sputter gun, where the argon gas was ionized by electron-beam ionization. The resulting ion distribution contained mainly Ar$^+$ and also Ar^{2+} in lower quantities.

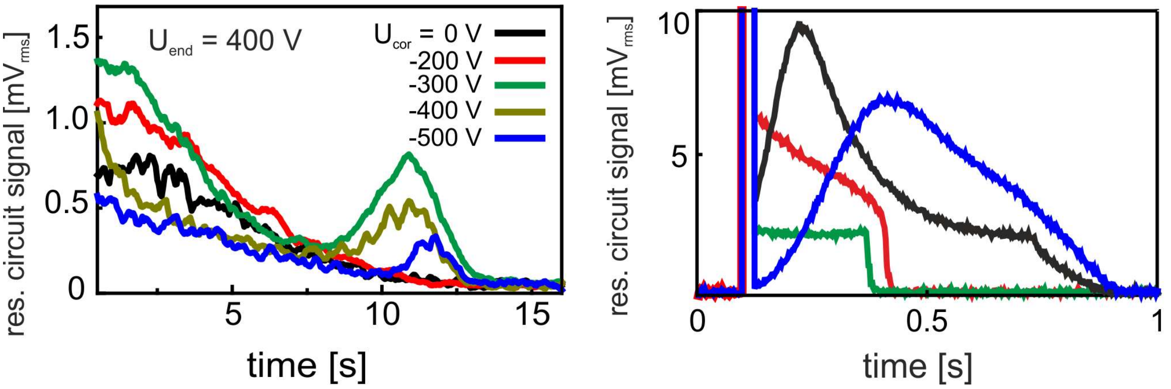

Figure 5.4: Left: Resonant circuit signal of Ar^+. The total energy dissipated was in the range of 200-1000 eV. Right: Signals of Mg^+ after excitation via the ring electrode. The measurements were not reproducible and representative signals were merely chosen to demonstrate the variety of the occurring signal shapes. The total energy dissipated was in the range of $150 - 1800$ eV. From the fluorescence rate, the ion number was determined to be in the range $N = 10^3$ to 10^4.

For the detection of the Ar^+ signals with the lower axial resonator (Fig. 5.4, left), the endcap voltage was raised after the ion injection to a value such that the ions' oscillation frequency matched the resonance frequency of the resonant circuit. The spectrum analyzer was set to a resolution bandwidth $B = 2.3\,\mathrm{kHz}$ comparable to the bandwidth of the lower resonant circuit. During the first seconds after injection, the ion energy is presumably of the order of the transport energy. The signal shape is dominated by an exponential decay with a time constant of a few seconds, which is also the expected buffer gas cooling time for the pressure of helium gas present during the experiments. Hence, although the ions dissipated energy via the resonant circuit, the cooling process is dominated by buffer gas cooling.

This evaluation can be confirmed by estimating the total dissipated energy via the resonant circuit. The amount of dissipated energy is obtained by integration of the power dissipation $P = (U/\alpha)^2 \cdot R$, where U is the measured signal voltage at the spectrum analyzer, U/α is the voltage induced in the resonant circuit, $\alpha = 156.25$ is the voltage amplification of the electronic components for signal processing, and R is the Ohmic, on-resonance impedance of the resonant circuit (see also the discussion of the electronic components in section 2.4.2). For the spectra of the Ar^+ ions (Fig. 5.4, left), the total energy dissipation of the ion ensemble ranges for the different curves from 200–1000 eV. In consideration of the initial energy of a few hundreds of eV per ion, one can conclude that the effect of resistive cooling is secondary to the one of buffer gas cooling.

In some of the Ar^+ spectra the signal develops a peak, just before the signal gets too weak to be resolved from the background. This effect can be attributed to an increasing overlap of the ions' axial frequency distribution with the bandwidth of the resonant circuit as the ions are getting colder by buffer gas cooling. This interpretation is supported by the observation that the peak is more pronounced when the correction electrodes are used for the compensation of the coefficient C_4: In the case of the anharmonic trap with $U_{\mathrm{cor}} = 0$, the frequency distribution $\Delta\omega_z$ remains finite in the limit $E_{\mathrm{kin}} \rightarrow 0$ due to the radial dependence of ω_z, as can be deduced from figure 5.2.

Signals obtained after axial excitation of a Mg^+ ion cloud via one electrode deviated even more from the expected exponential decay (Fig. 5.4, right). The excitation of the Mg^+ ion cloud for 20 ms via the ring electrode is observable as a strong saturated signal at the beginning of each spectrum. In many spectra the dominant feature is a strong signal increase that is probably due to increasing overlap of the ions' oscillation frequency with the resonant circuit resonance. The signal shapes were not reproducible for an excitation under (apparently) identical conditions, and the four spectra depicted have been selected as examples for the different observed signal shapes.

Similar to the resonant circuit signals after ion bunch injection, the decay after the signal maximum is much faster than the single-ion resistive cooling time $\tau_1 \approx 800\,\mathrm{s}$ and can be explained by buffer gas cooling. This is in agreement with the fact that the total dissipated energy was in the range of 150 eV to 1800 eV, which is much less than the expected total energy of a few thousands of ions after excitation with the given amplitude. However, it should be noted that these signal amplitudes after axial excitation exceeded by far the ones obtained directly after ion bunch injection. Since the total energy of an ion cloud after excitation is surely smaller than directly after injection, this means that a larger fraction of the total energy was accessible to resistive cooling. This is because the cloud is after excitation in a non-thermal state with higher proportion of energy stored in the center-of-charge motion and the axial degrees of freedom.

5.3 A model for resistive cooling of large ion clouds

In the following section, a model is developed to describe the resistive cooling of an ion cloud.

The section is structured as follows: First, the resistive cooling of a single ion and of an ion cloud consisting of N ions is described. The discussion of these sections follows the ideas presented in [52].

Next follows a discussion of the mechanisms that allow resistive cooling beyond the center-of-charge motion. These considerations will provide the motivation for a model of resistive cooling based on rate equations for the energies stored in the different degrees of freedom.

In the last section, the model will be used to reproduce the resistive cooling signals of actual experimental results. It will be shown how the model can be used to attribute characteristics of the cooling process to properties of the ion cloud that are experimentally not directly accessible.

5.3.1 Resistive cooling of a single ion

Resistive cooling of a single ion has already been discussed in section 2.4.2. For convenience, the most important equations are repeated here. The axial motion of an ion with mass m, charge q, and energy E is described by a sinusoidal oscillation with frequency ω_z:

$$z(t) = \frac{1}{\omega_z}\sqrt{\frac{2E}{m}}\sin(\omega_z t + \phi). \tag{5.1}$$

Making this ansatz means that all collisions between ions or other effects that introduce incoherence are neglected. The current induced in the endcap electrode by the ion is then

$$i(t) = \frac{q}{D}\frac{dz}{dt} = \frac{q}{D}\sqrt{\frac{2E}{m}}\cos(\omega_z t + \phi), \tag{5.2}$$

where the effective electrode distance is denoted D. The expectation value of the squared single-ion current I is given by

$$I^2(t) := \langle i(t)^2 \rangle = \frac{1}{T}\int_0^T i(t)^2 dt = \frac{q^2}{D^2 m}E. \tag{5.3}$$

The single-ion power dissipation is

$$\begin{aligned} -P &= \frac{dE}{dt} = -\gamma_1 E, & (5.4)\\ \text{with } \gamma_1 &= \frac{q^2 R}{D^2 m} = \tau_1^{-1}. & (5.5) \end{aligned}$$

The constants γ_1 and τ_1 denote the single-ion cooling rate and the single-ion cooling time constant, respectively, whereas R stands for the Ohmic resistance of the resonant circuit.

5.3.2 Resistive cooling of an N-particle cloud

The interaction of the resonant circuit with an ion cloud with total charge Q is to first order determined by the axial motion of the cloud's center of charge $Z(t) = \sum q_k z_k(t)/Q$. The total current I_N induced by the N ions in the endcap is given by the summation over the single-ion currents i_k and can be expressed by the motion of the center of charge with $\sum i_k(t) = \sum q_k v_{z_k}/D = \dot{Z}(t)Q/D$.

Usually, the cooling of N particles is treated in two different limits: The first one is the coherent particle motion, where the ions oscillate with the identical phase $\phi_k = \phi$ in equation 5.1. In this case, the cloud can be described as a rigid body that oscillates in the external potential with the center of charge excited to a macroscopic amplitude. The other limit is the incoherent motion that treats the cloud as a thermal ensemble, where all ions perform individual oscillations while the center of charge is – with the exception of stochastic fluctuations – at rest. In both cases, the ions are treated as individual particles with an oscillation frequency $\omega_{z,k}$ that is determined by the external potential.

For simplicity, in the case of a coherent motion all ions are described by the same energy $E = E_k$ instead of assuming a thermal distribution and the total energy of the ion cloud is therefore $E_N = N \cdot E$. The total induced current I_N thus becomes

$$\begin{aligned} \left\langle I_N^2 \right\rangle &= \left\langle \left(\sum_{k=1}^{N} i_k(t) \right)^2 \right\rangle = \frac{q^2 2E}{D^2 m} \left\langle \left(\sum_{k=1}^{N} \cos(\omega_z t + \phi) \right)^2 \right\rangle \\ &= \frac{q^2 2E}{D^2 m} \cdot \frac{N^2}{2} = \frac{q^2 (E \cdot N) N}{D^2 m} = \frac{q^2 E_N N}{D^2 m}. \end{aligned} \tag{5.6}$$

Hence, the total energy dissipation of the ion cloud can be expressed through the N-particle cooling rate γ_N:

$$\frac{\mathrm{d}E_N}{\mathrm{d}t} = -\left\langle I_N^2 \right\rangle R = -\frac{q^2 E_N N}{D^2 m} R = -(\gamma_1 N) E_N = -\gamma_N E_N. \tag{5.7}$$

The well-known result of equation (5.7) expresses that the energy stored in the center-of-charge motion is cooled with the rate $\gamma_N = N \cdot \gamma_1$. The same result follows from equation (5.5), if the cloud is treated as a single particle with mass $M = N \cdot m$ and charge $Q = N \cdot q$.

In the case of an N-particle cloud with single-ion phases ϕ_k randomly distributed in the interval $[0, 2\pi]$ the expectation value of the squared total current I_N is [47]

$$\begin{aligned} \left\langle I_N^2 \right\rangle =& \left\langle \left(\sum_{k=1}^{N} i_k(t) \right)^2 \right\rangle = \frac{q^2 2E}{D^2 m} \left\langle \left(\sum_{k=1}^{N} \cos(\omega_z t + \phi_k) \right)^2 \right\rangle \\ =& \frac{q^2 2E}{D^2 m} \left\langle [A \cos(\omega_z t + \phi)]^2 \right\rangle \\ =& \frac{q^2 2E}{D^2 m} \frac{A^2}{2} = \frac{q^2 E \cdot N}{D^2 m} = \frac{q^2 E_N}{D^2 m}. \end{aligned} \tag{5.8}$$

For this calculation, the fact has been used that the sum of N sine functions with the frequency ω results in a sine of the same frequency. The amplitude A and the global phase ϕ depend on the specific distribution of the phases ϕ_k. The (stochastic) expectation value $\langle A^2 \rangle = N$ for the sum over N sine functions with a random phase distribution and the (temporal) expectation value $\langle \cos^2 \rangle_T = 1/2$ over one oscillation period T were used in the last steps [148, 149].

From equation (5.8) the rate of energy dissipation via the resonant circuit is readily received:

$$\frac{\mathrm{d}E_N}{\mathrm{d}t} = -\left\langle I_N^2 \right\rangle R = -\frac{q^2 R}{m D^2} N E = -\gamma_1 N E = -\gamma_1 E_N. \tag{5.9}$$

This is the well-known result that the cooling of an N-particle cloud takes place with the single-ion rate γ_1. However, the result was derived with the assumption of a random distribution of the single-ion phases ϕ_k. Only if this condition holds throughout the cooling process, the total energy $E_N(t)$ can be described by an exponential decay:

$$E_N(t) = E_N(t_0)\exp(-\gamma_1 t). \tag{5.10}$$

If the axial motion of the center of charge is regarded as an independent degree of freedom with the energy $E_N/N = E_{\mathrm{cc}}$, this leads to an alternative interpretation of equation (5.9): Instead of the total energy E_N being dissipated with the rate γ_1, the center-of-charge motion can be regarded as being cooled with the rate $\gamma_1 \cdot N = \gamma_N$. If the axial energy is evenly distributed among the N degrees of freedom at all times, i.e. $E_{\mathrm{cc}} \equiv E_N/N = E$, this alternative perspective leads again to the conclusion that resistive cooling results in an exponential decay of the total energy E_N with the rate γ_1. Therefore, the condition of a random phase distribution that leads to equation (5.9) is equivalent to the requirement that at all times the axial energy stored in the center-of-charge motion is given by 1/N of the total axial energy E_N.

Due to these considerations, in the following sections the cooling process will be treated as an interaction between the resonant circuit and the center-of-charge motion. According to equation (5.9), the energy dissipation of the ion cloud is given by $P = -\gamma_N E_{\mathrm{cc}}$.

5.3.3 Resistive cooling beyond the center-of-charge motion

From the discussion in the previous section the question arises which processes determine the amount of energy stored in the center-of-charge motion (*cc-motion*).

It is obvious that without a continuous transfer of energy from the internal degrees of freedom to the cc-motion, persistent resistive cooling is not possible. This result is confirmed by the numerical simulations described in the Ph.D. thesis of J. Steinmann [51].

Below, I want to bring forward a simple argument to visualize the situation. Let us consider the motion of two identical ions with the instantaneous axial oscillations $z_{1,2}(t) = z^0_{1,2} \cdot \sin(\omega t + \phi_{1,2})$. The Coulomb interaction between the two ions is neglected, for example because the ions are located at different radial positions. There is, however, a mutual influence between the ions due to the common interaction with the resonant circuit.

The resistive cooling of the two ions is visualized in figure 5.5 for three different initial conditions. For counter-moving ions with $z_1 = z_2$ and a phase difference of $\Delta\phi = \pi$ (left graph) the induced current at the endcap is zero and the center of charge is at rest. Consequently, there is no energy dissipation and the amplitude of the oscillation remains unchanged.

For the initial conditions $z_1 = z_2$ and $\Delta\phi = 0$ the oscillation of both ions will be simultaneously damped until both ions are at rest and $z_1 = z_2 = 0$ (middle).

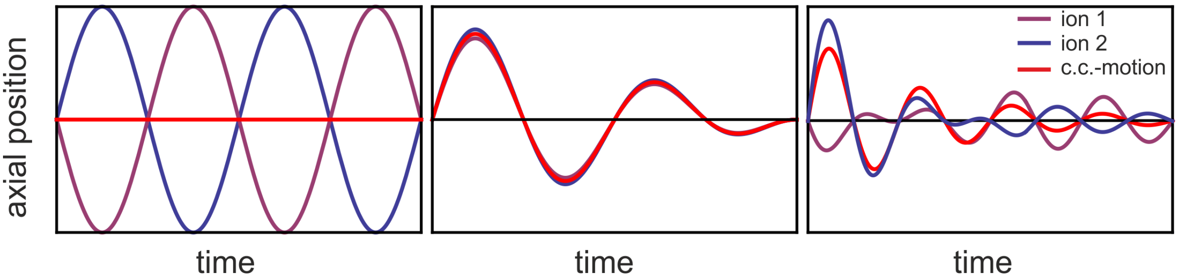

Figure 5.5: Visualization of the interaction between the resonant circuit and the center-of-charge motion of two ions. Three different initial conditions are depicted: Counter-moving ions with phase shift $\Delta\phi = \pi$ (left), in-phase moving ions with $\Delta\phi = 0$ (middle), and two ions with different initial amplitudes (right). Here, the resonant circuit mediates an energy transfer between the two ions. In all three cases the amplitude of the cc-motion is damped to zero for $t \rightarrow \infty$.

If the initial amplitude of both ions is different, an energy transfer between the two ions occurs at the same time as the common center-of-charge motion is damped to zero amplitude (right). In the final state there is a phase difference $\Delta\phi = \pi$ between the ions and the resistive cooling comes to an end although the ion motion does not.

For a model that describes persistent resistive cooling, additional effects have to be taken into account. For this purpose, I want to focus on three mechanisms that can lead to a redistribution of energy and allow resistive cooling of motions other than just the center-of-charge motion:

- the finite width of the axial frequency distribution $\Delta\omega_z$, caused by anharmonicities of the potential or by more than one ion species present in the ion cloud,
- the coupling between the axial and the radial motions by Coulomb collisions,
- and non-linear effects that allow resistive-cooling beyond the center-of-charge motion.

The effect of these contributions on resistive cooling has been studied with numerical methods in detail in reference [51].

The influence of the axial frequency distribution can be understood by looking at the motion of two counter-moving ions (Fig. 5.5, left). If the difference of the axial frequencies is $\omega_{ik} = \omega_i - \omega_k$, the cc-motion of the two ions will collapse and be restored on a timescale $\tau \approx 1/\omega_{ik}$.

The same result is valid for an N-particle cloud if the frequency difference is replaced by the width of the axial frequency distribution $\Delta\omega_z$. One can also observe this by looking at the Fourier-transform of the cc-motion $Z(t)$ (which is readily given by the frequency distribution of the individual ions): Unimpaired by an instantaneous amplitude $Z(t_0) = 0$, the expectation value $\langle Z(t)^2\rangle \propto \langle I_N(t)^2\rangle \propto N$ is always proportional to the number of particles, if the averaging is performed over a sufficiently long time interval. This time interval is in turn defined by the width of the frequency distribution $\tau \approx 1/\Delta\omega_z$ and is the consequence of the cc-motion being restored from an temporarily zero-amplitude $Z(t_0) = 0$ on the time scale τ. The same result is given in [150] without much explanation.

Although the restoration of the cc-mode from the other $(N-1)$ axial degrees of freedom is merely stochastic effect that occurs even without any actual interaction, I will refer to it as a coupling between the degrees of freedom with the frequency distribution $\Delta\omega_z$ as the respective coupling rate. A detailed evaluation of the contributions to the axial frequency distribution $\Delta\omega_z$ is given in section 5.3.6. The results presented therein allow the calculation of $\Delta\omega_z$ for a specific trap geometry.

Coulomb collisions between ions lead to thermalization between the axial and the radial degrees of freedom and thus allow the resistive cooling of the radial degrees of freedom, which are not coupled to the axial center-of-charge motion themselves. An estimate of the thermalization time, the Spitzer self-collision time τ_{sct} [151], is given in section 5.3.5. It is highly dependent on the temperature and density of the ion cloud: For a typical cooling process from energies of many electron-volts to 10^{-4} eV (corresponding to temperatures of a few kelvin), the self-collision time adopts values between several seconds and a few microseconds.

The energy transfer from the axial degrees of freedom to the center-of-charge motion is not influenced by Coulomb collisions, since conservation of momentum prohibits an excitation of the center-of-charge motion.

If the resonant circuit is not symmetrically connected to both endcap electrodes, the breakup of symmetry allows resistive cooling without an excitation of the center-of-charge mode. This is the case for the SpecTrap Penning trap, where both upper and lower resonant circuit form a connection between electric ground and the upper and lower endcap electrode, respectively. Hence, the effective electrode distance D that expresses the scaling between the induced current $i(t)$ in the endcap and the ion's axial velocity v_z (Eq. (5.2)), is different for positive and negative axial amplitudes z (see Fig. 2.20). Under these conditions, even motions with the center of charge at rest, e.g. the breathing mode of the cloud, will induce a total current in the resonant circuit that removes energy from the ions. However, in most cases and also in case of the SpecTrap Penning trap, the difference of effective electrode distance $\Delta = D(z) - D(-z)$ becomes significant only for large oscillation amplitudes. Therefore, this contribution to the center-of-charge cooling is usually negligible.

Based on the ideas presented in this section, in the following section a model for resistive cooling of an ion cloud is presented. The coupling mechanism between the different degrees of freedom will be mapped to a set of rate equations, each describing the energy (respectively temperature) of one degree of freedom.

5.3.4 The rate equation for resistive cooling

The model for resistive cooling describes an N-particle ion-cloud with three different temperatures: The temperature T_{cc} of the center-of-charge motion, the temperature T_{ax} of the $(N-1)$ internal, axial degrees of freedom, and the temperature T_{r} of the cyclotron motion. Consequently the total, thermal energy of the system is

$$E = k_B T_{\mathrm{cc}} + (N-1) k_B T_{\mathrm{ax}} + N k_B T_{\mathrm{r}}. \tag{5.11}$$

The interaction of the resonant circuit with the ion cloud is restricted to the center-of-charge motion, and the energy dissipation is given by the product of the rate γ_{cc} and the temperature difference between the axial degrees of freedom and the resonant circuit:

$$\frac{\mathrm{d}E}{\mathrm{d}t} = -\gamma_{\mathrm{cc}}(T_{\mathrm{cc}}(t) - 4\,\mathrm{K}). \tag{5.12}$$

The temporal evolution of the system is described by three coupled rate equations, where each equation describes one of the temperatures T_{cc}, T_{ax} and T_{r}. This approach is similar to the one described in [150], where resistive cooling of electrons in a Penning trap is with two coupled rate equations for the center-of-mass motion and the internal degrees of freedom.

$$\begin{aligned}
\frac{\mathrm{d}T_{\mathrm{cc}}(t)}{\mathrm{d}t} &= -\gamma_{\mathrm{cc}} \cdot [T_{\mathrm{cc}}(t) - 4\,\mathrm{K}] + \gamma_{\mathrm{ax}} \cdot [T_{\mathrm{ax}}(t) - T_{\mathrm{cc}}(t)], \\
\frac{\mathrm{d}}{\mathrm{d}t} T_{\mathrm{ax}}(t) &= -\gamma_{\mathrm{ax}} \cdot \frac{T_{\mathrm{ax}}(t) - T_{\mathrm{cc}}(t)}{N-1} - \gamma_{\mathrm{r}} \cdot [T_{\mathrm{ax}}(t) - T_{\mathrm{r}}(t)], \\
\frac{\mathrm{d}}{\mathrm{d}t} T_{\mathrm{r}}(t) &= \gamma_{\mathrm{r}} \cdot \frac{N-1}{N} \cdot [T_{\mathrm{ax}}(t) - T_{\mathrm{r}}(t)].
\end{aligned} \tag{5.13}$$

The three equations are coupled by the transfer of energy between the different degrees of freedom: The temperatures T_{cc} and T_{ax} equalize with the rate γ_{ax}, whereas equalizing between the radial T_{r} and the axial temperature T_{ax} is described by the rate γ_{r}. Normalization factors have been introduced to account for the respective weight of the three different temperatures and ensure the validity of equations (5.11) and (5.13).

The free parameters of the model are the three rates γ_{cc}, γ_r and γ_{ax}. They have to be either estimated or obtained by a fit to experimental data.

As follows from the previous discussion, the rate $\gamma_{\mathrm{cc}} = \kappa \cdot \gamma_N$ can be identified with the N-particle cooling rate of the resonant circuit. The coefficient $\kappa \leq 1$ accounts for an incomplete tuning of the ions' oscillation frequency to the resonant circuit, for instance due to a mismatch of the frequencies or because the frequency distribution $\Delta\omega_z$ is larger than the acceptance of the resonant circuit.

The rate γ_{ax} can be identified with the axial-frequency width $\Delta\omega_z$, and the rate γ_r with the ion-ion collision time. All parameters may depend on time since they depend on the density, temperature, and spatial extent of the ion cloud.

5.3.5 Thermalization by ion-ion collisions (Spitzer self-collision rate)

The thermalization of a non-neutral plasma by Coulomb interactions has been discussed by Spitzer and MacDonald [151, 152]. The inverse of the Coulomb collision rate, the Spitzer self-collision time, is estimated by [153] as

$$\tau_{\text{sct}} \approx (4\pi\epsilon_0)^2 \frac{3\sqrt{m}(k_B T)^{3/2}}{4\sqrt{\pi} n q^4 \ln\Lambda}. \tag{5.14}$$

In equation (5.14) $\ln\Lambda$ denotes the Coulomb logarithm, which is for ion-ion collisions given by [153]

$$\ln\Lambda = 23 - \ln\left[\frac{q_1 q_2 (m_1 + m_2)}{e^2(m_1 T_2 + m_2 T_1)}\left(\frac{n_1 q_1^2}{e^2 T_1} + \frac{n_2 q_2^2}{e^2 T_2}\right)^{1/2}\right] \tag{5.15}$$

and reduces to

$$\ln\Lambda = 23 - \ln\left(\frac{2nq^4}{e^4 T^3}\right)^{1/2} \tag{5.16}$$

for collisions amongst identical ions. The densities n, n_1, n_2 are given in cm^{-3} and the temperatures T are given in eV. Typical values for the Coulomb logarithm are $\ln\Lambda \approx 10 - 20$ [153].

For the thermalization of the ions within the resistive cooling model, the Spitzer self-collision time of a single-species ion cloud was calculated with equation (5.14) as a function of the axial temperature T_{ax}. Since the Coulomb logarithm is only weakly dependent on the temperature a constant value of $\ln\Lambda = 20$ was used.

The temperature dependence enters the self-collision time via the density $n(E)$. Following an idea presented in [52], the density $n(E)$ is calculated from the axial oscillation amplitude a(E) according to

$$\begin{aligned} n(E) &\approx \frac{N}{4/3\pi a(E) R^2}, \\ a(E) &\approx \sqrt{\frac{Ed^2}{qC_2U}} + \sqrt[3]{\frac{Nqd^2}{4\pi C_2 \epsilon_0 U}}, \end{aligned} \tag{5.17}$$

assuming a radial distribution of the ions with the radius R. The second term in $a(E)$, in which d denotes the characteristic trap dimension, ϵ_0 the electric constant, and U the trapping potential, ensures the correct number density for $T \rightarrow 0\,\text{K}$, but only applies for large ion clouds. Hence, for the simulation of the resistive cooling of 30 C^{5+} ions presented in section 5.3.7 only the first term of $a(E)$ was used.

5.3.6 Shifts of the axial frequency in a non-linear potential

The starting point for the analysis of the axial oscillation is the equation of motion of an ion in a non-linear potential $\phi = (1/2)\,\alpha z^2 + (1/4)\,\beta z^4 + (1/6)\,\gamma z^6$,

$$m\ddot{z} + \alpha z + \beta z^3 + \gamma z^5 = 0. \tag{5.18}$$

The force acting on the ion is created by the potential of the Penning trap, as given in equation (2.22):

$$\begin{aligned}\phi(z,r) \;&=\; \frac{C_2}{d^2}(z^2 - \frac{1}{2}r^2) + \frac{C_4}{d^4}(z^4 - 3z^2r^2 + \frac{3}{8}r^4) + \\ &\quad + \frac{C_6}{d^6}(z^6 - \frac{15}{2}z^4r^2 + \frac{45}{8}z^2r^4 - \frac{5}{16}r^6) + \ldots .\end{aligned} \tag{5.19}$$

Thus, the coefficients α,β and γ are directly obtained by regarding the axial gradient of the potential $\phi(z,r)$:

$$\begin{aligned}& q\frac{\partial\phi(z,r)}{\partial z} \\ &= q\left[\frac{2C_2}{d^2}z + \frac{4C_4z^3}{d^4} - \frac{6C_4zr^2}{d^4} + \frac{6C_6z^5}{d^6} - \frac{30C_6z^3r^2}{d^6} + \frac{45C_6zr^4}{4d^6} + \ldots\right] \\ &\approx \underbrace{q\left(\frac{2C_2}{d^2} - \frac{6C_4r^2}{d^4} + \frac{45C_6r^4}{4d^6}\right)}_{\alpha} z + \underbrace{q\left(\frac{4C_4}{d^4} - \frac{30C_6r^2}{d^6}\right)}_{\beta} z^3 + \underbrace{q\left(\frac{6C_6}{d^6}\right)}_{\gamma} z^5.\end{aligned} \tag{5.20}$$

In Eq. (5.20) the contributions to the potential gradient have been sorted by powers of the axial coordinate z. All terms in the potential $\phi(z,r)$ of the form z^2r^{2k} produce a force that is linear in the axial coordinate z. These terms alter the equation of motion such that it is solved by a harmonic oscillation with a frequency $\omega_z(r)$ that depends on the radial position r, but is independent of the ion's energy. From the equation of motion one can directly identify $\omega_z^2(r) = \alpha/m$:

$$\frac{\alpha}{m} = \omega_z^2(r) \;=\; \underbrace{\frac{2qC_2}{md^2}}_{\omega_z^2} + \underbrace{\left(-\frac{6r^2qC_4}{md^4} + \frac{45r^4qC_6}{4md^6}\right)}_{\Delta\omega_z^2(r)} + \ldots \tag{5.21}$$

$$\rightarrow \omega_z(r) \;\approx\; \sqrt{\omega_z^2 + \Delta\omega_z^2(r)} \approx \omega_z\left(1 + \frac{\Delta\omega_z^2(r)}{2\omega_z^2}\right). \tag{5.22}$$

The first term in equation (5.21) is the oscillation-frequency $\omega_z \equiv \omega_z(r{=}0)$ of an ion at the position $r = 0$, the other terms give rise to the radially dependent shift $\Delta\omega_z(r)$. To first order, the shift is determined by the coefficient C_4 that can be tuned to zero by means of the correction electrodes. However, for the SpecTrap Penning

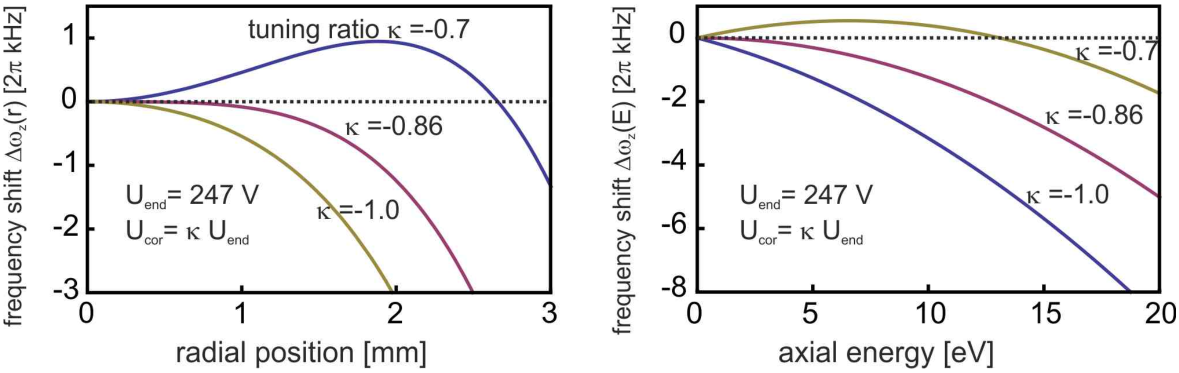

Figure 5.6: The frequency shift $\omega_z(r)$ for a Mg$^+$ ion depending on energy and radial position. For a tuning ratio $\kappa = -0.86$ the coefficient C_4 becomes zero .

trap the coefficient C_6, which is responsible for a frequency reduction proportional to r^2, becomes dominant for a radial position $r \geq 3\,\mathrm{mm}$ (Fig. 5.6).

The terms βz^3 and γz^5 in the equation of motion (5.18) result in both an energy-dependent frequency shift and a deviation from the harmonic motion. The solution of (5.18) must be a periodic function with the period $T = 2\pi/\omega$ and – since the potential $\phi(z)$ is symmetric – a solution can be found with the ansatz

$$z(t) = z_0 \sin(\omega t) + \epsilon z_0 \sin(3\omega t). \tag{5.23}$$

Using the trigonometric identities

$$\begin{aligned}\sin^3(\omega t) &= \frac{3}{4}\sin(\omega t) - \frac{1}{4}\sin(3\omega t),\\ \sin^5(\omega t) &= \frac{10}{16}\sin(\omega t) - \frac{5}{16}\sin(3\omega t) + \frac{1}{16}\sin(5\omega t),\end{aligned}$$

the second derivative and higher powers of $z(t)$ are found to first order in ϵ:

$$\begin{aligned}\ddot{z}(t) =& - \omega^2 z_0 \sin(\omega t) - \epsilon 9\omega^2 z_0 \sin(3\omega t),\\ z^3(t) =& z_0^3\left(\frac{3}{4}\sin(\omega t) - \frac{1}{4}\sin(3\omega t)\right) + \epsilon 3 z_0^3 \sin^2(\omega t)\sin(3\omega t) + \ldots,\\ z^5(t) =& z_0^5\left(\frac{10}{16}\sin(\omega t) - \frac{5}{16}\sin(3\omega t) + \frac{1}{16}\sin(5\omega t)\right) + \epsilon 5 z_0^5 \sin^4(\omega t)\sin(3\omega t) + \ldots\end{aligned}$$

Inserting these results in the equation of motion (5.18) leads to one equation each for $\sin(\omega t)$ and $\sin(3\omega t)$, since both frequency contributions must individually be equal to zero:

$$\left[-m\omega^2 z_0 + \alpha z_0 + \beta\frac{3z_0^3}{4} + \gamma\frac{10z_0^5}{16}\right]\sin(\omega t) = 0, \tag{5.24}$$

$$\begin{aligned}&\left[-m\epsilon 9\omega^2 z_0 - \alpha\epsilon z_0 + \beta\left(-\frac{z_0^3}{4} + \epsilon 3 z_0^3 \sin^2(\omega t)\right) + \right.\\ &\left.\gamma\left(-\frac{z_0^5 5}{16} + \epsilon 5 z_0^5 \sin^4(\omega t)\right)\right]\sin(3\omega t) = 0.\end{aligned} \tag{5.25}$$

Equation (5.25) can be used to derive an expression for ϵ, i.e. the deviation of the motion from a harmonic oscillation as defined in the ansatz (5.23). However, here we are only interested in the dependence of the frequency ω on the amplitude z_0. This amplitude-dependent frequency is derived from equation (5.24):

$$\begin{aligned}
\omega_z^2(E,r) &= \frac{\alpha}{m} + \frac{\beta}{m}\frac{3z_0^2}{4} + \frac{\gamma}{m}\frac{5z_0^4}{8} && (5.26)\\
&\approx \omega_z^2(r) + \frac{\beta}{m}\frac{3}{4}\left(\frac{Ed^2}{qC_2}\right) + \frac{\gamma}{m}\frac{5}{8}\left(\frac{Ed^2}{qC_2}\right)^2 && (5.27)\\
&= \omega_z^2(r) + \underbrace{\left(\frac{C_4}{C_2}\frac{3}{md^2} - \frac{45C_6}{C_2}\frac{r^2}{md^4}\right)E + \left(\frac{15}{4qmd^2}\frac{C_6}{C_2^2}\right)E^2}_{\Delta\omega_z^2(E,r)}. && (5.28)
\end{aligned}$$

For the expression above, the relation $\omega_z^2(r) = \alpha/m$, the definition of β and γ from equation (5.20), and the relation $z_0^2 = Ed^2/qC_2$ (Eq. (5.19)) were used.

In order to summarize these results, the three contributions to the axial frequency $\omega_z(E,r)$ are once more listed below:

$$\begin{aligned}
\omega_z(E,r) =& \omega_z(r) + \Delta\omega_z(E,r)\\
=& \omega_z + \Delta\omega_z(r) + \Delta\omega_z(E,r),
\end{aligned}$$

with $\omega_z(r) \equiv \omega_z(E{=}0,r)$ and $\omega_z \equiv \omega_z(r{=}0)$. The frequency shift $\Delta\omega_z(r)$, as defined in equation (5.21), contains all terms that are radially dependent but independent of the oscillation amplitude, i.e. the axial energy E. It determines the frequency distribution of a cold ion cloud. The energy-dependent shift $\Delta\omega_z(E,r)$, as defined in equation (5.28), describes all amplitude-dependent contributions to the axial oscillation frequency. It contains both radially dependent and radially independent terms.

By linear approximation of equation (5.28), an expression for the axial oscillation frequency $\omega_z(E,r)$ is obtained:

$$\begin{aligned}
\omega_z(E,r) =& \omega_z\sqrt{\frac{\omega_z^2(r)}{\omega_z^2} + \frac{\Delta\omega_z^2(E,r)}{\omega_z^2}}\\
\approx& \omega_z\left(\frac{\omega_z(r)}{\omega_z} + \frac{\omega_z}{2\omega_z(r)}\frac{\Delta\omega_z^2(E,r)}{\omega_z^2}\right),
\end{aligned}$$

and since $\omega_z(r) - \omega_z \ll \omega_z$, this can be approximated by:

$$\omega_z(E,r) \approx \omega_z\left(\frac{\omega_z(r)}{\omega_z} + \frac{\Delta\omega_z^2(E,r)}{2\omega_z^2}\right). \qquad (5.29)$$

The frequency shift $\Delta\omega_z \equiv \omega_z(E,r) - \omega_z$ follows from Eq. (5.29) by insertion of the expressions for $\Delta\omega_z^2(E,r)$ from Eq. (5.28):

$$\Delta\omega_z \approx \omega_z \left[\frac{\omega_z(r) - \omega_z}{\omega_z} + \left(\frac{3C_4}{2C_2} \frac{1}{\omega_z^2 m d^2} - \frac{45C_6}{2C_2} \frac{r^2}{\omega_z^2 m d^4} \right) E + \frac{15C_6}{4C_2} \left(\frac{E}{\omega_z^2 m d^2} \right)^2 \right]. \tag{5.30}$$

Equation (5.30) gives an approximation for all frequency contributions of the order C_2, C_4 and C_6. An explicit expression for $\omega_z(r)$ has been derived in equation (5.21).

The frequency shift, as presented in (5.30), is for $r = 0$ identical to an expression given by Gabrielse and Mackintosh [49]:

$$\begin{aligned} \frac{\Delta\omega_z}{\omega_z} &= \frac{3}{2}\frac{D_4}{D_2}\frac{E_z}{m\omega_z^2 d^2} + \frac{15}{4}\frac{D_6}{D_2}\left(\frac{E_z}{m\omega_z^2 d^2}\right)^2, && (5.31) \\ \text{where} \quad \omega_z^2 &= \frac{qV_0}{md^2} D_2. && (5.32) \end{aligned}$$

It should be noted that although the coefficients D_n of the trapping potential used by Gabrielse et al. are not identical to the coefficients C_n, the ratios $C_n/C_m = D_n/D_m$ are equal nonetheless.

5.3.7 Comparison of the model with experimental signals

In this section, different solutions to the rate equation model, represented by equations (5.13), will be discussed and compared to experimental results found in literature. At first, the cooling process with constant coupling rates γ_r and γ_ax will be analyzed and the characteristic features of the resonant circuit signal will be presented. In a second step, the temporal evolution of the rates γ_r, and γ_ax will be taken into account. It will be discussed how the dependencies of the coupling rates on the temperature and density give rise to some unique features of the resonant circuit signal. By this means, the model allows for an interpretation of the underlying dynamics and gives insight into the development of properties such as temperature and density without their direct experimental accessibility.

As a first case, the solution with constant transfer rates γ_r, γ_ax and a constant frequency matching $\kappa = 1$ is regarded. Figure 5.7 depicts two examples of the evolution of the temperatures T_cc, T_ax, T_r, the total energy E, and the detected signal that is proportional to the root of the dissipated power.

For the upper graph, the parameters were chosen to resemble the conditions for a Mg^+ ion cloud in SpecTrap with $N = 1000$ particles. The single-ion cooling time is $\tau_1 = 1000\,\mathrm{s}$ and accordingly $\gamma_\mathrm{cc} = \kappa N/\tau_1 = 1/\mathrm{s}$. The coupling rates to the other degrees of freedom are $\gamma_\mathrm{ax} = \gamma_\mathrm{r} = 1000/\mathrm{s}$ and an initial temperature of 500 K was chosen for all degrees of freedom. This condition of equal temperatures represents an ion cloud after irradiation of white noise via one electrode.

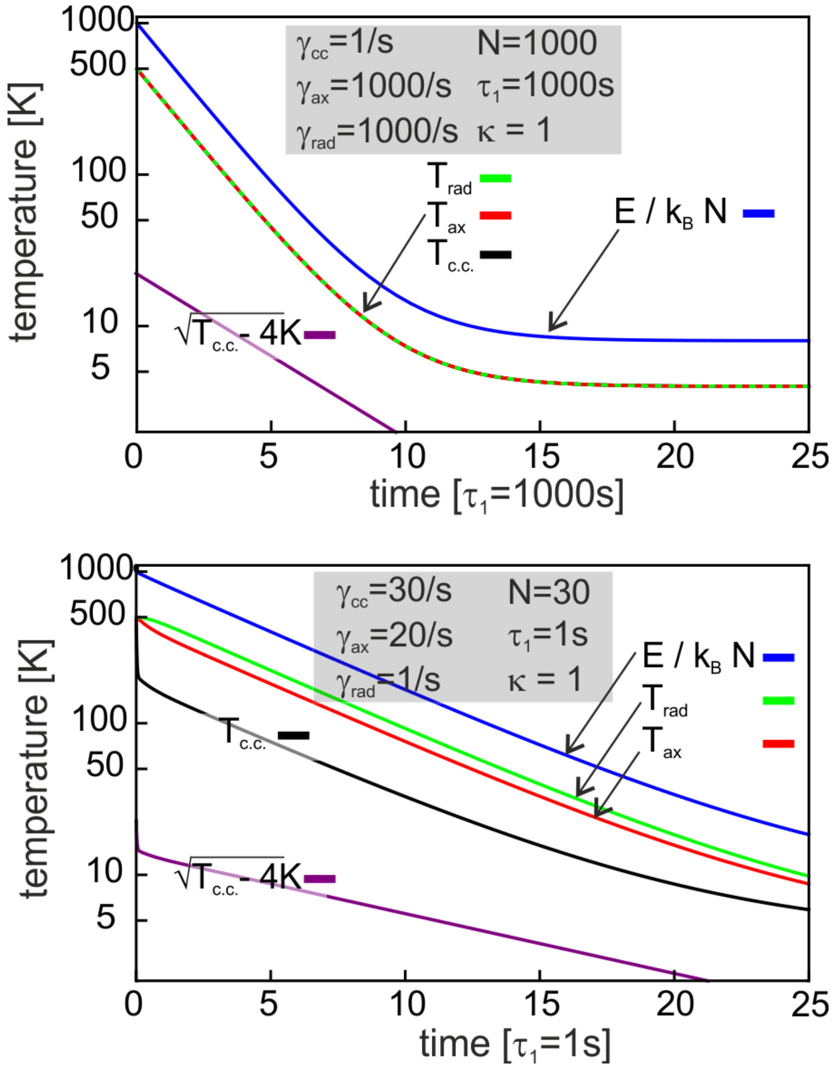

Figure 5.7: Simulation of the temperature evolution for different degrees of freedom under the influence of resistive cooling with constant coupling rates γ. Top: An ion cloud with N=1000 particles. Relevant parameters are given in the inset and represent realistic conditions for the resistive cooling of Mg^+ ions at SpecTrap. The graphs for the temperatures $T_{rad} \approx T_{ax} \approx T_{cc}$ overlap and are not resolved. Bottom: An ion cloud with N=30 particles. The parameters were chosen to represent realistic conditions for the resistive cooling of highly charged ions at SpecTrap.

Due to $\gamma_{cc} \ll \gamma_{ax}, \gamma_r$, the thermal equilibration between the degrees of freedom is fast compared to the cooling of the cc-mode. As a consequence, $T_{cc} \approx T_{ax} \approx T_r$ and the total energy is dissipated with the single-ion cooling rate γ_1, as follows from Eq. (5.10) and the corresponding discussion on page 113.

The lower graph in figure 5.7 shows the cooling of N=30 highly charged ions with $\tau_1 = 1\,\mathrm{s}$ and accordingly $\gamma_{cc} = \kappa N/\tau_1 = 30/\mathrm{s}$. Here, the rates $\gamma_{ax} = 20/\mathrm{s}$ and $\gamma_r = 1/\mathrm{s}$ are not sufficiently large to provide complete thermalization. Hence, the temperature T_{cc} is rapidly cooled below the temperatures of the other degrees of

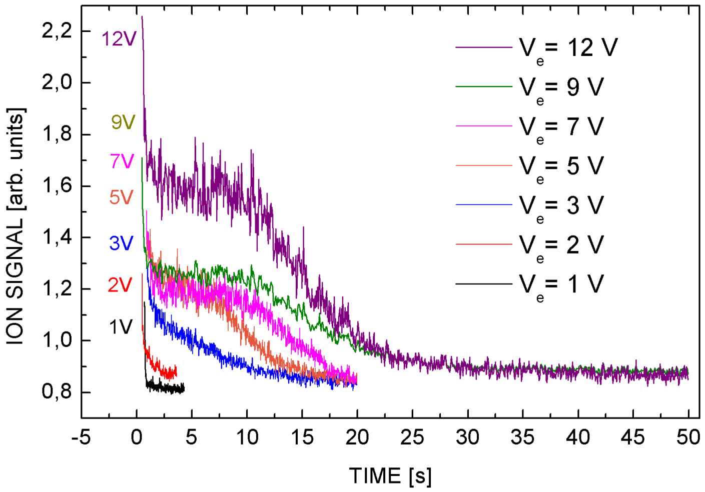

Figure 5.8: The resistive cooling signal of 30 C^{5+} ions after excitation with white noise of amplitude V_e. The thermal energy after the excitation was determined from the energy-dependent frequency shift and is of the order $\langle E \rangle \approx e \cdot V_e$ [154]. (Figure reproduced from [52]).

freedom. Since the energy stored in the center-of-charge motion is lower than in the case of thermal equilibrium, the energy dissipation is reduced and the process of cooling is prolonged (in units of τ_1).

Based on these examples one can state two facts: In the case of constant coupling parameters, the temperature T_{cc} (and thus the detected signal) is monotonously decreasing, and the energy dissipation is limited by $|dE/dt| \leq \gamma_1 E$. A possible exception to this cooling limit only exists if the energy stored in the center-of-charge motion exceeds the one of the other degrees of freedom, for example because the cc-mode was deliberately excited prior to resistive cooling.

Since at SpecTrap the process of resistive cooling is masked by the buffer gas cooling, no experiments could be performed to test this hypothesis. It is, however, in agreement with measurements performed by Gruber et al. [54]. The cooling of Xe^{44+} ions could be described by an exponential decay with a time constant exceeding the expected single-ion constant by more than an order of magnitude. Similar results were obtained for the cooling of Be^{2+}. The authors indicate that collisional coupling between the radial and axial degrees of freedom offers an explanation for the observed, prolonged time constant [54].

Another example for resistive cooling is presented by Häffner et al. While the experimentally observed cooling time constant of a single C^{5+} ion was found to be in good agreement with the theoretical expectation of $\tau \approx 130\,\mathrm{ms}$, the cooling of an ion cloud consisting of 30 C^{5+} ions occurred with a longer time constant of $\tau \approx 200\,\mathrm{ms}$ [53, 154]. Similar to the discussion presented here, the authors suggest this effect might be due to the resistive cooling of the center-of-charge mode and the energy transfer between the internal modes.

In addition to these exponentially decaying signals, cooling curves with a more complicated structure were observed by Häffner et al. Examples are given in [53], and especially in [52] where the results are discussed in more detail (Fig. 5.8). These cooling curves are produced by the interplay between the temperature-dependent cooling rates γ_r and γ_ax, as will be explained in the following. The measurements show the resonant circuit signals of 30 C^{5+} ions after excitation with different white noise amplitudes V_e between $1-12\,\mathrm{V}$. The signals show an initial, fast decay that is followed by a plateau and a much slower, exponential decay that expires to a constant signal just above the background signal. For lower excitation amplitudes, the signal plateau is less pronounced, but the overall shape is still similar.

In [52], the authors describe these signals with three exponential decays: The time constant for the initial cooling was fitted between 0.02 s and 2.5 s before the plateau. It was found to be in the range 250–450 ms and was assigned to the cooling of the axial degrees by the center-of-charge mode. For excitation voltages V_e between 2 V and 12 V the time constant of this initial stage decreased with increasing excitation voltage (e.g. $\tau_{2\mathrm{V}} \approx 450\,\mathrm{ms}$ and $\tau_{12\mathrm{V}} \approx 250\,\mathrm{ms}$), which implies that a larger axial frequency spread makes the energy transfer from the axial degrees of freedom to the center-of-charge mode more efficient. The effects dominating the later stages of the cooling were attributed to the energy flow from the radial modes to the center-of-charge mode with time constants between 4–8 seconds.

These experimental results can be compared to the signals calculated according to equations (5.13). Figure 5.9 shows the temperatures, the coupling rate, and the resonant circuit signal for an ensemble of 30 C^{5+} ions after an excitation to $\langle E\rangle = 10\,\mathrm{eV} \approx k_B \cdot 10^5\,\mathrm{K}$. The coupling rate γ_ax given by the axial frequency width $\Delta\omega_z$ was calculated with $\mathrm{C}_4 = 10^{-6}$ and $\mathrm{C}_6 = 10^{-3}$ [155], the rate $\gamma_\mathrm{r} = 1/\tau_\mathrm{sct}$ was calculated from the axial temperature T_ax as described in section 5.3.5.

The resonant circuit signal produced by the model displays similar features as the measurements shown in figure 5.8. The temporal evolution of the signal can be described in three stages:

- During the first few hundreds of milliseconds the rate $\gamma_\mathrm{ax} > \gamma_\mathrm{cc}$ is large enough to provide efficient coupling of the axial degrees of freedom and the center-of-charge motion. As a consequence, both center of charge and the axial degrees of freedom are efficiently cooled for a duration of a few τ_1 (here: $\tau_1 = 100\,\mathrm{ms}$) with $\gamma_\mathrm{cc} \approx \gamma_1$. As a consequence of the fast cooling of the center-of-charge motion, the resonant circuit signal drops fast. During this first stage with high initial temperatures, the density – and thus the collisional thermalization γ_r – is low and radial degrees of freedom are only weakly coupled to the axial ones. Thus the temperature T_r is significantly larger than T_ax.

- During the second stage the signal develops a plateau when the exponential decay of the center-of-charge energy comes to a halt: The resistive cooling only reduces the energy of the axial and radial degrees of freedom, while the cc-mode temperature T_cc remains constant for many single-ion time constants τ_1.

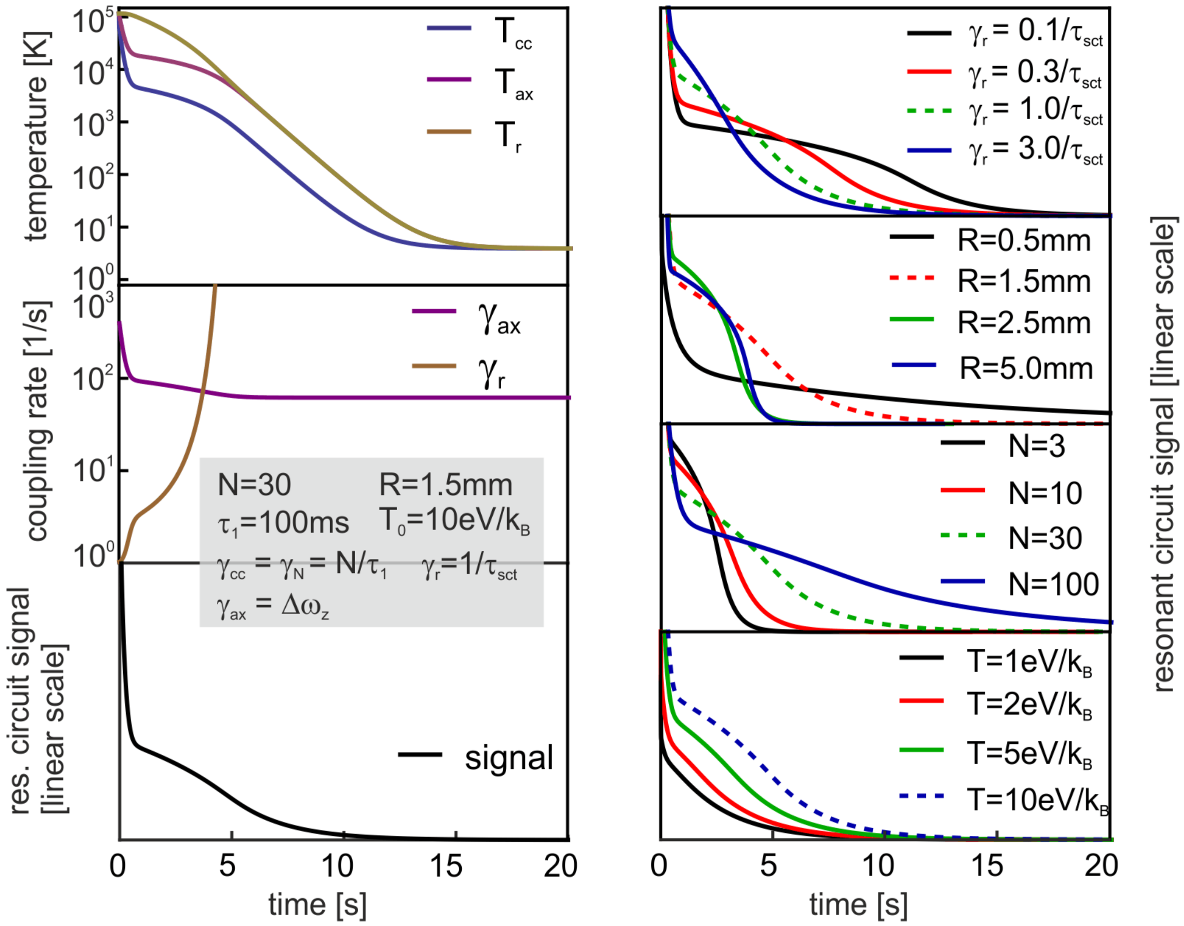

Figure 5.9: Left column: Simulation of the resistive cooling of 30 C^{5+} ions. The ion number $N = 30$, the width of the radial distribution $R = 1.5\,\text{mm}$, the initial temperature $T_0 = 10\,\text{eV}/k_B$, and the single-ion resistive cooling time $\tau_1 = 100\,\text{s}$ are fixed parameters. The coupling rates $\gamma_{\text{ax}} = \Delta\omega_z$ and $\gamma_{\text{r}} = \tau_{\text{sct}}$ are time dependent functions of the axial temperature T_{ax}. They are calculated according to equations (5.30) and (5.14). Right column: For each graph one of the simulation parameters given for the left column is varied while the not explicitly given parameters have the same values as before. In each graph the resonant circuit signal received with the standard parameter values is displayed with a dashed line.

The reason lies in the fact that both axial temperature T_{ax} (being coupled to the radial degrees of freedom) and axial coupling rate γ_{ax} are only weakly changing with time and provide a constant transfer of energy from the axial degrees of freedom to the center-of-charge mode.

Such a situation only occurs under certain circumstances: First, the radial distribution of the ions must give a significant contribution to the axial frequency width such that $\Delta\omega_z(E{=}0) \neq 0$. Else, a freeze-out of the axial coupling γ_{ax} occurs with decreasing temperature T_{ax}. As a consequence, the resonant circuit signal drops rapidly at first and shows a slow decay at later times, while cooling of the other degrees of freedom continues at a very low rate. An example for the described behavior can be seen in Fig. 5.9 (right column, R=0.5 mm).

A second condition is that the coupling γ_{r} strongly increases with decreasing T_{ax} so that the energy transfer remains constant for several seconds in spite of a decreasing temperature difference between axial and radial degrees of freedom. The increased coupling in the model is due to the Spitzer-self collision time that changes over several orders of magnitude in the course of the cooling process.

- The characteristic of the third stage is the thermalization between the axial and radial degrees of freedom, i.e. $T_{\mathrm{ax}} \approx T_{\mathrm{r}}$ because the density and therefore the Coulomb collision rate are high ($\gamma_{\mathrm{r}} \gg \gamma_{\mathrm{ax}}$). The axial temperature is already so low that the axial frequency width remains constant at a value that is solely determined by the radial dependence. The resulting resonant circuit signal shows an exponential decay, just like in the previously discussed case of resistive cooling with constant coupling rates (Fig. 5.7).

In the right column of figure 5.9 each graph demonstrates the influence of one specific parameter on the resonant circuit signal.

A reduction of the rate $\gamma_{\mathrm{r}} = 1/\tau_{\mathrm{sct}}$ by a factor of ten leads to a prolonged signal plateau that is even more similar to the experimental results. Since the Spitzer self-collision time τ_{sct} ranges over many orders of magnitude and several estimated parameters find their way into the calculation of τ_{sct}, this can still be considered as a good agreement between the model and the experiment.

The significance of the cloud radius R lies in the influence on the axial frequency width $\Delta\omega_z$. Under the given condition with a very small coefficient $C_4 = 10^{-6}$ the rate γ_{ax} for low temperatures $T_{\mathrm{ax}} \leq 10^4\,\mathrm{K}$ solely is determined by the radial dependency of ω_z. Since the signal plateau transforms into an exponential decay once $\gamma_{\mathrm{r}} \gg \gamma_{\mathrm{ax}}$, the plateau duration decreases with a too small radial ion distribution.

The signal shape obviously depends on the particle number N, since it scales the amount of energy that can be transferred from the $(2N-1)$ degrees of freedom to the center-of-charge mode. For an ion ensemble with N=100, the initial exponential decay during the first second ends at lower signal (i.e. lower temperature T_{cc}) than for smaller ion numbers. This effect can be attributed to the increased density and hence increased collision rate γ_{r}, which leads to a more efficient cooling of the indirectly cooled degrees of freedom during the initial phase. As a consequence, the temperatures T_{cc}, T_{ax} and T_{r} during the plateau phase are lowest for N=100. For times $t \geq 10\,\mathrm{s}$ the signal of the N=100 ion cloud still exceeds the ones of the smaller clouds, because of the larger amount of energy stored in the $(2N-1)$ degrees of freedom.

In both the experimental measurements (Fig. 5.8) and the results produced by the model (Fig. 5.9), it can be observed that the signal plateau is more pronounced for excitation energies larger than 5 eV. This can be explained by the fact that the initial rate γ_{ax} increases with a stronger excitation and the collision rate γ_{r} decreases due to the reduced density at higher temperatures: Hence the temperature difference

$T_\mathrm{r} - T_\mathrm{ax}$ that promotes the creation of the plateau increases for higher excitation energies.

Regarding the resistive cooling of highly charged ions at SpecTrap, the findings of the previous discussion allow several conclusions that may be relevant for future experiments.

Since the storage time of the HCI will be limited by collisions with residual gas, a rapid cooling is necessary and requires the choice of an adequate coefficient C_4. There will always be a trade-off between the coupling of the axial degrees of freedom to the center of charge – requesting a large coefficient C_4 – and the matching of the ions' oscillation frequency to the limited resonant circuit bandwidth on the other side. Since the requirements for C_4 may vary during the cooling process, this favors the current design with an electric compensation over a trap design that features geometrical compensation.

There are only few examples for the resistive cooling of highly charged ions reported in the literature and the understanding of the involved processes is relatively limited. This demonstrates that resistive cooling of HCI is not only a means for the cold probe preparation for spectroscopic experiments, but an interesting field of investigation by itself. Since the cooling process is determined by the different scaling of the coupling rates and the energy stored in the internal degrees of freedom, especially experiments with controllable ion numbers seem rewarding.

Experiments with a single or few HCI embedded in a cloud of a different ion species could offer insight into the internal structure of the cloud. For a two-species ion cloud, a mutual influence on the center-of-charge motion of each ion species was found [156]. In analogy to this, a single or a few highly charged ions could be treated as a test particle within a cloud of singly charged ions and thus directly probe the density and space charge of the surrounding ions. For a single ion embedded in a plasma, the axial oscillation frequency is expected to shift to lower frequencies due to the Debye shielding of the trap potential. Thus – as long the Debye length exceeds the dimension of the ion cloud – an excitation of the axial oscillation would directly probe the internal properties of the ion cloud.

6 Conclusion and outlook

During this work, laser-cooled ion crystals containing 10^3 to 10^5 singly charged magnesium ions (Mg^+) have been prepared in a Penning trap. The structure of the Coulomb crystals was analyzed and found to be in agreement with the planar shell model [84]. The ion crystals were prepared within seconds after their injection into the trap with an approach using a combination of buffer-gas and Doppler laser cooling. As a first step towards sympathetic cooling, additional ion species – both singly (H_2^+, C^+, N_2^+, CO_2^+) and multiply (Ar^{3+}) charged – were injected into the Mg^+ ion crystals without loss of the already stored Mg^+ ions. Sympathetic cooling was demonstrated via the charge-state lifetime of the Ar^{3+}, that was increased by several orders of magnitude as a consequence of the sympathetic cooling. These results pave the way to future investigations with highly charged ions, which will allow a stringent test of bound-state quantum electrodynamics.

In the course of this work, the external ion source for singly charged Mg^+ was developed and characterized. The maximal achieved ion number was 10^6 Mg^+ ions per bunch, which allows to load Mg^+ ion clouds that are large enough for sympathetic cooling with a single capture process. Compared to the previously used ion source design, where Mg^+ ion numbers of 10 to 50 Mg^+ ions per bunch were achieved [45], this new design features much higher ion production rates.

A LabVIEW based software was developed for control of the experimental devices and the data acquisition. With this software, the process of ion production, transport, capture into the trap and the consecutive laser cooling have been automated.

The creation of highly charged ions (Ar^{13+}) with an electron beam ion source (EBIS) and the transport via the HITRAP low-energy beamline were commissioned during this work, and bunches with several tens of thousands ions have been delivered to SpecTrap. The achieved ion numbers demonstrate that the ion production of mid-Z HCI with the EBIS is sufficient for the spectroscopy of laser-accessible fine structure transitions.

The capture of HCI into the trap was successfully demonstrated. However, a leak in the helium container of the superconducting magnet system contaminated the vacuum with helium gas. The partial pressure of the residual helium of $p \approx 10^{-8}$ mbar was orders of magnitudes larger than the pressure of other residual atoms and molecules. The elevated level of helium gas reduces the storage time of Ar^{13+} by several orders of magnitude to just a few milliseconds, as could be shown in the master thesis by K. König [38]. With such short storage times it was not possible to realize the cooling of the HCI or the intended spectroscopic experiments.

For this reason, it is planned to continue the experiments with a new magnet system. Commissioning is scheduled for 2018 and the system is expected to be opera-

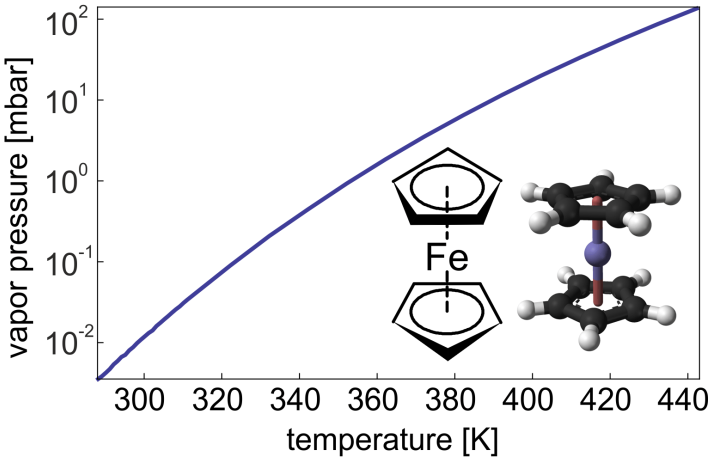

Figure 6.1: Vapor pressure of ferrocene $Fe(C_5H_5)_2$ [164]. Graphical representation of the molecule structure from [165].

tional in 2019. The new design differs from the old one in a few aspects: Instead of a liquid helium container, it will feature a superconducting magnet with a warm bore and the Penning trap and the cryo-electronic components will be cooled by a pulse tube cryocooler. The main advantage of this design is the reduction of liquid-helium consumption, which will reduce financial costs and allow a continuous use of the experiment. The pulse tube cryocooler is designed to reduce the temperature of the trap electrodes to a temperature of about 10 kelvin, so that cryo-cooling will reduce the residual gas pressure to much less than $p \ll 10^{-12}$ mbar. This will increase the storage time of HCI by several orders of magnitude compared to the current SpecTrap setup.

ion species	wavelength λ [nm]	lifetime	reference
$^{165}Ho^{66+}$	572.8(2)	-	[18]
$^{185}Re^{74+}$	456.0(3)	-	[9]
$^{187}Re^{74+}$	451.7(3)	-	[9]
$^{203}Tl^{80+}$	385.82(3)	-	[166]
$^{205}Tl^{80+}$	382.18(4)	-	[166]
$^{207}Pb^{81+}$	1019.7(2)	-	[20]
$^{209}Bi^{80+}$	1554.66(33)(10)	106.8(4.2) ms	[21, 73]
$^{209}Bi^{82+}$	243.8210(26)(28)	556(14) µs	[22, 73]

Table 6.1: A selection of optical transitions in high-Z HCI. All listed ions have a H-like electronic configuration, except for $^{209}Bi^{80+}$, which has a Li-like configuration.

First candidates for laser spectroscopy with the new magnet system are boron-like Ar^{13+} with a fine structure transition at 441 nm and potassium-like Kr^{17+} with a transition at 637 nm. Boron-like argon allows to study QED contributions to the fine structure transition energy and the upper-state lifetime [17, 71], whereas potassium-like krypton is an interesting exception from the Madelung rule with an 3d valence electron assigned to the ground state (instead of a 4s electron as in the case of potassium) [167].

A still wider range of ion candidates can be produced from metallocenes. Metallocene are compounds of typically two cyclopentadienyl anions ($C_5H_5^-$) which are bound to a metal center (M) in the oxidation state II, with the resulting general formula $(C_5H_5)_2M$. The prototype of a metallocene is ferrocene, which is stable under air and for temperatures up to 400°C, which makes it easy to handle [168]. Furthermore, it has already at ambient temperatures a large vapor pressure (Fig. 6.1), which allows to introduce it into an EBIT via a needle valve as easy as gaseous substances. This way the class of metallocenes allows in combination with an EBIS the production of metal ions without the need of a metal-ion source. Several iron charge states ($Fe^{9+,10+,12+,13+}$) have laser-accessible transitions in the wavelength range 530–1089 nm. The large variety of transitions in different iron charge states is a good opportunity to investigate an isonuclear series or for testing the sensitivity of the detectors designated for the transitions in high-Z highly charged ions.

Finally, once the HITRAP facility is fully operational, high-Z HCI will become available for SpecTrap and other experiments of the HITRAP collaboration. A selection of possible HCI candidates with a ground-state hyperfine structure splitting in the optical regime is given in table 6.1, with H-like $^{209}Bi^{82+}$ being the targeted candidate for a first set of measurements. The laser system for the hyperfine structure transition of H-like $^{209}Bi^{82+}$ with a wavelength of $\lambda = 244\,nm$ has already been developed and is described in [157] and [158].

B-like, $2P_{1/2} \rightarrow 2P_{3/2}$ ([159], p. 153)

	Si^{9+}	P^{10+}	S^{11+}	Cl^{12+}	Ar^{13+}	K^{14+}	Ca^{15+}
λ [nm]	1431.02	1030.82	761.28	574.34	441.39	344.74	273.13

C-like, $3P_0 \rightarrow 3P_1$ ([159], p. 55)

	P^{9+}	S^{10+}	Cl^{11+}	Ar^{12+}	K^{13+}	Ca^{14+}	Sc^{15+}
λ [nm]	2706.36	1913.51	1379.69	1011.94	755.29	571.69	417.89

O-like, $2P_2 \rightarrow 3P_1$ ([159], p. 159)

	S^{8+}	Cl^{9+}	Ar^{10+}	K^{11+}	Ca^{12+}	Sc^{13+}
λ [nm]	1252.03	921.74	691.75	527.87	408.83	320.82

F-like, ${}^2P_{3/2} \rightarrow {}^2P_{1/2}$ ([159], p. 160)

	P^{6+}	S^{7+}	Cl^{8+}	Ar^{9+}	Kr^{10+}	Ca^{11+}
λ [nm]	1376.63	992.03	735.79	553.81	425.86	333.02

Al-like, $2P_{1/2} \rightarrow 2P_{3/2}$ [160]

	Ti^{9+}	V^{10+}	Cr^{11+}	Mn^{12+}	Fe^{13+}	Co^{14+}	Ni^{15+}	Cu^{16+}
λ [nm]	1314.07	1026.63	813.79	653.46	530.82	435.7	360.99	301.64

Si-like, $3P_0 \rightarrow 3P_1$ ([161], p. 74–75)

	Fe^{12+}	Co^{13+}	Ni^{14+}	Cu^{15+}	Zn^{16+}
λ [nm]	1088.7				440.3

S-like, ${}^3P_1 \rightarrow {}^3P_2$ ([162], p. 354)

	Cr^{8+}	Mn^{9+}	Fe^{10+}	Co^{11+}	Ni^{12+}	Cu^{13+}	Zn^{14+}
λ [nm]	1278.6	998.1	789.4	632.1	511.7	418.2	344.9

Cl-like, ${}^2P^0_{3/2} \rightarrow {}^2P^0_{1/2}$ ([163], p. 368)

	Cr^{7+}	Mn^{8+}	Fe^{9+}	Co^{10+}	Ni^{11+}	Cu^{12+}	Zn^{13+}
λ [nm]	1076	841.3	688.1	538	438.5	361.3	300.5

Table 6.2: Ground-state fine structure transitions of medium-Z HCI in the laser-accessible regime.

A Additional material

A.1 QED contributions to atomic quantities

contributions	free electron g factor
Dirac value	1
(α/π)	$1.161\,409\,735\,4 \cdot 10^{-3} \pm 8 \cdot 10^{-12}$
$(\alpha/\pi)^2$	$-1.772\,305\,070 \cdot 10^{-6} \pm 2 \cdot 10^{-14}$
$(\alpha/\pi)^2$-muon	$2.804\,24 \cdot 10^{-12} \pm 4 \cdot 10^{-20}$
$(\alpha/\pi)^3$	$1.480\,42 \cdot 10^{-8} \pm 2 \cdot 10^{-16}$
$(\alpha/\pi)^4$	$-5.031\,31 \cdot 10^{-11} \pm 1 \cdot 10^{-18}$
exp. uncertainty	$2.8 \cdot 10^{-13}$

Table A.1: QED contributions to g/2 for the free electron. The values have been calculated with the expansion coefficients given in [169] and $\alpha^{-1} = 137.035\,998\,78(91)$ [170], which was determined independent of the electron g factor. All theoretical uncertainties are due to the uncertainty in α.

Lamb shift contributions	hydrogen [MHz]	U^{91+} [eV]
self-energy	8396.456(1)	
vacuum polarization	−215.168(1)	
QED first order	8181.288(2)	266.45
QED higher order	0.724(24)	−1.26(33)
radiative recoil corr.	−12.778(6)	
non-radiative recoil corr.	2.402(1)	
finite nuclear size	1.167(32)	
total	8172.802(40)	464.26(50)
experimental	8172.874(60)	460.20(460)

Table A.2: Contributions to the Lamb shift in hydrogen and H-like uranium. The values for hydrogen are dating 1995, using 0.862(12) fm as proton charge radius and are not including recent doubts on the reliability of the proton charge radius [171]. As of 2016, the current CODATA value for the proton charge radius is 0.8751(61). Values for U^{91+} taken from [12].

A.2 Digital-trigger processing

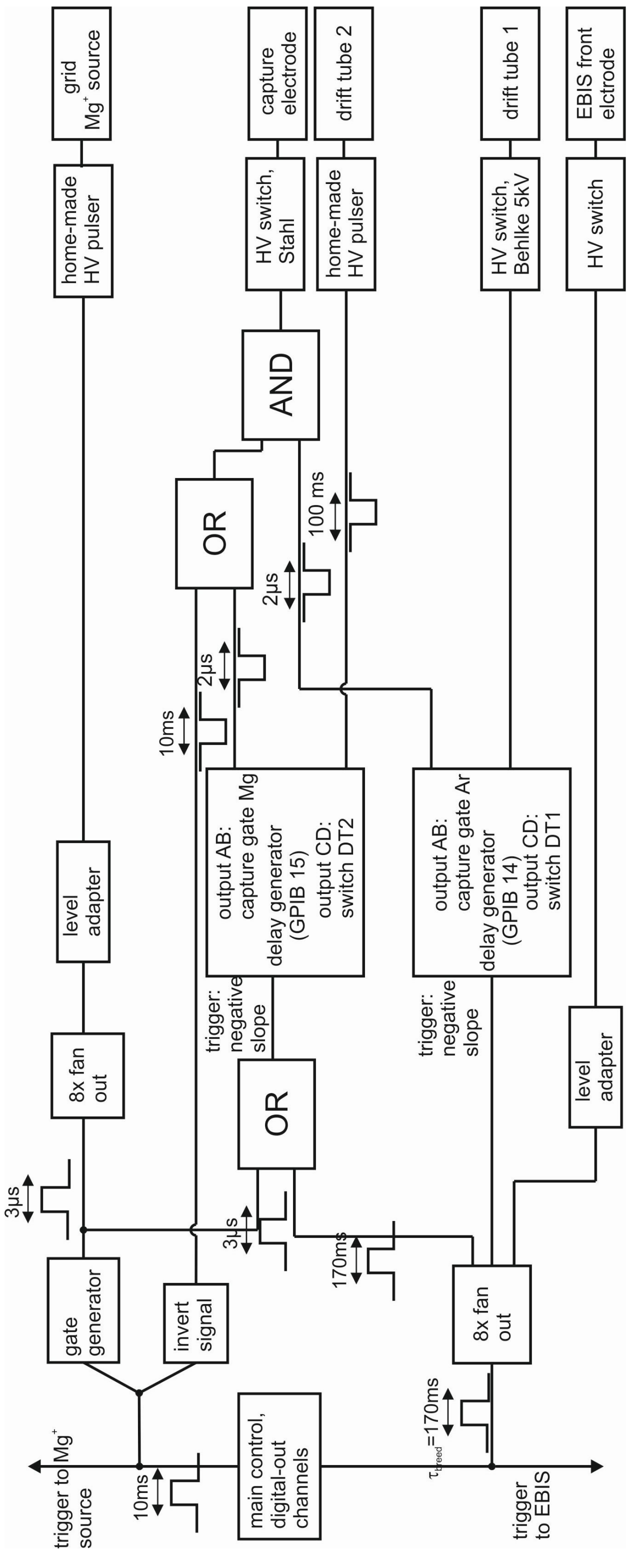
grid
Mg$^+$ source
home-made
HV pulser
capture
electrode
drift tube 2
HV switch,
Stahl
home-made
HV pulser
drift tube 1
EBIS front
elctrode
HV switch,
Behlke 5kV
HV switch
AND
OR
100 ms
2µs
2µs
10ms
output AB:
capture gate Mg
delay generator
(GPIB 15)
output CD:
switch DT2
output AB:
capture gate Ar
delay generator
(GPIB 14)
output CD:
switch DT1
level
adapter
trigger:
negative
slope
trigger:
negative
slope
8x fan
out
OR
level
adapter
3µs
3µs
170ms
gate
generator
invert
signal
8x fan
out
τ_{breed}=170ms
trigger to Mg$^+$
source
10ms
main control,
digital-out
channels
trigger
to EBIS

Figure A.1: Digital-trigger processing for ion capture.

A.3 Parameters of the HITRAP and SpecTrap beamline

HITRAP beamline		SpecTrap beamline	
	position [mm]		position [mm]
EBIS	0	Mg^+ source	0
FC EBIS	620	electrostatic bender	700
DK21	2620	DT2 (center)	2348
DK22	4830	NID / capture electrode center	2504
DK23	7380	trap center	2548
DK24	10720	SpecTrap MCP	3402
DT1	13740		
DK25	14210		

Table A.3: Positions of beamline elements of the (horizontal) HITRAP low-energy beamline and the (vertical) SpecTrap beamline.

cathode	−800 V
filament	12.5 V / 1.9 A
electron emission	20 mA
back capture electrode	4117 V
front capture electrode U_{hi} (U_{lo})	4070 V (3200 V)
extractor	−1800 V
breeding time	170 ms

Table A.4: EBIS settings for production of Ar^{13+}.

	up	down	left	right
segmented einzel lens	1120 V	1158 V	1139 V	1195 V

Table A.5: Voltages of the segmented einzel lens after the EBIS for ion transport with an energy per charge of 4 keV.

	bender +	bender -	kicker +	kicker -
dipole kicker-bender	435 V	490 V	320 V	200 V

Table A.6: Voltages of the dipole kicker-bender between DK3 and DK4 for ion transport with an energy per charge 4 keV.

	front electrodes		back electrodes		Δ back electrodes	
	horizontal	vertical	horizontal	vertical	horizontal	vertical
TR6QD5	140 V	110 V	180 V	120 V	-25 V	-20 V
TR7DQ1	82 V	82 V	87 V	92 V	0 V	0 V
TR7QD2	60 V	60 V	20 V	20 V	0 V	20 V
TR7QD3	190 V	220 V	190 V	210 V	-55 V	50 V
TR7QD4	280 V	280 V	280 V	280 V	-30 V	20 V
TR7QD5	240 V	240 V	240 V	240 V	-10 V	30 V
TR7QD6	202 V	204 V	202 V	190 V	-10 V	0 V
TR7QD7	0 V	0 V	0 V	0 V	0 V	0 V
TR7QD8	185 V	185 V	185 V	185 V	35 V	-10 V
TR7QD9	30 V	30 V	40 V	50 V	-30 V	18 V

Table A.7: Settings of the quadrupole doublets of the low-energy beamline. The values of the ISEG control software are given. The actual voltages may vary by an individual offset of the power supplies.

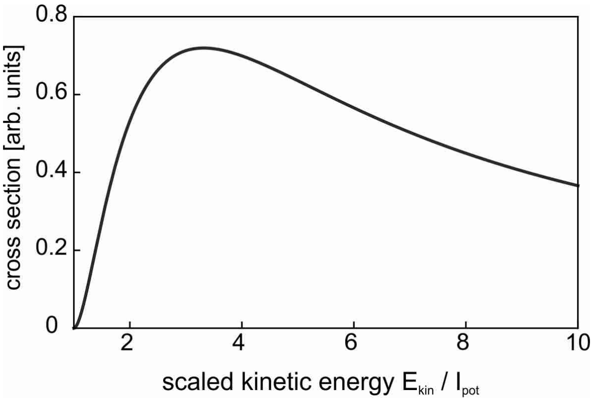

Figure A.2: Approximation of the electron-impact cross section. The electron kinetic energy is scaled by the ionization potential [173]. The ionization potentials for Mg and for typical residual gas molecules like H_2, N_2 and H_2O are $I_{\text{pot}} = 7.65$ eV, 15.43 eV, 15.58 eV and 12.62 eV, respectively [175].

	τ_{breed} [ms]	I_{MPS} [A]	TOF_{DT1} [μs]
Ar^{3+}	10	22.15	58.9
Ar^{4+}	13	18.93	50.6
Ar^{5+}	14	16.83	45.3
Ar^{6+}	16	15.28	41.25
Ar^{7+}	18	14.10	38.25
Ar^{8+}	25	13.15	35.7
Ar^{9+}	40	12.32	33.7
Ar^{10+}	60	11.65	32.0
Ar^{11+}	80	11.08	30.4
Ar^{12+}	155	10.58	29.1
Ar^{13+}	170	10.15	28.0
Ar^{14+}	230	9.70	26.9
Ar^{15+}	550	9.37	25.9
Ar^{16+}	800	9.05	25.2

Table A.8: The breeding time τ_{breed} in the EBIS and the current I_{MPS} at the MPS for production and transport of Ar^{n+} ions. The parameter TOF_{DT1} denotes the times of flight from the EBIS to the drift tube 1 with a kinetic energy of 4 keV per charge.

coefficient C_n^i	C_1^i	C_2^i	C_4^i	C_6^i
electrode i				
upper endcap	0.2542	0.1404	-0.0265	-0.0019
upper correction	0.0908	-0.0047	-0.0251	0.0150
capture electrode	0.00095	0.0007	0.00015	0.00001
ring electrode	0	-0.2729	0.1029	-0.0261

z_g=0.70 mm, z_0=6.3 mm, $d = 6.924\,\text{mm}$

tuning ratio $r = -C_4^{\text{up.end}}/C_4^{\text{up.cor}} = -1.05197$

coefficient C_n^i	C_1^i	C_2^i	C_4^i	C_6^i
electrode i				
upper endcap	0.2515	0.1429	-0.0259	-0.0027
upper correction	0.0961	-0.0029	-0.0281	0.0164
capture electrode	0.00091	0.0007	0.00015	0.00001
ring electrode	0	-0.2801	0.1084	-0.0283

z_g=0.80 mm, z_0=6.5 mm, $d = 7.015\,\text{mm}$

tuning ratio $r = -C_4^{\text{up.end}}/C_4^{\text{up.cor}} = -0.919148$

coefficient C_n^i	C_1^i	C_2^i	C_4^i	C_6^i
electrode i				
upper endcap	0.2501	0.1441	-0.0256	-0.0030
upper correction	0.0988	-0.0019	-0.0296	0.0171
capture electrode	0.00089	0.00071	0.00015	0.000013
ring electrode	0	-0.2837	0.1112	-0.0293

z_g=0.85 mm, z_0=6.6 mm, $d = 7.062\,\text{mm}$

tuning ratio $r = -C_4^{\text{up.end}}/C_4^{\text{up.cor}} = -0.8596$

coefficient C_n^i	C_1^i	C_2^i	C_4^i	C_6^i
electrode i				
upper endcap	0.2487	0.1453	-0.0253	-0.0035
upper correction	0.1015	-0.0009	-0.0312	0.0178
capture electrode	0.00087	0.0007	0.00015	0.000013
ring electrode	0	-0.2874	0.1142	-0.0306

z_g=0.90 mm, z_0=6.7 mm, $d = 7.109\,\text{mm}$

tuning ratio $r = -C_4^{\text{up.end}}/C_4^{\text{up.cor}} = -0.8041$

Table A.9: The expansion coefficients C_n^i of individual electrodes i and the tuning ratio r for different gap widths z_g. For each value of z_g, the values of the center-endcap distance z_0 and the characteristic distance d (as defined in Eq. (2.5)) are given.

	$\nu_z = 536.5\,\mathrm{kHz}$	$\nu_z = 1138.9\,\mathrm{kHz}$
$^{1}\mathrm{H}^{+}$	10.0 V	45.0 V
$^{4}\mathrm{He}^{2+}$	20.0 V	89.9 V
$^{209}\mathrm{Bi}^{82+}$	25.4 V	114.6 V
$^{4}\mathrm{He}^{+}$	39.9 V	179.9 V
$^{40}\mathrm{Ar}^{4+}$	99.8 V	449.7 V
$^{40}\mathrm{Ar}^{3+}$	133.0 V	599.6 V
$^{40}\mathrm{Ar}^{2+}$	199.6 V	899.3 V
$^{24}\mathrm{Mg}^{+}$	239.5 V	1079.2 V
$^{25}\mathrm{Mg}^{+}$	249.5 V	1124.2 V
$^{26}\mathrm{Mg}^{+}$	259.5 V	1169.2 V
$^{40}\mathrm{Ar}^{+}$	399.1 V	1798.7 V

Table A.10: Endcap voltages for the resonant circuit detection of various ions. The values were calculated for an ion at the trap center $r = 0$ with zero kinetic energy and a trap potential with the correction electrodes set to $U_{\mathrm{cor}} = -1.1\,U_{\mathrm{end}}$. The coefficients C_n^i as given in table 2.3 have been used.

A.4 Laser system, optical detection and atomic transitions

level	m$_j$	g$_j$	ΔE/(h·B) [GHz/T]
$^2S_{1/2}$	-1/2	2.0023	-14.0123
$^2S_{1/2}$	+1/2	2.0023	14.0123
$^2P_{3/2}$	-3/2	1+1.0023/3	-28.0085
$^2P_{3/2}$	-1/2	1+1.0023/3	-9.3362
$^2P_{3/2}$	+1/2	1+1.0023/3	9.3362
$^2P_{3/2}$	+3/2	1+1.0023/3	28.0085

Table A.11: Zeeman shift for the $^2\mathrm{S}_{1/2} \rightarrow {}^2\mathrm{P}_{3/2}$ transition in $^{24}\mathrm{Mg}^+$ according to $\Delta E = g_j m_j \mu_B B$, where g_j is the Landé factor, $\mu_B = -2\pi \cdot 13.9962\hbar$ GHz/T the Bohr magneton, and B the magnetic field ([64], p. 239).

fundamental (IR)	output power P= 2.0 W wavelength $\lambda = 1118.5408$ nm frequency $\nu = 2.680\,210 \cdot 10^{14}$Hz linewidth $\Delta\nu < 100$ kHz thermal tuning range 450 pm (25–45 °C) piezo tuning range 19 pm (0–200 V) piezo tuning range 4.6 GHz (0–200 V)
second harmonic (green)	output power 400 mW wavelength 560 nm
fourth harmonic (UV)	output power max. 20 mW (typ. 4 mW) wavelength 280 nm
beam profile at the trap center	$I(\rho) = I_0 e^{-2\rho^2/w_0^2}$, with $w_0 = 1 \pm 0.1$ mm
mean (peak) intensity for P=4 mW	1.27 (2.55) mW mm^{-2}
saturation intensity I_0 of Mg$^+$	2.4 mW mm^{-2}

Table A.12: Specifications of the laser system for Mg$^+$ laser cooling. Additional information can be found in [61].

element	transmission
lens at the ring electrode	0.92·0.95
LHe dewar window	0.92·0.95
vaccuum viewport	0.92·0.95
lens before detector/camera	0.92·0.95
cumulated transmission	$0.92^4 \cdot 0.95^4 = 0.58$
detector: diode front facet	0.96
CCD camera: window before chip & filter	0.92·0.95·0.55=0.48
total transmission: detector (CCD)	0.56 (0.28)
solid angle	$7.34 \cdot 10^{-3}$
QE at 280 nm for detector (CCD)	0.18 (0.05 to 0.35)
total detection efficiency ξ_{det} (ξ_{CCD})	$7 \cdot 10^{-4}$ ($1 \cdot 10^{-4}$ to $7 \cdot 10^{-4}$)

Table A.13: The detection efficiency of the SpecTrap imaging system for Mg^+ fluorescence at 280 nm. Transmission losses are accounted with 4% per boundary, the UV absorption with 5% for each optical element.

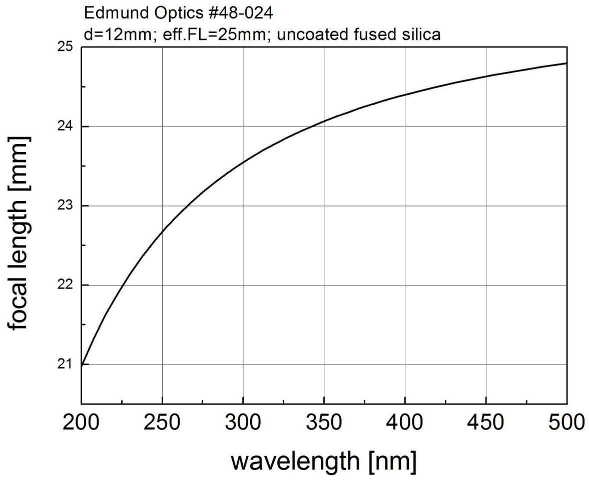

Figure A.3: The focal length of the lens for fluorescence imaging. Edmund Optics #48-024, d=12mm, effective focal length=25 mm, uncoated fused silica.

A.5 Emission characteristic of an oscillating dipole

In the framework of classical electrodynamics, the radiative power dissipation P of a charge oscillation along the z-axis of a spherical coordinate system is given by [70]

$$P = \oint \langle S \rangle \cdot \mathrm{d}A = \oint \frac{q^2 d^2 \omega^4 \sin^2\theta}{32\pi^2 \epsilon_0 c^3 r^2} \cdot \mathrm{d}A = \frac{q^2 d^2 \omega^4}{48\pi^2 \epsilon_0 c^3 r^2} \cdot 4\pi r^2, \tag{A.1}$$

where $\langle S \rangle$ denotes the temporal expectation value of the Poynting vector S. Looking at equation A.1, one finds that in the direction θ with the maximum intensity the Poynting vector is 1.5 times larger than the 4π-average.

A.6 The lineshape of atomic transitions

Natural linewidth

The line profile of a single atom or ion at rest can be characterized by merely two constants: the transition frequency ω_0 and the natural linewidth Γ. The normalized line shape is then given by the Fourier transform of a damped oscillation, which is a Lorentz curve (p. 43 in [174]):

$$\frac{I(\omega)}{I(\omega_0)} = g(\omega) = \frac{\Gamma/2\pi}{(\omega-\omega_0)^2 + (\Gamma/2)^2}, \quad \text{with} \int_0^\infty g(\omega) = 1. \tag{A.2}$$

The natural linewidth Γ is the full width at half maximum (FWHM) of the Lorentz curve defined by equation A.2.

Saturation broadening

The scattering rate Γ_{sc} is given by the product of the excited state population ρ_e and the natural linewidth Γ (Eq. 2.25 in [68]):

$$\Gamma_{sc} = \Gamma \cdot \rho_e. \tag{A.3}$$

In literature, the natural linewidth Γ is also denoted as the transition rate A. Both quantities can be used to express the upper state lifetime $\tau = 1/\Gamma = 1/A$.

In the case of a laser fluorescence experiment, all but the optical excitation mechanisms (as e.g. thermal excitation) can be neglected. Hence, the upper state population ρ_e is solely defined by the parameters of the irradiating laser light (Eq. 2.24–2.26 in [68]):

$$\rho_e = \frac{s}{2(1+s)} = \frac{s_0/2}{1 + s_0 + (2\Delta/\Gamma)^2}, \tag{A.4}$$

$$\text{with } s = \frac{s_0}{1 + (2\Delta/\Gamma)^2}, \tag{A.5}$$

$$\text{and with } s_0 = I/I_0 = I \cdot \frac{3\lambda_0^3}{\pi h c \Gamma}. \tag{A.6}$$

Here, s denotes the detuning dependent saturation parameter, $\Delta \equiv \omega - \omega_0$ the laser detuning, s_0 the on-resonance saturation, I the laser intensity, and λ_0 the transition wavelength. Equation A.6 defines the saturation intensity I_0, which is a function of the characteristics of the transition only.

Inserting equation (A.4), (A.5) into (A.3) one receives the total scattering rate Γ_{sc} in terms of the laser intensity and detuning (Eq. 2.26 in [68]):

$$\Gamma_{sc} = \Gamma \cdot \rho_e = \Gamma \cdot \frac{s_0/2}{1 + s_0 + (2\Delta/\Gamma)^2}. \tag{A.7}$$

The maximum possible scattering rate is achieved in the limit of high intensities when $s_0 \gg 1$ and the scattering rate Γ_{sc} saturates to $\Gamma/2$. When $I = I_0$, the on-resonance saturation becomes $s_0 = 1$ and the on-resonance scattering rate thus is $\Gamma/4$.

Equation A.7 can be rewritten to

$$\begin{aligned} \Gamma_{sc} &= \left(\frac{s_0}{1+s_0}\right)\left(\frac{\Gamma/2}{1+(2\Delta/\Gamma')^2}\right), && \text{(A.8)} \\ \text{where } \Gamma' &= \Gamma\sqrt{1+s_0}. && \text{(A.9)} \end{aligned}$$

Comparison with equation A.2 shows that under the influence of laser irradiation the lineprofile has again a Lorentzian lineshape with the power-broadened FWHM Γ'. This broadening of an atomic resonance under influence of (laser) irradiation is consequently referred to as saturation broadening.

For Mg^+ ions the natural linewidth Γ and the saturation intensity I_0 of the ${}^2S_{1/2} \rightarrow {}^2P_{3/2}$ transition is given by [62, 63]

$$\begin{aligned} \Gamma &= \frac{16\pi^3\nu^3}{3\epsilon_0 hc^3}|M_{ik}| = 2.60(1)\cdot 10^8 \mathrm{s}^{-1} = 2\pi \cdot 41.5(2)\cdot 10^6\,\mathrm{s}^{-1}, && \text{(A.10)} \\ \tau &= 1/\Gamma = 3.84(10)\,\mathrm{ns}, && \text{(A.11)} \\ I_0 &= \pi hc/(3\lambda_0^3\tau) = 2.46\,\mathrm{mW/mm^2}. && \text{(A.12)} \end{aligned}$$

Doppler broadening

For a single ion moving with velocity v_z the absorption frequency ω_0 is altered by the Doppler effect in first order to the frequency ω (p. 46 in [174]):

$$\omega = \omega_0 \cdot (1 + v_z/c). \tag{A.13}$$

In (A.13) the speed of light is denoted c. For an ensemble of particles at thermal equilibrium, the probabilities for the ion velocities are distributed according to the Maxwellian distribution

$$n(v_z)\,\mathrm{d}v_z = \frac{N}{v_w\sqrt{\pi}} e^{-(v_z/v_w)^2}\,\mathrm{d}v_z, \quad \text{where} \quad v_w = \sqrt{2k_B T/m}. \tag{A.14}$$

Using (A.13), equation (A.14) can be rewritten to yield the number of particles with resonance frequencies between ω and $\omega + \mathrm{d}\omega$:

$$n_i(\omega)\,\mathrm{d}\omega = N\frac{c}{v_w \omega_0 \sqrt{\pi}} \exp\left[-\left(\frac{\omega - \omega_0}{\omega_0 v_w / c}\right)^2\right] \mathrm{d}\omega. \tag{A.15}$$

In Eq. (A.14, A.15), $v_w = (2k_B T/m)^{1/2}$ denotes the velocity with highest probability, N the total number of particles, m the ion mass, T the temperature and k_B the Boltzmann constant. For typical temperatures of $T \geq 300\,\mathrm{K}$ the line profile is dominated by Doppler broadening and is then given by a Gaussian distribution

$$I(\omega) = I(\omega_0) \exp\left[-\left(\frac{\omega - \omega_0}{\omega_0 v_w / c}\right)^2\right], \tag{A.16}$$

with standard deviation $\sigma_D = \omega_0 v_w / (\sqrt{2}c)$ and FWHM $\delta\omega_D = \sigma_D \cdot 2\sqrt{2 \ln 2}$:

$$\delta\omega_D = 2\sqrt{\ln 2}\,\omega_0 v_w / c = \frac{\omega_0}{c}\sqrt{\frac{8 k_B T \ln 2}{m}}. \tag{A.17}$$

However, for laser cooled ions with temperatures in the millikelvin regime, the Doppler width is typically smaller than or comparable to the natural linewidth. In this case, the line shape is not of purely Gaussian shape but exhibits a Voigt profile, which is the convolution of the Lorentzian line shape given by Eq. (A.2) with a normal distribution as defined in Eq. (A.16):

$$I(\omega) = C \int_0^\infty \frac{\exp\left(-c^2(\omega - \omega')^2 / (\omega'^2 v_w^2)\right)}{(\omega - \omega')^2 + (\Gamma/2)^2}, \quad \text{where } C = \Gamma I_0 N c / (2\pi^{3/2} \omega_0 v_w). \tag{A.18}$$

A.7 Matrix element for electric dipole transitions

The transition probabilities of the $\sigma^\pm$- and π-transitions of an electric dipole transition are defined by the matrix elements of the transition [176]:

$$\langle \phi_n | \hat{\epsilon} \cdot r | \phi_i \rangle = \sqrt{\frac{(2l_i + 1)}{(2n_i + 1)}} \langle l_n 0 | l_i 100 \rangle \int_0^\infty r^3 dr R^*_{n_n l_n} R_{n_i l_i} \tag{A.19}$$

$$\left(\epsilon_z \langle l_n m_n | l_i 1 m_i 0 \rangle + \frac{-\epsilon_x + \epsilon_y}{\sqrt{2}} \langle l_n m_n | l_i 1 m_i 1 \rangle + \frac{\epsilon_x + \epsilon_y}{\sqrt{2}} \langle l_n m_n | l_i 1 m_i - 1 \rangle \right) \tag{A.20}$$

Here, the angular momentums of the final state, the initial state and the photon are denoted l_n, l_i and 1. The respective z-components of the angular momentums are denoted m_n, m_i, m, and $\langle l_n m_n | l_i 1 m_i m \rangle$ denotes the Clebsch-Gordan coefficient for a transition from the initial state i to the final state n.

B List of publications

Publications in peer-reviewed journals

T. Murböck, S. Schmidt, G. Birkl, W. Nörtershäuser, R.C. Thompson, and M. Vogel
Rapid crystallization of externally produced ions in a Penning trap, Phys. Rev. A **94**, 043410 (2016)

T. Murböck, S. Schmidt, Z. Andelkovic, G. Birkl, W. Nörtershäuser, and M. Vogel
A compact source for bunches of singly charged atomic ions, Rev. Sci. Instrum. **87**, 043302 (2016)

S. Schmidt, T. Murböck, Z. Andelkovic, G. Birkl, W. Nörtershäuser, S. Stahl, and M. Vogel
Non-destructive single-pass low-noise detection of ions in a beamline, Rev. Sci. Instrum. **86**, 113302 (2015)

Z. Andelkovic, F. Herfurth, N. Kotovskiy, K. König, B. Maaß, T. Murböck, D. Neidherr, S. Schmidt, J. Steinmann, M. Vogel, and G. Vorobjev
Beamline for low-energy transport of highly charged ions at HITRAP, Nucl. Instr. Meth. Phys. Res. A **795**, 109 (2015)

J. Ullmann, Z. Andelkovic, A. Dax, W. Geithner, C. Geppert, C. Gorges, M. Hammen, V. Hannen, S. Kaufmann, K. König, Y. Litvinov, M. Lochmann, B. Maass, J. Meisner, T. Murböck, R. Sánchez, M. Schmidt, S. Schmidt, M. Steck, T. Stöhlker, R.C. Thompson, J. Vollbrecht, C. Weinheimer and W. Nörtershäuser
An improved value for the hyperfine splitting of hydrogen-like $^{209}Bi^{82+}$, J. Phys. B **48**, 144022 (2015)

Conference contributions

Z. Andelkovic, G. Birkl, S. Fedotova, V. Hannen, F. Herfurth, K. König, N. Kotovskiy, B. Maaß, J. Vollbrecht, T. Murböck, D. Neidherr, W. Nörtershäuser, S. Schmidt, M. Vogel, G. Vorobjev, C. Weinheimer
Status of deceleration and laser spectroscopy of highly charged ions at HITRAP, Hyperfine Interact **235**, 37 (2015)

R. Sánchez, J. Ullmann, J. Vollbrecht, Z. Andelkovic, A. Dax, W. Geithner, Ch. Geppert, Ch. Gorges, M. Hammen, V. Hannen, S. Kaufmann, K. König, Yu.A. Litvinov, M. Lochmann, B. Maaß, J. Meisner, T. Murböck, W. Nörtershäuser, S. Schmidt, M. Schmidt, M. Steck, Th. Stöhlker, R.C. Thompson and Ch. Weinheimer, *Hyperfine transition in* $^{209}Bi^{80+}$ *– one step forward*, Phys. Scripta **T166**, (2015)

M. Vogel, Z. Andelkovic, G. Birkl, S. Ebrahimi, V. Hannen, D. von Lindenfels, A. Martin, T. Murböck, W. Nörtershäuser, W. Quint, S. Schmidt, D.M. Segal, R.C. Thompson, J. Vollbrecht, Ch. Weinheimer and M. Wiesel
Penning-trap experiments for spectroscopy of highly-charged ions at HITRAP, Phys. Scr. **2015**, 014066 (2015)

T. Murböck, S. Albrecht, Z. Andelkovic, R. Cazan, V. Hannen, R. Jöhren, J. Vollbrecht, S. Schmidt, D. Segal, R. Thompson, M. Vogel, C. Weinheimer, W. Nörtershäuser, and G. Birkl
SpecTrap: precision spectroscopy of highly charged ions – status and prospects, Phys. Scr. **T156**, 014096 (2013)

Bibliography

[1] W.E. Lamb and R.C. Retherford, *Fine Structure of the Hydrogen Atom by a Microwave Method*, Phys. Rev. **72**, 241 (1947)

[2] N.M. Kroll and W.E. Lamb, *On the Self-Energy of a Bound Electron*, Phys. Rev. **75**, 288 (1949)

[3] D.J. Berkeland, E.A. Hinds, and M. G. Boshier, *Precise Optical Measurement of Lamb Shifts in Atomic Hydrogen*, Phys. Rev. Lett. **75**, 2470 (1995)

[4] R.S. Van Dyck, Jr., P.B. Schwinberg, and H.G. Dehmelt, in *Atomic Physics 9*, edited by R.S. Van Dyck, Jr., and E.N. Fortson (World Scientific, Singapore, 1984), p. 53

[5] R.S. Van Dyck, Jr., P.B. Schwinberg, and H.G. Dehmelt, *New High-Precision Comparison of Electron and Positron g Factors*, Phys. Rev. Lett. **59**, 26 (1987)

[6] D. Hanneke, S. Fogwell, and G. Gabrielse, *New Measurement of the Electron Magnetic Moment and the Fine Structure Constant*, Phys. Rev. Lett. **100**, 120801 (2008)

[7] T. Beier, *The g_j factor of a bound electron and the hyperfine structure splitting in hydrogenlike ions*, Phys. Rep. **339**, 79 (2000)

[8] V.M. Shabaev, Hyperfine structure of hydrogen-like ions, J. Phys. B **27**, 5825 (1994)

[9] J.R. Crespo López-Urrutia, P. Beiersdorfer, K. Widmann, B.B. Birkett, A.-M. Martensson-Pendrill, and M.G.H. Gustavsson, *Nuclear magnetization distribution radii determined by hyperfine transitions in the 1s level of H-like ions $^{185}Re^{74+}$ and $^{187}Re^{74+}$*, Phys. Rev. A **57**, 879 (1998)

[10] Th. Stöhlker, P.H. Mokler, K. Beckert, F. Bosch, H. Eickhoff, B. Franzke, M. Jung, Y. Kandler, O. Klepper, C. Kozhuharov, R. Moshammer, F. Nolden, H. Reich, P. Rymuza, P. Spädtke, and M. Steck, *Ground-state Lamb shift for hydrogenlike uranium measured at the ESR storage ring*, Phys. Rev. Lett. **71**, 2184 (1993)

[11] Th. Stöhlker, P.H. Mokler, F. Bosch, R.W. Dunford, F. Franzke, O. Klepper, C. Kozhuharov, T. Ludziejewski, F. Nolden, H. Reich, P. Rymuza, Z. Stachura, M. Steck, P. Swiat, and A. Warczak, *1s Lamb Shift in Hydrogenlike Uranium Measured on Cooled, Decelerated Ion Beams*, Phys. Rev. Lett. **85**, 3109 (2000)

[12] A. Gumberidze, Th. Stöhlker, D. Banaś, K. Beckert, P. Beller, H.F. Beyer, F. Bosch, S. Hagmann, C. Kozhuharov, D. Liesen, F. Nolden, X. Ma, P.H. Mokler, M. Steck, D. Sierpowski, and S. Tashenov, *Quantum Electrodynamics in Strong Electric Fields: The Ground-State Lamb Shift in Hydrogenlike Uranium*, Phys. Rev. Lett. **94**, 223001 (2005)

[13] M. Vogel, *The anomalous magnetic moment of the electron*, Contemporary Physics **50**, 437 (2009)

[14] S. Sturm, A. Wagner, M. Kretzschmar, W. Quint, G. Werth, and K. Blaum, *g-factor measurement of hydrogen-like* $^{28}Si^{13+}$ *as a challenge to QED calculations*, Phys. Rev. A **87**, 030501(R) (2013)

[15] M. Vogel and W. Quint, *Trap-assisted precision spectroscopy of forbidden transitions in highly-charged ions*, Phys. Rep. **490**, 1 (2010)

[16] K. Hosaka, D.N. Crosby, K. Gaarde-Widdowson, C.J. Smith, J.D. Silver, T. Kinugawa, S. Ohtani, and E.G. Myers, *Laser spectroscopy of hydrogenlike nitrogen in an electron beam ion trap*, Phys. Rev. A **69**, 011802 (2004)

[17] V. Mäckel, R. Klawitter, G. Brenner, J.R. Crespo López-Urrutia, and J. Ullrich, *Laser Spectroscopy on Forbidden Transitions in Trapped Highly Charged* Ar^{13+} *Ions*, Phys. Rev. Lett. **107**, 143002 (2011)

[18] J.R. Crespo López-Urrutia, P. Beiersdorfer, D.W. Savin, and Klaus Widmann, *Direct Observation of the Spontaneous Emission of the Hyperfine Transition F=4 to F=3 in Ground State Hydrogenlike* $^{165}Ho^{66+}$ *in an Electron Beam Ion Trap*, Phys. Rev. Lett. **77**, 826 (1996)

[19] I. Klaft, S. Borneis, T. Engel, B. Fricke, R. Grieser, G. Huber, T. Kühl, D. Marx, R. Neumann, S. Schröder, P. Seelig, and L. Völker, *Precision Laser Spectroscopy of the Ground State Hyperfine Splitting of Hydrogenlike* $^{209}Bi^{82+}$, Phys. Rev. Lett. **73**, 2425 (1994)

[20] P. Seelig, S. Borneis, A. Dax, T. Engel, S. Faber, M. Gerlach, C. Holbrow, G. Huber, T. Kühl, D. Marx, K. Meier, P. Merz, W. Quint, F. Schmitt, M. Tomaselli, L. Völker, H. Winter, M. Würtz, K. Beckert, B. Franzke, F. Nolden, H. Reich, M. Steck, and T. Winkler, Phys. Rev. Lett. **81**, 4824 (1998)

[21] M. Lochmann, R. Jöhren, C. Geppert, Z. Andelkovic, D. Anielski, B. Botermann, M. Bussmann, A. Dax, N. Frömmgen, M. Hammen, V. Hannen, T. Kühl, Y.A. Litvinov, R. López-Coto, Thomas Stöhlker, R.C. Thompson, J. Vollbrecht, A. Volotka, C. Weinheimer, W. Wen, E. Will, D. Winters, R. Sánchez, and W. Nörtershäuser, *Observation of the hyperfine transition in lithium-like bismuth* $^{209}Bi^{80+}$*: Towards a test of QED in strong magnetic fields*, Phys. Rev. A **90**, 030501 (2014)

[22] J. Ullmann, Z. Andelkovic, A. Dax, W. Geithner, C. Geppert, C. Gorges, M. Hammen, V. Hannen, S. Kaufmann, K. König, Y. Litvinov, M. Lochmann, B. Maaß,

J. Meisner, T. Murböck, R. Sánchez, M. Schmidt, S. Schmidt, M. Steck, T. Stöhlker, R.C. Thompson, J. Vollbrecht, C. Weinheimer and W. Nörtershäuser, *An improved value for the hyperfine splitting of hydrogen-like* $^{209}Bi^{82+}$, J. Phys. B **48**, 144022 (2015)

[23] A. Martin, P. Baus, and G. Birkl, *External Cavity Diode Laser Setup with Two Interference Filters*, submitted to Applied Physics B

[24] Ingolf V. Hertel and Claus-Peter Schulz, *Atome, Moleküle und optische Physik I*, Springer-Verlag Berlin Heidelberg (2008)

[25] J.D. Gillaspy, *Highly charged ions*, J. Phys. B **34**, R93 (2001)

[26] V.M. Shabaev, M.B. Shabaeva, I.I. Tupitsyn, V.A. Yerokhin, A.N. Artemyev, T.Kühl, M.Tomaselli, and O.M. Zherebtsov, *Transition energy and lifetime for the ground-state hyperfine splitting of high-Z lithiumlike ions*, Phys. Rev. A **57**, 149 (1998)

[27] O.V. Andreev, D.A. Glazov, A.V. Volotka, V.M. Shabaev, and G. Plunien, *Evaluation of the screened vacuum-polarization corrections to the hyperfine splitting of Li-like bismuth*, Phys. Rev. A **85**, 022510 (2012)

[28] V.M. Shabaev, A.N. Artemyev, V.A. Yerokhin, O.M. Zherebtsov, and G. Soff, *Towards a Test of QED in Investigations of the Hyperfine Splitting in Heavy Ions*, Phys. Rev. Lett. **86**, 3959 (2001)

[29] J. Ullmann, Z. Andelkovic, C. Brandau, A. Dax, W. Geithner, C. Geppert, C. Gorges, M. Hammen, V. Hannen, S. Kaufmann, K. König, Y. Litvinov, M. Lochmann, B. Maaß, J. Meisner, T. Murböck, R. Sánchez, M. Schmidt, S. Schmidt, M. Steck, T. Stöhlker, R.C. Thompson, C. Trageser, J. Vollbrecht, C. Weinheimer and W. Nörtershäuser, *High precision hyperfine measurements in* $^{209}Bi^{80+}$ *and* $^{209}Bi^{82+}$ *challenge bound-state strong-field QED*, in preparation

[30] H.-J. Kluge, T. Beier, K. Blaum, L. Dahl, S. Eliseev, F. Herfurth, B. Hofmann, O. Kester, S. Koszudowski, C. Kozhuharov, G. Maero, W. Nörtershäuser, J. Pfister, W. Quint, U. Ratzinger, A. Schempp, R. Schuch, T. Stöhlker, R.C. Thompson, M. Vogel, G. Vorobjev, D.F.A. Winters, and G. Werth, *HITRAP: A facility at GSI for highly charged ions*, Adv. Quantum Chem. **53**, 83 (2008)

[31] S. Fedotova, E. Boulton, N.P.M. Brantjes, F. Herfurth, N. Kotovskiy, C. Krantz, D. Neidherr, J. Steinmann and G. Vorobjev, *Cooling of highly charged ions - the HITRAP facility and Cooler trap*, Phys. Scripta **T156**, 014095 (2013)

[32] R. Geller, *Electron Cyclotron Resonance Ion Sources and ECR Plasmas*, Institute of Physics Publishing, Bristol and Philadelphia, ISBN 978-0-7503-0107-7 (1996)

[33] T. Ditmire, J.W.G. Tisch, E. Springate, M.B. Mason, N. Hay, R.A. Smith, J. Marangos, and M.H.R. Hutchinson, *High-energy ions produced in explosions of superheated atomic clusters*, Nature **386**, 54 (1997)

[34] R.E. Marrs, S.R. Elliott, and D.A. Knapp, *Production and Trapping of Hydrogen-like and Bare Uranium Ions in an Electron Beam Ion Trap*, Phys. Rev. Lett. **72**, 4082 (1994)

[35] J.W. McDonald, R.W. Bauer, and D.H.G. Schneider, *Extraction of highly charged ions (up to 90+) from a high-energy electron-beam ion trap*, Rev. Sci. Instrum. **73**, 30 (2002)

[36] Z. Andelkovic, F. Herfurth, N. Kotovskiy, K. König, B. Maaß, T. Murböck, D. Neidherr, S. Schmidt, J. Steinmann, M. Vogel, and G. Vorobjev, *Beamline for low-energy transport of highly charged ions at HITRAP*, Nucl. Instr. Meth. Phys. Res. A **795**, 109 (2015)

[37] T. Murböck, S. Schmidt, Z. Andelkovic, G. Birkl, W. Nörtershäuser, and M. Vogel, *A compact source for bunches of singly charged atomic ions*, Rev. Sci. Instrum. **87**, 043302 (2016)

[38] K. König, *Inbetriebnahme der Niederenergiestrahlstrecke bei HITRAP und erstmaliger Einfang hochgeladener Ionen in der SpecTrap Penningfalle*, Master thesis, Technische Universität Darmstadt (2014)

[39] S. Schmidt, T. Murböck, Z. Andelkovic, G. Birkl, W. Nörtershäuser, S. Stahl, and M. Vogel, *Non-destructive single-pass low-noise detection of ions in a beamline*, Rev. Sci. Instrum. **86**, 113302 (2015)

[40] A. Sokolov, *Charge breeding investigation in EBIS/T and collision study of ions with cold atoms for HITRAP*, Ph.D. dissertation, Universität Heidelberg (2010)

[41] Z. Andelkovic, *Setup of a Penning trap for precision laser spectroscopy at HITRAP*, Ph.D. dissertation, Universität Mainz (2012)

[42] C.L. Yaws, *Handbook of Vapor Pressure: Volume 4*, Gulf Publishing, Houston (1995)

[43] R. Boiviny and S. Srivastava, *Electron-impact ionization of Mg*, J. Phys. B **31**, 2381 (1998)

[44] I. Bray, K. McNamara, and D.V. Fursa, *Calculation of electron-impact ionization of Mg and Al$^+$*, Phys. Rev. A **92**, 022705 (2015)

[45] R. Cazan, *Preparation of Cold Mg$^+$ Ion Clouds for Sympathetic Cooling of Highly Charged Ions at SPECTRAP*, Ph.D. dissertation, Universität Mainz (2012)

[46] G. Werth, V.N. Gheorghe, F.G. MajorRef. Werth, *Charged Particle Traps II*, Springer-Verlag Berlin Heidelberg (2009)

[47] P. Ghosh, *Ion Traps*, Oxford Science Publications (1995)

[48] L.S. Brown and G. Gabrielse, *Geonium theory: Physics of a single electron or ion in a Penning trap*, Rev. Mod. Phys. **58**, 233 (1986)

[49] G. Gabrielse and F.C. Mackintosh, *Cylindcrical Penning traps with orthogonalized anharmonicity compensation*, Int. J. Mass Spectrom. **57**, 1 (1984)

[50] D. von Lindenfels, *Development of an Ion Trap Experiment for the Measurement of the Electron Magnetic Moment by Double-Resonance Spectroscopy*, diploma thesis, Universität Heidelberg (2010)

[51] J. Steinmann, *Analytical and numerical investigations of resistive cooling of trapped ion clouds*, Ph.D. dissertation, Universität Erlangen-Nürnberg (2016)

[52] M. Vogel, H. Häffner, K. Hermanspahn, S. Stahl, J. Steinmann, and W. Quint, *Resistive and sympathetic cooling of highly-charged-ion clouds in a Penning trap*, Phys. Rev. A **90**, 043412 (2014)

[53] H. Häffner, T. Beier, S. Djekic, N. Hermanspahn, H.-J. Kluge, W. Quint, S. Stahl, J. Verdu, T. Valenzuela, and G. Werth, *Double Penning trap technique for precise g factor determinations in highly charged ions*, Eur. Phys. J. D **22**, 163 (2003)

[54] L. Gruber, J.P. Holder, and D. Schneider, *Formation of Strongly Coupled Plasmas from Multi-Component Ions in a Penning Trap*, Phys. Scr. **71**, 60 (2005)

[55] S. Ulmer, H. Kracke, K. Blaum, S. Kreim, A. Mooser, W. Quint, C.C. Rodegheri, and J. Walz, *The quality factor of a superconducting rf resonator in a magnetic field*, Rev. Sci. Instrum. **80**, 123302 (2009)

[56] M. Diederich, H. Häffner, N. Hermanspahn, M. Immel, H.J. Kluge, R. Ley, R. Mann, W. Quint, S. Stahl, and G. Werth, *Observation of the Continuous Stern-Gerlach Effect on an Electron Bound in an Atomic Ion*, Hyperfine Interact. **115**, 185 (1998)

[57] St. Stahl, *Aufbau eines Experimentes zur Bestimmung elektronischer g-Faktoren einzelner wasserstoffähnlicher Ionen*, Ph.D. dissertation, Universität Mainz (1998)

[58] P. Horowitz, and W. Hill, *The art of electronics*, Cambridge University Press (1994)

[59] S.M. Brewer, N.D. Guise, and J.N. Tan, *Capture and isolation of highly charged ions in a unitary Penning trap*, Phys. Rev. A **88**, 063403 (2013)

[60] R. Cazan, C. Geppert, W. Nörtershäuser, and R. Sánchez, *Towards sympathetic cooling of trapped ions with laser-cooled* Mg^+ *ions for mass spectrometry and laser spectroscopy*, Hyperfine Interact. **196**, 177 (2010)

[61] S. Schmidt, *Untersuchung mesoskopischer Coulomb-Kristalle zum sympathetischen Kühlen hochgeladener Ionen und direkte Bestimmung der Massendifferenz von* ^{123}Te *und* ^{123}Sb, Ph.D. dissertation, Universität Mainz (2016)

[62] M. Herrmann, V. Batteiger, S. Knünz, G. Saathoff, Th. Udem, and T.W. Hänsch, *Frequency metrology on single trapped ions in the weak binding limit: the* $3s_{1/2}$ – $3p_{3/2}$ *transition in* $^{24}Mg^{+}$, Phys. Rev. Lett. **102**, 013006 (2009)

[63] NIST atomic spectra database

[64] H. Haken and C. Wolf, *Atom- und Quantenphysik*, 7th edition, Springer (2000)

[65] D.J. Wineland, J.C. Bergquist, W.M. Itano, and R.E. Drullinger, *Double-resonance and optical-pumping experiments on electromagnetically confined, laser-cooled ions*, Optics Letters **5**, 245 (1980)

[66] R.G. Hulet and D.J. Wineland, *Quantum jumps via spontaneous Raman scattering*, Phys. Rev. A **36**, 2758 (1987)

[67] H.F. Powell, M.A. van Eijkelenborg, W. Irvine, D.M. Segal and R.C. Thompson, *Quantum jumps in singly ionized magnesium*, J. Phys. B **35**, 205 (2002)

[68] H. Metcalf and P. van der Straten, *Laser Cooling and Trapping*, Springer-Verlag New York, 2nd printing (2002)

[69] D. Budker, D. Kimball, and D. DeMille, *Atomic Physics*, 2nd edition, Oxford University Press (2008), p. 152ff

[70] W. Demtröder, *Experimentalphysik 2*, Springer-Verlag Berlin Heidelberg, 4. Auflage (2006), Seite 184

[71] A. Lapierre, U.D. Jentschura, J.R. Crespo López-Urrutia, J. Braun, G. Brenner, H. Bruhns, D. Fischer, A.J. González Martínez, Z. Harman, W.R. Johnson, C.H. Keitel, V. Mironov, C.J. Osborne, G. Sikler, R. Soria Orts, V. Shabaev, H. Tawara, I.I. Tupitsyn, J. Ullrich, and A. Volotka, *Relativistic Electron Correlation, Quantum Electrodynamics, and the Lifetime of the* $1s^2 2s^2 2p^2 P^o{}_{3/2}$ *Level in Boronlike Argon*, Phys. Rev. Lett. **95**, 183001 (2005)

[72] P. Beiersdorfer, A.L. Osterheld, J.H. Scofield, J.R. Crespo López-Urrutia, and K. Widmann, *Measurement of QED and Hyperfine Splitting in the* $2s_{1/2}$–$2p_{3/2}$ *X-Ray Transition in Li-like* $^{209}Bi^{80+}$ Phys. Rev. Lett. **80**, 3022 (1998)

[73] J. Vollbrecht, Z. Andelkovic, A. Dax, W. Geithner, C. Geppert, C. Gorges, M. Hammen, V. Hannen, S. Kaufmann, K. König, Y. Litvinov, M. Lochmann, B. Maaß, J. Meisner, T. Murböck, W. Nörtershäuser, R. Sánchez2, S. Schmidt, M. Schmidt, M. Steck, T. Stöhlker, R.C. Thompson, J. Ullmann and C. Weinheimer, *Laser spectroscopy of the ground-state hyperfine structure in H-like and Li-like bismuth*, J. Phys.: Conf. Ser. **583**, 012002 (2015)

[74] R. Jöhren, *Spectroscopy of the hyperfine transition in lithium-like bismuth at the ESR at GSI and an APD-based single-photon detector for laser spectroscopy on highly charged ions*, PhD dissertation, Münster (2013)

[75] J.H. Wesenberg, R.J. Epstein, D. Leibfried, R.B. Blakestad, J. Britton, J.P. Home, W.M. Itano, J.D. Jost, E. Knill, C. Langer, R. Ozeri, S. Seidelin, and D.J. Wineland, *Fluorescence during Doppler cooling of a single trapped atom*, Phys. Rev. A **76**, 053416 (2007)

[76] F. G. Major, V. N. Gheorge, and G. Werth, *Charged Particle Traps*, Springer (2005)

[77] M. König, G. Bollen, H.-J. Kluge b, T. Otto, and J. Szerypo, *Quadrupole excitation of stored ion motion at the true cyclotron frequency*, Int. J. Mass Spectrom. **142**, 95 (1995)

[78] M. Kretzschmar, *Calculating damping effects for the ion motion in a Penning trap*, Eur. Phys. J. D **48**, 313 (2008)

[79] S. George, K. Blaum, M. Block, M. Breitenfeldt, M. Dworschak, F. Herfurth, A. Herlert, M. Kowalska, M. Kretzschmar, E. Minaya Ramirez, D. Neidherr, S. Schwarz, and L. Schweikhard, *Damping effects in Penning trap mass spectrometry*, Int. J. Mass Spectrom. **299**, 102 (2011)

[80] E.W. McDaniel and E.A. Mason, *The Mobility and Diffusion of Ions in Gases*, Wiley, New York (1973)

[81] L. Chanin and M. Biondi, *Mobilities of Mercury Ions in Helium, Neon, and Argon*, Phys. Rev. **107**, 1219 (1957)

[82] A. M. Tyndall, *The Mobility of Positive Ions in Gases*, Cambridge University Press, Secs. 30, 31 (1938)

[83] M.J. Jensen, T. Hasegawa, and J.J. Bollinger, *Temperature and heating rate of ion crystals in Penning traps*, Phys. Rev. A **70**, 033401 (2004)

[84] D.H.E. Dubin and T.M. O'Neil, *Trapped nonneutral plasmas, liquids, and crystals (the thermal equilibrium states)*, Rev. Mod. Phys. **71**, 87 (1999)

[85] R.C. Thompson, G.P. Barwood, and P. Gill, *Progress Towards an Optical Frequency Standard Based on Ion Traps*, Appl. Phys. B **46**, 87 (1988)

[86] C.F. Driscoll and J.H. Malmberg, *Length-Dependent Containment of a Pure Electron-Plasma Column*, Phys. Rev. Lett. **50**, 167 (1983)

[87] C.F. Driscoll, K.S. Fine, and J.H. Malmberg, *Reduction of radial losses in a pure electron plasma*, Phys. Fluids **29**, 2015 (1986)

[88] D. Eggleston et al., *Collective Enhancement of Radial Transport in a Nonneutral Plasma*, Phys. Rev. Lett. **53**, 982 (1984)

[89] D. Eggleston and J. Malmberg, *Observation of an Induced-Scattering Instability Driven by Static Field Asymmetries in a Pure Electron Plasma*, Phys. Rev. Lett. **59**, 1675 (1987)

[90] D.J. Wineland, J.J. Bollinger, W.M. Itano, and J.D. Prestage, *Angular momentum of trapped atomic particles*, J. Opt. Soc. Am. B **2**, 1721 (1985)

[91] J.D. Crawford, T.M. O'Neil, and J.H. Malmberg, *Effect of Nonlinear Collective Processes on the Confinement of a Pure-Electron Plasma*, Phys. Rev. Lett. **54**, 697 (1985)

[92] J.D. Crawford and T.M. O'Neil, *Nonlinear collective processes on the confinement of a pure-electron plasma*, Phys. Fluids **30**, 2076 (1987)

[93] D.L. Eggleston and T.M. O'Neil, *Theory of asymmetry-induced transport in a non-neutral plasma*, Phys. Plasmas **6**, 2699 (1999)

[94] T. Hänsch and A. Schawlow, *Cooling of gases by laser radiation*, Opt. Commun. **13**, 68 (1975)

[95] D.J. Wineland and H.G. Dehmelt, Bull. Am. Phys. Soc. **20**, 637 (1975)

[96] D. Leibfried, R. Blatt, C. Monroe, and D. Wineland, *Quantum dynamics of single trapped ions*, Rev. Mod. Phys. **75**, 281 (2003)

[97] S. Stenholm, *The semiclassical theory of laser cooling*, Rev. Mod. Phys. **58**, 699 (1986)

[98] Knünz, M. Herrmann, V. Batteiger, G. Saathoff, T. W. Hänsch, and Th. Udem, *Sub-milliKelvin spatial thermometry of a single Doppler cooled ion in a Paul trap*, Phys. Rev. A **85**, 023427 (2012)

[99] W. M. Itano and D. J. Wineland, *Laser cooling of ions stored in harmonic and Penning traps*, Phys. Rev. A **25**, 35 (1982)

[100] P.D. Lett, R.N. Watts, C.I. Westbrook, W.D. Phillips, P.L. Gould, and H.J. Metcalf, *Observation of Atoms Laser Cooled below the Doppler Limit*, Phys. Rev. Lett. **61**, 169 (1988)

[101] J. Dalibard and C. Cohen-Tannoudji, *Laser cooling below the Doppler limit by polarization gradients: simple theoretical models*, J. Opt. Soc. Am. B **6**, 2023 (1989)

[102] Z. Andelkovic, R. Cazan, W. Nörtershäuser, S. Bharadia, D.M. Segal, R.C. Thompson, R. Jöhren, J. Vollbrecht, V. Hannen, and M. Vogel, *Laser cooling of externally produced Mg ions in a Penning trap for sympathetic cooling of highly charged ions*, Phys. Rev. A **87**, 033423 (2013)

[103] R. Blümel, J.M. Chen, E. Peik, W. Quint, W. Schleich, Y.R. Shen, and H. Walther *Phase transitions of stores laser-cooled ions*, Nature **334**, 309 (1988)

[104] L. Hornekaer and M. Drewsen, *Formation process of large ion Coulomb crystals in linear Paul traps*, Phys. Rev. A **66**, 013412 (2002)

[105] S.B. Torrisi, J.W. Britton, J.G. Bohnet, and J.J. Bollinger, *Perpendicular laser cooling with a rotating-wall potential in a Penning trap*, Phys. Rev. A **93**, 043421 (2016)

[106] L.R. Brewer, J.D. Prestage, J.J. Bollinger, W.M. Itano, D.J. Larson, and D.J. Wineland, *Static properties of a non-neutral* $^9B^+$*-ion plasma*, Phys. Rev. A **38**, 859 (1988)

[107] S.L. Gilbert, J.J. Bollinger, and D.J. Wineland, *Shell-Structure Phase of Magnetically Confined Strongly Coupled Plasmas*, Phys. Rev. Lett. **60**, 2022 (1988)

[108] J.J. Bollinger, J.D. Prestage, W.M. Itano, and D.J. Wineland, *Laser-Cooled-Atomic Frequency Standard*, Phys. Rev. Lett. **54**, 1000 (1985)

[109] L. Gruber, *Cooling of Highly Charged Ions in a Penning Trap*, PhD dissertation, Livermore (2000)

[110] W.M. Itano, L.R. Brewer, D.J. Larson, and D.J. Wineland, *Perpendicular laser cooling of a rotating ion plasma in a Penning trap*, Phys. Rev. A **38**, 5698 (1988)

[111] T. Murböck, S. Schmidt, G. Birkl, W. Nörtershäuser, R.C. Thompson, and M. Vogel, *Rapid crystallization of externally produced ions in a Penning trap*, Phys. Rev. A **94**, 043410 (2016)

[112] F. Diedrich, E. Peik, J.M. Chen, W. Quint, and H. Walther, *Observation of a Phase Transition of Stored Laser-Cooled Ions*, Phys. Rev. Lett. **59**, 2931 (1987)

[113] D.H.E. Dubin, *Effect of correlations on the thermal equilibrium and normal modes of a non-neutral plasma*, Phys. Rev. E, **53**, 5268 (1996)

[114] G. Chabrier, N.W. Ashcroft, and H.E. DeWitt, *White dwarfs as quantum crystals*, Nature **360**, 48 (1992)

[115] M. Hernanz, E. García-Berro, J. Isern, R. Mochkovitch, L. Segratain, and G. Chabrier, *The influence of crystallization on the luminosity function of white dwarfs*, Astrophys. J. **434**, 652 (1994)

[116] J. Isern, E. García-Berro, M. Hernanz, and G. Chabrier, *The energetics of crystallizing white dwarfs revisited again*, Astrophys. J. **528**, 397 (2000)

[117] C.J. Pethick and A.Y. Potekhin, *Liquid crystals in the mantles of neutron stars*, Phys. Lett. B **427**, 7 (1998)

[118] N. Chamel and P. Haensel, *Physics of Neutron Star Crusts*, Living Rev. Relativity **11**, (2008) 10. [Online Article]: cited [07/30 2016], http://www.livingreviews.org/lrr-2008-10

[119] X.-P. Huang, J.J. Bollinger, T.B. Mitchell, and W.M. Itano, *Phase-Locked Rotation of Crystallized Non-neutral Plasmas by Rotating Electric Fields*, Phys. Rev. Lett. **80**, 73 (1998)

[120] J. Tan, J.J. Bollinger, B. Jelenkovic, and D.J. Wineland, *Long-Range Order in Laser-Cooled, Atomic-Ion Wigner Crystals Observed by Bragg Scattering*, Phys. Rev. Lett. **75**, 4198 (1995)

[121] S. Mavadia, J.F. Goodwin, G.Stutter, S.Bharadia, D.R. Crick, D.M. Segal, and R.C. Thompson, *Control of the conformations of ion Coulomb crystals in a Penning trap*, Nat. Commun. **4**, 2571 (2013)

[122] D.J. Wineland, J.C. Bergquist, W.M. Itano, J.J. Bollinger, and C.H. Manney, *Atomic-Ion Coulomb Clusters in an Ion Trap*, Phys. Rev. Lett., **59** 2935 (1987)

[123] B.J. Alder, and T.E. Wainwright, *Phase Transition for a Hard Sphere System*, J. Chem. Phys. **27**, 1208 (1957)

[124] S.G. Brush, H.L. Sahlin, and E. Teller, *Monte Carlo Study of a One-Component Plasma. I*, J. Chem. Phys. **45**, 2102 (1966)

[125] E.L. Pollock and J.P. Hansen, *Statistical Mechanics of Dense Ionized Matter. II. Equilibrium Properties and Melting Transition of the Crystallized One-Component Plasma*, Phys. Rev. A **8**, 3110 (1973)

[126] W.L. Slattery and G D. Doolen, *Improved equation of state for the classical one-component plasma*, Phys. Rev. A **21**, 2087 (1980)

[127] S. Ichimaru, H. Iyetomi, and S. Tanaka, *Statistical physics of dense plasmas: thermodynamics, transport coefficients and dynamic correlations*, Phys. Rep. **149**, 91 (1987)

[128] G.S. Stringfellow, H.E. DeWitt, W.L. Slattery, *Equation of state of the one-component plasma derived from precision Monte Carlo calculations*, Phys. Rev. A **41**, 1105 (1990)

[129] D.H.E. Dubin, *First-order anharmonic correction to the free energy of a Coulomb crystal in periodic boundary conditions*, Phys. Rev. A **42**, 4972 (1990)

[130] page 89 in [84]

[131] M.J. Jensen, T. Hasegawa, J.J. Bollinger, and D.H.E. Dubin, *Rapid Heating of a Strongly Coupled Plasma near the Solid-Liquid Phase Transition*, Phys. Rev. Lett. **94**, 025001 (2005)

[132] T.B. Mitchell, J.J. Bollinger, D.H.E. Dubin, X.-P. Huang, W.M. Itano, and R.H. Baughman, *Direct observations of structural phase transitions*, Science **282**, 1290 (1998)

[133] H. Totsuji, T. Kishimoto, C. Totsuji, and K. Tsuruta, *Competition between Two Forms of Ordering in Finite Coulomb Clusters*, Phys. Rev. Lett. **88**, 125002 (2002)

[134] S. Bharadia, *Towards Laser Spectroscopy of Highly Charged Ions: Dynamics of $^{40}Ca^{+}$ Ions in a Penning Trap*, Ph.D. dissertation, Imperial College London (2011)

[135] J.J. Bollinger, D.J. Heinzen, F.L. Moore, W.M. Itano, and D.J. Wineland, *Electrostatic modes of ion-trap-plasmas*, Phys. Rev. A **48**, 525 (1993)

[136] D.F.A. Winters, M. Vogel, D.M. Segal, and R.C. Thompson, *Electronic detection of charged particle effects in a Penning trap*, J. Phys. B **39**, 3131 (2006)

[137] R.C. Davidson, *Physics of Nonneutral Plasmas*, Frontiers in Physics **81**, (1990)

[138] X.-P. Huang, F. Anderegg, E.M. Hollmann, C.F. Driscoll, and T.M. O'Neil, *Steady-State Confinement of Non-neutral Plasmas by Rotating Electric Fields*, Phys. Rev. Lett. **78**, 875 (1997)

[139] S. Bharadia, M. Vogel, D.M. Segal, and R.C. Thompson, *Dynamics of laser-cooled Ca^{+} ions in a Penning trap with a rotating wall*, Appl. Phys. B **107**, 1105 (2012)

[140] L. Brillouin, *A theorem of Larmor and its importance for electrons in magnetic fields*, Phys. Rev. **67**, 260 (1945)

[141] T.M. O'Neil, *Centrifugal separation of a multispecies pure ion plasma*, Phys. Fluids **24**, 1447 (1981)

[142] D.J. Larson, J.C. Bergquist, J.J. Bollinger, W.M. Itano, and D.J. Wineland, *sympathetic Cooling of Trapped Ions: A Laser-Cooled Two-Species Nonneutral Ion Plasma*, Phys. Rev. Lett. **57**, 70 (1986)

[143] D.H.E. Dubin, *Correlation energies of simple bounded Coulomb lattices*, Phys. Rev. A **40**, 1140 (1989)

[144] C.B. Zhang, D. Offenberg, B. Roth, M.A. Wilson, and S. Schiller, *Molecular-dynamics simulations of cold single-species and multispecies ion ensembles in a linear Paul trap*, Phys. Rev. A **76**, 012719 (2007)

[145] A. Müller and E. Salzborn, *Scaling of cross sections for multiple electron transfer to highly charged ions colliding with atoms and molecules*, Phys. Lett. A **62**, 391 (1977)

[146] E. Justiniano, C.I. Cocke, T.J. Gray, R.Dubois, C. Can, and W. Waggoner, *Total cross sections for electron capture and transfer ionization by highly stripped, slow Ne, Ar, Kr, and Xe projectiles on helium* , Phys. Rev. A **29**, 1088 (1984)

[147] R. Mann, *Total One Electron Capture Cross Sections for Ar^{q+} and I^{I+} in Slow Collisions*, Z. Phys. D **3**, 85 (1986)

[148] P. Beckmann, *Statistical Distribution of the Amplitude and Phase of a Multiply Scattered Field*, J. Res. Natl. Bur. Stand. **66D, No. 3**, (1962)

[149] J.W. Strutt, 3rd B. Rayleigh, *The Theory of Sound*, Sec. 42d, 3d ed., London (1896)

[150] D.J. Wineland and H.G. Dehmelt, *Principles of the stored ion calorimeter*, J. Appl. Phys. **46**, 919 (1975)

[151] L. Spitzer, *Physics of Fully Ionized Gases*, Interscience Publishers, Inc., NewYork, (1956).

[152] W.M. MacDonald, M.N. Rosenbluth, and Wong Chuck, *Relaxation of a System of Particles with Coulomb Interactions*, Phys. Rev. **107**, 350 (1957)

[153] *NRL Plasma Formulary*, J.D. Huba, Beam Physics Branch, Plasma Physics Division, Naval Research Laboratory, Washington, DC 20375 (2013)

[154] H. Häffner, *Präparation einzelner hochgeladener Ionen in einer Penningfalle*, diploma thesis, Universität Mainz (1998)

[155] H. Häffner, *Präzisionsmessung des magnetischen Moments des Elektrons in wasserstoffähnlichem Kohlenstoff*, Ph.D. thesis, Universität Mainz (2000)

[156] M.A. van Eijkelenborg, M.E.M. Storkey, D.M. Segal, and R.C. Thompson, *Sympathetic cooling and detection of molecular ions in a Penning trap*, Phys. Rev. A **60**, 3903 (1999)

[157] S. Albrecht, S. Altenburg, C. Siegel, N. Herschbach and G. Birkl, *A laser system for the spectroscopy of highly charged bismuth ions*, Appl. Phys. B **107**, 1069 (2012)

[158] S. Albrecht, *Ein Lasersystem zur Spektroskopie von hochgeladenen Ionen, Tellurmolekülen und Rubidium-Rydberg-Zuständen*, Ph.D. dissertation, Technische Universität Darmstadt (2014)

[159] B.C. Fawcett, *Wavelengths and classification of emission lines due to* $2s^22p^n$-$2s2p^{n+1}$ *and* $2s^22p^n$-$2p^{n+1}$ *transitions,* $Z \leq 28$, Atomic Data and Nuclear Data Tables **16**, 135 (1975)

[160] K. Huang, *Energy-level scheme and transition probabilities of Al-like ions*, Atomic Data and Nuclear Data Tables, **34**, 1 (1986)

[161] C. Kohstall, S. Fritzsche, B. Fricke, and W.-D. Sepp, *Calculated level energies, transition probabilities, and lifetimes of silicon-like ions*, Atomic Data and Nuclear Data Tables **70**, 63 (1998)

[162] E. Saloman, *Energy levels and transition probabilities in the ground-state configuration of sulfur-like ions*, Atomic Data and Nuclear Data Tables **41**, 339 (1989)

[163] K.-N. Huang, Y.-K. Kim, and K.T. Cheng, *Energy-level scheme and transition probabilities of Cl-like ions*, Atomic Data and Nuclear Data Tables **28**, 355 (1983)

[164] Michal Fulem, Kvetoslav Ruzicka, Ctirad Cervinka, Marisa A.A. Rocha, Luis M.N.B.F. Santos, and R.F. Berg, *Recommended vapor pressure and thermophysical data for ferrocene*, J. Chem. Thermodynamics **57**, 530 (2013)

[165] https://en.wikipedia.org/wiki/Ferrocene dated October, 2016. The used graphics were released into the public domain.

[166] P. Beiersdorfer, S.B. Utter, K.L. Wong, J.R. Crespo López-Urrutia, J.A. Britten, H. Chen, C.L. Harris, R.S. Thoe, D.B. Thorn, and Elmar Träbert, M.G.H. Gustavsson, C. Forssén, and A.-M. Mårtensson-Pendrill, *Hyperfine structure of hydrogenlike thallium isotopes*, Phys. Rev. A **64**, 032506 (2001)

[167] N.D. Guise, J.N. Tan, S.M. Brewer, C.F. Fischer, and Per Jönsson, *Measurement of the Kr XVIII 3d $^2D_{5/2}$ lifetime at low energy in a unitary Penning trap*, Phys. Rev. A **89**, 040502(R) (2014)

[168] T.W. Graham Solomons, Craig B. Fryhle, *Organic Chemistry*, John Wiley & Sons.

[169] G. Gabrielse, D. Hanneke, T. Kinoshita, M. Nio, and B. Odom, *New Determination of the Fine Structure Constant from the Electron g Value and QED*, Phys. Rev. Lett. **97**, 030802 (2006)

[170] V. Gerginov, K. Calkins, C.E. Tanner, J.J. McFerran, S. Diddams, A. Bartels, and L. Hollberg, *Optical frequency measurements of 6s $^2S_{1/2}$—$6p^2P_{1/2}$ (D1) transitions in ^{133}Cs and their impact on the fine-structure constant*, Phys. Rev. A **73**, 032504 (2006)

[171] M. Weitz, A. Huber, F. Schmidt-Kaler, D. Leibfried, W. Vassen, C. Zimmermann, K. Pachucki, and T.W. Hf̈ansch, *Precision measurement of the 1S ground-state Lamb shift in atomic hydrogen and deuterium by frequency comparison*, Phys. Rev. A **52**, 2664 (1995)

[172] J. Gillaspy (ed.), *Trapping Highly Charged Ions: Fundamentals and Applications*, Nova Science Publishers, New York, ISBN 1- 56072-725-X (1999)

[173] V. Fisher, Yu. Ralchenko, A. Goldgirsh, D. Fisher, and Y. Maron, *A scaling of multiple ionization cross sections*, J. Phys. B **28**, 3027 (1995)

[174] W. Demtröder, *Laserspektroskopie*, 5. Auflage, Springer-Verlag Berlin Heidelberg (2007)

[175] http://webbook.nist.gov

[176] http://quantummechanics.ucsd.edu/ph130a/130_notes/node422.html, Jim Branson, University of California, San Diego, lecture notes on quantum physics.

List of Figures

1.1 Expectation value of the electric field in the 1s ground state. 4

2.1 Technical drawing of the HITRAP platform. 14
2.2 Schematic drawing of an EBIS. 15
2.3 TOF signal of Ar^{n+} ions produced with different breeding times. 16
2.4 To-scale drawing of the HITRAP low-energy beamline. 17
2.5 Beam profiles at DK5 and DT1 efficiency. 19
2.6 Drawing of the SpecTrap magnet and beamline. 20
2.7 DT2 efficiency for Ar^{13+} deceleration. 21
2.8 Schematic of the ion source and its electric configuration. 22
2.9 The potential inside the Mg-source grid, and a TOF spectrum of ions produced from residual gas. 24
2.10 SIMION simulation of the electron emission from the filament. 25
2.11 TOF spectrum of Mg^+, and histograms of Mg^+ TOFs and kinetic energies. 26
2.12 Mg^+ production depending on the grid-pulse duration and e^- emission. 27
2.13 SpecTrap magnet cross section and Penning trap drawing. 28
2.14 Penning trap and the motion of a single ion. 32
2.15 Drawing of the SpecTrap Penning trap. 34
2.16 Measurements of C_2^i for endcap and correction electrodes. 39
2.17 Shift of the axial cloud position in an asymmetric potential. 41
2.18 Equivalent circuit diagram of the resonant circuits with amplifiers. . . . 45
2.19 Johnson-noise at 4 K of the lower and upper resonant circuit. 46
2.20 Geometry function G, and effective electrode distance D. 48
2.21 Axial Mg^+ excitation by induced excitation of the resonant circuit. . . 49
2.22 Experimental componont and control. 51
2.23 Trap potential during the capture process and accumulation of Mg^+. . 53
2.24 Ion deceleration with elevated trap potential without magnetic field. . 54
2.25 Ion deceleration with elevated trap potential with magnetic field. . . . 56
2.26 The SpecTrap imaging system. 58
2.27 Level scheme of Mg^+ and Zeeman shifts. 59
2.28 Fluorescence of a single Mg^+ ion. 61
2.29 Emission profiles of π- and $\sigma^{\pm}$-transitions in a magnetic field. 62
2.30 Histogram of Mg^+ single-ion fluorescence. 63

3.1 Buffer gas cooling time for Mg^+ ions. 66
3.2 Doppler broadening and temperature of Mg^+. 70
3.3 Doppler shift distribution for a harmonic oscillator. 72

3.4 Optimum detuning for laser cooling. 73
3.5 Laser cooling for an axially irradiated laser beam. 74
3.6 Mg^+ fluorescence and temperature after injection. 75
3.7 Mg^+ fluorescence with various laser parameters. 77
3.8 Doppler-cooling peak depending on various cooling parameters. 77
3.9 Cooling and heating rates for a Mg^+ ion trapped in a harmonic potential. 79

4.1 Phase diagram of the plasma parameter Γ_p. 82
4.2 Forces acting on a single ion in a Penning trap. 84
4.3 Plasma density depending on the rotation frequency, and Penning trap frequencies depending on the trapping potential. 86
4.4 The space charge potential parameters a and b as a function of the aspect ratio and the rotation frequency. 87
4.5 The aspect ratio α as a function of the rotation frequency ω_r. 88
4.6 Strength of centrifugal separation depending on the cloud temperature. 89
4.7 Energy per particel and shell distance in the planer-shell model. 91
4.8 Visualization of the vertical cross section through a planer-shell crystal. 92
4.9 Images of a Mg^+ crystal with shell structure. 93
4.10 Temporal evolution of a Mg^+ ion crystal. 93
4.11 Images of an ion cloud containing Mg^+ and CO_2^+ ions. 96
4.12 Ion cloud containing Mg^+ and N_2^+. 97
4.13 Images of an ion cloud containing Mg^+ and C^+ ions. 98
4.14 Images of an ion cloud containing Mg^+ and H_2^+ ions. 98
4.15 Ar^{3+} storage time. 101
4.16 Charge-transfer cross sections and storage times for argon ions. 102

5.1 Resonant circuit signals of Mg^+. 106
5.2 The energy dependence of the axial oscillation frequency ω_z of $^{24}Mg^+$. 107
5.3 Spectrum with resonant circuit after injection of Ar^{13+} and Ar^{4+}. 108
5.4 Time evolution of resonant circuit signals of Ar^+ and Mg^+. 109
5.5 Motion of two ions during resistive cooling. 114
5.6 The frequency shift $\Delta\omega_z(r)$ in dependence on the E and r. 119
5.7 Simulation of resistive cooling with constant coupling rates. 122
5.8 Resistive cooling signals of 30 C^{5+} ions. 123
5.9 Simulation of the resistive cooling of 30 C^+ ions. 125

6.1 Vapor pressure of ferrocene. 130

A.1 Digital-trigger processing for ion capture. 134
A.2 Cross section for electron impact ionization. 136
A.3 Focal-length wavelength dependence of the lens for fluorescence imaging. 141

List of Tables

1.1 Selection rules for atomic transisitions. 8
1.2 Hyperfine structure in ^{209}Bi^{82+} and ^{209}Bi^{80+}. 10

2.1 Magnetic field measurements. 29
2.2 Penning trap oscillation frequencies for typical trapping-parameters. . 33
2.3 Coefficients C_n^i obtained from numerical simulation. 38
2.4 Experimentally obtained values for coefficients C_n^i. 40
2.5 Cut-off frequencies of the filters to the trap electrodes. 42
2.6 Characteristics of the upper and lower resonant circuit. 46
2.7 Optical-regime transitions in selected ions. 64
2.8 Signal rates for HCI. 64

4.1 Electron transfer from He to Ar at low kinetic energies. 102

6.1 Optical transitions in high-Z highly charged ions. 130
6.2 Ground-state fine structure transitions of medium-Z HCI in the laser-accessible regime. 132

A.1 QED contributions to the free electron g-factor. 133
A.2 Contributions to the Lamb shift in hydrogen and H-like uranium. . . . 133
A.3 Positions of beamline elements of the HITRAP and SpecTrap beamline. 135
A.4 EBIS settings for production of Ar^{13+}. 135
A.5 Voltages of the segmented einzel lens after the EBIS. 135
A.6 Voltages of the dipole kicker-bender between DK3 and DK4. 136
A.7 Quadrupole doublet settings of the low-energy beamline. 136
A.8 Parameters for Ar^{n+} production in the EBIS. 137
A.9 Expansion coefficients C_n^i for individual electrodes. 138
A.10 Voltages for resonant circuit detection of various ion species. 139
A.11 Zeeman shift in ^{24}Mg^{+} ions. 140
A.12 Specifications of the laser system for Mg^{+} laser cooling. 140
A.13 Detection efficiency of the SpecTrap imaging system. 141

Curriculum Vitae

Personal data	Tobias Murböck
	born 08. October 1986, Recklinghausen

Graduation

10/2011–12/2016	Graduation in the group of Prof. Dr. Gerhard Birkl, Institut für Angewandte Physik, Technische Universität Darmstadt Thesis title: *Preparation and cooling of magnesium ion crystals for sympathetic cooling of highly charged ions in a Penning trap*

University education

10/2005–02/2011	Studies of physics, Philipps-Universität Marburg
10/2010–02/2011	Diploma thesis in the group of Prof. Dr. Gregor Witte, Philipps-Universität Marburg Thesis title: *Herstellung und Charakterisierung ultradünner Phthalocyanin-Filme und deren Metallisierung*
02/2011	Diplom

School education

06/2005	Abitur at the Theodor-Heuss-Gymnasium, Recklinghausen

Erklärung zur Dissertation

Hiermit versichere ich, die vorliegende Dissertation ohne Hilfe Dritter nur mit den angegebenen Quellen und Hilfsmitteln angefertigt zu haben. Alle Stellen, die aus Quellen entnommen wurden, sind als solche kenntlich gemacht. Diese Arbeit hat in gleicher oder ähnlicher Form noch keiner Prüfungsbehörde vorgelegen.

Darmstadt, den

(Tobias Murböck)